

JOINT INSTITUTE FOR AERONAUTICS AND ACOUSTICS

NASA-CR-201449

National Aeronautics and
Space Administration

Ames Research Center

JIAA TR 114



Stanford University

STUDY OF THE VELOCITY GRADIENT TENSOR IN TURBULENT FLOW

Wei-Ping Cheng and Brian Cantwell

*Department of Aeronautics and Astronautics
Stanford University
Stanford, CA 94305*

June 1996

Abstract

The behavior of the velocity gradient tensor, $A_{ij} = \partial u_i / \partial x_j$, was studied using three turbulent flows obtained from Direct Numerical Simulation. The flows studied were: an inviscid calculation of the interaction between two vortex tubes, a homogeneous isotropic flow, and a temporally evolving planar wake. Self-similar behavior for each flow was obtained when A_{ij} was normalized with the mean strain rate. The case of the interaction between two vortex tubes revealed a finite-sized coherent structure with topological characteristics predictable by a Restricted Euler model. This structure was found to evolve with the peak vorticity as the flow approached singularity. Invariants of A_{ij} within this structure followed a straight line relationship of the form: $\lambda^3 + \lambda Q + R = 0$, where Q and R are the second and third invariants of A_{ij} , and the eigenvalue λ is nearly constant over the volume of this structure. Data within this structure have local strain topology of unstable-node/saddle/saddle. The characteristics of the velocity gradient tensor and the anisotropic part of a related acceleration gradient tensor H_{ij} were also studied for a homogeneous isotropic flow and a temporally evolving planar wake. It was found that the intermediate principal eigenvalue of the rate-of-strain tensor of H_{ij} tended to be negative, with local strain topology of the type stable-node/saddle/saddle. There was also a preferential alignment between the equivalent vorticity vector and this intermediate principal eigenvalue direction. The magnitude of H_{ij} in the wake flow was found to be very small when data were conditioned at high local dissipation regions. This result was not observed in the relatively low Reynolds number simulation of homogeneous isotropic flow. A Restricted Euler model of the evolution of A_{ij} was found to reproduce many of the topological features identified in the simulations.

Acknowledgments

Many people were involved in making this report successful, and we are thankful to each and everyone of them:

- Professors Peter Bradshaw, Sanjiva Lele and Nicholas Rott, for their invaluable inputs and comments.
- Rolf Sondergaard, for his support and suggestions.
- Robert M. Kerr, for sharing his very interesting simulation data and helping us with access to the computing facilities in the National Center for Atmospheric Research (NCAR).
- Nagi Mansour, for help using the computing facilities in the National Aeronautics and Space Administration (NASA) for my research.
- The Singapore government, for awarding Wei-Ping Cheng the scholarship to pursue a Ph.D. at Stanford University.
- The support provided by the Joint Institute for Aeronautics and Acoustics (JIAA).

Contents

Abstract

Acknowledgement

Nomenclature

1	Introduction	1
1.1	Background	1
1.2	Time-averaged turbulence models	2
1.3	Motivation	3
1.4	Previous studies of the velocity gradient tensor	4
1.5	Classification of local flow topology	9
1.5.1	Invariants of the velocity gradient tensor	10
1.5.2	General three-dimensional flows	10
1.5.3	Incompressible three-dimensional flows	11
1.5.4	Construction of a typical Q - R invariant plot	12
1.5.5	Invariants of the rate-of-strain and rate-of-rotation tensors	14
1.5.6	Physical meanings of various invariants	15
1.6	Outline of thesis	16
2	Equations for the velocity gradient tensor	19
2.1	Introduction	19
2.2	The Restricted Euler model	21
2.2.1	Analytical solutions of $q(\tau)$ and $r(\tau)$	22

2.2.2	Analytical solution of $a_{ij}(\tau)$	23
2.2.3	Numerical procedure in obtaining $A_{ij}(t)$	24
2.2.4	Asymptotic solution of $a_{ij}(\tau)$	25
2.3	Gradient tensor evolving with the Restricted Euler model	28
2.3.1	Evolution of a_{ij}	29
2.3.2	Evolution towards the asymptotic solution	30
2.3.3	Evolution of dimensional A_{ij}	32
3	Inviscid interaction of vortex tubes	43
3.1	Introduction	43
3.2	Brief description of the flow	44
3.2.1	Numerical method	45
3.2.2	Initial condition	45
3.3	Classification of local flow topologies	45
3.3.1	Classification of local flow topologies for identified data points	51
3.3.2	Classification of local flow topologies for data points with different $Q_w/(R_s - R)$ slopes	58
3.3.3	Classification of local flow topologies for other interesting structures	72
4	Homogeneous isotropic flow	79
4.1	Approach	79
4.1.1	Derivation of governing equation	80
4.1.2	Numerical method	82
4.1.3	Initial condition	84
4.1.4	Accuracy and Stability analysis	85
4.1.5	Aliasing errors	88
4.2	Classification of local flow topologies of A_{ij} tensor	88
4.2.1	Effects of conditioning with local dissipation	93
4.2.2	Strain-rate distribution	102
4.2.3	Vorticity-strain alignment	102
4.3	Validation of the pressure Hessian tensor	104

4.4	Classification of local flow topologies of H_{ij}	106
4.4.1	Contribution from components of H_{ij}	114
4.4.2	Effects of conditioning with local dissipation	115
4.4.3	Acceleration strain-rate distribution	115
4.4.4	Equivalent vorticity - acceleration strain alignment	115
5	Temporally evolving plane wake	121
5.1	Introduction	121
5.2	Brief description of the flow	122
5.2.1	Numerical method	122
5.2.2	Initial condition	123
5.3	Classification of local flow topologies of A_{ij}	123
5.4	Classification of local flow topologies of H_{ij}	126
5.4.1	Effects of Reynolds number	135
5.4.2	Effects of conditioning with local dissipation	135
5.4.3	Effects of conditioning with local enstrophy density	144
5.4.4	Acceleration strain-rate distribution	161
5.4.5	Equivalent vorticity-acceleration strain alignment	161
6	Conclusions	171
A	Velocity gradient tensor with random components	173
B	De-aliasing technique	177
C	Energy and velocity derivatives spectra	181
D	Acceleration gradient tensor of Burgers vortex	185
D.1	The velocity gradient tensor A_{ij}	185
D.2	The acceleration gradient tensor, H_{ij}	186
D.3	Behavior of $Q(H_{ij})$ and $R(H_{ij})$ with r	188

List of Tables

3.1	Values of λ corresponding to selected slopes.	65
-----	---	----

List of Figures

1.1	Contour plot of iso-ensrophy surfaces in an evolving plane wake. \rightarrow indicates free stream flow direction.	5
1.2	y - z plane in the evolving planar wake showing contour plots of (a) local ensrophy density. (b) dissipation.	6
1.3	Three dimensional topologies in Q - R ($P = 0$) invariant space	12
1.4	A typical contour plot of joint pdf of Q vs R	13
1.5	Contour plots of iso-ensrophy surfaces. (a) Inviscid calculation of interaction between two vortex tubes. (b) Homogeneous isotropic flow in a periodic box.	17
2.1	Relationships between invariants of K_{ij} tensor. (a) Q vs R . (b) Q_s vs R_s . (c) $-Q_s$ vs Q_w . (d) Q_w vs $(R_s - R)$	27
2.2	Time evolution of Q vs R . A_{ij} normalized by local discriminant so that all data points must lie on three separate curves with discriminant $D = +1$, $D = 0$ or $D = -1$. (a) $t=0.0$. (b) $t=2.0$. (c) $t=5.0$. (d) $t=10.0$	31
2.3	Time evolution Q vs R . A_{ij} normalized by local discriminant and local $R^{1/3}$ so that all data points must lie on the line $R = 1.0$. (a) $t=0.0$. (b) $t=5.0$. (c) $t=10.0$. (d) $t=20.0$	33
2.4	Time evolution of Q_s vs R_s . A_{ij} normalized by local discriminant and local $R^{1/3}$. (a) $t=0.0$. (b) $t=5.0$. (c) $t=10.0$. (d) $t=20.0$	34
2.5	Time evolution of $-Q_s$ vs Q_w . A_{ij} normalized by local discriminant and local $R^{1/3}$. (a) $t=0.0$. (b) $t=5.0$. (c) $t=10.0$. (d) $t=20.0$	35

2.6	Time evolution of Q_w vs $(R_s - R)$. A_{ij} normalized by local discriminant and local $R^{1/3}$. (a) $t=0.0$. (b) $t=5.0$. (c) $t=10.0$. (d) $t=20.0$	36
2.7	Time evolution of logarithmic contour plots of joint pdf of Q vs R . A_{ij} is not normalized. (a) $t=0.0$. (b) $t=0.2$. (c) $t=0.5$. (d) $t=1.0$	39
2.8	Time evolution of logarithmic contour plots of joint pdf of Q_s vs R_s . A_{ij} is not normalized. (a) $t=0.0$. (b) $t=0.2$. (c) $t=0.5$. (d) $t=1.0$	40
2.9	Time evolution of logarithmic contour plots of joint pdf of $-Q_s$ vs Q_w . A_{ij} not normalized. (a) $t=0.0$. (b) $t=0.2$. (c) $t=0.5$. (d) $t=1.0$	41
2.10	Time evolution of logarithmic contour plots of joint pdf of Q_w vs $(R_s - R)$. A_{ij} is not normalized. (a) $t=0.0$. (b) $t=0.2$. (c) $t=0.5$. (d) $t=1.0$	42
3.1	The anti-parallel vortex tubes at initial condition.	44
3.2	Contour plot of iso- ϵ density surfaces in a domain surrounding the peak vorticity.	47
3.3	Time evolution of logarithmic contour plots of joint pdf of Q vs R for un-normalized A_{ij} . (a) $\tau = 12.5$. (b) $\tau = 15.0$. (c) $\tau = 17.0$. (d) $\tau = 17.5$	49
3.4	Time evolution of logarithmic contour plots of joint pdf of Q_s vs R_s for un-normalized A_{ij} . (a) $\tau = 12.5$. (b) $\tau = 15.0$. (c) $\tau = 17.0$. (d) $\tau = 17.5$	50
3.5	Time evolution of logarithmic contour plots of joint pdf of Q vs R . (a) $\tau = 12.5$. (b) $\tau = 15.0$. (c) $\tau = 17.0$. (d) $\tau = 17.5$	52
3.6	Time evolution of logarithmic contour plots of joint pdf of Q_s vs R_s . (a) $\tau = 12.5$. (b) $\tau = 15.0$. (c) $\tau = 17.0$. (d) $\tau = 17.5$	53
3.7	Time evolution of logarithmic contour plots of joint pdf of Q_s vs R_s . (a) $\tau = 12.5, \gamma/\alpha = -1.287$. (b) $\tau = 15.0, \gamma/\alpha = -1.256$. (c) $\tau = 17.0, \gamma/\alpha = -1.227$. (d) $\tau = 17.5, \gamma/\alpha = -1.173$	54
3.8	Time evolution of logarithmic contour plots of joint pdf of $-Q_s$ vs Q_w . (a) $\tau = 12.5$. (b) $\tau = 15.0$. (c) $\tau = 17.0$. (d) $\tau = 17.5$	55
3.9	Time evolution of logarithmic contour plots of joint pdf of Q_w vs $(R_s - R)$. (a) $\tau = 12.5$. (b) $\tau = 15.0$. (c) $\tau = 17.0$. (d) $\tau = 17.5$	56

3.10	Invariant plots of the identified data points with $Q_w/(R_s - R) \doteq 2.30$. (a) Q vs R . (b) Q_s vs R_s . (c) $-Q_s$ vs Q_w . (d) Q_w vs $(R_s - R)$	59
3.11	Principal eigenvalues of identified data points with $Q_w/(R_s - R) \doteq 2.30$. $x:\alpha$, $o:\beta$ and $+: \gamma$. (a) rate-of-strain tensor S_{ij} . $\bar{\beta} = 0.40$. (b) velocity gradient tensor A_{ij} . $\bar{\alpha} = 0.40$	60
3.12	Linear lines that best-fit the identified data points with $Q_w/(R_s - R) \doteq$ 2.30. (a) $-Q_s = 0.89Q_w + 0.41$. (b) $Q_w = 2.30(R_s - R)$	61
3.13	Q_s vs R_s for data points that lie on the right boundary of the Q_w vs $(R_s - R)$ plot. Equation of straight line: $0.40^3 + 0.40Q_s + R_s = 0$. (a) $\tau = 12.5$. (b) $\tau = 15.0$. (c) $\tau = 17.0$. (d) $\tau = 17.5$	62
3.14	Time evolution of the contour plots of local enstrophy density in the symmetry plane. Contour levels range from 0.445 to 4.45 at interval of 0.445. $+$: data points that lie on the right boundary of the Q_w vs $(R_s - R)$ plots. (a) $\tau = 12.5$. (b) $\tau = 15.0$. (c) $\tau = 17.0$. (d) $\tau = 17.5$	63
3.15	Q vs R for data points with various $Q_w/(R_s - R)$ slopes. (a) 5.00. (b) ∞ . (c) -8.00. (d) -4.40.	66
3.16	Q_s vs R_s for data points with various $Q_w/(R_s - R)$ slopes. (a) 5.00. (b) ∞ . (c) -8.00. (d) -4.40.	67
3.17	Principal eigenvalues of data points with $Q_w/(R_s - R) \doteq -4.4$. $x:\alpha$, $o:\beta$ and $+: \gamma$. (a) rate-of-strain tensor S_{ij} . (b) velocity gradient tensor A_{ij}	68
3.18	$-Q_s$ vs Q_w for data points with various $Q_w/(R_s - R)$ slopes. (a) 5.00. (b) ∞ . (c) -8.00. (d) -4.40.	69
3.19	Q_w vs $(R_s - R)$ for data points with various $Q_w/(R_s - R)$ slopes. (a) 5.00. (b) ∞ . (c) -8.00. (d) -4.40.	70
3.20	Contour plots of local enstrophy density in the symmetry plane. Con- tour levels range from 0.445 to 4.45 at interval of 0.445. $+$: data points with various $Q_w/(R_s - R)$ slopes. (a) 5.00. (b) ∞ . (c) -8.00. (d) -4.40.	71
3.21	Data points with $Q_w \leq 5\%$ of $Q_w _{max}$. (a) Q vs R . (b) Q_s vs R_s . (c) $-Q_s$ vs Q_w . (d) Q_w vs $(R_s - R)$	74

3.22	Data points with $Q_w \geq 70\%$ of $Q_w _{max}$. (a) Q vs R . (b) Q_s vs R_s . (c) $-Q_s$ vs Q_w . (d) Q_w vs $(R_s - R)$	75
3.23	Data points with $ Q_s \geq 70\%$ of $ Q_s _{max}$. (a) Q vs R . (b) Q_s vs R_s . (c) $-Q_s$ vs Q_w . (d) Q_w vs $(R_s - R)$	76
3.24	Data points with $-Q_s \approx Q_w$. (a) Q vs R . (b) Q_s vs R_s . (c) $-Q_s$ vs Q_w . (d) Q_w vs $(R_s - R)$	77
3.25	Contour plots of enstrophy density in the symmetry plane. Contour levels range from 0.445 to 4.45 at interval of 0.445. +: data points with (a) $Q_w \leq 5\%Q_w _{max}$. (b) $Q_w \geq 70\%Q_w _{max}$. (c) $ Q_s \geq 70\% Q_s _{max}$. (d) $-Q_s \approx Q_w$	78
4.1	Initial energy spectrum.	86
4.2	Stability region for second order Adams-Bashforth marching scheme .	87
4.3	Aliasing error due to insufficient number of grid points used in Fourier transform. —: actual sine wave to be represented. 'o': Fourier coeffi- cients represented by the grid points. ---: "aliased" sine wave repre- sented by the grid points. (a) $\sin(3\theta)$. (b) $\sin(9\theta)$	89
4.4	Time history of (a) mean kinetic energy. (b) log-log plot of mean kinetic energy. (c) mean strain rate. (d) log-log plot of mean strain rate. (e) Taylor microscale Reynolds number. (f) log-log plot of Taylor microscale Reynolds number.	91
4.5	Iso-contour surfaces for homogeneous isotropic flow at $\tau = 5.30$. (a) lo- cal enstrophy density $ \omega = 2.8$. (b) local discriminant $D = 6.0$	92
4.6	Time evolution of logarithmic contour plots of joint pdf of Q vs R for A'_{ij} at (a) $\tau = 0.0$. (b) $\tau = 1.32$. (c) $\tau = 2.65$. (d) $\tau = 5.30$	94
4.7	Time evolution of logarithmic contour plots of joint pdf of Q_s vs R_s for A'_{ij} at (a) $\tau = 0.0$. (b) $\tau = 1.32$. (c) $\tau = 2.65$. (d) $\tau = 5.30$	95
4.8	Time evolution of logarithmic contour plots of joint pdf of Q vs R for A_{ij} at (a) $\tau = 0.0$. (b) $\tau = 1.32$. (c) $\tau = 2.65$. (d) $\tau = 5.30$	96
4.9	Time evolution of logarithmic contour plots of joint pdf of Q_s vs R_s for A_{ij} at (a) $\tau = 0.0$. (b) $\tau = 1.32$. (c) $\tau = 2.65$. (d) $\tau = 5.30$	97

4.10	Time evolution of logarithmic contour plots of joint pdf of $-Q_s$ vs Q_w for A_{ij} at (a) $\tau = 0.0$. (b) $\tau = 1.32$. (c) $\tau = 2.65$. (d) $\tau = 5.30$	98
4.11	Time evolution of logarithmic contour plots of joint pdf of Q_w vs $(R_s - R)$ for A_{ij} at (a) $\tau = 0.0$. (b) $\tau = 1.32$. (c) $\tau = 2.65$. (d) $\tau = 5.30$	99
4.12	Logarithmic contour plots of joint pdf of Q vs R for A_{ij} . $\tau = 5.3$. Data conditioned at various levels of maximum local dissipation. (a) 0% (All data points). (b) 25%. (c) 50%. (d) 75%.	100
4.13	Logarithmic contour plots of joint pdf of Q_s vs R_s for A_{ij} . $\tau = 5.3$. Data conditioned at various levels of maximum local dissipation. (a) 0% (All data points). (b) 25%. (c) 50%. (d) 75%.	101
4.14	Probability density function of principal strain-rates normalized by $ \beta $. $\tau = 5.30$. —: α . ---: β: γ . (a) All data points. (b) $ Q_s(A_{ij}) \geq 25\% Q_s(A_{ij}) _{max}$	103
4.15	Probability density function of cosine of angle θ between vorticity vector and principal strain-rate directions. $\tau = 5.30$. —: α . ---: β: γ . (a) All data points. (b) $ Q_s(A_{ij}) \geq 25\% Q_s(A_{ij}) _{max}$	105
4.16	Comparison of $Q(A_{ij})$ with $0.5P(P_{ij})$	106
4.17	Logarithmic contour plots of joint pdf of Q vs R for H_{ij} obtained using (a) time derivatives and product of A_{ij} . (b) pressure cross-derivatives and second derivative of A_{ij}	108
4.18	Time evolution of logarithmic contour plots of joint pdf of Q vs R for H_{ij} at (a) $\tau = 0.0$. (b) $\tau = 1.32$. (c) $\tau = 2.65$. (d) $\tau = 5.30$	110
4.19	Time evolution of logarithmic contour plots of joint pdf of Q_s vs R_s for H_{ij} at (a) $\tau = 0.0$. (b) $\tau = 1.32$. (c) $\tau = 2.65$. (d) $\tau = 5.30$	111
4.20	Time evolution of logarithmic contour plots of joint pdf of $-Q_s$ vs Q_w for H_{ij} at (a) $\tau = 0.0$. (b) $\tau = 1.32$. (c) $\tau = 2.65$. (d) $\tau = 5.30$	112
4.21	Time evolution of logarithmic contour plots of joint pdf of Q_w vs $(R_s - R)$ for H_{ij} at (a) $\tau = 0.0$ (b) $\tau = 1.32$ (c) $\tau = 2.65$ (d) $\tau = 5.30$	113
4.22	Logarithmic contour plots of joint pdf of Q vs R for (a) $-(\partial^2 p / \partial x_i \partial x_j - (\delta_{ij}/3)\partial^2 p / \partial x_k \partial x_k)$. (b) $\nu \partial^2 A_{ij} / \partial x_k \partial x_k$. $\tau = 5.30$	114

4.23	Logarithmic contour plots of joint pdf of Q vs R for H_{ij} . $\tau = 5.3$. Data conditioned at various levels of maximum local dissipation: (a) 0% (All data points). (b) 25%. (c) 50%. (d) 75%.	116
4.24	Logarithmic contour plots of joint pdf of Q_s vs R_s for H_{ij} . $\tau = 5.3$. Data conditioned at various levels of maximum local dissipation. (a) 0% (All data points). (b) 25%. (c) 50%. (d) 75%.	117
4.25	Probability density function of acceleration strain-rates normalized by $ \beta_h $. $\tau = 5.30$. —: α_h . ---: β_h . . . : γ_h . (a) All data points. (b) $ Q_s(A_{ij}) \geq 25\% Q_s(A_{ij}) _{max}$	118
4.26	Probability density function of cosine of angle θ between equivalent vorticity vector and the acceleration strain-rate directions. $\tau = 5.30$. —: α_h . ---: β_h . . . : γ_h . (a) All data points. (b) $ Q_s(A_{ij}) \geq 25\% Q_s(A_{ij}) _{max}$	120
5.1	Iso-contour surfaces for wk346 at $t = 102.7$. (a) local enstrophy density $ \omega = 2.8$. (b) local discriminant $D = 5.0$	125
5.2	Time evolution of logarithmic contour plots of joint pdf of Q vs R for wk346, A_{ij} . (a) $t=22.8$. (b) $t=52.8$. (c) $t=102.7$. (d) $t=204.8$	127
5.3	Time evolution of logarithmic contour plots of joint pdf of Q_s vs R_s for wk346, A_{ij} . (a) $t=22.8$. (b) $t=52.8$. (c) $t=102.7$. (d) $t=204.8$. . .	128
5.4	Time evolution of logarithmic contour plots of the joint pdf of $-Q_s$ vs Q_w for wk346, A_{ij} . (a) $t=22.8$. (b) $t=52.8$. (c) $t=102.7$. (d) $t=204.8$	129
5.5	Time evolution of logarithmic contour plots of joint pdf of Q_w vs $(R_s - R)$ for wk346, A_{ij} . (a) $t=22.8$. (b) $t=52.8$. (c) $t=102.7$. (d) $t=204.8$	130
5.6	Time evolution of logarithmic contour plots of joint pdf of Q vs R for wk2768, A_{ij} . (a) $t=99.8$. (b) $t=194.6$	131
5.7	Time evolution of logarithmic contour plots of the joint pdf of Q_s vs R_s for wk2768, A_{ij} . (a) $t=99.8$. (b) $t=194.6$	132
5.8	Time evolution of logarithmic contour plots of joint pdf of $-Q_s$ vs Q_w for wk2768, A_{ij} . (a) $t=99.8$. (b) $t=194.6$	133

5.9	Time evolution of logarithmic contour plots of joint pdf of Q_w vs $(R_s - R)$ for wk2768, A_{ij} . (a) $t=99.8$. (b) $t=194.6$	134
5.10	Time evolution of logarithmic contour plots of joint pdf of Q vs R for wk346, H_{ij} . (a) $t=102.7$. (b) $t=204.8$. (c) same as (b), with magnified axis scales.	136
5.11	Time evolution of logarithmic contour plots of joint pdf of Q_s vs R_s wk346, H_{ij} . (a) $t=102.7$. (b) $t=204.8$. (c) same as (b), with magnified axis scales.	137
5.12	Time evolution of logarithmic contour plots of joint pdf of $-Q_s$ vs Q_w for wk346, H_{ij} . (a) $t=102.7$. (b) $t=204.8$	138
5.13	Time evolution of logarithmic contour plots of joint pdf of Q_w vs $(R_s - R)$ for wk346, H_{ij} . (a) $t=102.7$. (b) $t=204.8$	139
5.14	Time evolution of logarithmic contour plots of the joint pdf of Q vs R for wk2768, H_{ij} . (a) $t=99.8$. (b) $t=194.6$	140
5.15	Time evolution of logarithmic contour plots of joint pdf of Q_s vs R_s for wk2768, H_{ij} . (a) $t=99.8$. (b) $t=194.6$	141
5.16	Time evolution of logarithmic contour plots of joint pdf of $-Q_s$ vs Q_w for wk2768, H_{ij} . (a) $t=99.8$. (b) $t=194.6$	142
5.17	Time evolution of logarithmic contour plots of joint pdf of Q_w vs $(R_s - R)$ for wk2768, H_{ij} . (a) $t=99.8$. (b) $t=194.6$	143
5.18	Logarithmic contour plots of joint pdf of Q vs R for wk346, H_{ij} . $t=102.7$. Data conditioned at various levels of maximum local dissipation. (a) 0% (All data points). (b) 25%. (c) 50%. (d) 75%. . . .	145
5.19	Logarithmic contour plots of joint pdf of Q_s vs R_s for wk346, H_{ij} . $t=102.7$. Data conditioned at various levels of maximum local dissipation. (a) 0% (All data points). (b) 25%. (c) 50%. (d) 75%.	146
5.20	Logarithmic contour plots of joint pdf of Q vs R for wk346, H_{ij} . $t=204.8$. Data conditioned at various levels of maximum local dissipation. (a) 0% (All data points). (b) 25%. (c) 50%. (d) 75%. . . .	147

5.21	Logarithmic contour plots of joint pdf of Q_s vs R_s for wk346, H_{ij} . t=204.8. Data conditioned at various levels of maximum local dissipation. (a) 0% (All data points). (b) 25%. (c) 50%. (d) 75%.	148
5.22	Logarithmic contour plots of joint pdf of Q vs R for wk2768, H_{ij} . t=99.8. Data conditioned at various levels of maximum local dissipation. (a) 0% (All data points). (b) 25%. (c) 50%. (d) 75%.	149
5.23	Logarithmic contour plots of joint pdf of Q_s vs R_s for wk2768, t=99.8. Data conditioned at various levels of maximum local dissipation. (a) 0% (All data points). (b) 25%. (c) 50%. (d) 75%.	150
5.24	Logarithmic contour plots of joint pdf of Q vs R for wk2768, H_{ij} . t=194.6. Data conditioned at various levels of maximum local dissipation. (a) 0% (All data points). (b) 25%. (c) 50%. (d) 75%.	151
5.25	Logarithmic contour plots of joint pdf of Q_s vs R_s for wk2768, H_{ij} . t=194.6. Data conditioned at various levels of maximum local dissipation. (a) 0% (All data points). (b) 25%. (c) 50%. (d) 75%.	152
5.26	Logarithmic contour plots of joint pdf of Q vs R for wk346, H_{ij} . t=102.7. Data conditioned at various levels of maximum local enstrophy density. (a) 0% (All data points). (b) 25%. (c) 50%. (d) 75%.	153
5.27	Logarithmic contour plots of joint pdf of Q_s vs R_s for wk346, H_{ij} . t=102.7. Data conditioned at various levels of maximum local enstrophy density. (a) 0% (All data points). (b) 25%. (c) 50%. (d) 75%.	154
5.28	Logarithmic contour plots of joint pdf of Q vs R for wk346, H_{ij} . t=204.8. Data conditioned at various levels of maximum local enstrophy density. (a) 0% (All data points). (b) 25%. (c) 50%. (d) 75%.	155
5.29	Logarithmic contour plots of joint pdf of Q_s vs R_s for wk346, H_{ij} . t=204.8. Data conditioned at various levels of maximum local enstrophy density. (a) 0% (All data points). (b) 25%. (c) 50%. (d) 75%.	156
5.30	Logarithmic contour plots of joint pdf of Q vs R for wk2768, H_{ij} . t=99.8. Data conditioned at various levels of maximum local enstrophy density. (a) 0% (All data points). (b) 25%. (c) 50%. (d) 75%.	157

5.31	Logarithmic contour plots of joint pdf of Q_s vs R_s for wk2768, H_{ij} . t=99.8. Data conditioned at various levels of maximum local enstrophy density. (a) 0% (All data points). (b) 25%. (c) 50%. (d) 75%.	158
5.32	Logarithmic contour plots of joint pdf of Q vs R for wk2768, H_{ij} . t=194.6. Data conditioned at various levels of maximum local en- strophy density. (a) 0% (All data points). (b) 25%. (c) 50%. (d) 75%.	159
5.33	Logarithmic contour plots of joint pdf of Q_s vs R_s for wk2768, H_{ij} . t=194.6. Data conditioned at various levels of maximum local (a) 0% (All data points). (b) 25%. (c) 50%. (d) 75%.	160
5.34	Probability density function of the principal acceleration strain-rates normalized by $ \beta_h $ for wk346, t=102.7. —: α_h . ---: β_h: γ_h . (a) All data points. (b) $ Q_s(A_{ij}) \geq 25\% Q_s(A_{ij}) _{max}$	162
5.35	Probability density function of the principal acceleration strain-rates normalized by $ \beta_h $ for wk346, t=204.8. —: α_h . ---: β_h: γ_h . (a) All data points. (b) $ Q_s(A_{ij}) \geq 25\% Q_s(A_{ij}) _{max}$	163
5.36	Probability density function of the principal acceleration strain-rates normalized by $ \beta_h $ for wk2768, t=99.8. —: α_h . ---: β_h: γ_h . (a) All data points. (b) $ Q_s(A_{ij}) \geq 25\% Q_s(A_{ij}) _{max}$	164
5.37	Probability density function of the principal acceleration strain-rates normalized by $ \beta_h $ for wk2768, t=194.6. —: α_h . ---: β_h: γ_h . (a) All data points. (b) $ Q_s(A_{ij}) \geq 25\% Q_s(A_{ij}) _{max}$	165
5.38	Probability density function of cosine of angle θ between the equivalent vorticity vector and the equivalent principal strain-rate directions for wk346, t=102.7. —: α_h . ---: β_h: γ_h . (a) All data points. (b) $ Q_s(A_{ij}) \geq 25\% Q_s(A_{ij}) _{max}$	167
5.39	Probability density function of cosine of angle θ between the equivalent vorticity vector and the equivalent principal strain-rate directions for wk346, t=204.8. —: α_h . ---: β_h: γ_h . (a) All data points. (b) $ Q_s(A_{ij}) \geq 25\% Q_s(A_{ij}) _{max}$	168

5.40	Probability density function of cosine of angle θ between the equivalent vorticity vector and the equivalent principal strain-rate directions for wk2768, $t=99.8$. —: α_h . ---: β_h: γ_h . (a) All data points. (b) $ Q_s(A_{ij}) \geq 25\% Q_s(A_{ij}) _{max}$	169
5.41	Probability density function of cosine of angle θ between the equivalent vorticity vector and the equivalent principal strain-rate directions for wk2768, $t=194.6$. —: α_h . ---: β_h: γ_h . (a) All data points. (b) $ Q_s(A_{ij}) \geq 25\% Q_s(A_{ij}) _{max}$	170
B.1	Region of retained Fourier modes defined by D	178
C.1	Energy and velocity gradient spectra for homogeneous isotropic flow at $\tau = 5.30$. \uparrow indicates the maximum wave number, k_{max} , resolved in the simulation. (a) —: energy spectrum. ---: Kolmogorov $k^{-5/3}$ scaling. (b) A_{ij} spectrum.	183
C.2	Spectra for the higher derivatives of the velocity gradient tensor for homogeneous isotropic flow at $\tau = 5.30$. \uparrow indicates the maximum wave number, k_{max} , resolved in the simulation. (a) $\partial A_{ij}/\partial x_m$ spectrum. (b) $\partial^2 A_{ij}/\partial x_m \partial x_m$ spectrum.	184
D.1	Normalized $Q(H_{ij})$ and $R(H_{ij})$ versus r . ●●●: $Re = 2$: $Re = 5$. ----: $Re = 10$. ---: $Re = 20$. —: $Re = 50$. (a) $Q(H_{ij})/Re^4$ vs r . (b) $R(H_{ij})/Re^6$ vs r	189
D.2	$Q(H_{ij})/Re^4$ versus $R(H_{ij})/Re^6$. ●●●: $Re = 2$: $Re = 5$. ----: $Re = 10$, ---: $Re = 20$. —: $Re = 50$	190

Chapter 1

Introduction

1.1 Background

Turbulence is one of the most complicated types of fluid motion. Turbulent flow is generally random, disordered and unpredictable, yet it is governed by the Navier-Stokes equations. Almost every fluid motion in nature, engineering applications, and everyday life contains turbulence. The magnificent photosphere of the Sun, the gigantic cloud systems that affect the Earth's weather pattern, the boundary layers growing on aircraft wings, the wakes of submarines, the pouring of cream into a cup of coffee, and the flight of a golf ball; all may contain turbulent motions.

In 1937, G. I. Taylor and T. Von Kármán[16] defined turbulence in the following way:

Turbulence is an *irregular* motion which in general makes its appearance in fluids, gaseous or liquid, when they flow past solid surfaces or even when neighboring streams of the same fluid flow past or over one another.

Hinze[14] formulated a more precise definition of turbulence:

Turbulent fluid motion is an irregular condition of flow in which the various quantities show a random variation with *time* and *space* coordinates, so that statistically distinct average values can be discerned.

According to Hinze, it is not sufficient to define turbulent motion as being irregular in time alone, but in space as well. Therefore, it is impossible to describe turbulent motion in all detail as a function of time and space coordinates. Instead, one has to rely on laws of probability and statistics. It is important to note that for any study of turbulence to be possible, one has to accept that no matter how confusing turbulence is, it must still be governed by laws of physics.

1.2 Time-averaged turbulence models

In the time-averaged (Reynolds-averaged) description of turbulence, the number of unknown variables is larger than the number of equations. At present, most turbulent models rely on intuition, experience and dimensional analysis in an attempt to close the system of governing equations.

Kline, Cantwell & Lilley[19] concluded that despite intensive computer-assisted activity in turbulence research, none of the existing modeling methods could predict a worthwhile range of perturbed shear layers with a constant set of empirical coefficients. Finding a “universal” turbulence model capable of predicting any flow to acceptable engineering accuracy remains a challenge to research scientists world-wide. Ferziger, Kline, Avva, Bordalo & Tzuoo[10] modified Kline’s “zonal” modeling into a framework for adjusting the coefficients of a chosen turbulence model from one part of the flow to another. A zone is defined as a region in which a chosen turbulence model will perform acceptably with a given set of coefficients, which may be functions of local parameters rather than absolute constants. It is usually an identifiable species of turbulent flow (e.g. boundary layer, wake or jet) or a *strong* perturbation of a given species, such as a shock-wave/boundary interaction. Zonal modeling is needed because current turbulent models cannot accurately simulate all the flows with a single set of coefficients. One of the most widely used turbulent models today is the “ $\kappa - \varepsilon$ ” model[26, 27]. Using transport equations for both the turbulent kinetic energy κ and dissipation ε , this model predicts some aspects of the behavior of turbulent flows adequately within its assumptions. Many existing turbulent models are variations of the “ $\kappa - \varepsilon$ ” model. The purpose of these models is to solve the Reynolds

averaged Navier-Stokes equations in the hope of predicting the general behavior of turbulent flows. This behavior depends strongly on the turbulent kinetic energy and dissipation, the later being governed by the instantaneous velocity gradient $\partial u_i / \partial x_j$ in the flow. A good understanding of this instantaneous velocity gradient tensor is therefore essential to the studies of turbulence.

1.3 Motivation

Instantaneous velocity gradient tensor, defined as $A_{ij} = \partial u_i / \partial x_j$, in a turbulent flow governs the behavior of the turbulent kinetic energy dissipation, ε . The transport equation for the turbulent kinetic energy is:

$$\frac{D\overline{q^2}}{Dt} = \underbrace{-\frac{\partial}{\partial x_k} \overline{u_k (p + q^2)}}_{\mathcal{D}} - \underbrace{\overline{u_i u_k} \frac{\partial \overline{U_i}}{\partial x_k}}_{\mathcal{P}} + \underbrace{\nu \left(\frac{\partial^2 \overline{u_i^2}}{\partial x_k^2} + \frac{\partial^2 \overline{u_i u_k}}{\partial x_i \partial x_k} \right)}_{\mathcal{V}} - \underbrace{\nu \frac{\partial u_i}{\partial x_j} \left(\frac{\partial u_i}{\partial x_j} + \frac{\partial u_j}{\partial x_i} \right)}_{\varepsilon}. \quad (1.1)$$

$q^2 = u_i u_i / 2$ is the turbulent kinetic energy while \mathcal{D} , \mathcal{P} , \mathcal{V} and ε are the convective diffusion, production, viscous diffusion and mean rate of dissipation of turbulent kinetic energy respectively.

Among these terms, ε is of the greatest interest since it is governed by the velocity gradient tensor, A_{ij} :

$$\varepsilon = \nu \overline{\frac{\partial u_i}{\partial x_j} \left(\frac{\partial u_i}{\partial x_j} + \frac{\partial u_j}{\partial x_i} \right)} = \nu \overline{A_{ij} (A_{ij} + A_{ji})}. \quad (1.2)$$

Dimensional analysis is applied to the transport equation for turbulent kinetic energy to obtain the relative scaling of A_{ij} . Both velocity fluctuation u_i , and the mean velocity U_i , scale with the free stream velocity U_o . Using this velocity scale U_o together with the mean flow length scale δ , the relative scaling of production \mathcal{P} is:

$$\mathcal{P} = \overline{u_i u_k} \frac{\partial \overline{U_i}}{\partial x_k} \sim \frac{U_o^3}{\delta}. \quad (1.3)$$

In most homogeneous shear flows, $\mathcal{P} \approx \varepsilon$. Hence,

$$\varepsilon = \nu \overline{A_{ij} (A_{ij} + A_{ji})} \sim \frac{U_o^3}{\delta}. \quad (1.4)$$

This relation implies that:

$$A_{ij}^2 \sim \frac{U_o \delta}{\nu} \cdot \frac{U_o^2}{\delta^2} \sim Re_\delta \cdot \left(\frac{U_o}{\delta} \right)^2. \quad (1.5)$$

Therefore,

$$A_{ij} \sim Re_\delta^{1/2} \cdot \frac{U_o}{\delta} \quad (1.6)$$

Dimensional arguments applied to the transport equation for turbulent kinetic energy indicates that the instantaneous velocity gradient is larger than the mean gradient U_o/δ by at least a factor of $Re_\delta^{1/2}$.

In addition to dissipation, velocity gradient tensor also governs the behavior of vorticity ω_i in turbulent flows:

$$\omega_i = \epsilon_{ijk} A_{kj}, \quad (1.7)$$

where ϵ_{ijk} is the alternating unit tensor such that:

$$\epsilon_{ijk} = \begin{cases} +1; & \text{if } ijk \text{ are in cyclic order } 123123 \\ -1; & \text{if } ijk \text{ are in anticyclic order } 321321 \\ 0; & \text{otherwise} \end{cases} \quad (1.8)$$

Figure 1.1 shows a contour plot of iso-entrophy (magnitude of vorticity) surfaces in a direct numerical simulation of an evolving planar wake[30]. Free stream flows from left to right, as indicated by the arrow. A cross section (y - z plane) is cut across the x -axis to illustrate the microscale regions. Figure 1.2 shows the contour plots of entrophy and dissipation along this cross section, looking along the flow direction. The highest contour is indicated in bright red. It is observed that the highest intensities of both vorticity and dissipation (hence velocity gradients) occur in regions with very small length scale compared to the mean flow.

1.4 Previous studies of the velocity gradient tensor

A considerable amount of research has been directed at understanding the instantaneous velocity gradient in turbulent flows. Large instantaneous velocity gradients

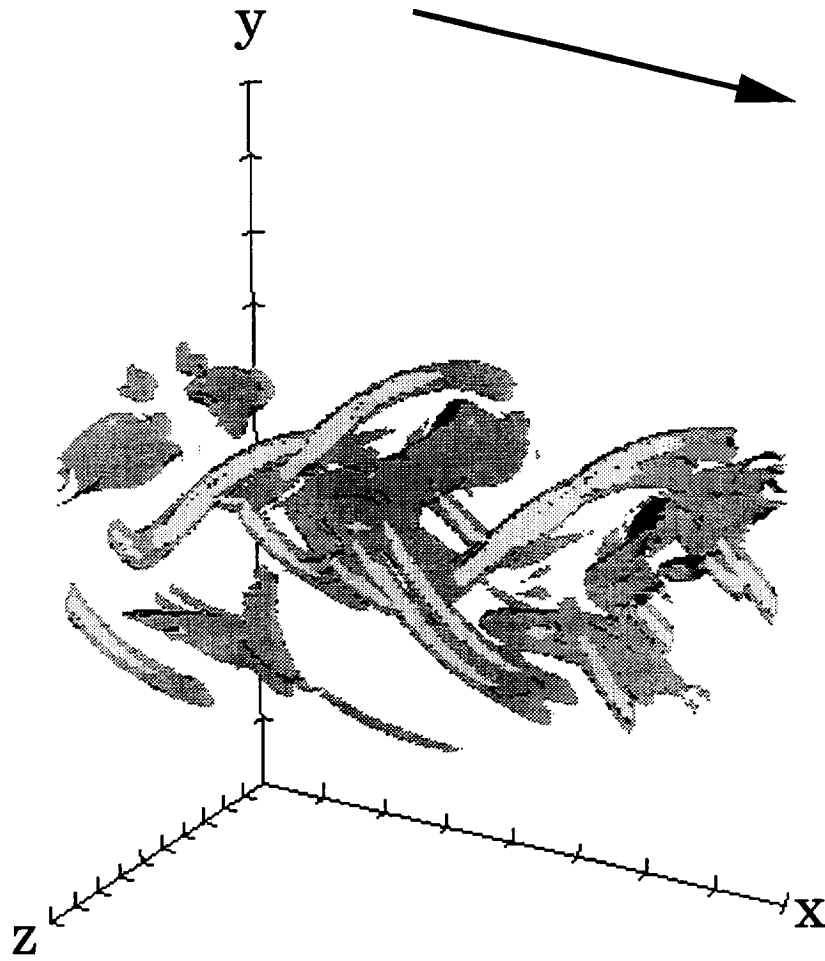
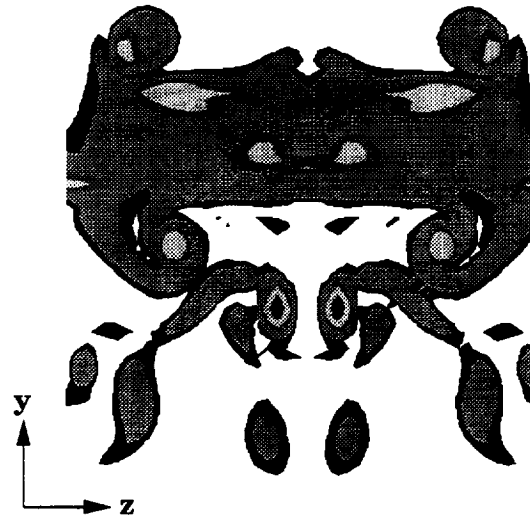
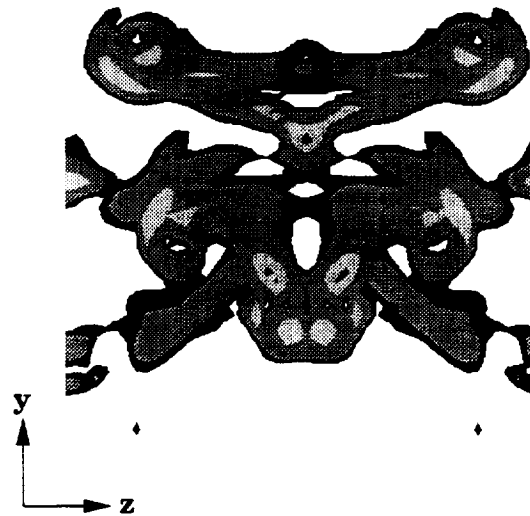


Figure 1.1: Contour plot of iso-entropy surfaces in an evolving plane wake. \rightarrow indicates free stream flow direction.



(a)



(b)

Figure 1.2: y - z plane in the evolving planar wake showing contour plots of (a) local enstrophy density. (b) dissipation.

usually occur in small-scale structures whose characteristic length scales are much smaller than the mean flow, as shown in figure 1.2.

Recent studies of small-scale structures using direct numerical simulations (DNS) and laboratory experiments suggested common behavior in the small scale velocity gradients; even when the large-scale motions are very different. Ashurst, Kerstein, Kerr & Gibson[1] studied the behavior of the velocity gradient in an incompressible, isotropic homogeneous flow in a periodic box by analyzing the velocity gradient tensor (each tensor consists of nine components of $\partial u_i / \partial x_j$) at each grid point in the flow. The study was done using direct numerical simulation, with Taylor microscale Reynolds number $Re_\lambda \approx 83$. By looking at the probability distribution function of the cosine of the angle between the vorticity vector and the three principal eigenvectors of the rate-of-strain tensor (the symmetric part of the velocity gradient tensor), they concluded that there was a strong preferential alignment of the vorticity vector with the intermediate eigenvector. This same conclusion was also reached by studying an incompressible homogeneous shear flow with similar Reynolds number. They also found that the principal eigenvalues of the rate-of-strain tensor (sorted in descending order such that $\alpha > \beta > \gamma$) have a preferred ratio of $\alpha : \beta : \gamma \approx 3 : 1 : -4$ in regions of high dissipations.

Vincent & Meneguzzi[35] performed a direct numerical simulation of a homogeneous isotropic turbulence at a higher Reynolds number, with $Re_\lambda \approx 150$ and $Re_L \approx 1000$. Visualization of the flow field at different times showed that the strongest vorticity in the flow was organized in very elongated thin tubes, in agreement with the findings of Ruetsch & Maxey[29] in a similar flow with $Re_\lambda \approx 60$. Vincent & Meneguzzi also concluded from this study that there is a preferential alignment of the vorticity vector with the intermediate principal eigenvector of the rate-of-strain tensor.

Soria, Sondergaard, Cantwell, Chong & Perry[31] studied the dissipating motions of an incompressible mixing layer with both laminar and turbulent initial conditions, at $Re_\delta \approx 250$. Their results showed that regardless of initial conditions, the bulk of the total kinetic energy dissipation is contributed by fluid structures with local strain rate topology characterized as unstable-node/saddle/saddle ($\alpha > \beta > \gamma; \beta > 0$).

Blackburn, Mansour & Cantwell[2] investigated the topological features of the velocity gradient field in turbulent channel flow. The Reynolds number of this simulation was $Re = 7860$, based on half channel width and the center-line velocity. In all regions of the flow, there was a strong preference for the vorticity to align with the intermediate principal eigenvector of the rate-of-strain tensor. Away from the wall regions, the intermediate principal eigenvalue of the rate-of-strain tensor (these principal eigenvalues are also known as strain rates) tends to be positive at sites of high viscous dissipation of kinetic energy. The velocity gradient tensor also showed preference for local flow topologies of unstable-node/saddle/saddle. They also used the discriminant of the velocity gradient tensor to identify flow structures which extends from very close to the wall to the free stream.

Tsinober, Kitt & Dracos[32] conducted laboratory experiments on turbulent grid flows and on the turbulent boundary layer over a smooth plate. To determine the invariant properties of the flows, all nine components of the velocity gradient tensor at every grid point in the flow were measured using a hot wire probe. In both flows, the probability density distribution of the alignment angle between the vorticity and the three principal eigenvectors of the rate-of-strain tensor was determined. As in the DNS studies mentioned above, they confirmed that there was a strong tendency for the vorticity to align itself with the intermediate eigenvector of the rate-of-strain tensor.

The DNS and experimental studies mentioned above demonstrated that small-scale motions exhibit common behavior even when the large-scale motions of various homogeneous turbulent flows are different. An analytical model capable of predicting the behavior of these small-scale motions would be very useful. To find such a model, an understanding of the behavior of the velocity gradient tensor in turbulent flows is essential. Jiménez[15] suggested a model which described the vorticity distribution of a stretched vortex tube. Using this model, Jiménez was able to explain the observed preferential alignment of the vorticity vector with the positive intermediate principal eigenvector of the strain-rate tensor using purely kinematic arguments. Girimaji & Pope[11] modelled the velocity gradient as a diffusion process. Using a stochastic

model by following fluid particles in incompressible, homogeneous isotropic turbulence, they reproduced one-time and two-time statistics in good agreement with those obtained from full turbulence simulations. Cantwell[4] derived an analytical solution to the Restricted Euler equation, first studied by Vieillefosse[33, 34]. The asymptotic solution reproduced the observations found in direct numerical simulations of turbulent flows: two of the principal eigenvalues are positive, and the vorticity vector aligns with the intermediate principal eigenvector exactly. Girimaji & Speziale[12] analyzed a modified version of the Restricted Euler equation numerically by including the effects of the mean velocity gradient tensor. This model preserved the balance of mean momentum for most homogeneous turbulent flows with mean velocity gradients.

1.5 Classification of local flow topology

Many studies of turbulent flows have been performed recently. Vast quantities of data have been collected either using sophisticated laboratory instruments or generated by computer simulations. With so much information available, the need for a systematic and efficient way to analyze these data is crucial. Classification of local flow topology in turbulent flow, using critical point theory as described by Chong, Perry & Cantwell[8] is one of the best ways to analyze the large amounts of data associated with these studies. A *critical point* is a point in the flow field where all three velocity components are zero and the streamline slope is indeterminate. The flow topology at each point in the flow may be accessed from the viewpoint of an observer travelling with the local velocity of the flow. For such an observer, each point is a critical point, and the topology can be categorized accordingly. In addition to Chong *et al.*, Soria *et al.*[31], Sondergaard[30], Chen *et al.*[7], Blackburn *et al.*[2] and others have also given insightful descriptions of the various classifications of local flow topologies in different types of turbulent flows.

Most of the results in this thesis will be expressed in terms of local flow topologies. Therefore, the basic definitions and physical interpretations of the various flow topologies will be briefly described in the following sections.

1.5.1 Invariants of the velocity gradient tensor

A vector field $\vec{u} = u_1(x_1, x_2, x_3), u_2(x_1, x_2, x_3), u_3(x_1, x_2, x_3)$, is linearized about a critical point O , i.e., $\vec{u}(O) = 0$. (x'_1, x'_2, x'_3) are the coordinates measured relative to the point O . Assuming that a Taylor series expansion can be carried out about the point O

$$\vec{u} = \underline{\underline{A}} \cdot \vec{x}' + \cdots = \begin{bmatrix} a_{11} & a_{12} & a_{13} \\ a_{21} & a_{22} & a_{23} \\ a_{31} & a_{32} & a_{33} \end{bmatrix} \begin{bmatrix} x'_1 \\ x'_2 \\ x'_3 \end{bmatrix} + \text{higher order terms.} \quad (1.9)$$

$$\underline{\underline{A}} = A_{ij} = \left. \frac{\partial u_i}{\partial x_j} \right|_O. \quad (1.10)$$

Since \vec{u} is the velocity field, A_{ij} is the velocity gradient tensor at the point O . The three eigenvalues, λ , of A are obtained as solutions of the characteristic equation

$$\lambda^3 + P\lambda^2 + Q\lambda + R = 0. \quad (1.11)$$

P , Q and R are the tensor invariants of A .

1.5.2 General three-dimensional flows

The definitions of these tensor invariants for general three-dimensional flows are given by:

$$P = -A_{ii} = -\text{trace}[A]. \quad (1.12)$$

$$Q = \frac{1}{2}(P^2 - \text{trace}[A^2]). \quad (1.13)$$

$$R = \frac{1}{3}(-P^3 + 3PQ - \text{trace}[A^3]) = -\det[A]. \quad (1.14)$$

The characteristic equation has three different combinations of roots, (1) all real roots which are distinct, (2) all real roots where at least two of them are equal, or (3) one real root and a conjugate pair of complex roots.

In P - Q - R space, the surface which divides the real solutions from the complex solutions is given by

$$27R^2 + (4P^3 - 18PQ)R + (4Q^3 - P^2Q^2) = 0, \quad (1.15)$$

where terms have been gathered to form a quadratic equation in R .

Chong *et al.*[8] gave very detailed descriptions of different types of critical points depending on the location of the invariants in the P - Q - R space.

1.5.3 Incompressible three-dimensional flows

The definitions of the three invariants for incompressible flows are much simpler due to the incompressibility condition, which forces the trace of the velocity gradient tensor, A , to zero. This condition greatly simplifies the expressions of the various invariants:

$$P = -A_{ii} = -\text{trace}[A] = 0. \quad (1.16)$$

$$Q = -\frac{1}{2}(\text{trace}[A^2]) = -\frac{1}{2}A_{im}A_{mi}. \quad (1.17)$$

$$R = -\frac{1}{3}(\text{trace}[A^3]) = -\det[A] = -\frac{1}{3}A_{im}A_{mk}A_{ki}. \quad (1.18)$$

Because the first invariant P is now zero for incompressible flows, the local flow geometry is completely determined by the location of the second and third invariants of the velocity gradient in the two-dimensional Q - R space.

The surface that separates real eigenvalues from complex eigenvalues now reduces to a curve given by:

$$D = (27/4)R^2 + Q^3 = 0. \quad (1.19)$$

The value of the discriminant, D determines the nature of the eigenvalues of A . When $D > 0$, A has one real and two complex eigenvalues. $D < 0$ implies that A has three distinct, real eigenvalues. When $R = \pm(2\sqrt{3}/9)(-Q)^{3/2}$ and $D = 0$, A has three real eigenvalues, two of which are equal. The curve $D = 0$ acts as a dividing line which separates solutions with three real eigenvalues from those with one real and two complex conjugate eigenvalues.

The curve $D = 0$ and the Q axis separate the Q - R space into four regions. Figure 1.3 illustrates the different topologies in these four regions:

1. above the dividing curve and to the left of Q axis, the local flow spirals in towards the local origin in a plane and then flows out along the third direction. This local flow geometry is referred to as stable-focus/stretching.

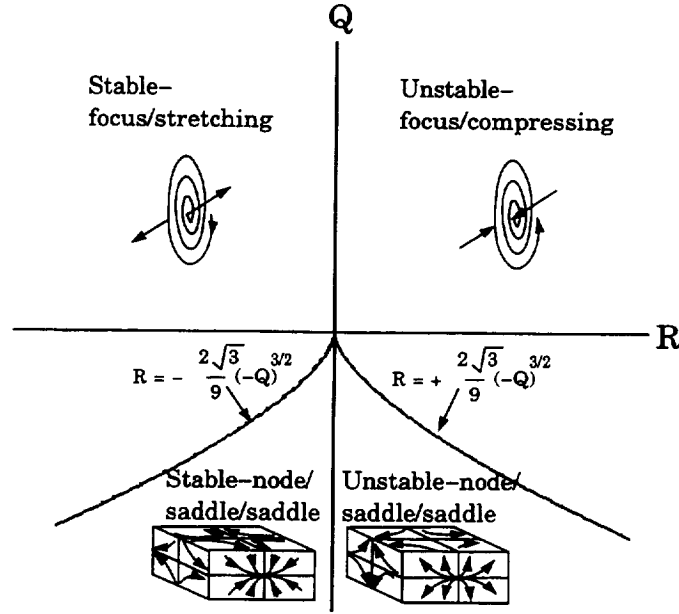


Figure 1.3: Three dimensional topologies in Q - R ($P = 0$) invariant space

2. above the dividing curve and to the right of Q axis, the local flow approaches the origin along one axis and spirals out in a plane. This local flow geometry is referred to as unstable-focus/compressing.
3. below the dividing curve and to the left of Q axis, the local flow approaches the origin along two axes and flows outward along the third. This local flow geometry is referred to as stable-node/saddle/saddle.
4. below the separator and to the right of Q axis, the local flow approaches the origin along one axis and flows outwards along the other two. This local flow geometry is referred to as unstable-node/saddle/saddle.

1.5.4 Construction of a typical Q - R invariant plot

Figure 1.4 illustrates a typical Q - R plot obtained for a direct numerical simulation of incompressible, homogeneous isotropic flow. At one instant in the simulation, the values of Q and R at each grid point are calculated using the definitions given in the

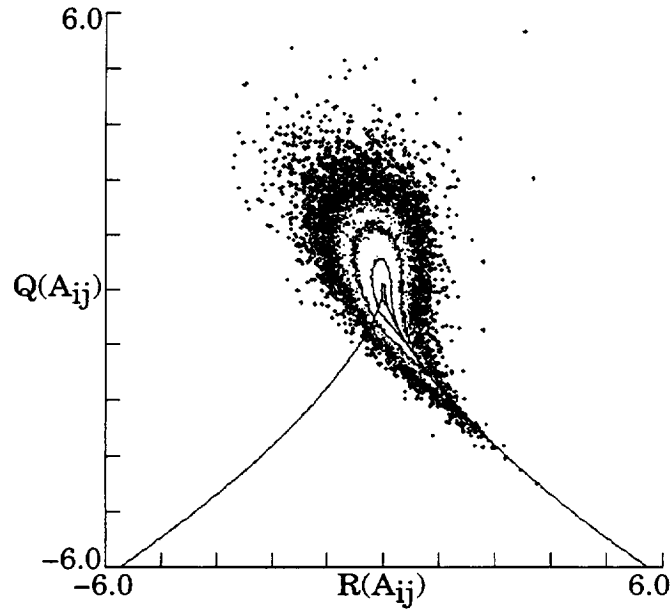


Figure 1.4: A typical contour plot of joint pdf of Q vs R .

previous section and cross-plotted to the Q - R space. This process is repeated for all grid points in the whole flow. Figure 1.4 plots the contours of the number density of points lying within a unit area in the invariant space. Logarithmic contour levels (1, 10, 100 etc.) are chosen due to extreme variations of the number density that occurs. In this way, isolated points far from the origin corresponding to the largest gradients in the flow (which occur in the smallest-scale structures) are captured with contour level of 1. At the same time, information about the distribution of invariants near the origin corresponding to intermediate-scale and large-scale structures is also provided by the higher contour levels. This invariant plot becomes the joint probability density function (pdf) between Q and R when the contour levels are normalized by the total number of data points in the plot.

1.5.5 Invariants of the rate-of-strain and rate-of-rotation tensors

Any velocity gradient tensor A_{ij} may be decomposed into the rate-of strain tensor S and the rate-of-rotation tensor W . The components of S and W are defined as :

$$S_{ij} = (A_{ij} + A_{ji})/2. \quad (1.20)$$

$$W_{ij} = (A_{ij} - A_{ji})/2. \quad (1.21)$$

Considering only incompressible flows, the invariants for S and W are :

$$P_s = -S_{ii} = -\text{trace}[S] = 0. \quad (1.22)$$

$$Q_s = -\frac{1}{2}S_{im}S_{mi} = -\frac{1}{2}\text{trace}[S^2]. \quad (1.23)$$

$$R_s = -\frac{1}{3}S_{im}S_{mk}S_{ki} = -\frac{1}{3}\text{trace}[S^3]. \quad (1.24)$$

$$P_w = -W_{ii} = -\text{trace}[W] = 0. \quad (1.25)$$

$$Q_w = -\frac{1}{2}W_{im}W_{mi} = -\frac{1}{2}\text{trace}[W^2]. \quad (1.26)$$

$$R_w = -\frac{1}{3}W_{im}W_{mk}W_{ki} = 0. \quad (1.27)$$

The invariants of the velocity gradient tensor are related to the invariants of the rate-of-strain and rate-of-rotation tensors in the following ways:

$$Q = Q_s + Q_w. \quad (1.28)$$

$$R = R_s - W_{im}W_{mk}S_{ki}. \quad (1.29)$$

Since S is a symmetric tensor, all the eigenvalues of S must be real. Therefore, all the data points must lie below the discriminant curve $D_s = (27/4)R_s^2 + Q_s^3 = 0$ in the Q_s - R_s invariant space.

1.5.6 Physical meanings of various invariants

The invariants obtained from the A , S and W tensors have direct implications for the fluid flows. In addition to classifying the local flow fields as observed by an observer travelling with the fluid, these invariant plots also reveal physical information about the flow:

1. the second invariant of S , Q_s , is directly proportional to the local dissipation.

$$\varepsilon = 2\nu S_{ij}S_{ji} = -4\nu Q_s. \quad (1.30)$$

Points with large negative values of Q_s correspond to high dissipation regions in the flow.

2. the second invariant of W , Q_w , is the magnitude of the vorticity squared, also known as the local enstrophy density.

$$Q_w = -\frac{1}{2}W_{im}W_{mi} = \omega_i\omega_i. \quad (1.31)$$

Points with large Q_w have high enstrophy density.

3. the difference between the third invariant of the rate-of-strain tensor and the third invariant of the velocity gradient tensor, $(R_s - R)$, reveals information about the vortex stretching rate, σ .

$$(R_s - R) = W_{im}W_{mk}S_{ki} = \sigma. \quad (1.32)$$

Information regarding the physical flows can therefore be obtained by inspecting the invariant plots. If Q is large and positive, the local enstrophy density is large and dominates the local dissipation ($Q_w \gg Q_s$), as in the case of solid body rotation near the center of a vortex tube. On the other hand, when Q is large and negative, the local dissipation is large and dominates the local enstrophy density ($Q_s \gg Q_w$), as found in flows with pure straining. Finally, when ($Q_s \approx Q_w$), the local dissipation and local enstrophy density are comparable in magnitude, as found in vortex sheets.

1.6 Outline of thesis

The main objective of this thesis is to study the characteristics of the velocity and acceleration gradient tensors in one inviscid flow simulation and two viscous flow simulations. The inviscid flow is chosen because it exhibits behavior consistent with the Restricted Euler model of the evolution of A_{ij} . All the flows studied in this thesis are obtained from direct numerical simulations, where the Navier-Stokes equation is solved exactly using “spectral” methods. There is no attempt to model any unresolved scales in these simulations.

Chapter 2 describes the Restricted Euler equation and its analytical solution. The definition of the acceleration gradient tensor, which governs the behavior of the velocity gradient tensor, is presented. A velocity gradient tensor with random components obtained from a Gaussian distribution with zero mean and unit variance evolving with the Restricted Euler model is also discussed.

Chapter 3 analyses the local flow topologies of an incompressible Euler calculation of two interacting vortex tubes simulated by Kerr[17]. Figure 1.5(a) depicts the domain surrounding the peak vorticity in this flow. Different regions with interesting local flow topologies are identified.

Chapter 4 describes the numerical approach used by the author to perform a direct numerical simulation of a homogeneous isotropic flow. A contour plot of iso-vorticity surfaces of this simulation is shown in figure 1.5(b). The behavior of the velocity and acceleration gradient tensors in this flow is analyzed using classification of local flow topologies.

Chapter 5 presents the results obtained from a simulation of a temporally evolving plane wake generated by Sondergaard[30]. Behavior of the velocity and acceleration gradient tensors in this relatively higher Reynolds number simulation is compared and contrast with results obtained from the homogeneous isotropic flow. A general view of this flow has been shown in figure 1.1.

Chapter 6 gives the major conclusions and outlines some recommendations for future studies.

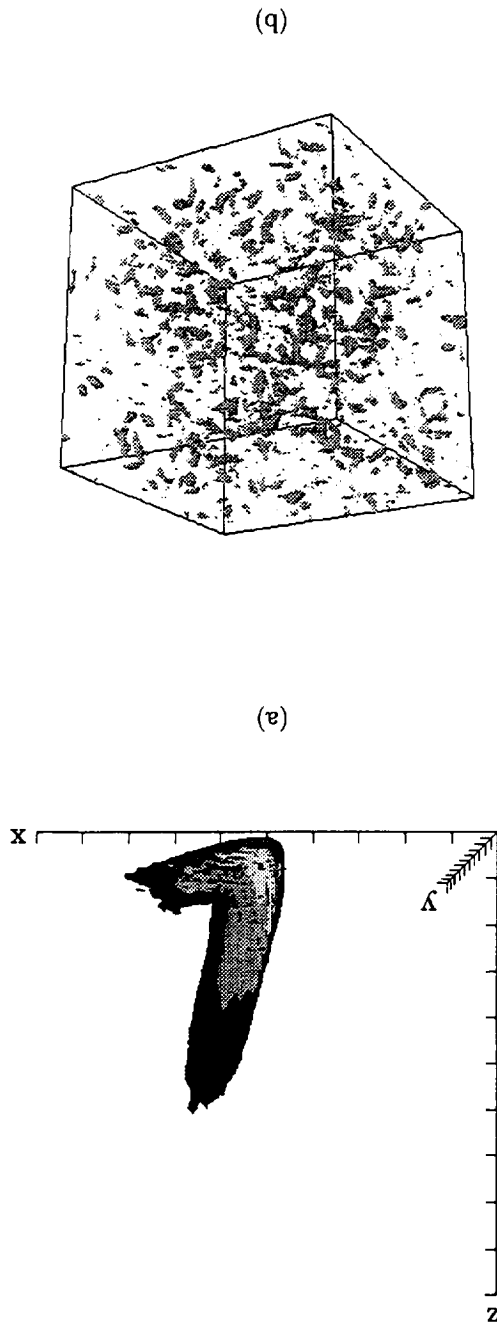


Figure 1.5: Contour plots of iso-entropy surfaces. (a) Inviscid calculation of interaction between two vortex tubes. (b) Homogeneous isotropic flow in a periodic box.

Chapter 2

Equations for the velocity gradient tensor

2.1 Introduction

Ashurst *et al.*[1] examined the statistical properties of the velocity gradient tensor in a forced isotropic turbulence and in a homogeneous shear flow, using DNS. They observed that there is a strong tendency for the velocity gradient tensor to approach a state where two of its principal rates-of-strain are positive while the remaining one is negative. There was also a preferential alignment between the vorticity vector and the intermediate principal eigenvector of the rate-of-strain tensor. Both tendencies became more pronounced when data were conditioned at higher dissipation regions. Similar observations were also reported in other studies of homogeneous turbulent flows.

To understand the behavior of velocity gradient tensor $A_{ij} = \partial u_i / \partial x_j$, the transport equation for A_{ij} needs to be studied closely. The derivation of this transport equation is described below.

The incompressible Navier-Stokes equations:

$$\frac{\partial u_i}{\partial t} + u_k \frac{\partial u_i}{\partial x_k} = -\frac{\partial p}{\partial x_i} + \nu \frac{\partial^2 u_i}{\partial x_k \partial x_k} \quad (2.1)$$

are differentiated with respect to x_j leading to

$$\frac{\partial A_{ij}}{\partial t} + u_k \frac{\partial A_{ij}}{\partial x_k} + A_{ik} A_{kj} = -\frac{\partial^2 p}{\partial x_i \partial x_j} + \nu \frac{\partial^2 A_{ij}}{\partial x_k \partial x_k}. \quad (2.2)$$

For incompressible flow, $A_{ii} = 0$. Therefore, the pressure is given by taking the trace of the above equation:

$$A_{ik} A_{ki} = -\frac{\partial^2 p}{\partial x_k \partial x_k}. \quad (2.3)$$

Subtracting equation 2.3 from equation 2.2 yields

$$\frac{\partial A_{ij}}{\partial t} + u_k \frac{\partial A_{ij}}{\partial x_k} + A_{ik} A_{kj} - A_{km} A_{mk} \frac{\delta_{ij}}{3} = H_{ij} \quad (2.4)$$

where δ_{ij} is the Kronecker delta, and

$$H_{ij} = -\left(\frac{\partial^2 p}{\partial x_i \partial x_i} - \frac{\partial^2 p}{\partial x_k \partial x_k} \frac{\delta_{ij}}{3} \right) + \nu \frac{\partial^2 A_{ij}}{\partial x_k \partial x_k}. \quad (2.5)$$

The H_{ij} tensor is composed of the cross derivatives of the pressure field and the viscous diffusion of the velocity gradient tensor. This H_{ij} tensor shall be termed the “acceleration gradient tensor” in the rest of this thesis, even though it is not the true acceleration gradient tensor. A true acceleration gradient tensor, \hat{H}_{ij} can be derived by expanding a vector field at a critical point using a Taylor series, the same way as the velocity gradient tensor A_{ij} was derived in equation 1.10.

$$\frac{dx_i}{dt} = u_i. \quad (2.6)$$

Differentiating this equation with time t , and using equation 2.1:

$$\frac{d^2 x_i}{dt^2} = \frac{du_i}{dt} = -\frac{\partial p}{\partial x_i} + \nu \frac{\partial^2 u_i}{\partial x_k \partial x_k} = a_i. \quad (2.7)$$

Therefore, true acceleration gradient tensor

$$\frac{\partial a_i}{\partial x_j} = \hat{H}_{ij} = -\frac{\partial^2 p}{\partial x_i \partial x_j} + \nu \frac{\partial^2 A_{ij}}{\partial x_k \partial x_k}. \quad (2.8)$$

Close inspection of the true acceleration gradient tensor reveals that \hat{H}_{ij} is almost identical to H_{ij} , except that H_{ij} has been forced to be trace-free, which makes the

analysis of this tensor easier. Therefore, H_{ij} is essentially the an-isotropic part of the true acceleration gradient tensor. The behavior of this H_{ij} tensor will be discussed in later chapters.

The evolution equations for the invariants of the velocity gradient tensor are derived by forming the appropriate double and triple products with equation 2.4 and taking the trace:

$$\frac{dQ}{dt} + 3R = -A_{ik}H_{ki}, \quad (2.9)$$

$$\frac{dR}{dt} - \frac{2}{3}Q^2 = -A_{in}A_{nm}H_{mi}. \quad (2.10)$$

2.2 The Restricted Euler model

Cantwell [4] analyzed the homogeneous case with $H_{ij} = 0$, which will be referred to as the Restricted Euler model for A_{ij} . This equation was first studied by Vieillefosse [33, 34]. Setting $H_{ij} = 0$ converts equation 2.4 into a system of coupled ordinary differential equations (ODE) for all nine components of $A_{ij}(t)$. Under this assumption, the velocity gradient tensor of a fluid particle evolves independently of other particles in the flow since the effects of the pressure and viscosity have been removed from the governing equation. This system of ODE's was solved analytically. A brief description of the derivation of this analytical solution is presented below.

Given an initial velocity gradient tensor, A_{ij} , its discriminant D is related to its second and third invariants such that:

$$D = Q^3 + \frac{27}{4}R^2 = Q_i^3 + \frac{27}{4}R_i^2 = Q_o^3. \quad (2.11)$$

The quantities Q_i and R_i are the initial values of Q and R respectively. Q_o is the value of Q when $R = 0$ and it is used to define the time scale for the evolution of $A_{ij}(t)$

$$t_o = \begin{cases} \frac{1}{\sqrt{\text{abs}(Q_o)}}; & Q_o \neq 0 \\ \frac{1}{\sqrt{-Q_i}}; & Q_o = 0 \end{cases} \quad (2.12)$$

All relevant variables are non-dimensionalised by t_o :

$$q = Qt_o^2, \quad r = Rt_o^3, \quad a_{ij} = A_{ij}t_o^2, \quad \tau = t/t_o \quad (2.13)$$

and equation 2.11 becomes:

$$\frac{27}{4}r^2 + q^3 = \text{sgn}(Q_o) \quad (2.14)$$

where

$$\text{sgn}(Q_o) = \begin{cases} +1; & Q_o > 0 \\ -1; & Q_o < 0 \\ 0; & Q_o = 0 \end{cases} \quad (2.15)$$

2.2.1 Analytical solutions of $q(\tau)$ and $r(\tau)$

By setting $H_{ij} = 0$, the non-dimensionalised forms of the coupled ordinary differential equations 2.9 and 2.10 become:

$$\frac{dq}{d\tau} = -3r. \quad (2.16)$$

$$\frac{dr}{d\tau} = \frac{2}{3}q^2. \quad (2.17)$$

Solutions to equations 2.16 and 2.17 are expressed in Jacobian elliptic integrals of the first kind, $F(\phi, k)$, and the cosine amplitude function, cn , where

$$F(\phi, k) = \int_0^\phi \frac{ds}{\sqrt{1 - k^2 \sin^2 s}}; \quad \cos(\phi) = cn(F). \quad (2.18)$$

The solutions depend on Q_o .

- $Q_o > 0$

$$q^+(\tau) = \frac{(1 - \sqrt{3}) - (1 + \sqrt{3})cn[(2/3^{1/4})\tau]}{1 - cn[(2/3^{1/4})\tau]}; \quad 0 < \tau < \tau_{max}^+. \quad (2.19)$$

$$r^+(\tau) = \sqrt{\frac{4}{27}(1 - q(\tau)^3)}; \quad 0 < \tau < \tau_{max}^+. \quad (2.20)$$

$$\tau_{max}^+ = (3^{1/4}/2)4F\left(\frac{\pi}{2}, \sin(5\pi/12)\right). \quad (2.21)$$

- $Q_o < 0$

$$q^-(\tau) = \frac{-(1 + \sqrt{3}) + (1 - \sqrt{3})cn[(2/3^{1/4})\tau]}{1 - cn[(2/3^{1/4})\tau]}; \quad 0 < \tau < \tau_{max}^-. \quad (2.22)$$

$$r^-(\tau) = \sqrt{\frac{4}{27}(-1 - q(\tau)^3)}; \quad 0 < \tau < \tau_{max}^-. \quad (2.23)$$

$$\tau_{max}^- = (3^{1/4}/2)4F\left(\frac{\pi}{2}, \sin\left(\frac{\pi}{12}\right)\right). \quad (2.24)$$

- when $Q_o = 0$, the solutions depend on the initial value of r as well.

1. $r(0) < 0$,

$$q^0(\tau) = -\left(\frac{1}{1 + (1/\sqrt{3})\tau}\right)^2; \quad 0 < \tau < \infty. \quad (2.25)$$

$$r^0(\tau) = -\frac{2}{3\sqrt{3}}\left(\frac{1}{1 + (1/\sqrt{3})\tau}\right)^3; \quad 0 < \tau < \infty. \quad (2.26)$$

2. $r(0) > 0$,

$$q^0(\tau) = -\left(\frac{1}{1 - (1/\sqrt{3})\tau}\right)^2; \quad 0 < \tau < \sqrt{3}. \quad (2.27)$$

$$r^0(\tau) = \frac{2}{3\sqrt{3}}\left(\frac{1}{1 - (1/\sqrt{3})\tau}\right)^3; \quad 0 < \tau < \sqrt{3}. \quad (2.28)$$

2.2.2 Analytical solution of $a_{ij}(\tau)$

A second order differential equation for a_{ij} can be obtained by differentiating equation 2.4 with respect to t and expressing the resultant equation in non-dimensional form:

$$\frac{d^2 a_{ij}}{d\tau^2} + \frac{2}{3}q(\tau)a_{ij} = 0. \quad (2.29)$$

Since the solution for $q(\tau)$ is in terms of the Jacobian elliptic integrals, the determination of the exact expression for $a_{ij}(\tau)$ is complicated. Fortunately, $r(\tau)$ is a monotonic function of τ . Expressing q as a function of r using the relationship in equation 2.14, and replacing the independent variable from τ to r yields:

$$\frac{4}{9}\left(\text{sgn}(Q_o) - \frac{27}{4}r^2\right)\frac{d^2 a_{ij}}{dr^2} - 4r\frac{da_{ij}}{dr} + \frac{2}{3}a_{ij} = 0. \quad (2.30)$$

The dependence of a_{ij} on τ is now assumed implicitly by the variable $r(\tau)$.

The solution of equation 2.30 is expressed in the simple form:

$$a_{ij}(r) = C_{ij}f_1(r) + D_{ij}f_2(r). \quad (2.31)$$

$f_1(r)$ is an even function of r and $f_2(r)$ is an odd function of r . $C_{ij}(r)$ and $D_{ij}(r)$ are matrix constants of integration determined by initial conditions.

The solutions of $f_1(r)$ and $f_2(r)$ are again dependent on the initial value of Q_o :

- $Q_o > 0$,

$$f_1^+(r) = \frac{1}{2} \left[\left(1 + \frac{3\sqrt{3}}{2}r\right)^{1/3} + \left(1 - \frac{3\sqrt{3}}{2}r\right)^{1/3} \right] \quad (2.32)$$

$$f_2^+(r) = \frac{1}{\sqrt{3}} \left[\left(1 + \frac{3\sqrt{3}}{2}r\right)^{1/3} - \left(1 - \frac{3\sqrt{3}}{2}r\right)^{1/3} \right] \quad (2.33)$$

- $Q_o < 0$,

$$f_1^-(r) = \left(1 + \frac{27}{4}r^2\right)^{1/6} \cos \left\{ \frac{1}{3} \tan^{-1}[(3\sqrt{3}/2)r] \right\} \quad (2.34)$$

$$f_2^-(r) = (2/\sqrt{3}) \left(1 + \frac{27}{4}r^2\right)^{1/6} \sin \left\{ \frac{1}{3} \tan^{-1}[(3\sqrt{3}/2)r] \right\} \quad (2.35)$$

- $Q_o = 0$,

$$f_1^0(r) = 2^{1/3}[(3\sqrt{3}/2)r]^{-2/3} \quad (2.36)$$

$$f_2^0(r) = (2^{2/3}/3\sqrt{3})[(3\sqrt{3}/2)r]^{1/3} \quad (2.37)$$

The solutions for $C_{ij}(r)$ and $D_{ij}(r)$ are expressed in terms of \hat{r} , \hat{a}_{ij} and $d\hat{a}/dr$, which are the initial values of r , a_{ij} and da_{ij}/dr respectively:

$$C_{ij} = \hat{a}_{ij}[q(\hat{r})]^2 \left(\frac{df_2}{d\hat{r}} \right)_{\hat{r}} + \left(\frac{3}{2}(\hat{a}_{ik}\hat{a}_{kj}) + q(\hat{r})\delta_{ij} \right) f_2(\hat{r}) \quad (2.38)$$

$$D_{ij} = -\hat{a}_{ij}[q(\hat{r})]^2 \left(\frac{df_1}{d\hat{r}} \right)_{\hat{r}} + - \left(\frac{3}{2}(\hat{a}_{ik}\hat{a}_{kj}) + q(\hat{r})\delta_{ij} \right) f_1(\hat{r}) \quad (2.39)$$

2.2.3 Numerical procedure in obtaining $A_{ij}(t)$

In summary, given an initial velocity gradient tensor, A_{ij} , the analytical expression of this tensor evolving with the Restricted Euler model after time t can be determined using the following procedure:

1. Obtain the characteristic time scale, t_o from equation 2.12.

2. Non-dimensionalize the velocity gradient tensor and its invariants by t_o , giving $\hat{a}_{ij}(\tau)$, $\hat{q}(\tau)$ and $\hat{r}(\tau)$.
3. Determine τ from $\hat{q}(\tau)$ from the inverse of equation 2.19, 2.22, 2.25 or 2.27, depending on $\text{sgn}(Q_o)$ and $\hat{r}(\tau)$.
4. Add the non-dimensionalised time increment $\Delta\tau = t/t_o$ to the calculated τ .
5. Obtain the new values of $q(\tau)$ and $r(\tau)$ from equations 2.19 to 2.28.
6. Determine $f_1(r)$ and $f_2(r)$ from equations 2.32 to 2.37, depending on the value of $r(\tau)$.
7. Get the derivatives of $f_1(r)$ and $f_2(r)$ by differentiating equations 2.32 to 2.37 analytically.
8. Obtain C_{ij} and D_{ij} from the initial values of \hat{r} , $q(\hat{r})$, $f_1(\hat{r})$, $f_2(\hat{r})$ and their derivatives.
9. Calculate the final velocity gradient tensor a_{ij} from equation 2.31.
10. If dimensional final velocity gradient tensor is desired, divide the calculated velocity gradient tensor by its own initial characteristic time scale, t_o .

2.2.4 Asymptotic solution of $a_{ij}(\tau)$

The asymptotic form of a_{ij} as $r \rightarrow \infty$ can be expressed as :

$$\lim_{r \rightarrow \infty} a_{ij}(r) \cong K_{ij} r(\tau)^{1/3}. \quad (2.40)$$

$r(\tau)$ is a function that becomes singular in finite time.

K_{ij} satisfies the algebraic equation

$$K_{im}K_{mj} + \frac{1}{2^{1/3}}K_{ij} - 2^{1/3}\delta_{ij} = 0. \quad (2.41)$$

The invariants of K_{ij} can be derived using equation 2.41 and the continuity constraint to be:

$$P(K_{ij}) = 0.0; \quad Q(K_{ij}) = \frac{3}{2^{2/3}}; \quad R(K_{ij}) = 1.0. \quad (2.42)$$

Notice that the second and third invariants of K_{ij} tensor lie on the boundary of the dividing curve since $Q(K_{ij})$ and $R(K_{ij})$ satisfy the equation:

$$\frac{27}{4}R^2 + Q^3 = 0. \quad (2.43)$$

The K_{ij} tensor can also be written as the sum of a symmetric tensor and an anti-symmetric tensor:

$$K_{ij} = S_{ij|k} + W_{ij|k}, \quad (2.44)$$

where

$$S_{ij|k} = \begin{bmatrix} S_{11|k} & 0 & 0 \\ 0 & S_{22|k} & 0 \\ 0 & 0 & -S_{11|k} - S_{22|k} \end{bmatrix} \quad (2.45)$$

and

$$W_{ij|k} = \begin{bmatrix} 0 & -\Omega_3|k & \Omega_2|k \\ \Omega_3|k & 0 & -\Omega_1|k \\ -\Omega_2|k & \Omega_1|k & 0 \end{bmatrix} \quad (2.46)$$

Substituting the components of K_{ij} into equation 2.41 produces nine equations, which are used to solve for $S_{ij|k}$ and $\Omega_i|k$. The solutions exhibit the same topological characteristics seen in direct numerical simulations, namely: (1) the intermediate strain rate $S_{22|k}$ must be non-negative, and (2) the vorticity vector must align with this intermediate strain rate.

Since $Q = Q_s + Q_w = -3/2^{2/3}$ for the K_{ij} tensor, there exists a linear relationship between $Q_s(K_{ij})$ and $Q_w(K_{ij})$ such that:

$$-Q_s(K_{ij}) = Q_w(K_{ij}) + \frac{3}{2^{2/3}}. \quad (2.47)$$

Other relevant relationships between various invariants of K_{ij} tensor are:

$$R_s(K_{ij}) = -\frac{1}{2^{1/3}}Q_s(K_{ij}) - \frac{1}{2}. \quad (2.48)$$

and

$$Q_w(K_{ij}) = \frac{1}{2^{1/3}}(R_s(K_{ij}) - R(K_{ij})). \quad (2.49)$$

Figures 2.1(a-d) depict the relationships between the different invariants of the K_{ij} tensor. In figure 2.1(a), all the asymptotic solutions collapse into a single point with

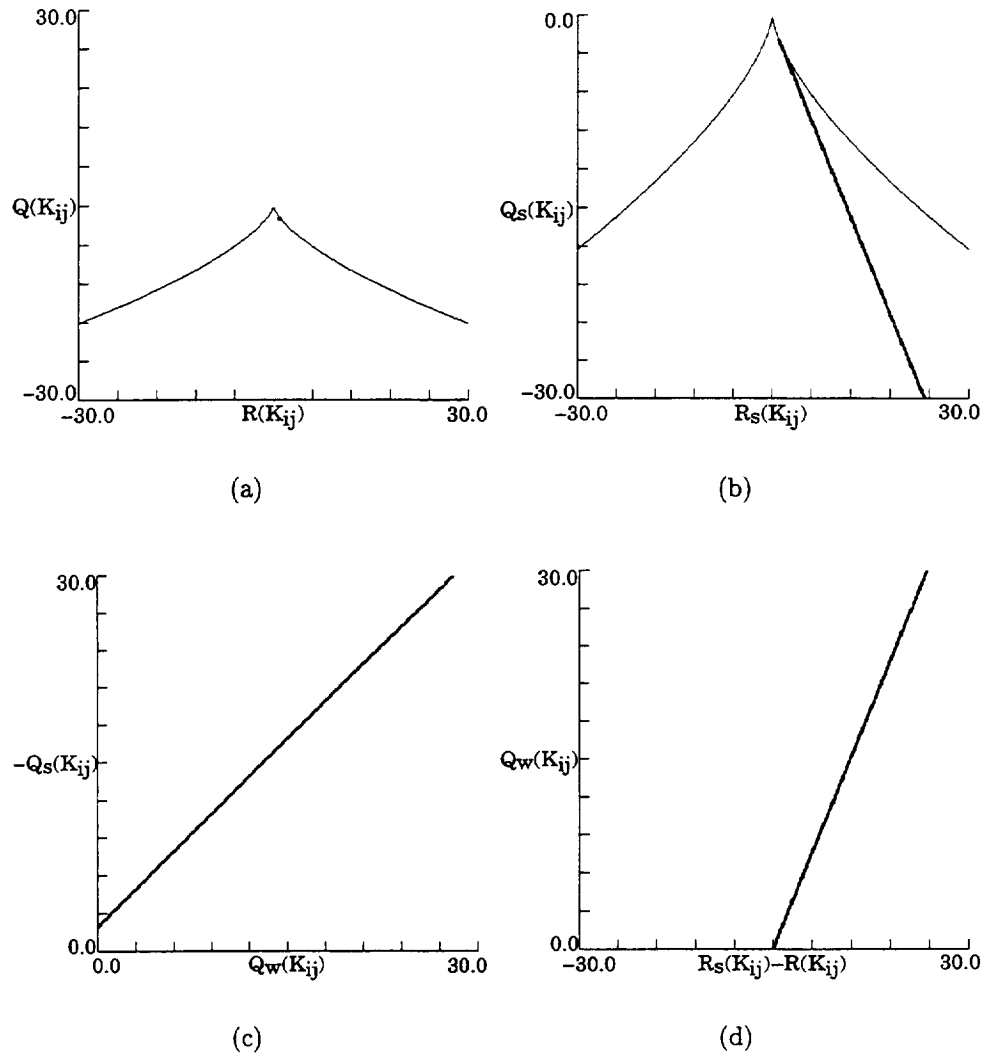


Figure 2.1: Relationships between invariants of K_{ij} tensor. (a) Q vs R . (b) Q_s vs R_s . (c) $-Q_s$ vs Q_w . (d) Q_w vs $(R_s - R)$.

$Q(K_{ij}) = -3/2^{2/3}$ and $R(K_{ij}) = 1.0$ — regardless of initial condition. Figure 2.1(b) shows the linear relationship between $Q_s(K_{ij})$ and $R_s(K_{ij})$. Notice that since $Q_s(K_{ij})$ and $R_s(K_{ij})$ also satisfy the characteristic equation:

$$\lambda^3 + \lambda Q_s(K_{ij}) + R_s(K_{ij}) = 0; \quad \lambda = 2^{-1/3} \quad (2.50)$$

the straight line osculates the dividing curve at a single point where $Q_s(K_{ij}) = -3/2^{2/3}$ and $R_s(K_{ij}) = 1.0$. Figures 2.1(c-d) plot the linear relationships derived in equations 2.47 and 2.49.

2.3 Gradient tensor evolving with the Restricted Euler model

The behavior of a velocity gradient tensor evolving with the Restricted Euler model was observed. The components of this velocity gradient tensor were generated with random numbers of Gaussian distribution with zero mean and unit variance. The trace of this tensor was forced to zero to satisfy the continuity constraint of an incompressible flow. In a homogeneous isotropic flow, the volume integral of the second invariant Q is zero due to the balance of pressure gradients acting on the surface of a control volume:

$$\int_V Q \, dV = \int_V \frac{1}{2} \nabla^2 P \, dV = \int_S \frac{1}{2} (\nabla P) \cdot \vec{n} \, dS = 0 \quad (2.51)$$

Therefore, the velocity gradient tensor was required to satisfy this condition as well.

To satisfy both conditions, the velocity gradient tensor A_{ij} is constructed from: $A_{ij} = S_{ij} + W_{ij}$, where S_{ij} is a symmetric tensor and W_{ij} is an anti-symmetric tensor. The components of both S_{ij} and W_{ij} tensors are obtained from the random number generator x_i with mean $E(x) = 0$ and variance $\sigma^2 = 1.0$. The components of S_{ij} and W_{ij} tensors are:

$$\begin{aligned} S_{11} &= x_1 - \frac{1}{3}(x_1 + x_2 + x_3), \\ S_{22} &= x_2 - \frac{1}{3}(x_1 + x_2 + x_3), \\ S_{33} &= x_3 - \frac{1}{3}(x_1 + x_2 + x_3), \end{aligned}$$

$$S_{12} = S_{21} = x_4,$$

$$S_{13} = S_{31} = x_5,$$

$$S_{23} = S_{32} = x_6,$$

$$W_{11} = W_{22} = W_{33} = 0,$$

$$W_{12} = -W_{21} = \sqrt{4/3}x_7,$$

$$W_{13} = -W_{31} = \sqrt{4/3}x_8,$$

$$W_{23} = -W_{32} = \sqrt{4/3}x_9. \quad (2.52)$$

x_1, x_2, \dots, x_9 are nine different random numbers obtained from the random number generator. The factor $\sqrt{4/3}$ is necessary to force the expected value of the second invariant Q of the A_{ij} tensor to zero. The derivation of this factor is explained in Appendix A.

The analytical solution of this tensor evolving according to the Restricted Euler model after time t is obtained using the procedure described in the previous section. This process is repeated for 10^5 data points to obtain the probability density distribution. The results are presented in the form of the local topologies, assuming a hypothetical “flow” where every initial component of the velocity gradient tensor has a Gaussian distribution slightly modified to satisfy the constraints described.

2.3.1 Evolution of a_{ij}

Figure 2.2 shows the relationship between the second and third invariants of the velocity gradient tensor, Q and R , after evolving for time t . The velocity gradient tensor and all its invariants have been non-dimensionalised by the characteristic time scale defined in equation 2.13. Figure 2.2(a) shows that all the data points collapse onto three curves, depending on the discriminant of each velocity gradient tensor. Positive initial discriminants were all normalized into a single value of +1, lying above the dividing plane which separates those tensors with all three real principal eigenvalues from those with complex eigenvalues. This positive discriminant of +1

curve crosses the Q -axis at a maximum of 1.0. This is the result of the normalizing factor, which is defined to be the value of Q at $R = 0$. On the other hand, all the negative initial discriminants were normalized into a single value of -1 , thus lying below the dividing curve. These tensors have three real principal eigenvalues. Velocity gradient tensors with discriminant of exactly 0 (which are extremely rare) satisfy the characteristic equation exactly. Therefore, these points will lie exactly on the dividing curve. Data points are evenly distributed on both sides of the Q -axis since all the data were generated randomly. Figure 2.2(b) shows the distribution of the invariants after evolving for $t = 2.0$. There is an obvious shift of data points towards positive R along their respective discriminant curves, due to the monotone relationship between R and t . The velocity gradient tensor evolves with increasing R until the solution becomes singular in finite time. Figures 2.2(c) and 2.2(d) illustrate the analytical solutions to the Restricted Euler model after evolving for $t = 5.0$ and $t = 10.0$. Most of the data points have now migrated towards the lower right quadrant of the Q - R plot, where their solutions ultimately become infinite.

2.3.2 Evolution towards the asymptotic solution

The evolution of the velocity gradient tensor towards the asymptotic solution is illustrated in figures 2.3 to 2.6. These figures depict the evolution of the initially random velocity gradient tensor shown in figure 2.2, normalized by the characteristic time scale and local $R^{1/3}$.

Figure 2.3(a) shows Q and R at initial time $t = 0$. All the data points collapsed into a single vertical line, parallel to the Q -axis and cutting the R -axis at the value of $R = 1.0$ since every tensor has been normalized by its own third invariant, R . However, the values of Q for this initial data set are not restricted. Hence the data points span along the vertical line for all values of Q . Figures 2.3(b-d) show the evolution of this data set after time $t = 5.0$, $t = 10.0$ and $t = 20.0$. In addition to having a unique value of $R = 1.0$, the data points converge slowly to the asymptotic value of $Q = -3/2^{2/3}$ as the tensors evolve in time. This behavior was predicted by the asymptotic solution derived for the K_{ij} tensor in equation 2.42.

2.3. GRADIENT TENSOR EVOLVING WITH THE RESTRICTED EULER MODEL31

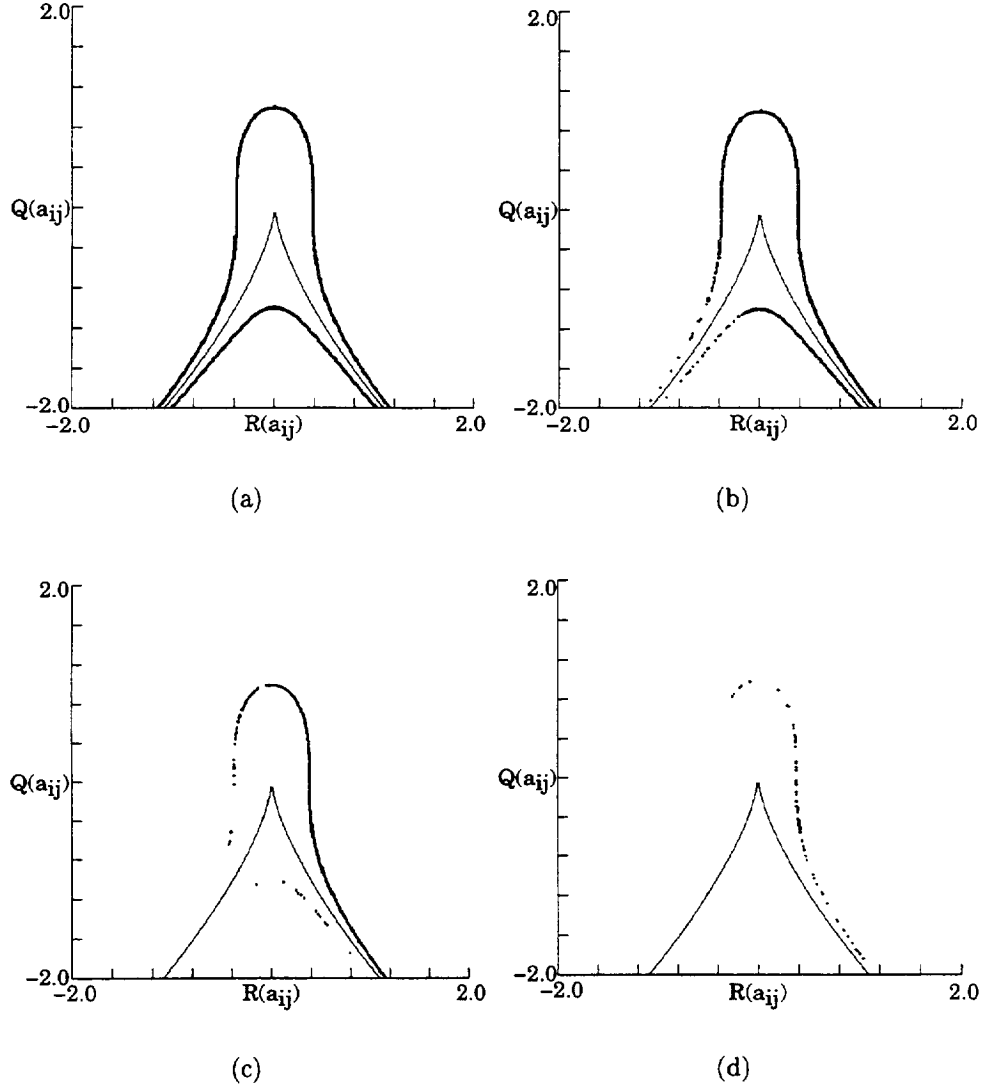


Figure 2.2: Time evolution of Q vs R . A_{ij} normalized by local discriminant so that all data points must lie on three separate curves with discriminant $D = +1$, $D = 0$ or $D = -1$. (a) $t=0.0$. (b) $t=2.0$. (c) $t=5.0$. (d) $t=10.0$.

The invariant plots of Q_s vs R_s at $t = 0.0$, $t = 5.0$, $t = 10.0$ and $t = 20.0$ are shown in figures 2.4. Initially, the data points distribute evenly below the dividing curve (the rate-of-strain tensor is symmetric and so all principal eigenvalues are real). However, for any velocity gradient tensor such that R_s is close to R (for example, a symmetric velocity gradient tensor), normalizing the velocity gradient tensor by $R^{1/3}$ forces R_s to 1.0. The consequence of this appears on the plot as a subtle structure near the vertical line at $R_s = 1.0$. The data points approach the asymptotic solution described in equation 2.48 as time increases. Figures 2.5 and Figures 2.6 show the time evolution of $-Q_s$ vs Q_w and Q_w vs $(R_s - R)$ respectively. Notice that the data points in figure 2.6(a) do not distribute evenly about the $(R_s - R) = 0$ axis. There is a structure along the $R_s - R = -1.0$ vertical line because R has been normalized to 1.0.

2.3.3 Evolution of dimensional A_{ij}

Figures 2.7 to 2.10 show the evolution of another set of random initial velocity gradient tensors. Every velocity gradient tensor in this set of data was normalized by the initial mean discriminant of the whole flow field of N total number of data points such that:

$$A_{ij} = A'_{ij}/\bar{D}^{1/6}, \quad \bar{D} = \sum_{n=1}^N D_n/N, \quad D = \frac{27}{4}R^2 + Q^3. \quad (2.53)$$

A'_{ij} is the initial velocity gradient tensor obtained from equation 2.52. The final velocity gradient tensor was obtained in the same way as described in the earlier section. However, each velocity gradient tensor was made dimensional by its own initial characteristic time scale t_o (refer to equation 2.12) to obtain the dimensional velocity gradient tensor, A_{ij} . The results are shown in figures 2.7 to 2.10.

Figures 2.7(a–d) show the contour plots of the joint pdf of Q vs R at four different times. At initial time $t = 0.0$, the contour plot shows that the data points are distributed fairly evenly on both sides of the Q -axis. However, due to the random way in which the velocity gradient tensors were constructed, tensors with complex principal eigenvalues (in which case the data points will lie above the dividing curve) outnumber those tensors with all three real principal eigenvalues (which lie below the

2.3. GRADIENT TENSOR EVOLVING WITH THE RESTRICTED EULER MODEL33

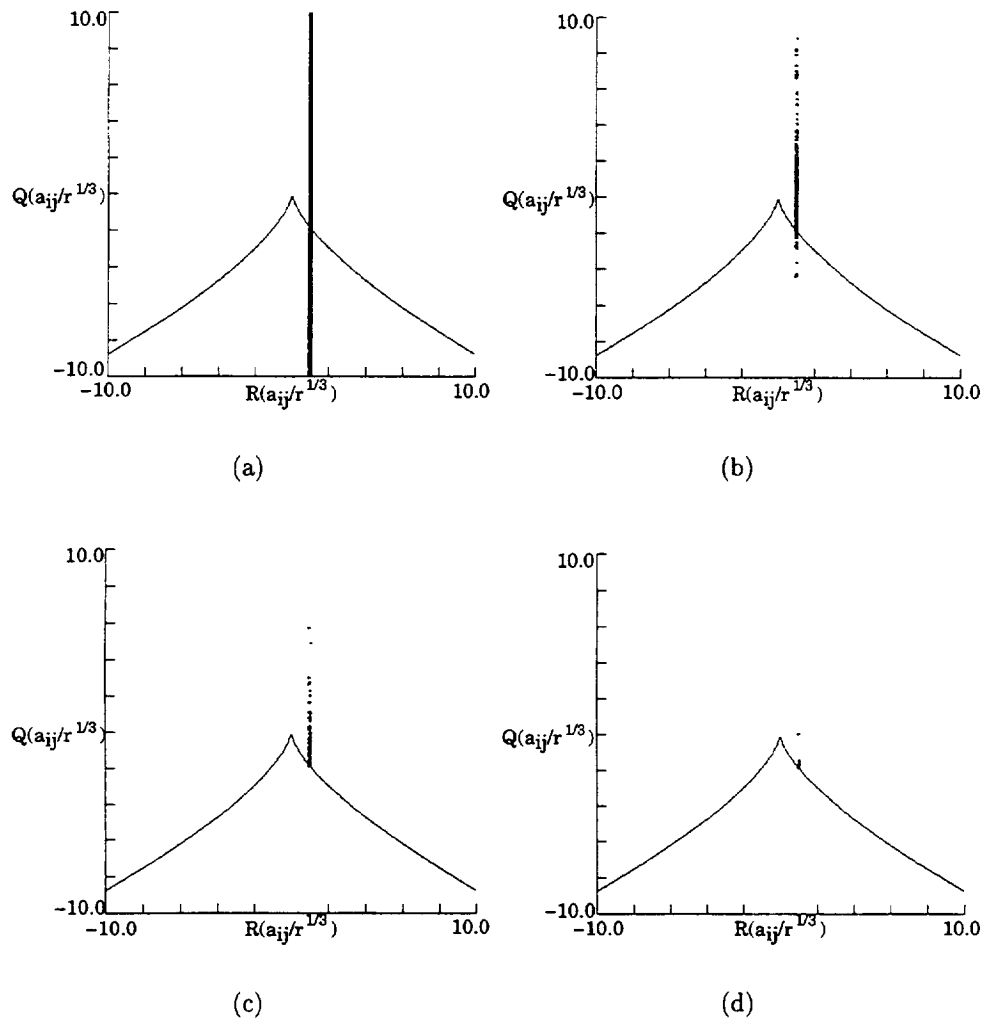


Figure 2.3: Time evolution Q vs R . A_{ij} normalized by local discriminant and local $R^{1/3}$ so that all data points must lie on the line $R = 1.0$. (a) $t=0.0$. (b) $t=5.0$. (c) $t=10.0$. (d) $t=20.0$.

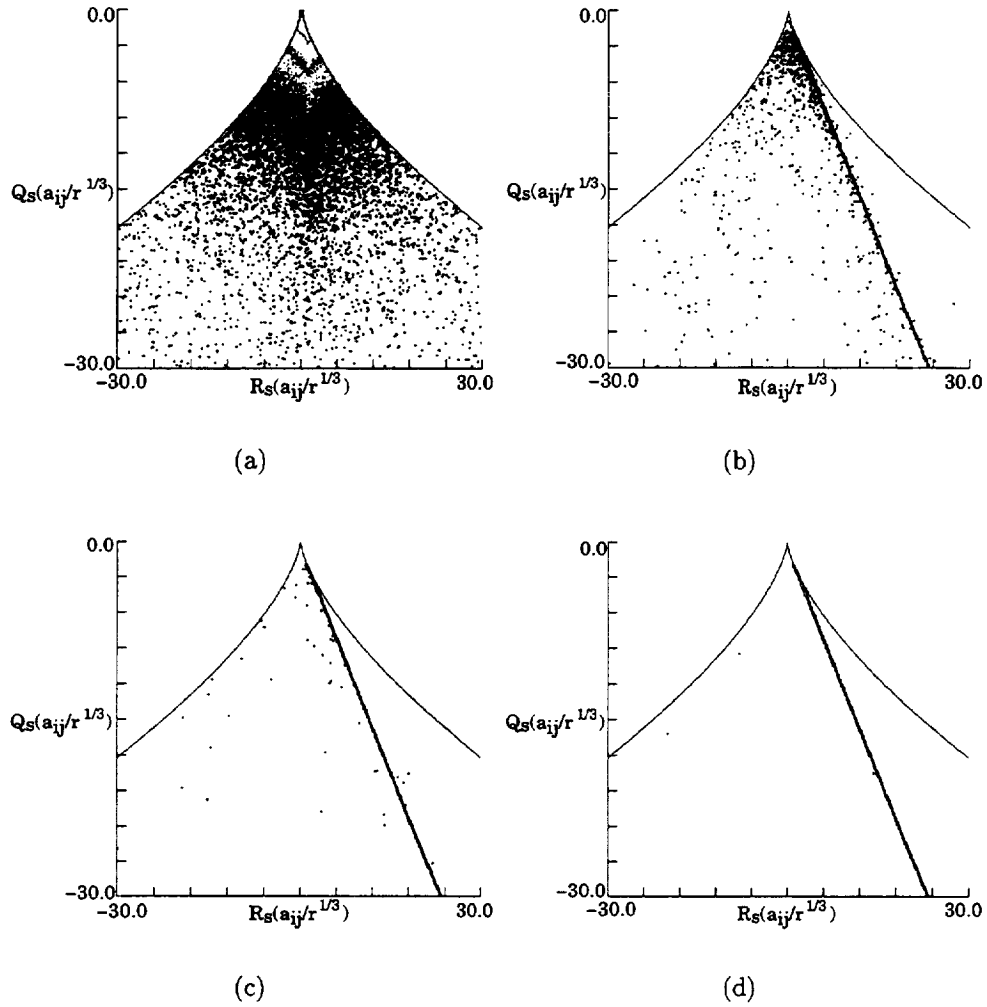


Figure 2.4: Time evolution of Q_s vs R_s . A_{ij} normalized by local discriminant and local $R^{1/3}$. (a) $t=0.0$. (b) $t=5.0$. (c) $t=10.0$. (d) $t=20.0$.

2.3. GRADIENT TENSOR EVOLVING WITH THE RESTRICTED EULER MODEL35

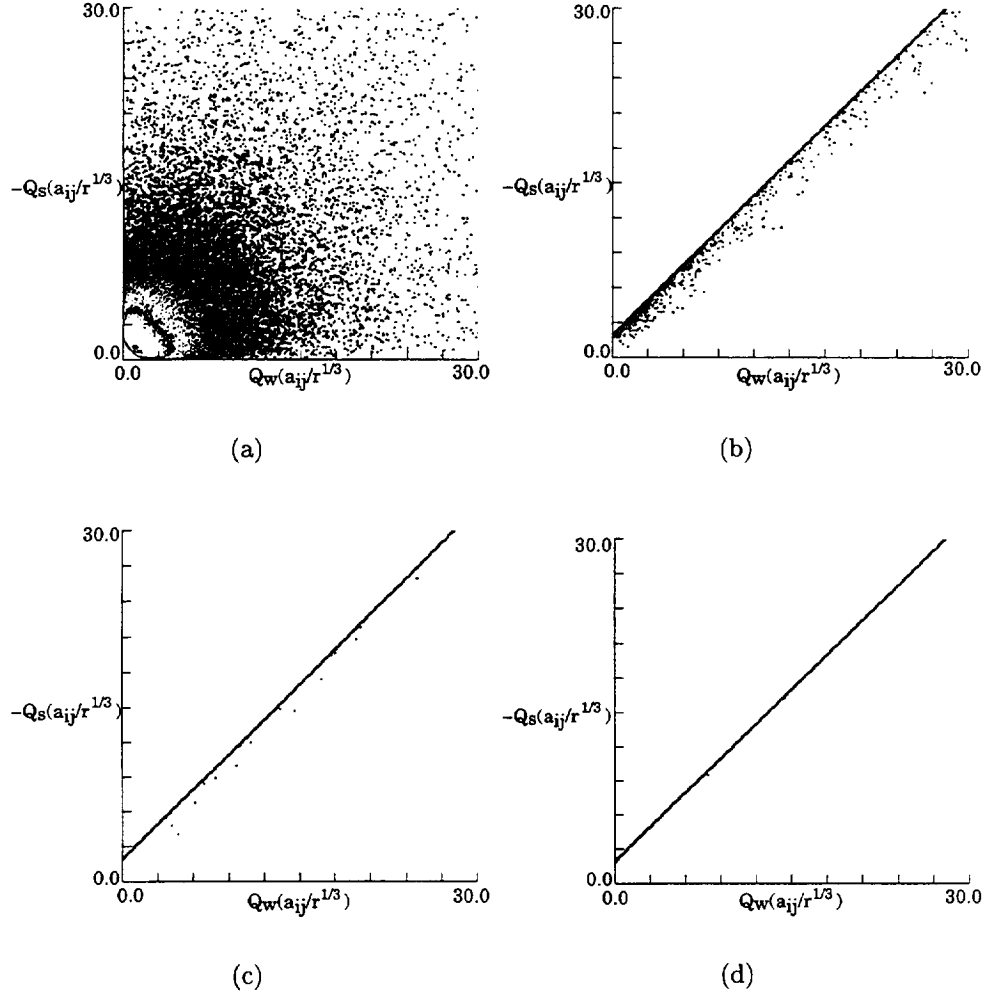


Figure 2.5: Time evolution of $-Q_s$ vs Q_w . A_{ij} normalized by local discriminant and local $R^{1/3}$. (a) $t=0.0$. (b) $t=5.0$. (c) $t=10.0$. (d) $t=20.0$.

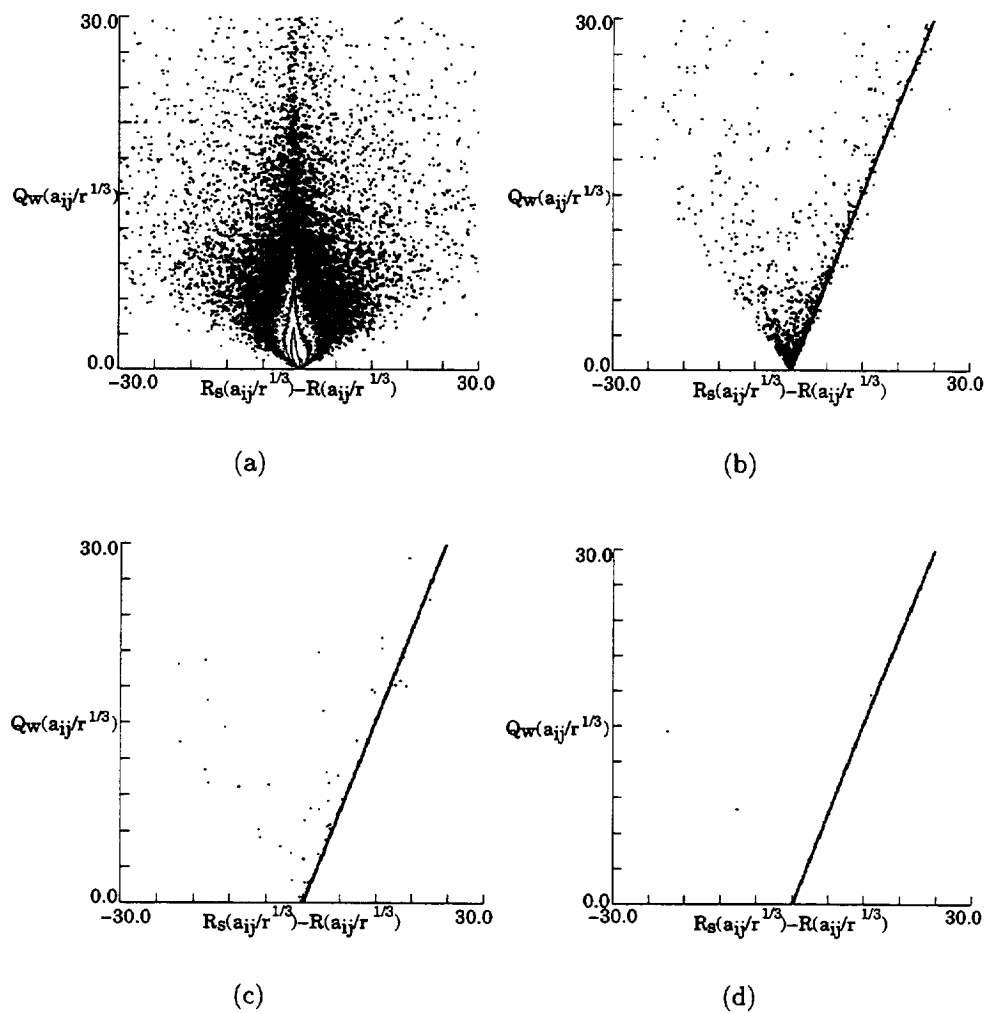


Figure 2.6: Time evolution of Q_w vs $(R_s - R)$. A_{ij} normalized by local discriminant and local $R^{1/3}$. (a) $t=0.0$. (b) $t=5.0$. (c) $t=10.0$. (d) $t=20.0$.

boundaries below the dividing curve). Figure 2.7(b) shows a very interesting result. There is an obvious shift of the data points toward the lower right quadrant. The overall structure is remarkably similar to the one obtained from the direct numerical simulation of a *viscous*, homogeneous isotropic flow shown in figure 4.8(d). The implication is that even though the Restricted Euler model is based upon the assumptions that the effects of both the viscosity and the off-diagonal pressure may be neglected, the solution may still be applicable in certain regions of a real flow. However, the presence of the viscosity in real flow tends to prevent the flow field quantities from becoming singular. In this solution, the bulk of the data shifts slowly towards the lower right quadrant of the Q - R plot as time increases.

The contour plots of the joint pdf between the second and third invariants of the symmetric tensor of this data set are shown in figure 2.8. At initial time $t = 0.0$, all the data points were evenly distributed below and within the boundaries of the dividing curve. As the velocity gradient tensor evolved from $t = 0.0$ to $t = 0.2$, an interesting result was observed. Most of the contour lines were relatively straight, extending from the upper left of the dividing curve towards the lower right. This same feature was also observed in DNS of a time-developing mixing layer[31], temporally evolving plane wake[30] and the homogeneous isotropic flow shown in figure 4.9. This linear characteristic of the contour lines persists until later times.

Figure 2.9 shows the relationship between $-Q_s$ and Q_w at different times. For most velocity gradient tensors, $-Q_s$ is comparable in magnitude to Q_w initially. However, as the tensor evolves with the Restricted Euler model, $-Q_s$ begins to dominate Q_w . This can be explained easily using the definition $Q = Q_s + Q_w$. Q_s is negative definite while Q_w is positive definite by definitions. As Q approaches $-\infty$ as dictated by the Restricted Euler model, $Q_s \rightarrow Q$ while $Q_w \rightarrow 0$, hence $-Q_s \gg Q_w$.

The sequence of evolution for Q_w and $(R_s - R)$ at four different times is shown in figure 2.10. At initial time $t = 0.0$, the data points formed a “tear-drop” shape structure, centered at the origin of the plot. As the solution evolves in time, the bulk of this structure slants towards the positive side of the $(R_s - R)$ axis. This result is

consistent with the evolution equation for enstrophy density shown by Cantwell[4]:

$$\frac{dQ_w}{dt} = 2(R_s - R). \quad (2.54)$$

The next chapter will allude to the results presented here by way of comparison with a computation of a flow which is inviscid but includes the pressure. This will be followed in later chapters by comparisons with viscous simulations.

2.3. GRADIENT TENSOR EVOLVING WITH THE RESTRICTED EULER MODEL39

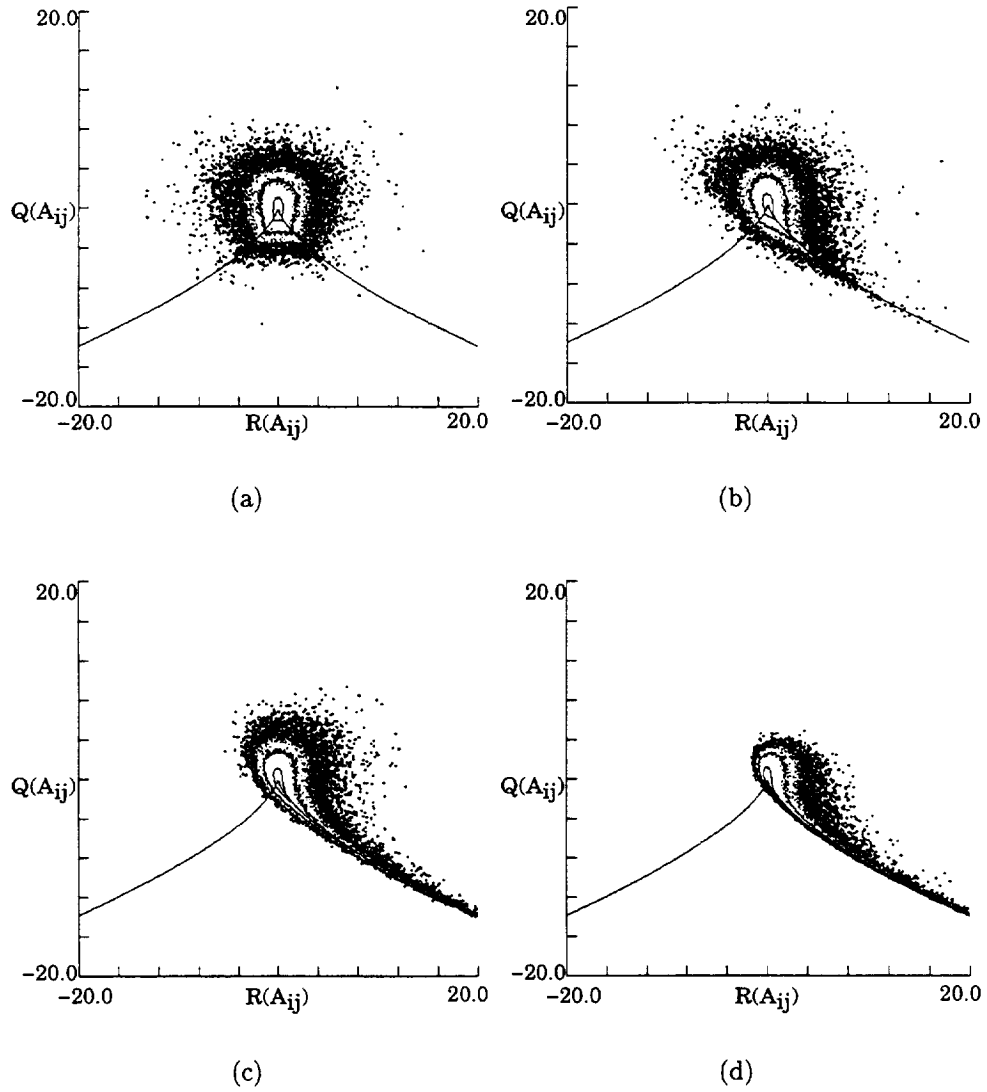


Figure 2.7: Time evolution of logarithmic contour plots of joint pdf of Q vs R . A_{ij} is not normalized. (a) $t=0.0$. (b) $t=0.2$. (c) $t=0.5$. (d) $t=1.0$.

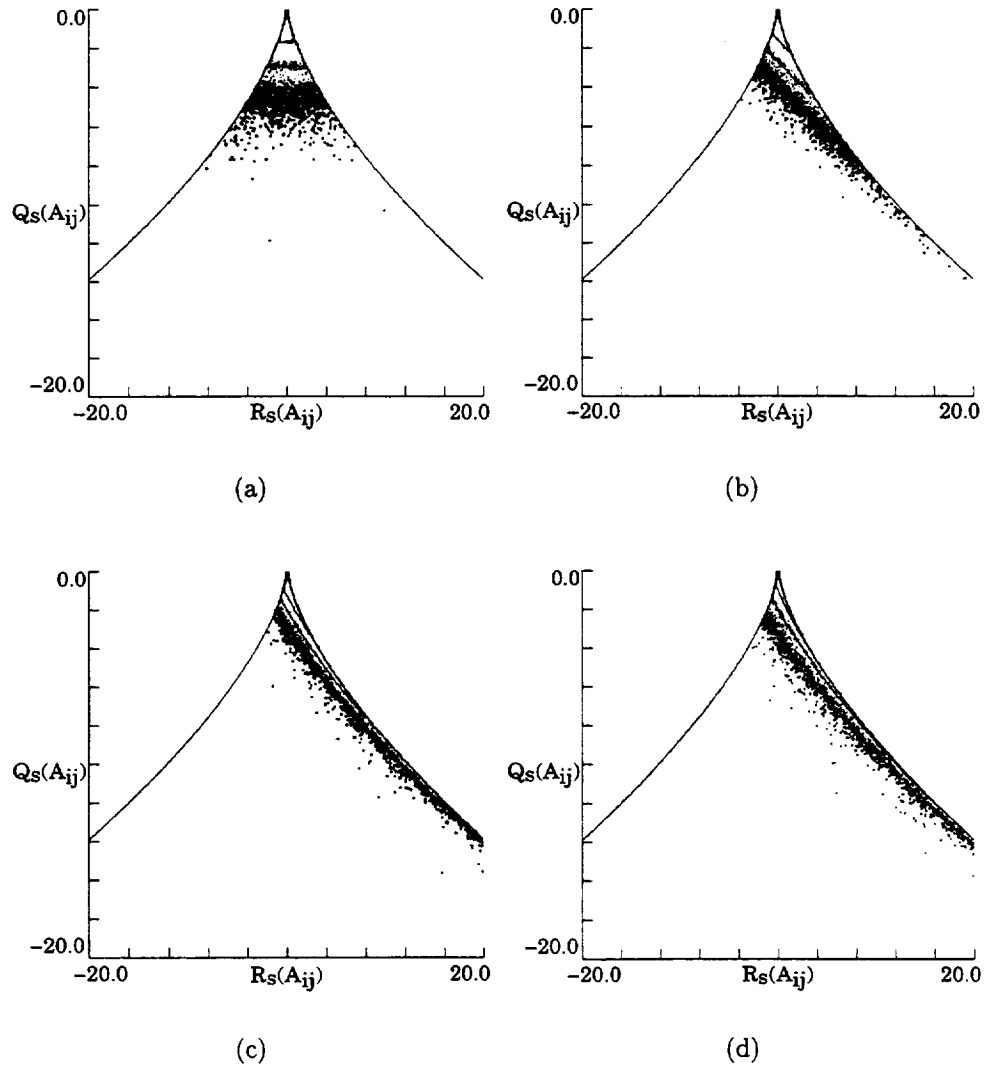


Figure 2.8: Time evolution of logarithmic contour plots of joint pdf of Q_s vs R_s . A_{ij} is not normalized. (a) $t=0.0$. (b) $t=0.2$. (c) $t=0.5$. (d) $t=1.0$.

2.3. GRADIENT TENSOR EVOLVING WITH THE RESTRICTED EULER MODEL41

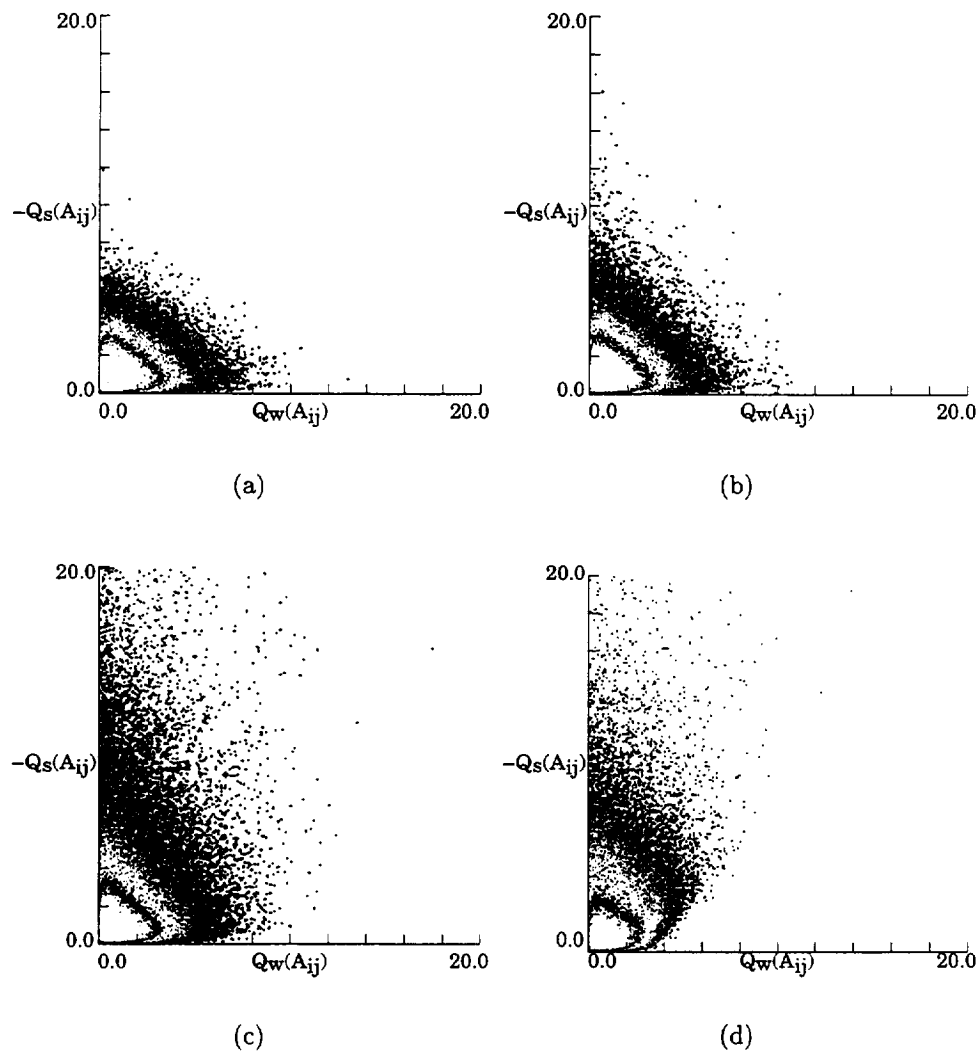


Figure 2.9: Time evolution of logarithmic contour plots of joint pdf of $-Q_s$ vs Q_w . A_{ij} not normalized. (a) $t=0.0$. (b) $t=0.2$. (c) $t=0.5$. (d) $t=1.0$.

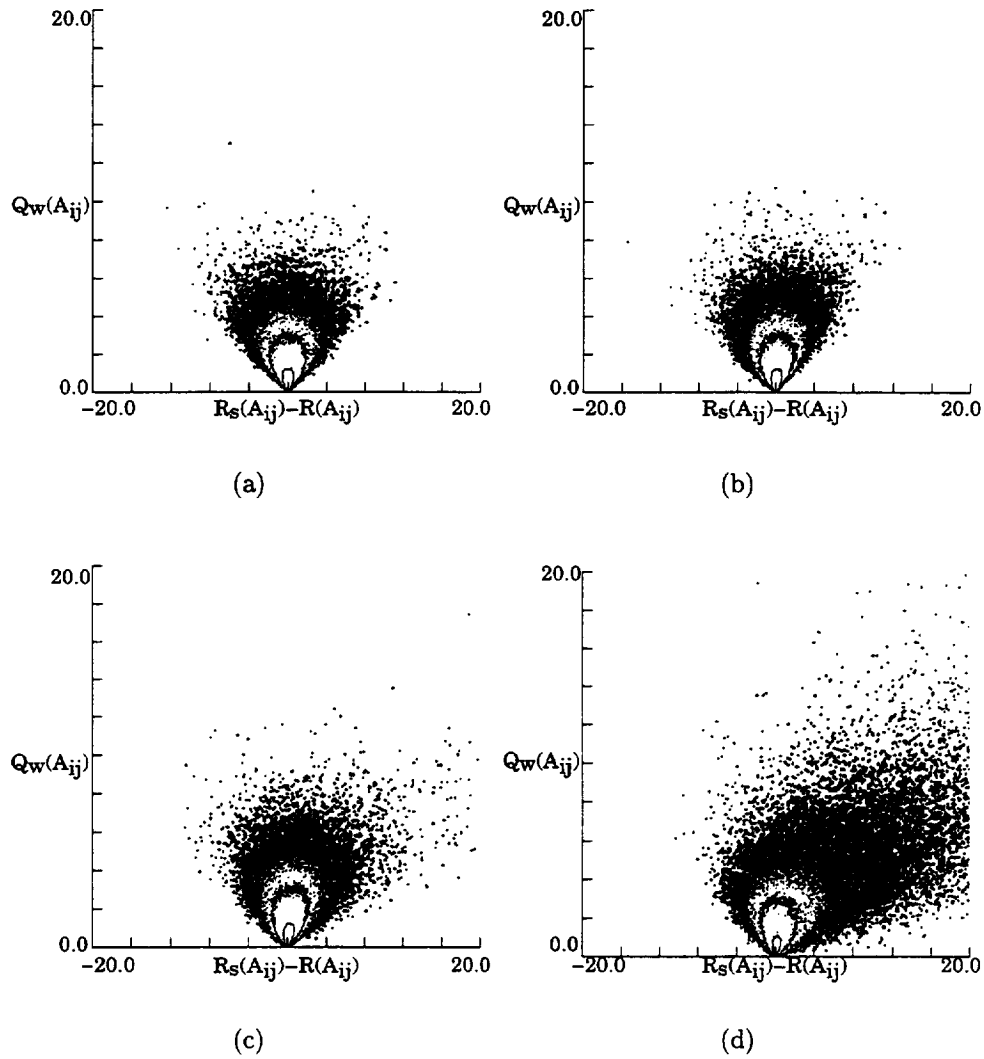


Figure 2.10: Time evolution of logarithmic contour plots of joint pdf of Q_w vs $(R_s - R)$. A_{ij} is not normalized. (a) $t=0.0$. (b) $t=0.2$. (c) $t=0.5$. (d) $t=1.0$.

Chapter 3

Inviscid interaction of vortex tubes

3.1 Introduction

After observing the behavior of a random distribution evolving with the Restricted Euler model, it is of interest to determine if any region within a turbulent flow exhibits similar behavior. An inviscid calculation of interactions between two perturbed anti-parallel vortex tubes was therefore selected for this study.

There are many debates on the existence of singularities in three-dimensional, incompressible Euler (inviscid) flow. Earlier inviscid simulations on two prescribed anti-parallel vortices by Pumir and Siggia [25] suggested that there is no singularity and the growth in peak vorticity at late times is at most exponential. Inviscid calculations with random initial conditions in a periodic box performed by Herring and Kerr [13] also appeared to grow at most at an exponential rate. Some viscous calculations [18, 20, 22] also suggested exponential growth when the trends of the calculations were extrapolated towards the limit of zero viscosity. Despite all these claims against the existence of singularities, Kerr [17] performed a simulation which provided evidence that supports the existence of a singularity. The simulation was of the interaction of perturbed anti-parallel vortex tubes using smooth initial profiles in a bounded domain. It was concluded by Kerr that the peak vorticity, the peak axial strain and the enstrophy density production scaled as $(t_c - t)^{-1}$ while the enstrophy

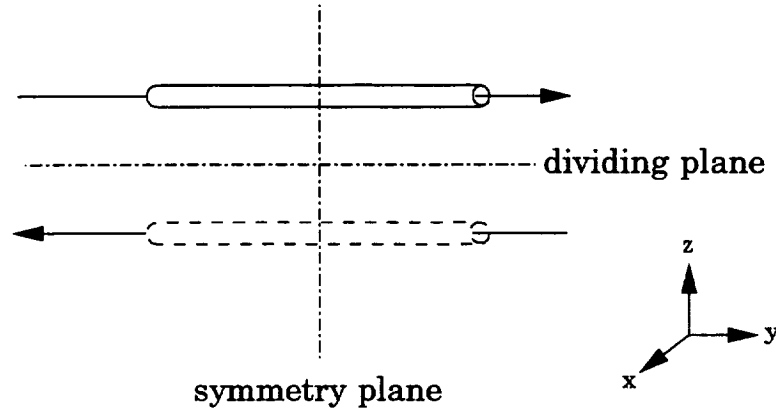


Figure 3.1: The anti-parallel vortex tubes at initial condition.

density grows logarithmically. t_c was the critical time in the flow at which it was hypothesized to approach singularity.

The objective of this thesis is not to address the debate on whether a singularity exists in Euler calculations, but to study the characteristics of this very interesting inviscid flow simulated by Kerr. The domain surrounding the peak vorticity in this flow was analyzed by classifying its local flow topologies. A coherent structure within this domain has been identified to exhibit similar characteristics predicted by the Restricted Euler model.

3.2 Brief description of the flow

Interaction of perturbed anti-parallel vortex tubes was simulated using DNS. Smooth initial profiles in a bounded domain with bounded initial vorticity were used to ensure symmetry in the flow. A sketch of this flow at the initial condition is shown in figure 3.1. The symmetries imposed were represented by free-slip boundary conditions at the “dividing” plane between the vortices and the “symmetry” plane of the maximum perturbation of the vortices. Both planes are identified in the sketch. The image vortex tube, shown in dashed lines in the figure, was included to impose symmetry condition.

3.2.1 Numerical method

Spectral methods that employed symmetries were employed in the simulation. The numerical method used Chebyshev polynomials which satisfy the free-slip boundary conditions at the dividing plane in the z -direction, Fourier transforms in the periodic x -direction, as well as sine and cosine transforms in the y direction that satisfy free-slip boundary conditions at the symmetry plane. The mesh size used in the calculation was 512:256:192 in a domain of $4\pi \times 4\pi \times 2\pi$, which was concluded to have the best resolution properties. Global quantities such as enstrophy density and enstrophy density production were determined to have time dependencies consistent with the trends for peak vorticity and rate of strain.

3.2.2 Initial condition

Initial vorticity profiles used in the calculations with a high-wave number filter are similar to those used in Melander & Hussain [21] and Kerr & Hussain [18]. However, the use of the Chebyshev method in the vertical z direction imposed several limitations. Kerr overcame the difficulties by using a rather sophisticated way of defining a compact vortex core such that the unfiltered vortex core goes to zero smoothly at a given radius r , but is still Gaussian in the center. A high order exponential filter was then imposed to smooth out the rough edges. This filtering also expanded the vortex such that its edge was just above the dividing plane.

3.3 Classification of local flow topologies

In the results presented below, the domain of the flow analyzed is in a $2\pi \times 2\pi \times \pi$ box. This domain is only a small part of the whole flow, surrounding the peak vorticity in the flow. The initial peak vorticity $w_p|_o$ was set to 1.0 at the beginning of the simulation. This vorticity, with dimension of characteristic frequency, was used to non-dimensionalize time t obtained from the simulation:

$$\tau = t \times w_p|_o. \quad (3.1)$$

Data were analyzed from $\tau = 12.5$ when this domain of flow began to develop, until the latest time of $\tau = 17.5$ when this domain was concluded to exhibit self-similar characteristics. The non-dimensionalized critical time at which the domain was hypothesized to approach singularity is $\tau_c = 18.9 \pm 0.1$. Significant resolution effects began to appear in the results after $\tau = 17.0$. However, the result at $\tau = 17.5$ was included in the analysis to infer the scaling of the quantities that develop asymptotic behavior. In the discussion of results in the following sections, emphasis will be placed on the data set at time $\tau = 17.0$ when the convergence of all the strain components is strongest and the resolution most reliable.

Figure 3.2 shows a contour plot of the iso-*enstrophy* density of the perturbation in the domain analyzed at time $\tau = 17.0$. This plot is presented from a perspective view looking along the stream-wise y -direction. The vertical z -axis has been stretched to five times its original value to show the development in the vertical direction more clearly. The horizontal x -axis is the dividing plane which separates the corresponding perturbation from the image vortex (not shown) directly below the dividing plane. Kerr labeled the region extending above the peak vorticity just behind the leading edge of the vortex as “head” while the vortex sheet extending behind the peak vorticity as “tail”. Both the “head” and “tail” were concluded to be vortex sheets, and remained so as the flow evolved to later times. The region of peak vorticity concentrates into a region where the vortex sheet of the head and tail meet at a sharp angle at the lower left corner.

Figure 3.3 shows the time evolution of the invariants Q and R from $\tau = 12.5$ when the flow began to develop, until $\tau = 17.5$. The invariants “explode” from the origin at early time since the velocity gradient scales $\approx 1/(\tau_c - \tau)$. Figure 3.4 also exhibit similar observations where the invariants grow very rapidly from the origin at early time. This huge difference in the scale of invariants at different times makes comparison of invariants relatively difficult. A normalizing factor based on the instantaneous mean strain-rate was therefore chosen to normalize the velocity gradient:

$$A_{ij} = A'_{ij}/\Omega; \quad \Omega = \left(\frac{(s_{ij}s_{ij})^2}{s_{ij}s_{ij}} \right)^{1/2}. \quad (3.2)$$

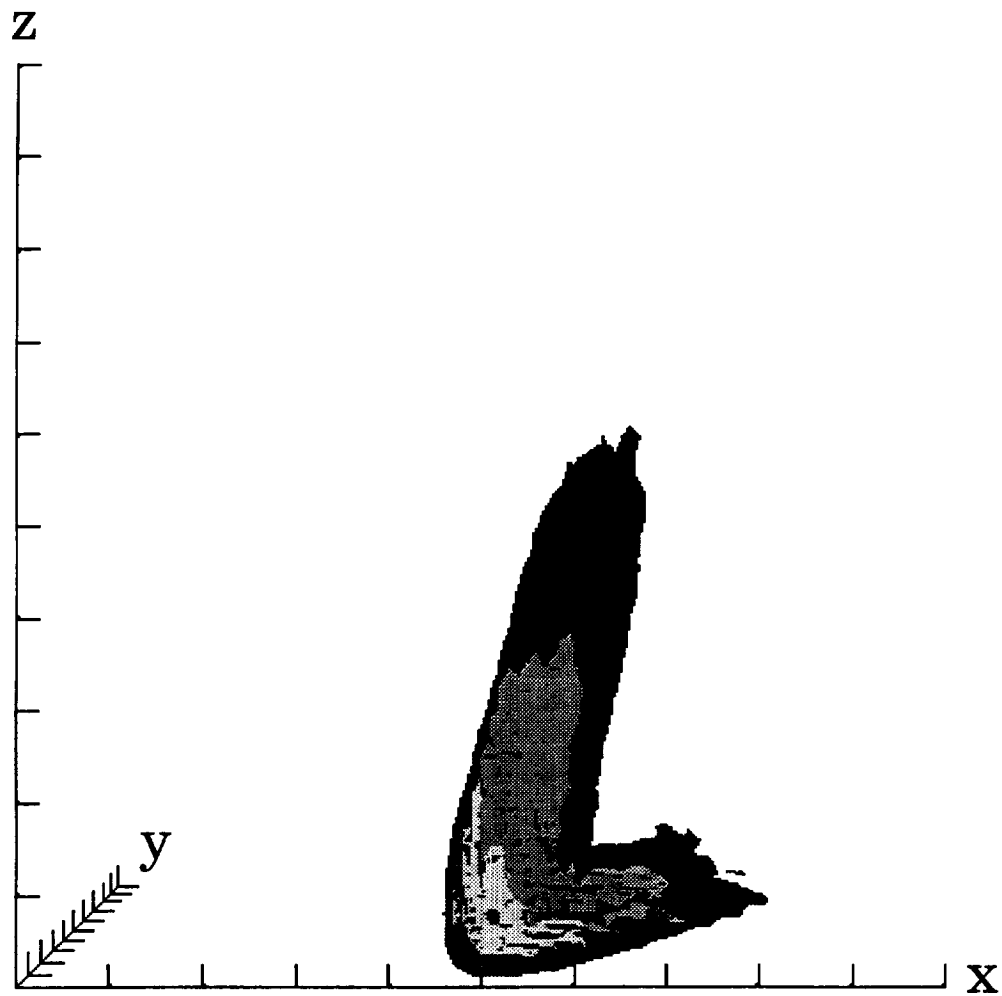


Figure 3.2: Contour plot of iso-entropy density surfaces in a domain surrounding the peak vorticity.

A'_{ij} is the dimensional velocity gradient obtained from the simulation.

Figure 3.5 shows the time evolution of the joint pdf between the second and third invariants of the normalized velocity gradient tensor. The contour plot of the joint pdf of the invariant approaches a self-similar shape. All the data points were observed to be at relatively low R values, almost hugging the Q -axis. No strong tendency of data points towards the right discriminant curve is observed.

Two distinct structures are observed from the Q_s - R_s plots shown in figure 3.6. One of the structures consists of data points that hug the Q_s -axis. The other structure is more complicated as it is actually a combination of different substructures. One of the substructures consists of data points that share the same ratio of $\alpha : \beta : \gamma$. Figure 3.7 re-plots the same invariant plots with curves of fixed $\alpha : \beta : \gamma$ ratio superimposed on the structures. Normalizing the eigenvalues by $|\beta|$, the ratio of $\gamma : \alpha$ ranges from -1.287 at $\tau = 12.5$ to -1.732 at $\tau = 17.5$.

The other substructure identified consists of data points with the linear relationship:

$$\lambda^3 + \lambda Q_s + R_s = 0. \quad (3.3)$$

λ is any one of the three principal eigenvalues of the strain-rate tensor, S_{ij} . This particular line osculates the discriminant curve at a single point and has the property that all the data points that lie on it have a common λ . The identification of data points that lie on this line in both the invariant and physical spaces will be discussed in section 3.3.1.

Figure 3.8 plots the relationship between $-Q_s$ and Q_w of the velocity gradient tensor. Most of the data points in the plots have comparable local enstrophy density and local dissipation, a direct result of data obtained from regions of high local enstrophy density due to the vortices and also high local strain due to the interaction/stretching between the two vortex tubes. Numerous data points in this flow have very high local dissipation but very low local enstrophy density. Another interesting observation from this figure is that data points with high local enstrophy density but very low local dissipation (eg. solid body rotation) are not identified in this flow.

Figure 3.9 reveals very interesting plots showing the relationship between the local enstrophy density and the vortex stretching terms in the flow. The invariant

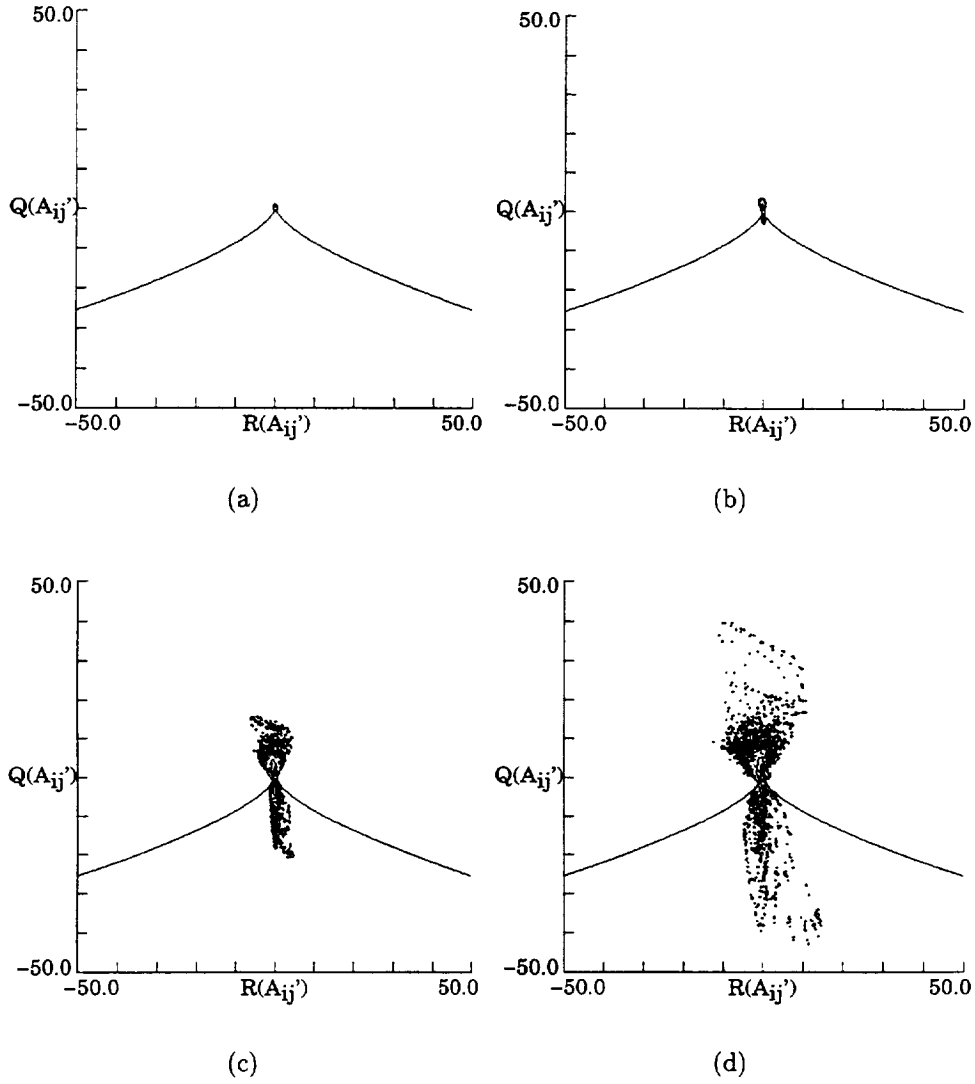


Figure 3.3: Time evolution of logarithmic contour plots of joint pdf of Q vs R for un-normalized A_{ij} . (a) $\tau = 12.5$. (b) $\tau = 15.0$. (c) $\tau = 17.0$. (d) $\tau = 17.5$.

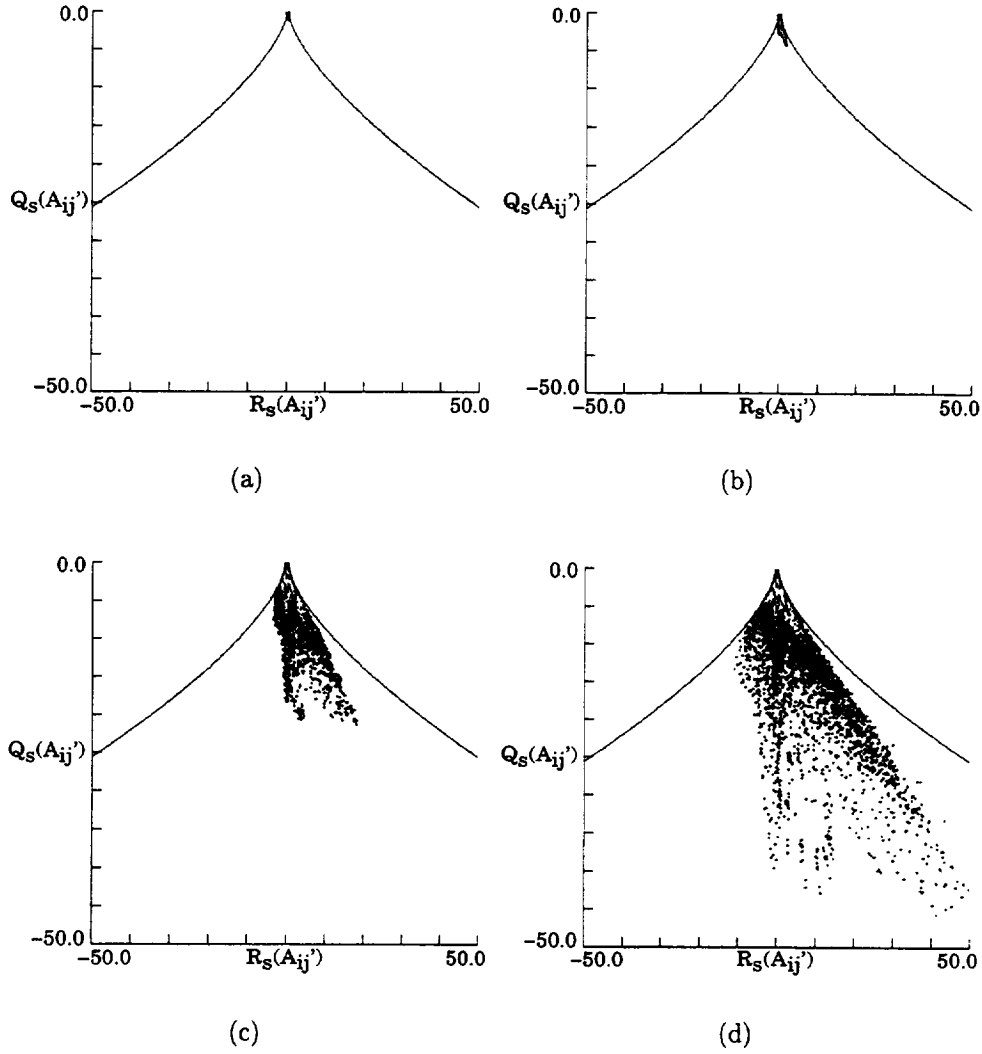


Figure 3.4: Time evolution of logarithmic contour plots of joint pdf of Q_s vs R_s for un-normalized A_{ij} . (a) $\tau = 12.5$. (b) $\tau = 15.0$. (c) $\tau = 17.0$. (d) $\tau = 17.5$.

plots show that all the data points are bounded within a fan-like structure, with no isolated data points outside the two distinct boundaries on both sides. Cantwell [4] concluded from the Restricted Euler model that there is a direct relationship between the evolution of local enstrophy density and the vortex stretching term:

$$\frac{dQ_w}{dt} = 2(R_s - R). \quad (3.4)$$

This relationship indicates that for data points evolving with the Restricted Euler model, there is an upper limit as to how fast the local enstrophy density of these data points can evolve in the flow. This limit is imposed by the vortex stretching term $(R_s - R)$. In addition, data points which satisfy the Restricted Euler model also approached an asymptotic state with relationship shown in equation 2.49 and figure 2.1. Therefore, data points that lie in the distinct right boundary of figure 3.9(c) were investigated further. These are the identified data points for further studies.

3.3.1 Classification of local flow topologies for identified data points

Figure 3.10 shows the various joint pdf for data points that are identified to lie on the right boundary of figure 3.9(c). The slope of Q_w to $(R_s - R)$ for these data points is determined to be $\doteq 2.30$.

The Q - R and Q_s - R_s invariant plots are very interesting because all the data points identified can be best-fit onto a straight line on both plots. The straight line is of the form $\lambda^3 + \lambda Q + R = 0$ in the Q - R plot and $\lambda^3 + \lambda Q_s + R_s = 0$ in the Q_s - R_s plot. These lines osculate the respective discriminant curves at a single point. λ is any one of the three principal eigenvalues of the velocity gradient tensor (in the case of Q - R plot) or the rate-of-strain tensor (in the case of Q_s - R_s plot). Therefore, all the data points that fall exactly on this line share the same eigenvalue. But which of the three principal eigenvalues (α , β or γ) does λ correspond to? To answer this question, the three principal eigenvalues of both the A_{ij} tensor (two of which may be complex) and the S_{ij} tensor (all three of which must be real) of these identified data points were determined and sorted in descending order such that $\alpha > \beta > \gamma$. These eigenvalues

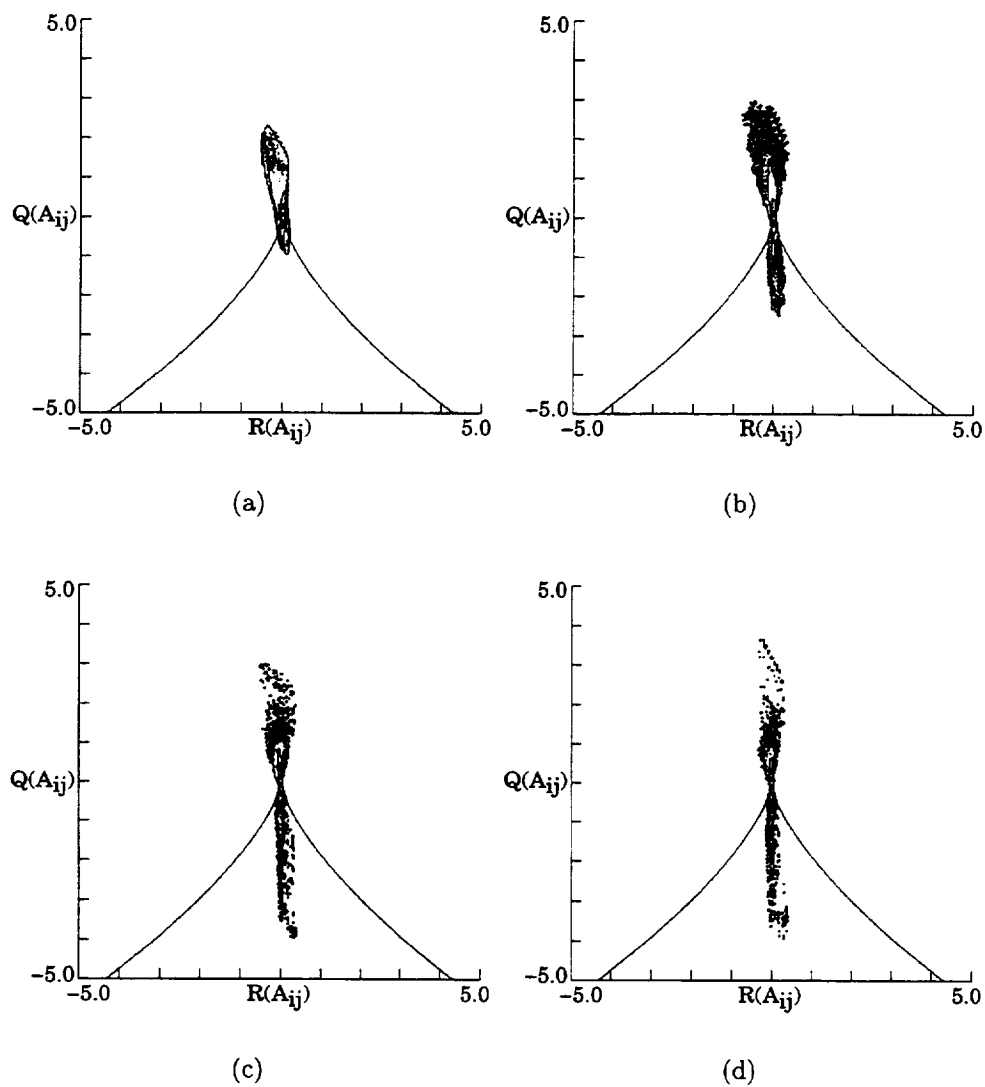


Figure 3.5: Time evolution of logarithmic contour plots of joint pdf of Q vs R .
 (a) $\tau = 12.5$. (b) $\tau = 15.0$. (c) $\tau = 17.0$. (d) $\tau = 17.5$.

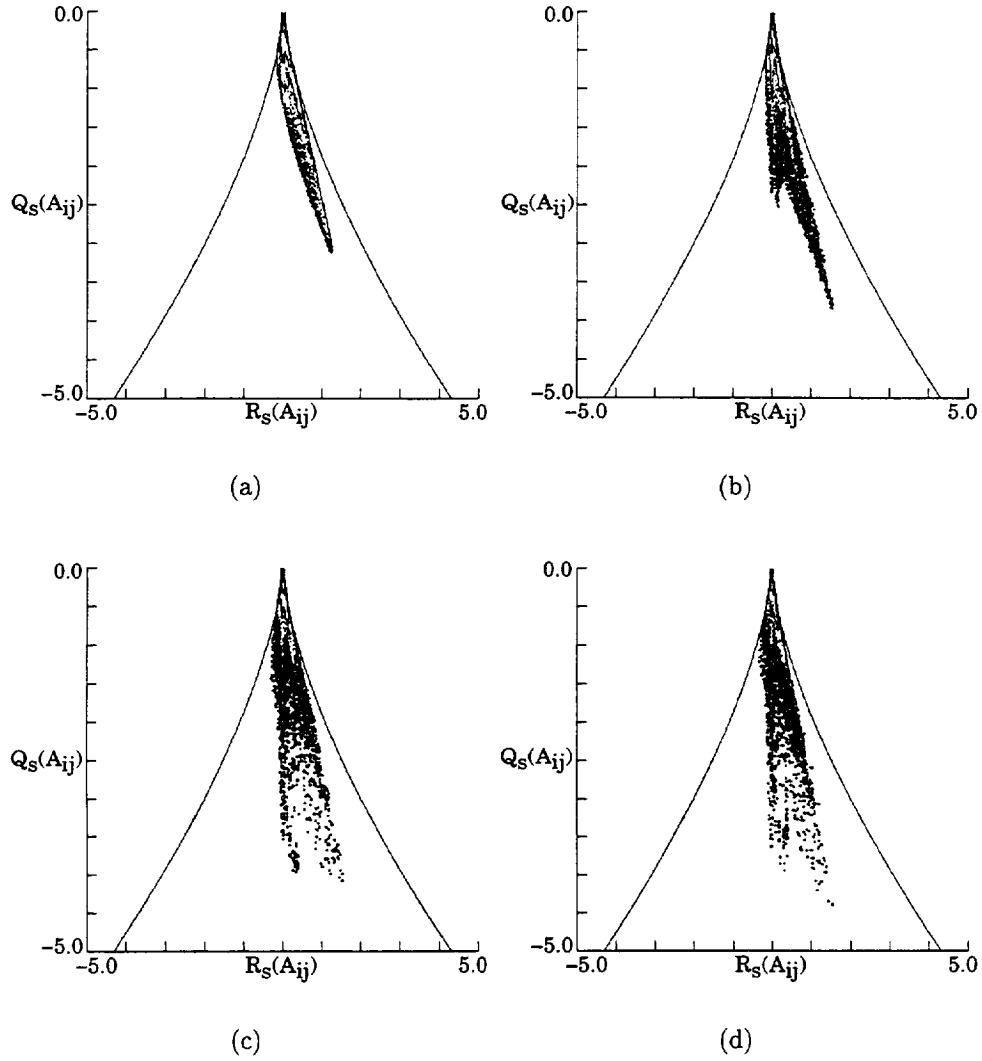


Figure 3.6: Time evolution of logarithmic contour plots of joint pdf of Q_s vs R_s .
 (a) $\tau = 12.5$. (b) $\tau = 15.0$. (c) $\tau = 17.0$. (d) $\tau = 17.5$.

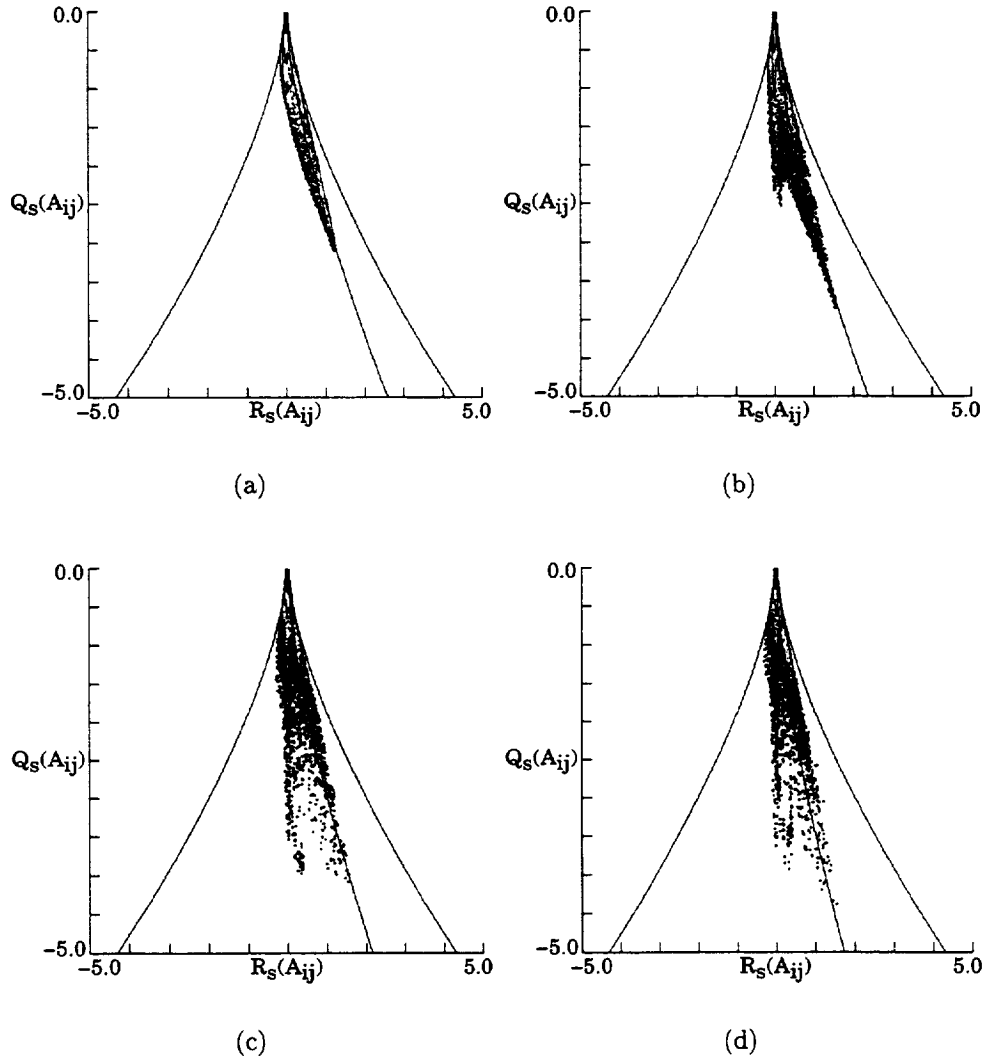


Figure 3.7: Time evolution of logarithmic contour plots of joint pdf of Q_s vs R_s . (a) $\tau = 12.5, \gamma/\alpha = -1.287$. (b) $\tau = 15.0, \gamma/\alpha = -1.256$. (c) $\tau = 17.0, \gamma/\alpha = -1.227$. (d) $\tau = 17.5, \gamma/\alpha = -1.173$.

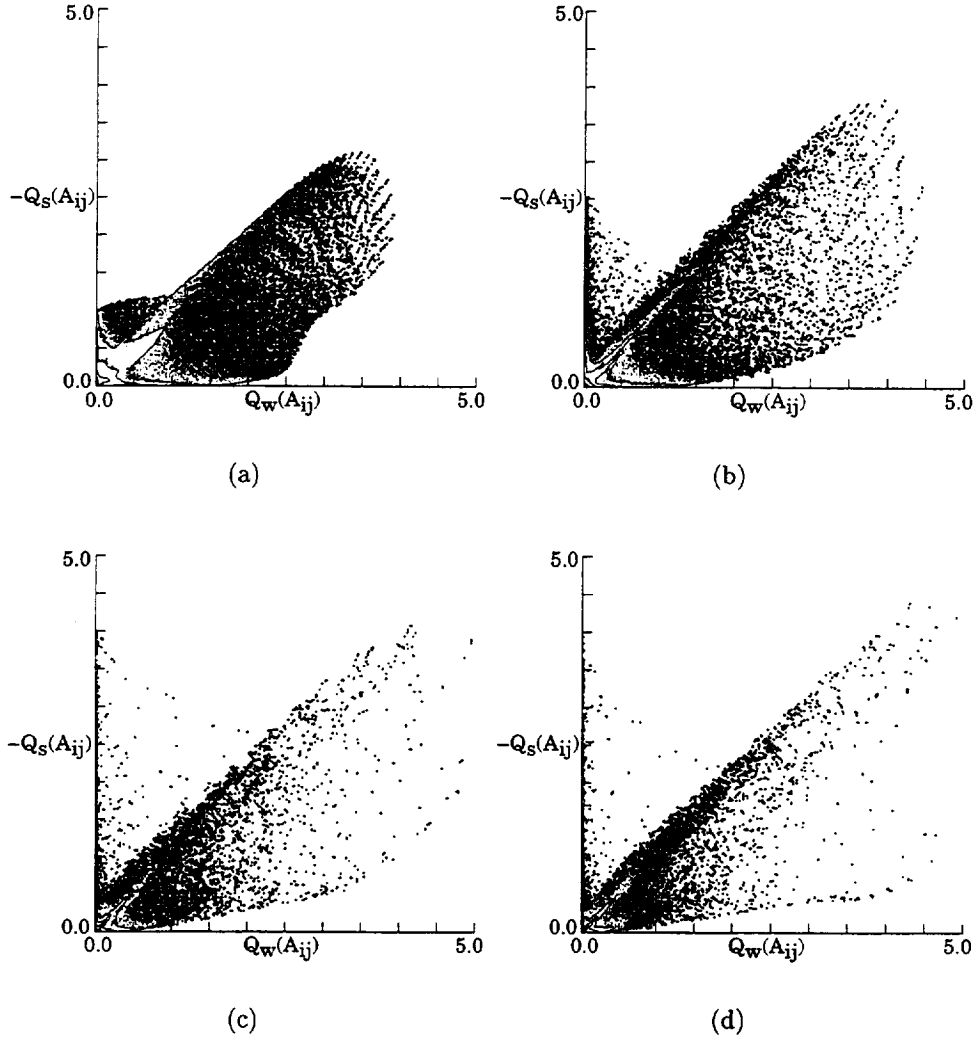


Figure 3.8: Time evolution of logarithmic contour plots of joint pdf of $-Q_s$ vs Q_w . (a) $\tau = 12.5$. (b) $\tau = 15.0$. (c) $\tau = 17.0$. (d) $\tau = 17.5$.

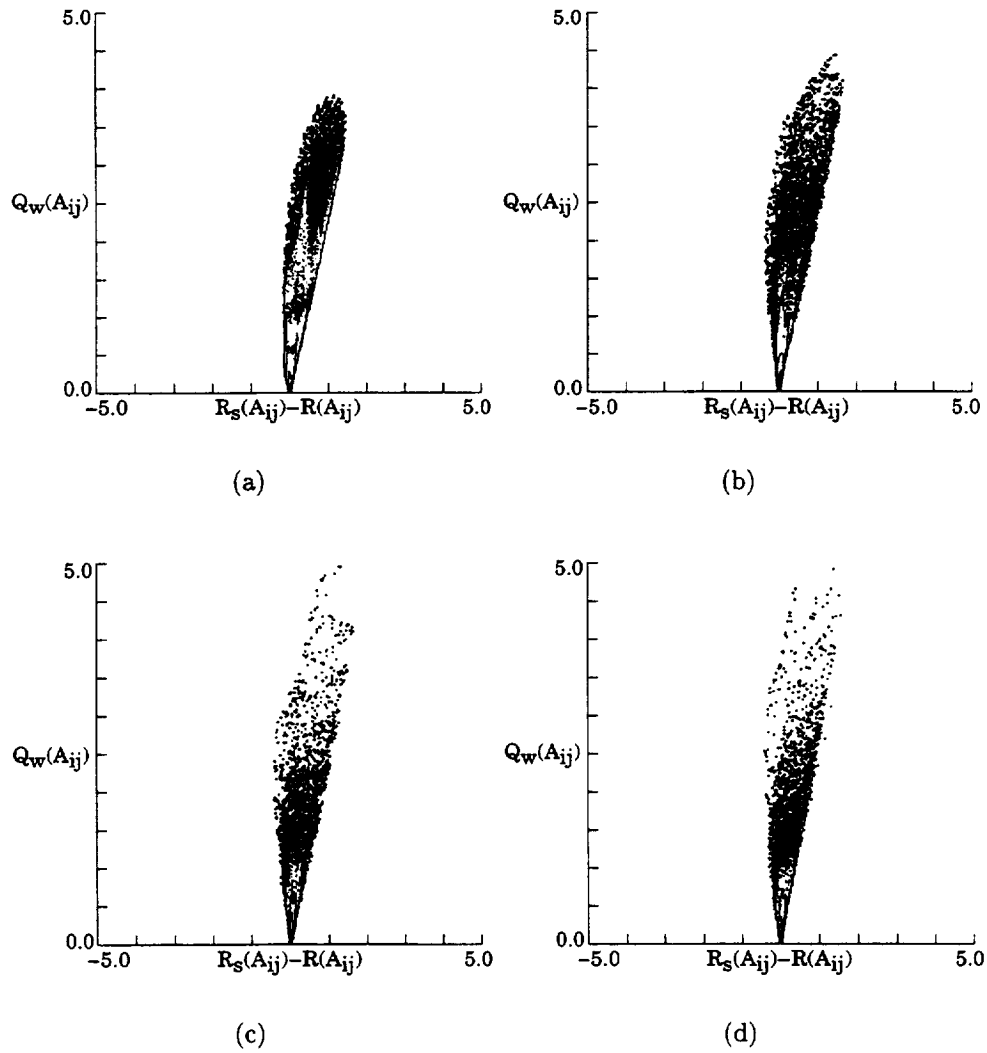


Figure 3.9: Time evolution of logarithmic contour plots of joint pdf of Q_w vs $(R_s - R)$. (a) $\tau = 12.5$. (b) $\tau = 15.0$. (c) $\tau = 17.0$. (d) $\tau = 17.5$.

are plotted in figure 3.11. Looking first at the eigenvalues for the S_{ij} tensor, there is a clear indication in figure 3.11(a) that the positive intermediate principal eigenvalue, β , is the eigenvalue that is shared by most of the data points. The mean value of β was determined to be 0.40. Figure 3.11(b) plots the principal eigenvalues of the A_{ij} tensor. At least one of the three eigenvalues is real, and that is the one shared by most of the data points. Data points with complex eigenvalues can usually be identified by those that have the same β and γ in the plot. It is clear from this plot that the eigenvalue of the A_{ij} tensor shared among the data points is the positive α . The mean value of α was also determined, and interestingly, it was also found to be 0.40. Therefore, λ corresponds to α in the Q - R plot and the positive β in the Q_s - R_s plot. The straight lines with $\lambda = 0.40$ are superimposed in both figures 3.10(a) and (b) to show how well the data points fit onto the line.

In the discussion of the behavior of the velocity gradient tensor in an incompressible flow where the acceleration gradient tensor $H_{ij} \neq 0$, Cantwell[5] hypothesized the existence of an intermediate asymptotic state for the velocity gradient tensor $A_{ij}(t)$. Cantwell theorizes that after a fluid particle is set into motion by any flow, the particle settles into a state similar to the Restricted Euler model where its velocity gradient tensor satisfies the asymptotic form:

$$A_{ij}(t) \approx K_{ij}[R(t)]^{1/3}. \quad (3.5)$$

The angular momentum of this fluid particle changes relatively slowly under the action arising from the flow when $H_{ij} \neq 0$. Cantwell proceeded to propose the intermediate asymptotic state for $A_{ij}(t)$:

$$A_{ij}(t) = M_{ij}e^{\int f(t)dt}; \quad \frac{dA_{ij}}{dt} = A_{ij}f(t). \quad (3.6)$$

For particles which satisfy this intermediate asymptotic model, a particular relationship that links the discriminant of H_{ij} , $D|_{H_{ij}}$ to that of A_{ij} , $D|_{A_{ij}}$ was derived:

$$D|_{H_{ij}} = D|_{A_{ij}}(R + fQ + f^3)^2 \quad (3.7)$$

The main consequence of this relationship is that the discriminants of A_{ij} and H_{ij} have the same sign, since the factor in brackets is squared. The eigenvalues of both

gradient tensors were therefore concluded to have the same character. The result that data points from the incompressible, Euler calculations were observed to have the same relationship as the factor in brackets lends support to the validity of this model.

The $-Q_s$ - Q_w and Q_w -($R_s - R$) invariant plots of these data points also reveal very interesting results. These data points also exhibit characteristics of the asymptotic state of the Restricted Euler model; described in equations 2.47 and 2.49. Most of these data points appear to lie on a straight line, intercepting the $-Q_s$ axis at a finite positive value in the $-Q_s$ - Q_w plot and the origin in the Q_w -($R_s - R$) plot. The straight lines that best fit these data points are found to be:

$$-Q_s = 0.89Q_w + 0.41; \quad (3.8)$$

$$Q_w = 2.30(R_s - R). \quad (3.9)$$

Similar data points were also identified in the same way at various times from $\tau = 12.5$ to $\tau = 17.5$. All the data points can be best-fit to a straight line with equation $\lambda^3 + \lambda Q_s + R_s = 0$. Figure 3.13 depicts these data points together with the straight line when $\lambda = 0.40$.

These same data points were also identified in the physical space as shown in figure 3.14, which is a contour plot of the local enstrophy density of the flow above the dividing plane. This figure illustrates the local enstrophy density level in the symmetry plane. The contour levels range from 0.445 to 4.45 at interval of 0.445 for all four plots. Data points that are identified in the right boundary have been superimposed on these plots, marked by the symbol '+'. These data points formed a very coherent structure from the earlier times when the flow began to develop until the later times; always located near the peak vorticity and evolved with it.

3.3.2 Classification of local flow topologies for data points with different $Q_w/(R_s - R)$ slopes

In addition to data points that are identified on the right boundary of the Q_w vs ($R_s - R$) plot of figure 3.9(c) (with slope $Q_w/(R_s - R) = 2.30$), other data points

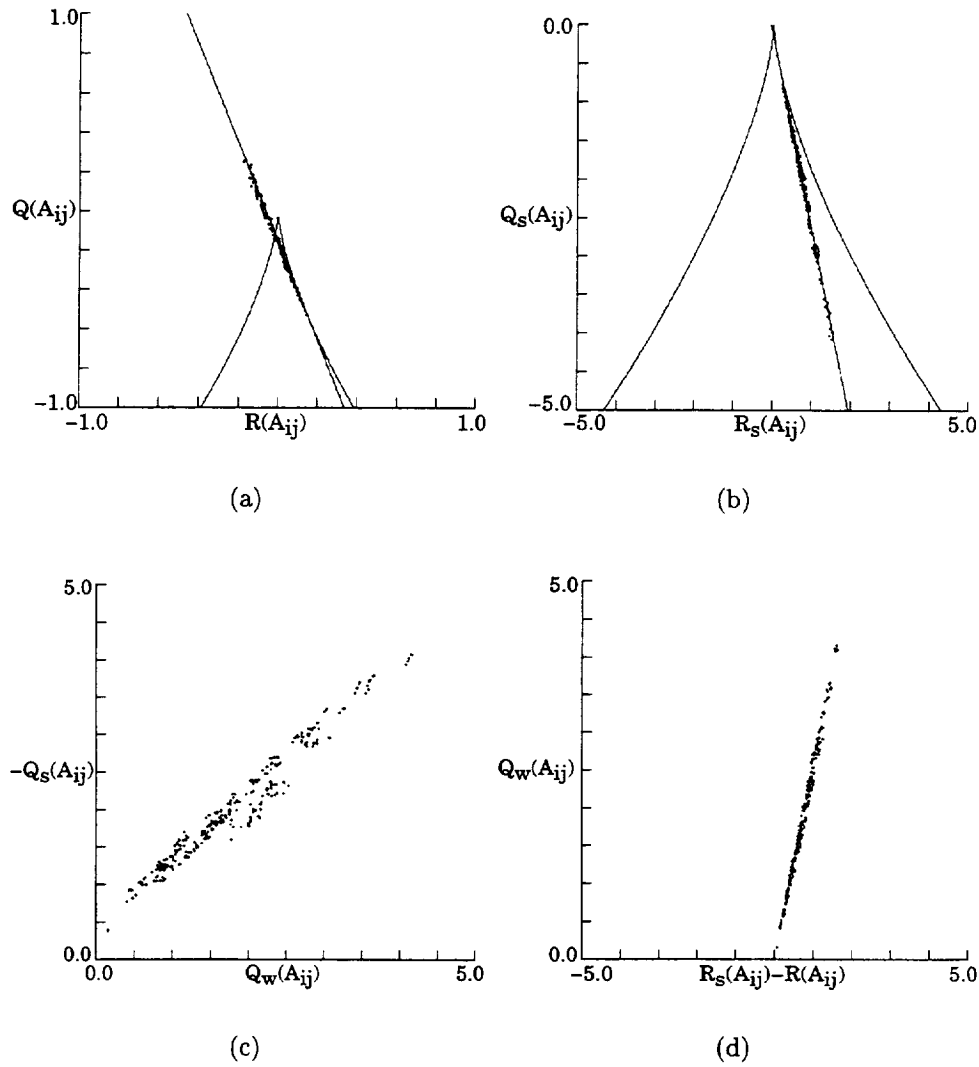
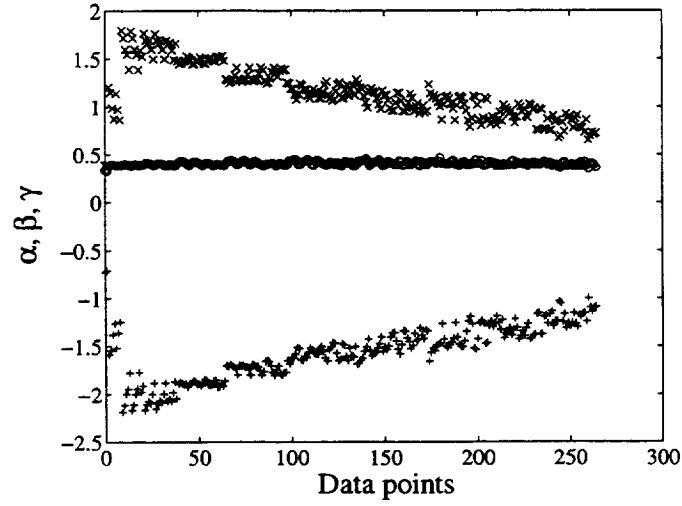
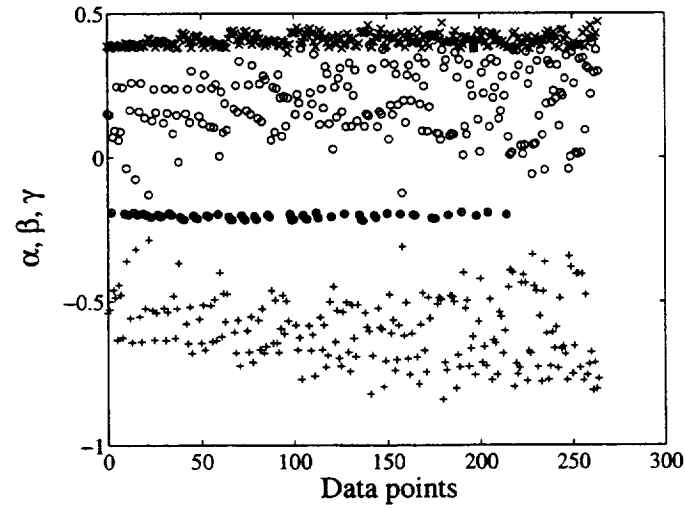


Figure 3.10: Invariant plots of the identified data points with $Q_w/(R_s - R) \doteq 2.30$. (a) Q vs R . (b) Q_s vs R_s . (c) $-Q_s$ vs Q_w . (d) Q_w vs $(R_s - R)$.

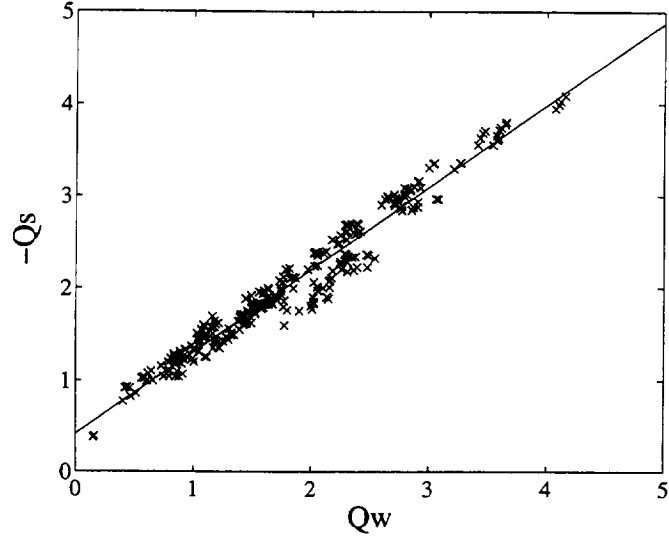


(a)

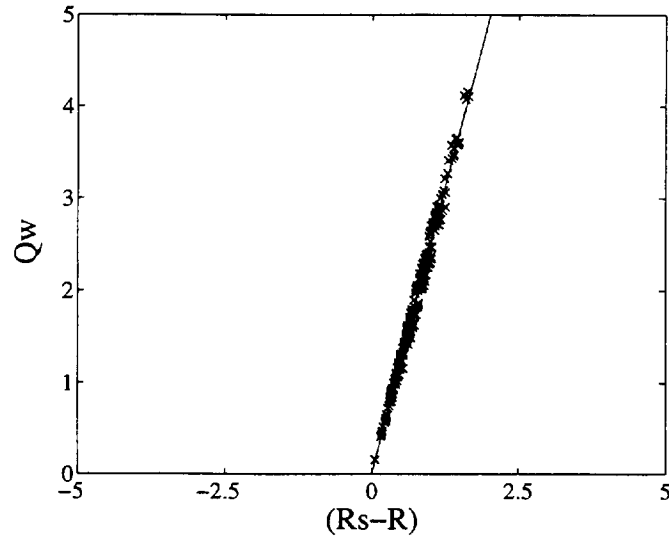


(b)

Figure 3.11: Principal eigenvalues of identified data points with $Q_w/(R_s - R) \doteq 2.30$. x: α , o: β and +: γ . (a) rate-of-strain tensor S_{ij} . $\bar{\beta} = 0.40$. (b) velocity gradient tensor A_{ij} . $\bar{\alpha} = 0.40$.



(a)



(b)

Figure 3.12: Linear lines that best-fit the identified data points with $Q_w/(R_s - R) \doteq 2.30$. (a) $-Q_s = 0.89Q_w + 0.41$. (b) $Q_w = 2.30(R_s - R)$.

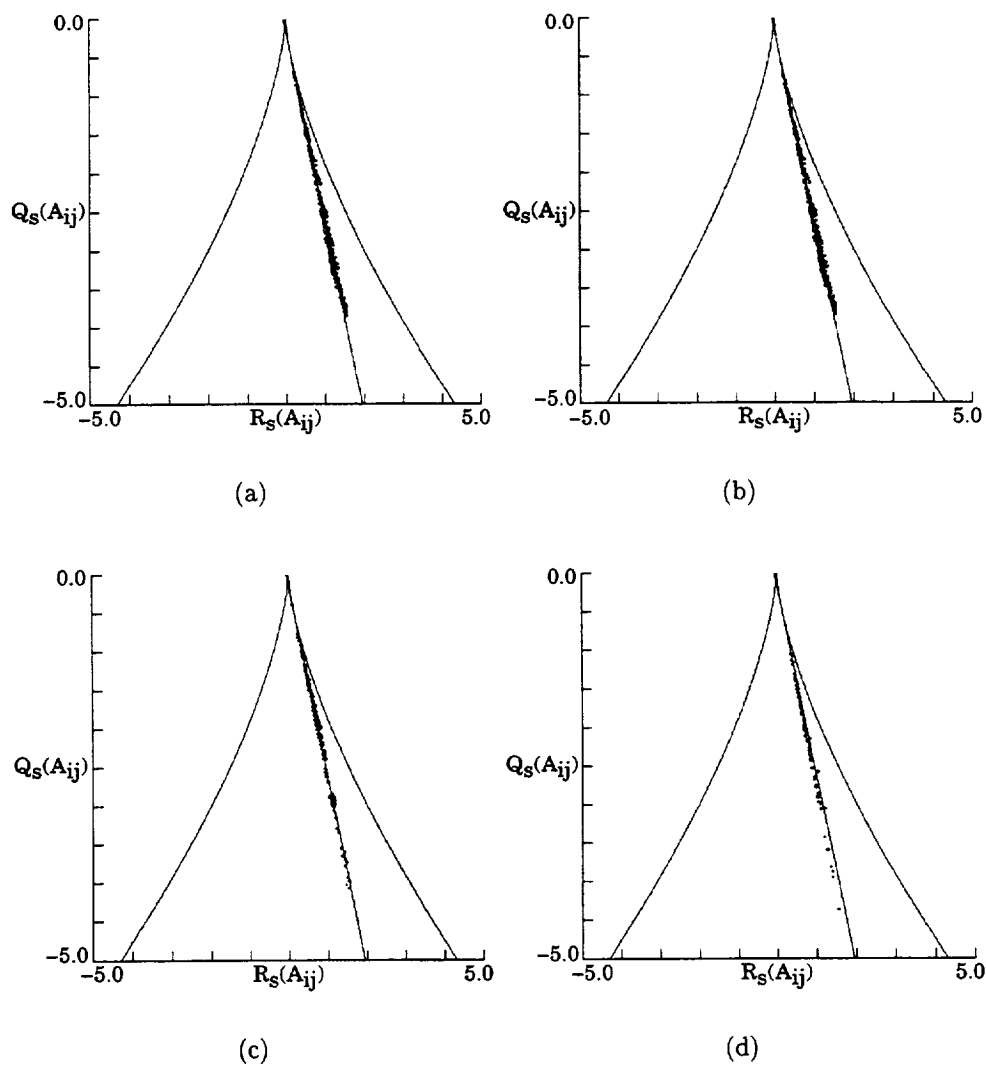


Figure 3.13: Q_s vs R_s for data points that lie on the right boundary of the Q_w vs $(R_s - R)$ plot. Equation of straight line: $0.40^3 + 0.40Q_s + R_s = 0$. (a) $\tau = 12.5$. (b) $\tau = 15.0$. (c) $\tau = 17.0$. (d) $\tau = 17.5$.

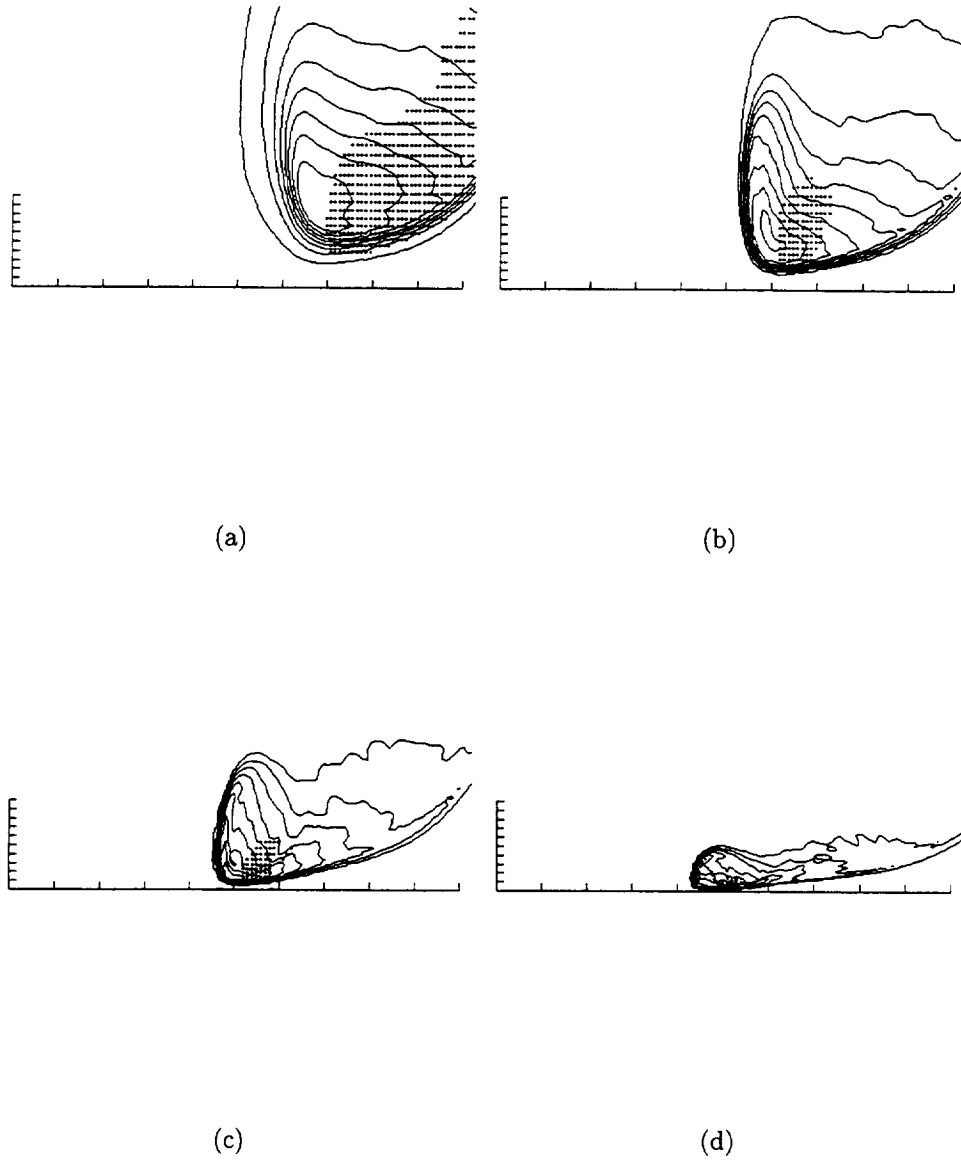


Figure 3.14: Time evolution of the contour plots of local enstrophy density in the symmetry plane. Contour levels range from 0.445 to 4.45 at interval of 0.445. +: data points that lie on the right boundary of the Q_w vs $(R_s - R)$ plots. (a) $\tau = 12.5$. (b) $\tau = 15.0$. (c) $\tau = 17.0$. (d) $\tau = 17.5$.

that lie on different $Q_w/(R_s - R)$ slopes at $\tau = 17.0$ are also identified and studied. These data points are within $\pm 15\%$ of slopes ranging from 5.00, -8.00 to the left boundary in figure 3.9(c), with slope of -3.80 . Due to the extremely small number of data points that lie on the left boundary, the slope of -4.40 was selected to replace -3.80 instead. Choosing a slope of -4.40 ensures that a reasonable number of data points are provided, and still include data points that lie on the left boundary. Data points that lie very close to the Q_w axis are also of interest. These data points have very large $Q_w/(R_s - R)$ values.

Figures 3.15 and 3.16 depict the Q - R and Q_s - R_s plots of the selected data points. Again, the points tend to lie on a straight line of: $\lambda^3 + \lambda Q_s + R_s = 0$. The value of λ was found to vary depending on the slope.

An interesting question arises as to which principal eigenvalue does λ correspond to when the slope selected is negative? To answer that, the principal eigenvalues of both the A_{ij} and S_{ij} tensors for selected data points with slope of -4.40 were determined and plotted in the same way as in figure 3.11 shown earlier. Figure 3.17(a) plots out the eigenvalues of the S_{ij} tensor. These data points do not show as strong a tendency to share an eigenvalue as those identified with slope of 2.30 in the earlier section. However, most of these data points have roughly equal value of the intermediate principal eigenvalue β , which is negative. The mean value of β was found to be -0.26 . When the principal eigenvalues of the A_{ij} tensors for these data were also determined, only a portion of the data points appear to have roughly equal value of γ .

Similar studies were done for data points that lie on other slopes. These data points share roughly equal value of the intermediate principal eigenvalue of the rate-of-strain tensor. This common principal eigenvalue is positive when the slope is positive, negative otherwise.

On the other hand, these data points do not have strong indication of having the same principal eigenvalue of the velocity gradient tensor when the slope selected deviates from the distinct right boundary with slope of 2.30. Among those data points that have roughly equal eigenvalue, the eigenvalue that these data points have in common is α when the slope is positive, γ otherwise.

Table 3.1 gives the corresponding λ value to the different slope selected. λ is determined from the mean β of the data points on these slopes. The same λ is also used in the equation of the straight line superimposed onto Q - R plots for these data points.

Table 3.1: Values of λ corresponding to selected slopes.

slope	2.30	5.00	∞	-8.00	-4.40
λ	0.40	0.20	≈ 0.0	-0.16	-0.26

Figure 3.18 shows that most of these points tend to have comparable local dissipation and local enstrophy while figure 3.19 identified the data points that correspond to the various slopes. These data points were also identified in the physical space shown in figure 3.20. Data points with positive slopes tend to lie closer to the “tail” of the vortex contour while those of negative slopes tend to lie close to the “head” of the vortex contour.

Results from subsections 3.3.1 and sections 3.3.2 and 3.3.3 indicated that data points that lie on the right boundary of the Q_w vs $(R_s - R)$ exhibit characteristics predicted by the Restricted Euler model. These data points have roughly the same intermediate principal eigenvalue of the rate of strain tensor, as well as the largest principal eigenvalue of the velocity gradient tensor. The relationship of $-Q_s$ and Q_w for these data points is also of the same form as the asymptotic solution of the Restricted Euler model. In the physical space, these data points form a coherent structure in the flow, always very close to the peak vorticity. These results indicate that even though Restricted Euler model assumes the acceleration gradient tensor $H_{ij} = 0$, its solution may still be applicable and useful in certain regions of a “real” flow. Similar results were not observed for data points that lie on other $Q_w/(R_s - R)$ slopes.

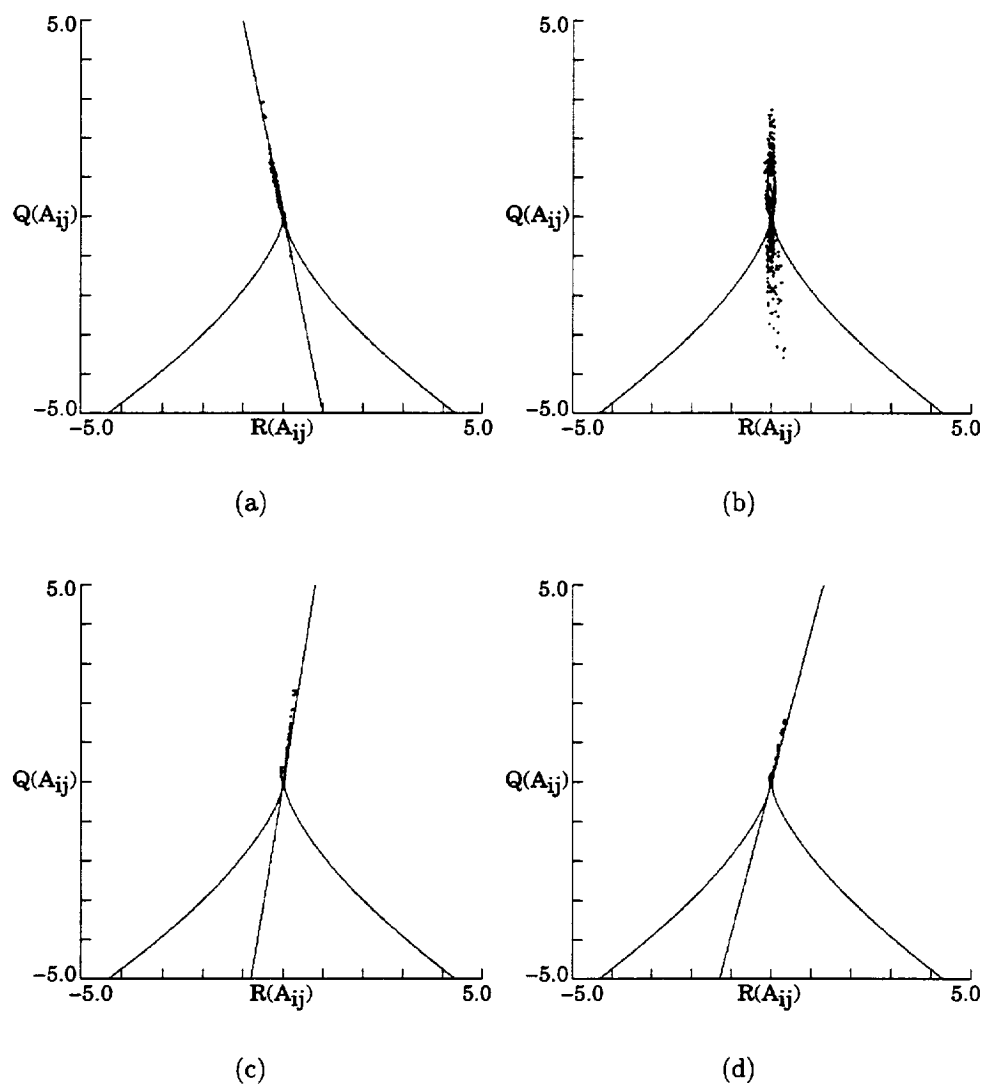


Figure 3.15: Q vs R for data points with various $Q_w/(R_s - R)$ slopes. (a) 5.00. (b) ∞ . (c) -8.00. (d) -4.40.

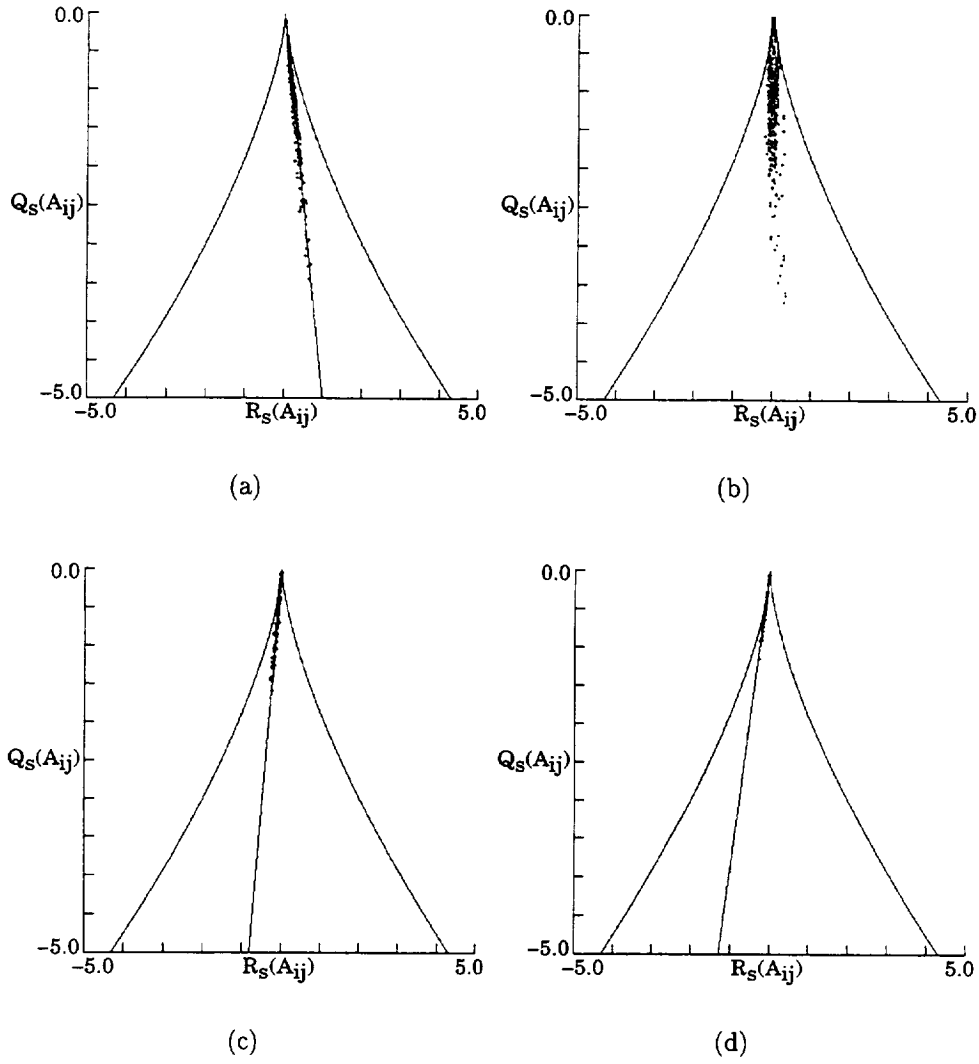
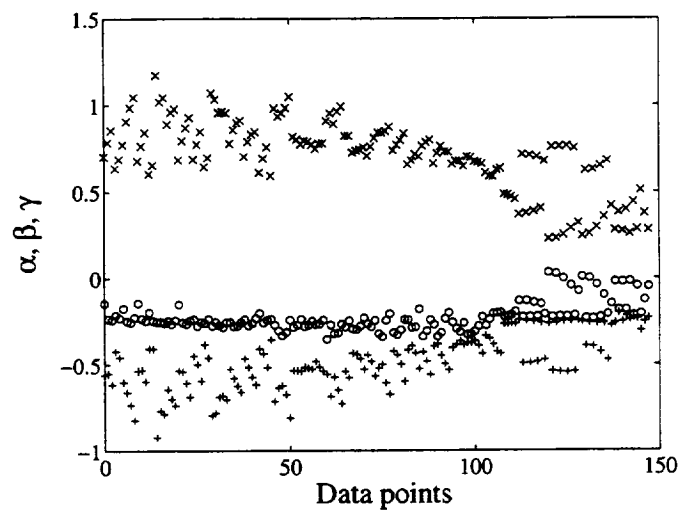
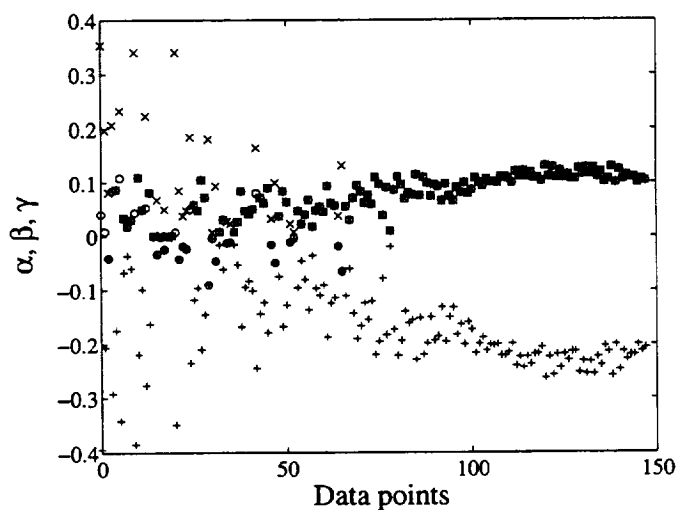


Figure 3.16: Q_s vs R_s for data points with various $Q_w/(R_s - R)$ slopes. (a) 5.00. (b) ∞ . (c) -8.00. (d) -4.40.



(a)



(b)

Figure 3.17: Principal eigenvalues of data points with $Q_w/(R_s - R) \doteq -4.4$. x: α , o: β and +: γ . (a) rate-of-strain tensor S_{ij} . (b) velocity gradient tensor A_{ij} .

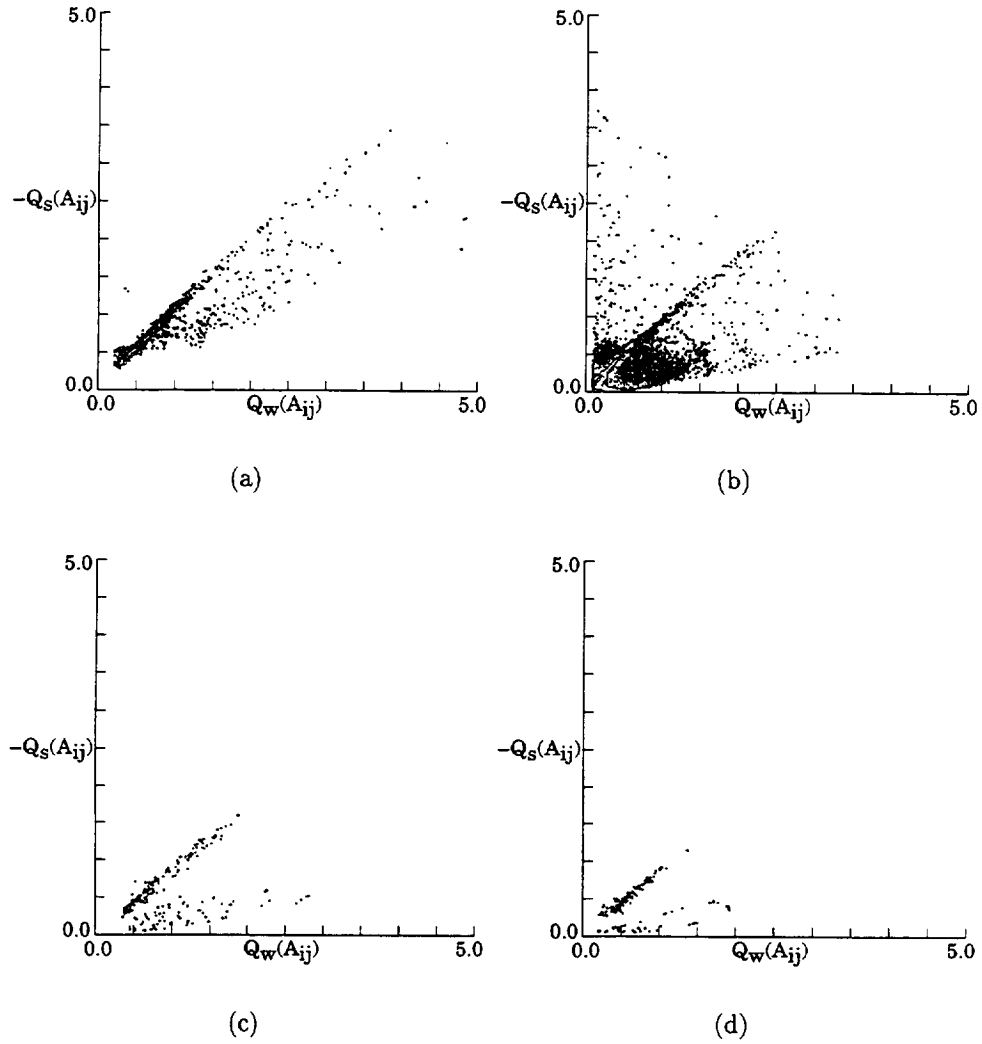


Figure 3.18: $-Q_s$ vs Q_w for data points with various $Q_w/(R_s - R)$ slopes. (a) 5.00. (b) ∞ . (c) -8.00. (d) -4.40.

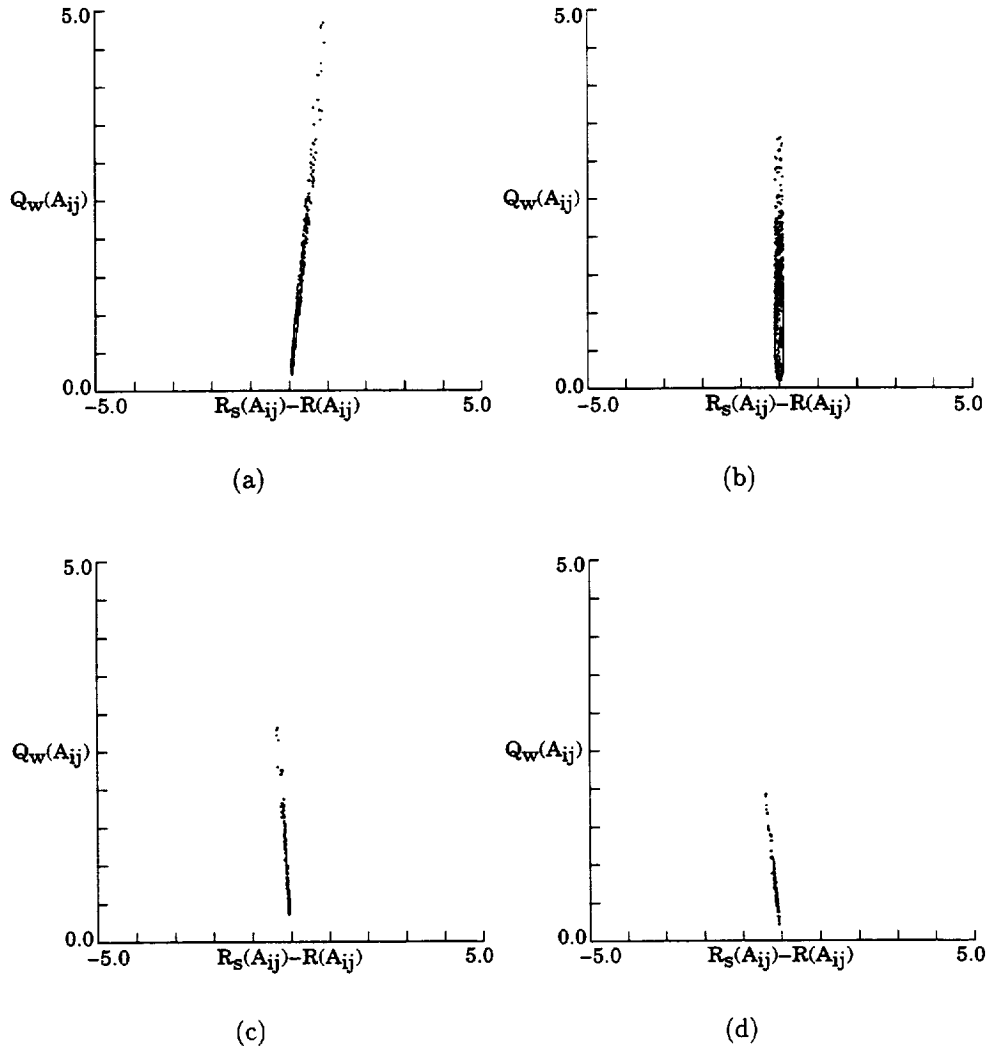


Figure 3.19: Q_w vs $(R_s - R)$ for data points with various $Q_w/(R_s - R)$ slopes. (a) 5.00. (b) ∞ . (c) -8.00. (d) -4.40.

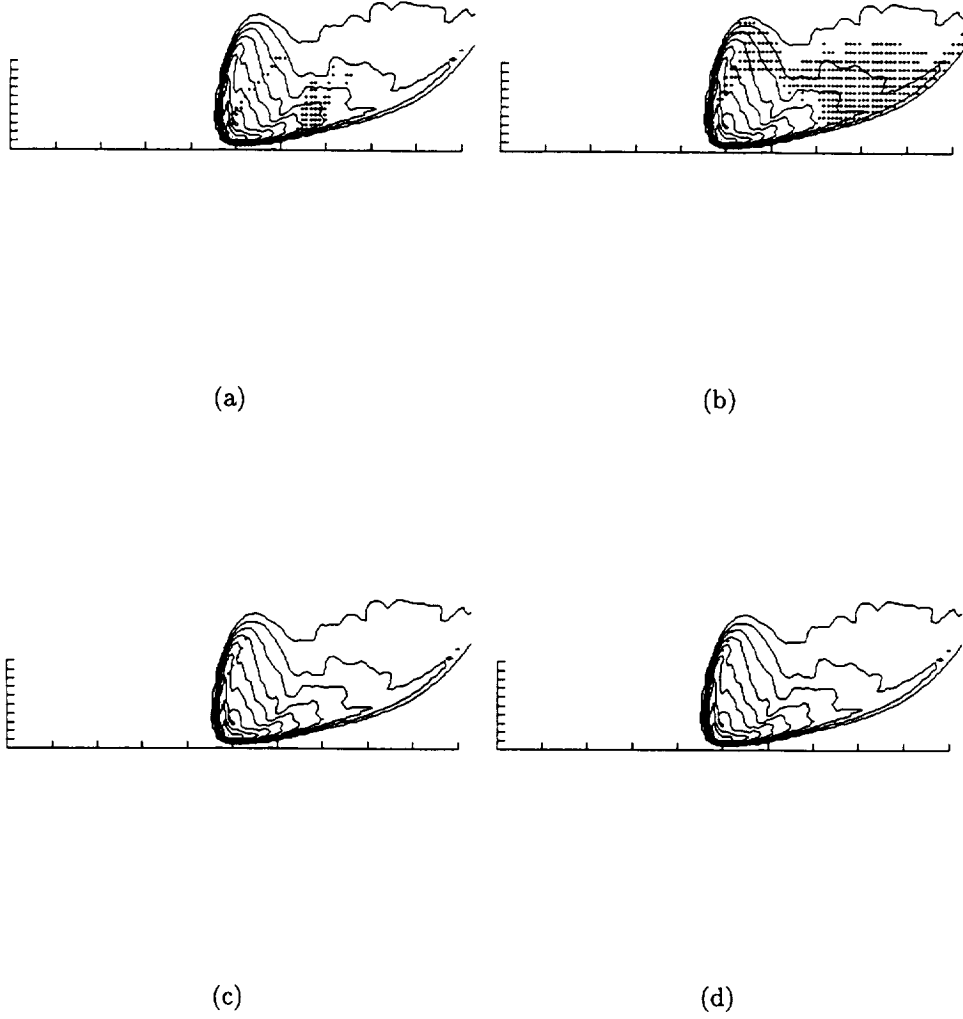


Figure 3.20: Contour plots of local enstrophy density in the symmetry plane. Contour levels range from 0.445 to 4.45 at interval of 0.445. +: data points with various $Q_w/(R_s - R)$ slopes. (a) 5.00. (b) ∞ . (c) -8.00. (d) -4.40.

3.3.3 Classification of local flow topologies for other interesting structures

In addition to studying the local flow topologies for data points with various slopes of Q_w and $(R_s - R)$ as well as locating them at the corresponding physical space, data points that lie within other interesting structures were also identified.

Data points with low local enstrophy density

Figure 3.21 depicts the invariant plots of data points with local enstrophy density less than or equal to five percent of the maximum enstrophy density in the flow at time $\tau = 17.0$. Referring to figure 3.8(c), these are the data points with relatively high local dissipation. Figures 3.21(a) and (b) are almost identical. This is because $Q = Q_s + Q_w$ by definition, which implies that $Q \approx Q_s$ since these data points have very low Q_w . These data points were identified in the low contours of the vorticity contour plot in figure 3.25(a).

Data points with high local enstrophy density

The invariants of data points with local enstrophy density of more than 70% of the maximum enstrophy in the flow were also examined. Both Q - R and Q_s - R_s plots gave early indication that all these data points might have the same γ/α ratio. However, figure 3.22(b) reveals that these data points do not correspond to any of the ratios superimposed onto the plot. The reason is because the tendency for data points to have the same γ/α ratio is usually observed only in regions of high local dissipation. In this flow, data points with high local enstrophy density do not always have high local dissipation, as observed in figure 3.22(c). Therefore, these data points do not fit onto any of the γ/α ratio curves. Figure 3.25(b) identified these data points in the physical space, which all lie within the vortex core with the highest contour level at the lower left corner where the “head” meets the “tail”.

Data points with high local dissipation

Two distinct structures were formed by data points with local dissipation greater than 70% of the maximum dissipation in the flow shown in the Q - R plot in figure 3.23(a). The first structure with mostly positive Q and negative R is very similar to the one shown in figure 3.23(a). In fact, these are the data points that also have high local enstrophy, a subset of those data points discussed in the preceding subsection. The other structure is formed by data points with high local dissipation but with low local enstrophy density. Two separate structures are also formed by these data points in figure 3.23(b). One of the structures hugs the Q_s axis, while the other fits onto a curve of common γ/α ratio shown in figure 3.7(c). These data points are indicated in the physical space shown in figure 3.25(c).

Data points with comparable local enstrophy and dissipation

Finally, data points of local enstrophy density within 15% of the local dissipation are identified in figure 3.24. These data points have very low Q , as shown in the Q - R plot. This is because Q_s is always negative while Q_w is always positive. Therefore, Q for data points with exactly the same magnitude of Q_s and Q_w would be zero by definition. Figures 3.24(c) and (d) show that these points formed a very coherent structure in both plots while figure 3.25(d) identified these data points in the physical space.

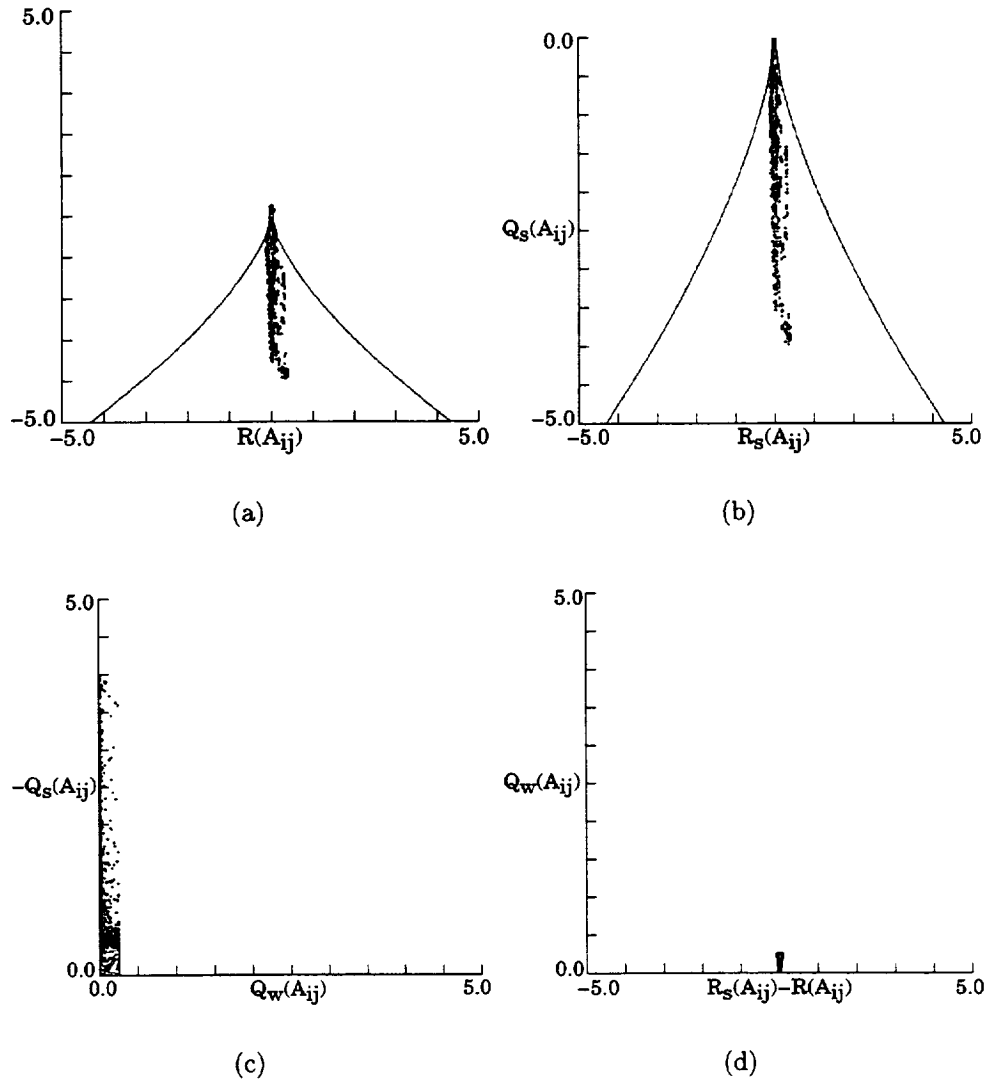


Figure 3.21: Data points with $Q_w \leq 5\%$ of $Q_w|_{max}$. (a) Q vs R . (b) Q_s vs R_s . (c) $-Q_s$ vs Q_w . (d) Q_w vs $(R_s - R)$.

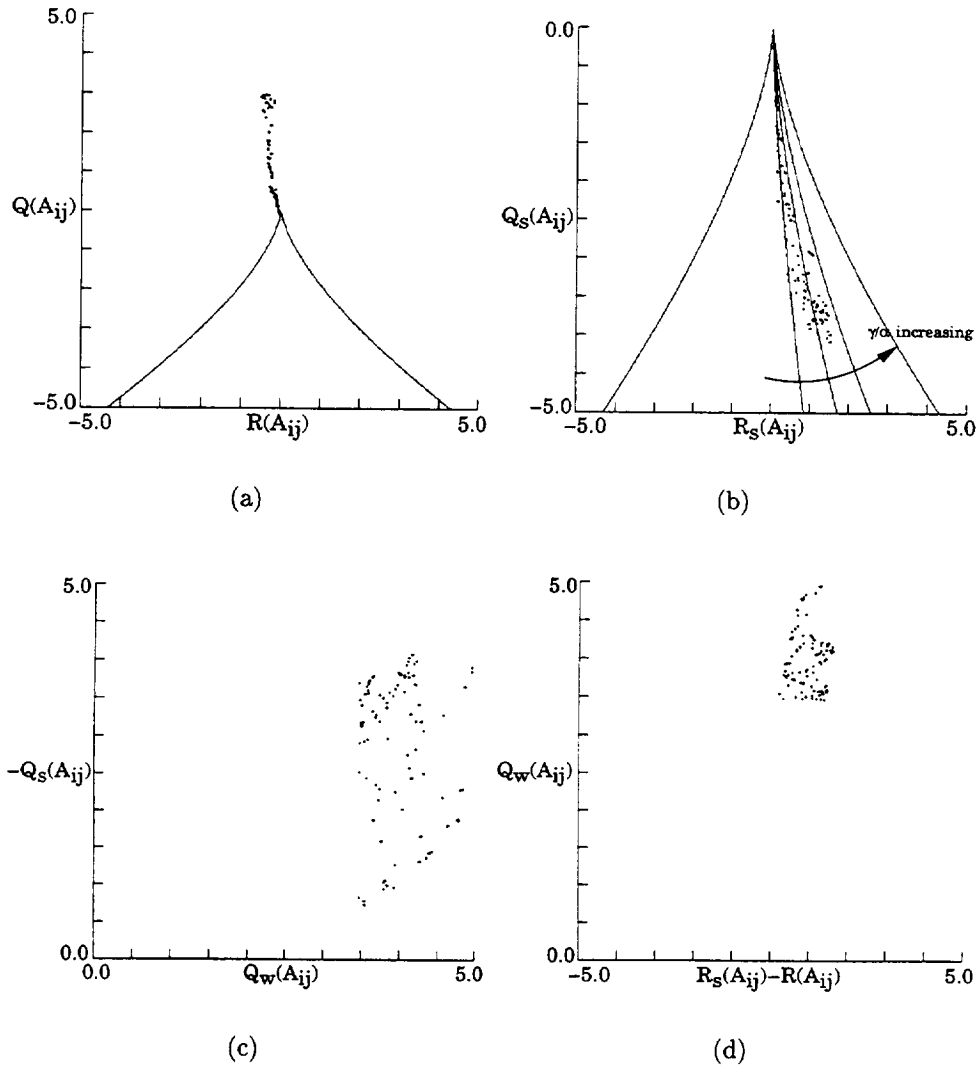


Figure 3.22: Data points with $Q_w \geq 70\%$ of $Q_w|_{max}$. (a) Q vs R . (b) Q_s vs R_s . (c) $-Q_s$ vs Q_w . (d) Q_w vs $(R_s - R)$.

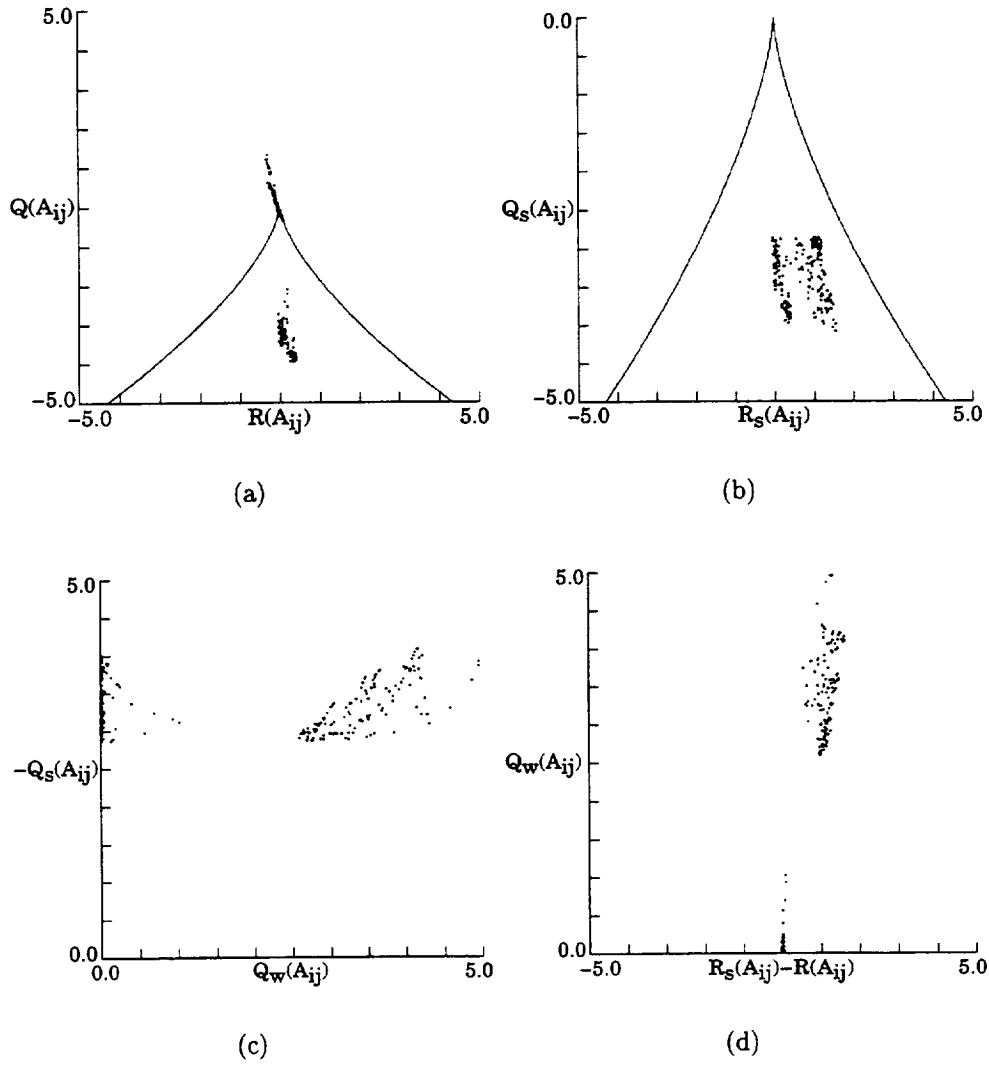
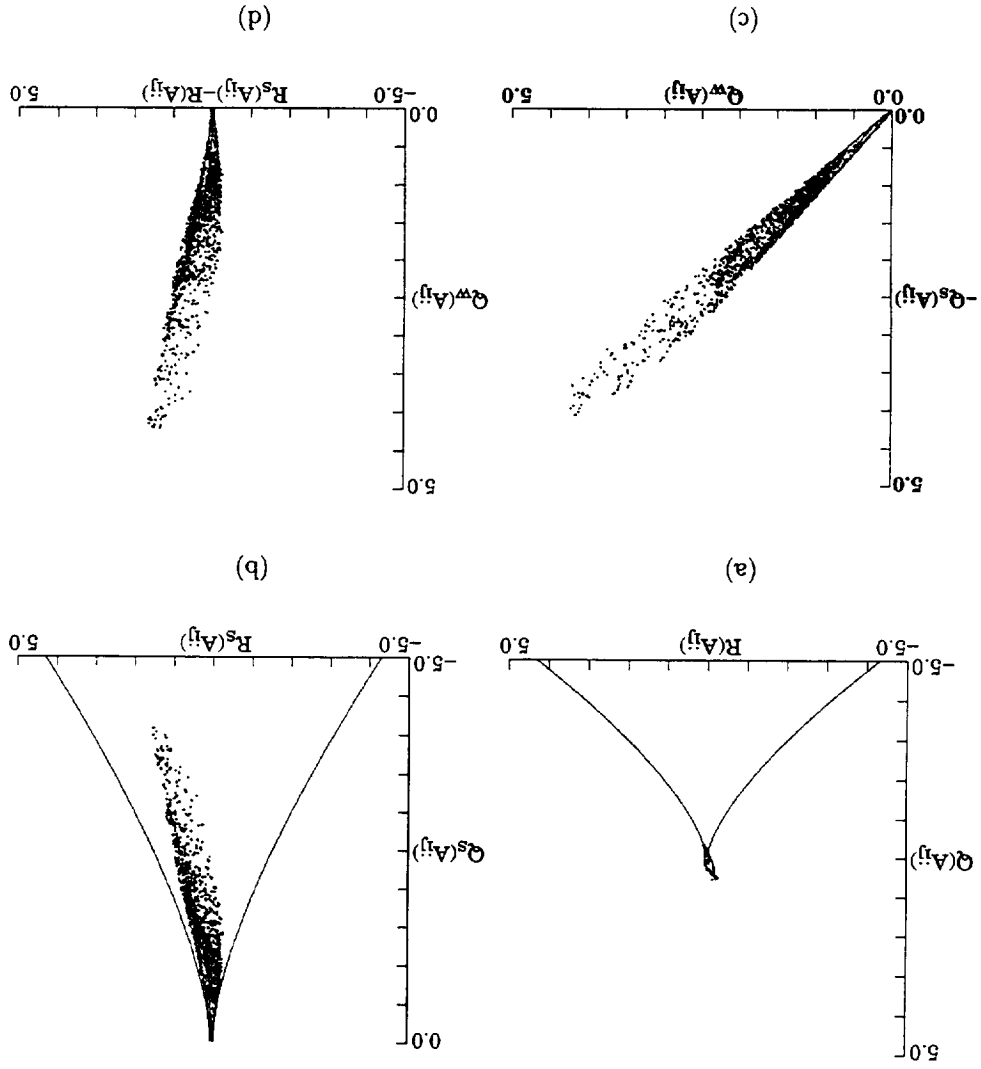


Figure 3.23: Data points with $|Q_s| \geq 70\%$ of $|Q_s|_{max}$. (a) Q vs R . (b) Q_s vs R_s . (c) $-Q_s$ vs Q_w . (d) Q_w vs $(R_s - R)$.

Figure 3.24: Data points with $-Q_s \approx Q_w$. (a) Q vs R . (b) Q_s vs R_s . (c) $-Q_s$ vs Q_w . (d) Q_w vs $(R_s - R)$.



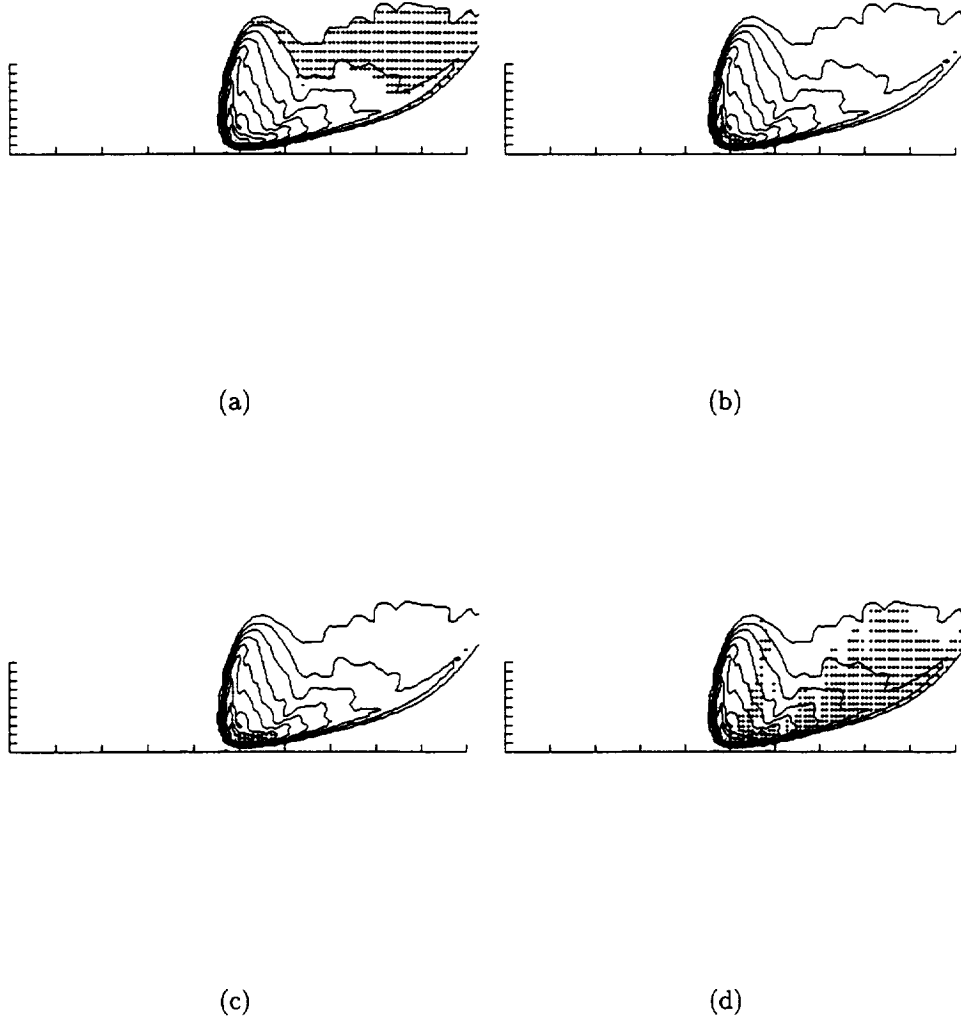


Figure 3.25: Contour plots of enstrophy density in the symmetry plane. Contour levels range from 0.445 to 4.45 at interval of 0.445. +: data points with (a) $Q_w \leq 5\%Q_w|_{max}$. (b) $Q_w \geq 70\%Q_w|_{max}$. (c) $|Q_s| \geq 70\%|Q_s|_{max}$. (d) $-Q_s \approx Q_w$.

Chapter 4

Homogeneous isotropic flow

A random field is *homogeneous* if its statistical properties are invariant under a translation of the coordinate system. The one-point statistics of a homogeneous field are independent of position, and multiple-point statistical properties depend only on the separation of the sampling points. A random field is *isotropic* if all its statistical properties are invariant under a rotation of the coordinate system. The one-point statistics of such a field are independent of the orientation of the coordinate system. Turbulent fluid motion is usually homogeneous if it is isotropic. Although ideal homogeneous and isotropic turbulence rarely exists, regions within turbulent flows often exhibit characteristics of homogeneous and isotropic flow.

This chapter focuses on a direct numerical simulation of a homogeneous and isotropic flow in a periodic box. This relatively low Reynolds number flow simulation was performed on a Silicon Graphics Indy workstation.

4.1 Approach

The three dimensional Navier-Stokes equations for incompressible flow were solved numerically using a pseudo-spectral method. The flow was assumed to be homogeneous and isotropic, with periodic boundary conditions imposed on all sides of a cube. The length of each side of this cube is 2π . The computational procedure involves transforming the velocity field from the physical space to Fourier space. Calculations of

solutions to the Navier-Stokes equation are performed in this spectral wave-vector space. The convolution sum that appears in the Fourier transformed Navier-Stokes equation is most efficiently calculated using a discrete form of the convolution theorem and the Fast Fourier algorithm. The non-linear products are first calculated in physical space and then transformed back to the spectral wave-vector space. A straight forward application of the Fast Fourier transform introduces “aliasing” errors. This is because the Fast Fourier transform is a discrete Fourier transform with no distinction made between wave-vector components of modulo $2mk_c$; where k_c is the maximum wave-vector (Nyquist “frequency”) considered in the calculations and m is any integer. Energy of high wave-vector components unresolved in the simulation is thus “aliased” into components of lower wave numbers. One way of removing the aliasing errors more efficiently is to truncate the interactions outside a specified boundary in Fourier space. This method does not significantly affect the resolution because only the high-wavenumber tail of the spectrum, containing a small fraction of the total energy, is truncated.

4.1.1 Derivation of governing equation

Given a velocity field in physical space, $\mathbf{u} = \mathbf{u}(\mathbf{x}, t)$, the direct Fourier transform of \mathbf{u} from physical space to spectral wave-space is:

$$\hat{\mathbf{u}}(\mathbf{k}, t) = \frac{1}{(2\pi)^3} \int [\exp(-i\mathbf{k} \cdot \mathbf{x}) \mathbf{u}(\mathbf{x}, t) d\mathbf{x}], \quad (4.1)$$

where $\hat{\mathbf{u}}(\mathbf{k}, t)$ denotes the transformed velocity field in spectral wave-space. To convert $\hat{\mathbf{u}}(\mathbf{k}, t)$ to physical space, apply the inverse Fourier transforms to $\hat{\mathbf{u}}(\mathbf{k}, t)$:

$$\mathbf{u}(\mathbf{x}, t) = \int [\exp(i\mathbf{k} \cdot \mathbf{x}) \hat{\mathbf{u}}(\mathbf{k}, t) d\mathbf{k}]. \quad (4.2)$$

Both integrals involved in the direct and inverse transforms are carried out over an infinite three-dimensional domain. In subsequent sections, the symbol “ $\hat{}$ ” will be used to denote the transformed quantities in the Fourier wave-space.

Consider the incompressible Navier-Stokes where the continuity and the momentum equations are, respectively:

$$\nabla \cdot \mathbf{u} = 0, \quad (4.3)$$

$$\frac{\partial \mathbf{u}}{\partial t} + \mathbf{u} \cdot \nabla \mathbf{u} = -\nabla P + \nu \nabla^2 \mathbf{u}. \quad (4.4)$$

$P = p/\rho$ is the kinematic pressure and $\nu = \mu/\rho$ is the kinematic viscosity.

The Fourier transform of the continuity equation is:

$$\widehat{\nabla \cdot \mathbf{u}} = 0 = \mathbf{k} \cdot \hat{\mathbf{u}}(\mathbf{k}, t) \quad (4.5)$$

Equation 4.5 reveals an important result: the Fourier transform of the velocity, $\hat{\mathbf{u}}$, is constrained to lie in a plane in wave-space, π , perpendicular to \mathbf{k} since the dot-product between \mathbf{k} and $\hat{\mathbf{u}}$ is zero at all times.

Taking the Fourier transform of the momentum equation:

$$\frac{\partial \hat{\mathbf{u}}(\mathbf{k}, t)}{\partial t} + \nu k^2 \hat{\mathbf{u}}(\mathbf{k}, t) = -i\mathbf{k} \hat{P}(\mathbf{k}, t) - \mathbf{u} \cdot \widehat{\nabla \mathbf{u}} \quad (4.6)$$

or

$$\left(\frac{\partial}{\partial t} + \nu k^2\right) \hat{\mathbf{u}}(\mathbf{k}, t) = -i\mathbf{k} \hat{P}(\mathbf{k}, t) - \mathbf{u} \cdot \widehat{\nabla \mathbf{u}} \quad (4.7)$$

The terms on the left hand side of the above equation involve only the velocity, $\hat{\mathbf{u}}$, which evolves only in the wave-space plane π . Therefore, all the terms on the right hand side must also evolve in the same wave-space plane. However, $\mathbf{k} \hat{P}(\mathbf{k}, t)$ is parallel to \mathbf{k} and perpendicular to the plane π . Hence, this quantity must be equal and opposite to the out-of-plane component of $\mathbf{u} \cdot \widehat{\nabla \mathbf{u}}$. This constraint was used to remove the pressure term from the momentum equation. Since $i\mathbf{k} \hat{P}(\mathbf{k}, t) + \mathbf{u} \cdot \widehat{\nabla \mathbf{u}}$ must lie in π - plane, this quantity can be rewritten as:

$$\mathbf{k} \cdot (i\mathbf{k} \hat{P} + \mathbf{u} \cdot \widehat{\nabla \mathbf{u}}) = 0, \quad (4.8)$$

or

$$ik^2 \hat{P} + \mathbf{k} \cdot \mathbf{u} \cdot \widehat{\nabla \mathbf{u}} = 0. \quad (4.9)$$

Multiplying equation 4.9 through by i , an expression for \hat{P} is obtained:

$$\hat{P} = \frac{i\mathbf{k} \cdot \mathbf{u} \cdot \widehat{\nabla \mathbf{u}}}{k^2} \quad (4.10)$$

Finally, the momentum equation can be rearranged to obtain the governing equation for $\hat{\mathbf{u}}$:

$$\frac{\partial}{\partial t} \hat{\mathbf{u}}(\mathbf{k}, t) = \left[\frac{\mathbf{k} \cdot \mathbf{u} \cdot \widehat{\nabla \mathbf{u}}}{k^2} \right] \vec{k} - \mathbf{u} \cdot \widehat{\nabla \mathbf{u}} - \nu k^2 \hat{\mathbf{u}} \quad (4.11)$$

The quantity $\mathbf{u} \cdot \widehat{\nabla} \mathbf{u}$ is not written as a convolution sum in wave-space because it is most efficient to carry out the product in physical space during the numerical implementation. This method of calculating the non-linear term is the pseudo-spectral method (also known as the Fast Fourier transform method).

4.1.2 Numerical method

The governing equation for \hat{u}_i in equation 4.11 was simplified further so that a numerical algorithm could be implemented to solve it more efficiently.

Treatment of the non-linear term

The non-linear term $\mathbf{u} \cdot \widehat{\nabla} \mathbf{u}$ is the convolution sum, responsible for most of the algorithmic complexities of the numerical scheme. Using the expression \mathcal{FT} to denote the direct Fourier transform and \mathcal{FT}^{-1} for the inverse Fourier transform, the convolution sum could be replaced by \hat{f}_{jm} :

$$(\mathbf{u} \cdot \widehat{\nabla} \mathbf{u})_j = \mathcal{FT}(\mathbf{u} \cdot \nabla \mathbf{u}) = ik_m \underbrace{\mathcal{FT}[\mathcal{FT}^{-1}(\hat{u}_m) \mathcal{FT}^{-1}(\hat{u}_j)]}_{\hat{f}_{jm}} \quad (4.12)$$

Equation 4.11 becomes:

$$\left(\frac{\partial}{\partial t} + \nu k^2 \right) \hat{u}_l(\mathbf{k}, t) = \left[\frac{\mathbf{k} \cdot \mathbf{u} \cdot \widehat{\nabla} \mathbf{u}}{k^2} \right] \mathbf{k} - \mathbf{u} \cdot \widehat{\nabla} \mathbf{u} = -ik_m \hat{f}_{lm} + ik_m \frac{k_l k_j}{k^2} \hat{f}_{jm}, \quad (4.13)$$

or

$$\frac{\partial \hat{u}_l(\mathbf{k}, t)}{\partial t} = -ik_m \hat{f}_{lm} + ik_m \frac{k_l k_j}{k^2} \hat{f}_{jm} - \nu k^2 \hat{u}_l(\mathbf{k}, t). \quad (4.14)$$

Treatment of the viscous term

The numerical implementation of equation 4.14 could be simplified by removing the viscous term on the right hand side. This viscous term can be absorbed into the main source term using a very elegant technique employed by Rogallo[28]. Given an Ordinary Differential Equation (ODE) of the form:

$$\frac{d\hat{u}_l}{dt} = G + \nu k^2 \hat{u}_l, \quad (4.15)$$

this equation can be simplified by introducing an integrating factor, $\phi = e^{\nu k^2 t}$ such that:

$$\frac{d}{dt}(\phi \hat{u}_l) = \phi \frac{d\hat{u}_l}{dt} + \phi \nu k^2 \hat{u}_l = \phi G. \quad (4.16)$$

This same technique is used to simplify equation 4.14:

$$\frac{d\hat{u}_l}{dt} - \nu k^2 \hat{u}_l = i[k_l \frac{k_j k_m}{k^2} \hat{f}_{jm} - k_m \hat{f}_{lm}] = G_l, \quad (4.17)$$

$$\frac{d}{dt} (e^{\nu k^2 t} u_l) = e^{\nu k^2 t} \left[-i k_m \hat{f}_{lm} + i \frac{k_l k_j}{k^2} \hat{f}_{jm} \right]. \quad (4.18)$$

Time marching scheme

A second-order Adams-Bashforth time marching scheme was selected to discretize equation 4.18 forward in time. The Adams-Bashforth scheme converts an ODE from:

$$\frac{du_l}{dt} = F. \quad (4.19)$$

to

$$u_l^{n+1} - u_l^n = \frac{\Delta t}{2} [3F^n - F^{n-1}]. \quad (4.20)$$

Applying the same scheme to equation 4.18 gives

$$(\phi \hat{u}_l)^{n+1} - (\phi \hat{u}_l)^n = \frac{\Delta t}{2} [3(\phi G_l)^n - (\phi G_l)^{n-1}]. \quad (4.21)$$

Substituting $\phi = e^{\nu k^2 t}$ into the above equation,

$$e^{\nu k^2 (t_n + \nabla t)} \hat{u}_l^{n+1} - e^{\nu k^2 t_n} \hat{u}_l^n = \frac{\Delta t}{2} [3e^{\nu k^2 t_n} G_l^n - e^{\nu k^2 (t_n - \nabla t)} G_l^{n-1}]. \quad (4.22)$$

Dividing this equation by $e^{\nu k^2 t_n} \cdot e^{\nu k^2 \nabla t}$, and rearranging:

$$\boxed{\hat{u}_l^{n+1} = e^{-\nu k^2 \Delta t} \hat{u}_l^n + \frac{\Delta t}{2} [3e^{-\nu k^2 \Delta t} G_l^n - e^{-2\nu k^2 \Delta t} G_l^{n-1}].} \quad (4.23)$$

$G_l = i[k_l \frac{k_j k_m}{k^2} \hat{f}_{jm} - k_m \hat{f}_{lm}]$ Equation 4.23 is the evolution equation for velocity in wave space \hat{u}_l .

Evolution of the zero-wave number component

An apparent singularity is observed in equation 4.23 at the zero wave number (where $k = \sqrt{k_1^2 + k_2^2 + k_3^2} = 0$). This singularity can be removed by considering equation 4.6. At zero wave number, this equation becomes:

$$\begin{aligned}
 \frac{\partial \hat{\mathbf{u}}(0, t)}{\partial t} &= -i\mathbf{k}\hat{P}(0, t) - \mathbf{u} \cdot \widehat{\nabla} \mathbf{u}(0, t) \\
 &= -ik_j \mathcal{FT}[\mathcal{FT}^{-1}(\hat{u}_j) \cdot \mathcal{FT}^{-1}(\hat{u}_l)] \\
 &= -ik_j \hat{f}_{lj}(0, t) \\
 &= 0
 \end{aligned}$$

Therefore, the zero wave number component of the velocity does not evolve. This apparent singularity due to the zero wave number component can be avoided by considering only the non-zero wave number components in the evolution equation.

4.1.3 Initial condition

The velocity in the simulation was initialized to satisfy both the continuity and isotropy conditions. This initial condition was first used by Rogallo[28]. Given an initial energy spectrum, the continuity condition is satisfied by assuming velocity $\hat{\mathbf{u}}$:

$$\hat{\mathbf{u}} = \hat{u}_l e_l = \alpha(\vec{k}) e'_1 + \beta(\vec{k}) e'_2. \quad (4.24)$$

e_i is the computation vector basis and e'_i is any vector basis having e'_3 parallel to \vec{k} . The complex components α and β in general are random in amplitude and phase, subject only to the constraint that:

$$\int \langle \mathbf{u} \cdot \mathbf{u}^* \rangle dA(k) = E(k) = \int \langle \alpha\alpha^* + \beta\beta^* \rangle dA(k). \quad (4.25)$$

$E(k)$ is the desired energy spectrum and the bracket $\langle \rangle$ denotes the inner product between the vectors. Rogallo selected α and β to be:

$$\alpha = \left(\frac{E(k)}{4\pi k^2} \right)^{1/2} e_1^{i\theta} \cos \phi, \quad \beta = \left(\frac{E(k)}{4\pi k^2} \right)^{1/2} e_2^{i\theta} \sin \phi. \quad (4.26)$$

θ_1 , θ_2 and ϕ are any random numbers uniformly distributed within the interval $(0, 2\pi)$.

To complete the formulation, the basis \vec{e}_i' needs to be related to the computational basis \vec{e}_i . This is achieved by using any basis subjected to the constraint:

$$k\vec{e}_3' = k_1\vec{e}_1 + k_2\vec{e}_2 + k_3\vec{e}_3 = \mathbf{k}. \quad (4.27)$$

Rotation about \vec{e}_3' is absorbed into the random phase ϕ . A particular basis is arbitrarily chosen such that:

$$\vec{e}_1' \cdot \vec{e}_3 = 0. \quad (4.28)$$

This choice of basis leads to a solution for \vec{e}_i' :

$$(k_1^2 + k_2^2)^{1/2} \vec{e}_1' = k_2\vec{e}_1 - k_1\vec{e}_2 \quad (4.29)$$

$$k(k_1^2 + k_2^2)^{1/2} \vec{e}_2' = k_1k_3\vec{e}_1 + k_2k_3\vec{e}_2 - (k_1^2 + k_2^2)\vec{e}_3. \quad (4.30)$$

Therefore, an initial velocity with an energy spectrum $E(k)$ that satisfies both the continuity and isotropy conditions is:

$$\hat{\mathbf{u}} = \left(\frac{\alpha k k_2 + \beta k_1 k_3}{k(k_1^2 + k_2^2)^{1/2}} \vec{e}_1 + \frac{\beta k_2 k_3 - \alpha k k_1}{k(k_1^2 + k_2^2)^{1/2}} \vec{e}_2 + \frac{\beta(k_1^2 + k_2^2)^{1/2}}{k} \vec{e}_3 \right) \quad (4.31)$$

In the simulation, the initial energy spectrum was chosen to be of the form “Top-hat”, as shown in figure 4.1. The energy for wave numbers $k = \sqrt{k_1^2 + k_2^2 + k_3^2}$ in the range between $k_c/3$ and $2k_c/3$ were initialized to a uniform magnitude. Energy for wave numbers outside this range was set to 0.0. k_c is the Nyquist wave number, which is half the number of grid points used in the simulation on each side of the cube.

4.1.4 Accuracy and Stability analysis

The numerical scheme used in this simulation is spectrally accurate in all the spatial directions, and second order accurate in time.

The stability of the numerical scheme can be analyzed by applying the second order Adams-Bashforth time marching scheme to a model equation. This model equation is a one dimensional linear convection-diffusion equation:

$$\frac{\partial u}{\partial t} + a \frac{\partial u}{\partial x} = \nu \frac{\partial^2 u}{\partial x^2}. \quad (4.32)$$

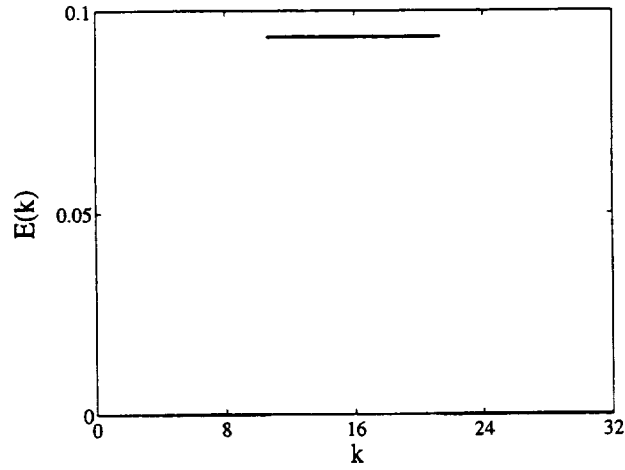


Figure 4.1: Initial energy spectrum.

Both a and ν are constants in this equation. When $2\pi = N\nabla x$, velocity u at a single Fourier component k can be expressed in a general form as:

$$u = e^{\alpha t} e^{2\pi i k x / N \nabla x} = e^{\alpha t} \cdot e^{i k x}. \quad (4.33)$$

Substituting the expression of u into equation 4.32:

$$\frac{\partial u}{\partial t} = -(\nu k^2 + i a k) u = L u. \quad (4.34)$$

A second order Adams-Bashforth time marching scheme is used to discretize the above ODE into:

$$u^{n+1} = u^n + \frac{\nabla t}{2} (3L u^n - L u^{n-1}). \quad (4.35)$$

Let σ denotes $e^{\alpha \nabla t}$. Since $e^{\alpha t} = (e^{\alpha \nabla t})^n = \sigma^n$, it is clear that the criterion for numerical stability is $|\sigma| \leq 1$.

Substituting $u^n = \sigma^n e^{i k x}$ into equation 4.35:

$$\sigma^2 - (1 + \frac{3}{2} L \nabla t) \sigma + \frac{1}{2} L \nabla t = 0. \quad (4.36)$$

The roots for this equation are:

$$\sigma_{1,2} = \frac{1}{2} \left[1 + \frac{3}{2} \pm \sqrt{1 + L \nabla t + \frac{9}{4} L^2 \nabla t^2} \right]. \quad (4.37)$$

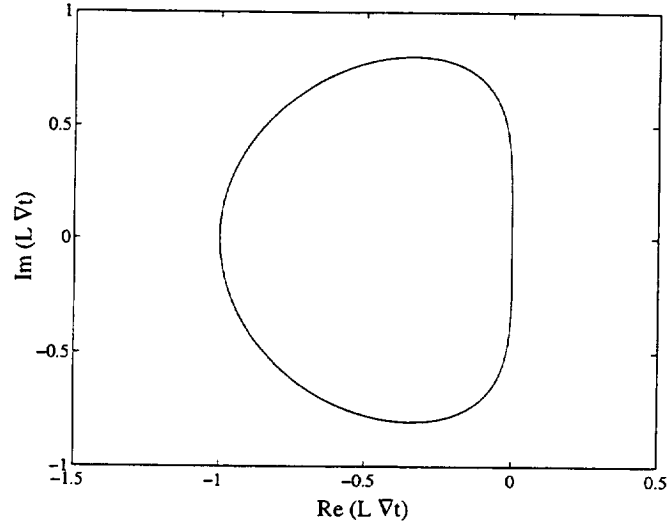


Figure 4.2: Stability region for second order Adams-Bashforth marching scheme

Using power series to expand the terms within the square-root:

$$\begin{aligned} \sqrt{1 + L\nabla t + \frac{9}{4}L^2\nabla t^2} &= 1 + \frac{1}{2}(L\nabla t + \frac{9}{4}L^2\nabla t^2) - \frac{1}{8}(L\nabla t + \frac{9}{4}L^2\nabla t^2)^2 + \\ &\quad \frac{3}{48}(L\nabla t + \frac{9}{4}L^2\nabla t^2)^3 + \dots \end{aligned} \quad (4.38)$$

The two roots of equation 4.36 are:

$$\begin{aligned} \sigma_1 &= 1 + L\nabla t + \frac{1}{2}L^2\nabla t^2 + O(\nabla t^3); \\ \sigma_2 &= \frac{1}{2}L\nabla t - \frac{1}{2}L^2\nabla t^2 + O(\nabla t^3). \end{aligned} \quad (4.39)$$

The first root shows that Adams-Bashforth scheme is second order accurate in time. The second root σ_2 is spurious. The presence of spurious root is a characteristic of all multi-step time marching schemes. In the case of second order Adams-Bashforth, this spurious root is of less concern since $\sigma_2 \rightarrow 0$ as $\nabla t \rightarrow 0$. Figure 4.2 shows the stability region when the numerical scheme is stable. The stability contour crosses the $Re(L\nabla t)$ at -1 and tangent to the imaginary axis. Strictly, the method is unstable for purely imaginary L (when $\nu = 0$). However, this instability is very mild. In viscous flow, the scheme is stable.

4.1.5 Aliasing errors

One of the complications arises in using the pseudo-spectral method to evaluate the convolution sum is the “aliasing” of high wave-number components into the lower ones. This is due to the fact that fast Fourier transform is incapable of distinguishing between wave-vector components of modulo $2mk_c$, where k_c is the Nyquist wavenumber and m is any integer. In Fourier transform, each Fourier coefficient denotes the contribution of a specific wave number to the velocity represented. Aliasing refers to the error in some Fourier coefficients due to contamination by other Fourier coefficients with wave numbers outside the range $-k_c < k < k_c$. Figure 4.3 illustrates this error when the number of grid points used in the simulation ($N = 8$) cannot resolve the wave-vector components represented by the higher wave numbers outside the range of $-k_c < k < k_c$, ($k_c = N/2 = 4$). Figure 4.3 shows that there are enough grid points to represent a sine wave of $\sin(3\theta)$ but not $\sin(9\theta)$. The information captured by the grid points made the sine wave $\sin(9\theta)$ appears to be $\sin(\theta)$.

In this simulation, the aliasing error is eliminated by the use of two sets of shifted grids as well as truncating Fourier wave components higher than a specific range. The details of this de-aliasing technique are described in Appendix B.

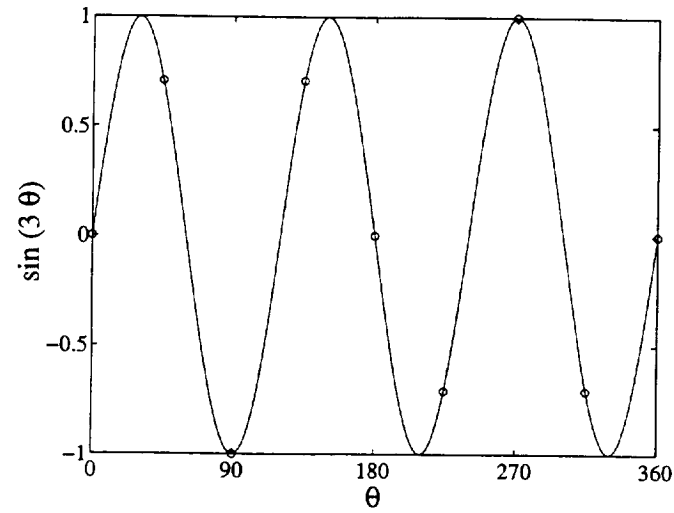
4.2 Classification of local flow topologies of A_{ij} tensor

The characteristic time scale t_o (eddy turn-over time) is used to normalize the dimensional time t obtained from the simulation:

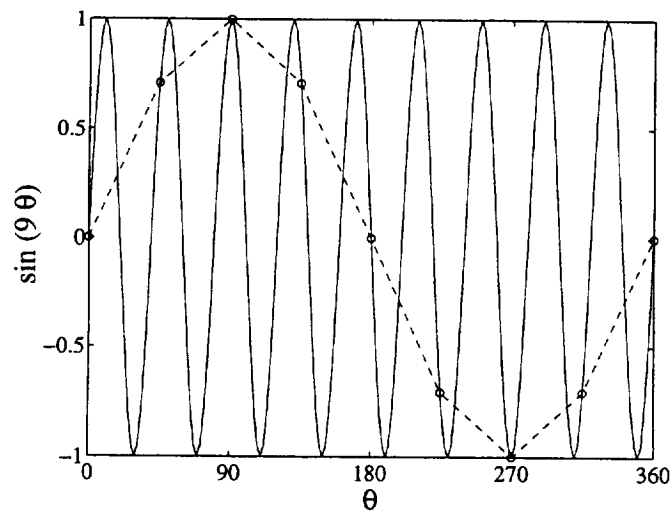
$$\tau = t/t_o; \quad t_o = \overline{q_o^2}/\overline{\varepsilon_o}, \quad (4.40)$$

where $\overline{q_o^2} = \frac{1}{2}\overline{u_i u_i}$ and $\overline{\varepsilon_o} = 2\nu\overline{s_{ij}s_{ij}}$ are the mean kinetic energy and the mean dissipation at initial condition. Figure 4.4 plots the time history of the mean kinetic energy, the mean strain-rate and the mean Reynolds number based on Taylor microscale λ . λ is defined to be:

$$\lambda = \left(5 \frac{\overline{q^2}}{\overline{s_{ij}s_{ij}}} \right)^{1/2}. \quad (4.41)$$



(a)



(b)

Figure 4.3: Aliasing error due to insufficient number of grid points used in Fourier transform. —: actual sine wave to be represented. 'o': Fourier coefficients represented by the grid points. ---: "aliased" sine wave represented by the grid points. (a) $\sin(3\theta)$. (b) $\sin(9\theta)$.

Self-similar solutions obtained from dimensional analysis[3] in homogeneous shear flow indicates that length δ and velocity u scale with time t as:

$$\delta \sim t^k; \quad u_o \sim t^{k-1}. \quad (4.42)$$

Therefore,

$$A_{ij} \sim u_o/\delta \sim t^{-1}. \quad (4.43)$$

Using this scaling relation for the length and velocity scales, the similarity solution dictates that the mean kinetic energy, mean strain-rate and the mean Reynolds number should scale with time t in the following ways:

$$\begin{aligned} q^2 &\sim u_i u_i \sim t^{2k-2}, \\ s_{ij} s_{ij} &\sim A_{ij} A_{ij} \sim t^{-2}, \\ Re_\lambda &\sim u_o \cdot \delta \sim t^{2k-1}. \end{aligned} \quad (4.44)$$

These predicted scalings were superimposed on the plots with $k = 0.31$.

The energy spectrum and other related spectra for the various velocity derivatives of this homogeneous isotropic flow are presented in Appendix C.

Figure 4.5 shows a general view of a homogeneous isotropic flow in a periodic box obtained from the simulation. Figure 4.5(a) is a contour plot of iso-*enstrophy* density surfaces, with $|\omega| = 2.8$. The characteristic length scales of the structures shown in this plot are relatively small, due to the relatively low Reynolds number in the simulation. This plot is compared to a contour plot of discriminant D in the same flow, shown in figure 4.5(b). Recall from the definitions of invariants that $D = (27/4)R^2 + Q^3$, where Q and R are the second and third invariants of A_{ij} respectively. Therefore, the same velocity gradient tensor A_{ij} that was used to determine vorticity in the flow was also used to determine D in corresponding grid points. Figure 1.3 depicts various topologies in an incompressible flow, depending on D . For positive D , the local topology is either a stable-vortex/stretching or an unstable-vortex/compressing. Figure 4.5(b) plots the iso-contour surfaces with $D = 6.0$. This plot reproduces structures obtained from contour plots of iso-*enstrophy* density surfaces.

Figure 4.6 shows the time evolution of the invariant plots from $\tau = 0.0$ to $\tau = 5.30$. At initial time $\tau = 0.0$, the contour plot of this joint pdf is evenly distributed on both

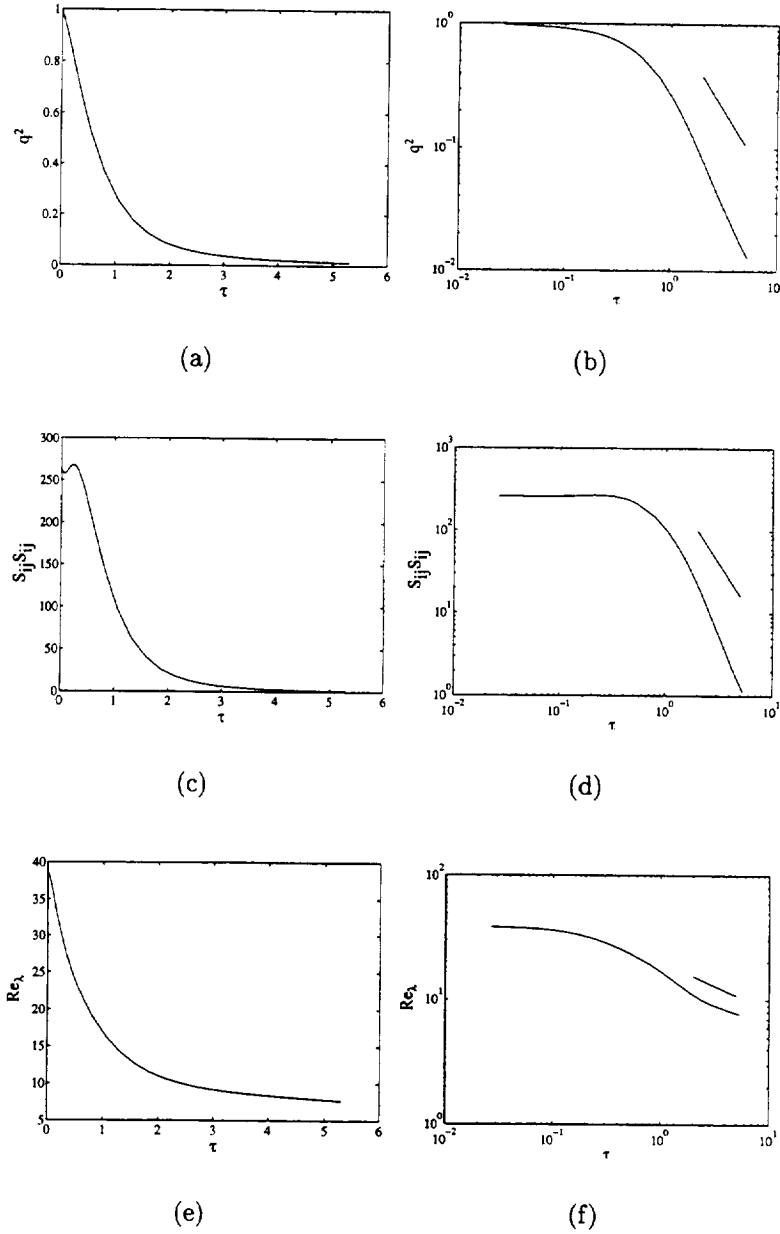
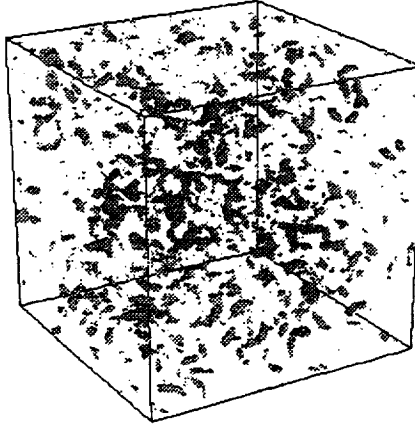
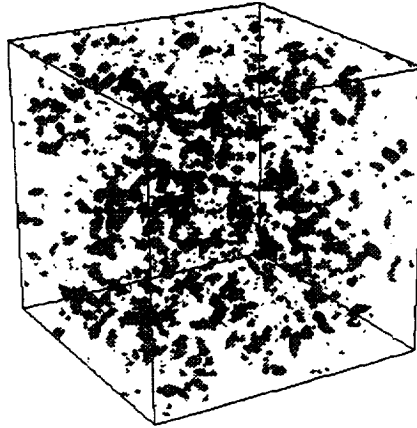


Figure 4.4: Time history of (a) mean kinetic energy. (b) log-log plot of mean kinetic energy. (c) mean strain rate. (d) log-log plot of mean strain rate. (e) Taylor microscale Reynolds number. (f) log-log plot of Taylor microscale Reynolds number.



(a)



(b)

Figure 4.5: Iso-contour surfaces for homogeneous isotropic flow at $\tau = 5.30$. (a) local enstrophy density $|\omega| = 2.8$. (b) local discriminant $D = 6.0$.

sides of the Q -axis. As the flow evolves, the velocity gradient decays at a rate $\approx 1/\tau$. Therefore, the invariants at later times are very small compared to the initial values. Figure 4.7 shows similar observations for the Q_s - R_s invariant plots. This rapid decay of invariants makes comparison of velocity gradient tensors at different times relatively difficult. To overcome this problem, the instantaneous mean strain-rate was used to normalize the velocity gradient tensor:

$$A_{ij} = \frac{A'_{ij}}{(s_{ij}s_{ij})^{1/2}}. \quad (4.45)$$

A'_{ij} is the dimensional velocity gradient tensor obtained from the simulation.

Figure 4.8 shows the time evolution of the normalized Q - R invariant plots from $\tau = 0.0$ to $\tau = 5.30$. As the flow evolves, the joint pdf of the invariants of normalized velocity gradient approaches a self-similar shape. Data points with higher gradients tend to have local flow topologies of stable-focus/stretching and unstable-node/saddle/saddle. Similar trends have been observed in other turbulent flows [7, 30, 31]. Figure 4.9 shows the time evolution of the contour plots of the joint pdf of Q_s versus R_s . Data points of high gradients are again observed to lie close to the lower right quadrant of the Q_s - R_s plot. Since dissipation is directly related to Q_s , these data points are concluded to reside in high local dissipation regions. Figure 4.10 indicates that local dissipation and local enstrophy density of this flow are comparable in magnitude. Figure 4.11 depicts the “tear-drop” shape structure formed by the contour plots of the joint pdf of Q_w versus $(R_s - R)$. This structure centers at the origin and tilts towards the positive $(R_s - R)$ axis as the flow evolves.

4.2.1 Effects of conditioning with local dissipation

When data points are conditioned at higher local dissipation levels, there is a tendency for data points to move close to the right discriminant curve. These data points have strong preference for local flow topology of unstable-node/saddle/saddle as shown in figures 4.12 and 4.13.

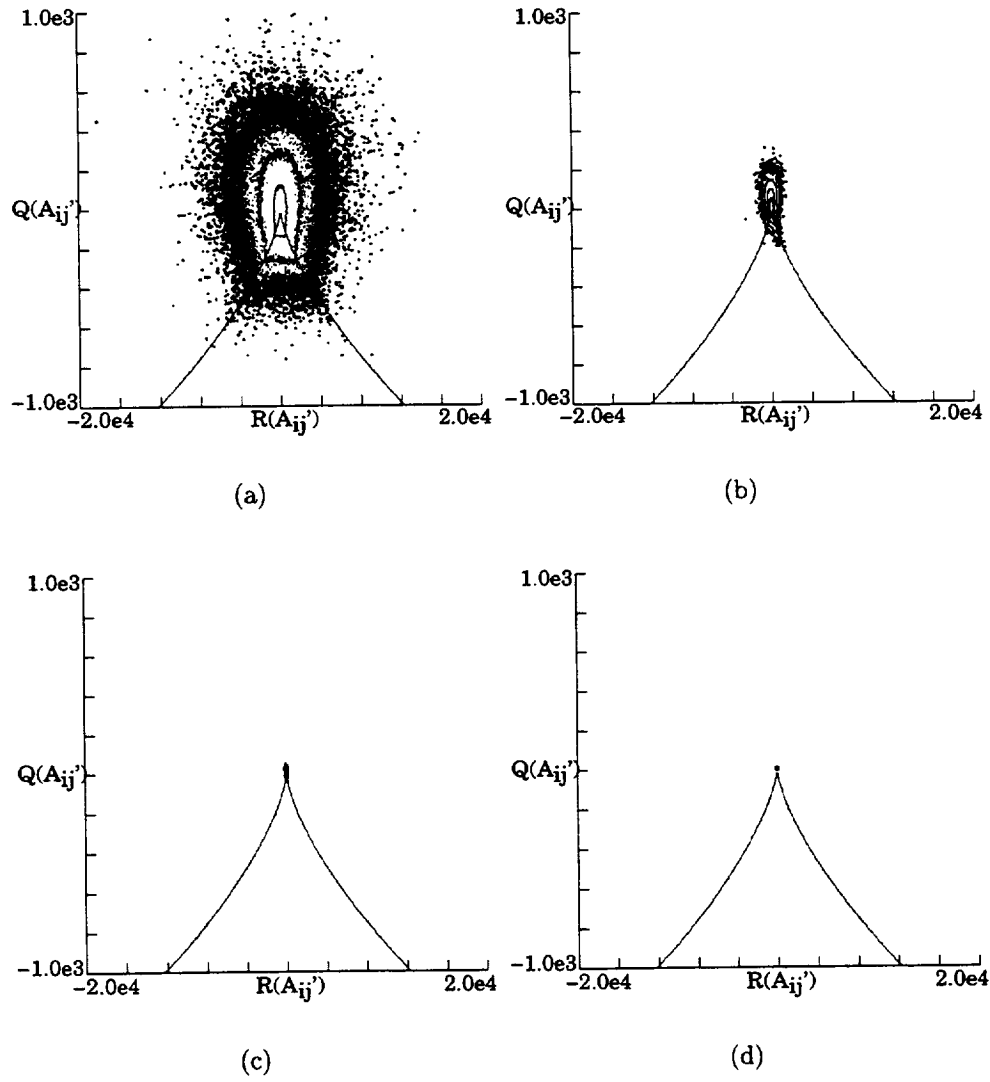


Figure 4.6: Time evolution of logarithmic contour plots of joint pdf of Q vs R for A'_{ij} at (a) $\tau = 0.0$. (b) $\tau = 1.32$. (c) $\tau = 2.65$. (d) $\tau = 5.30$.

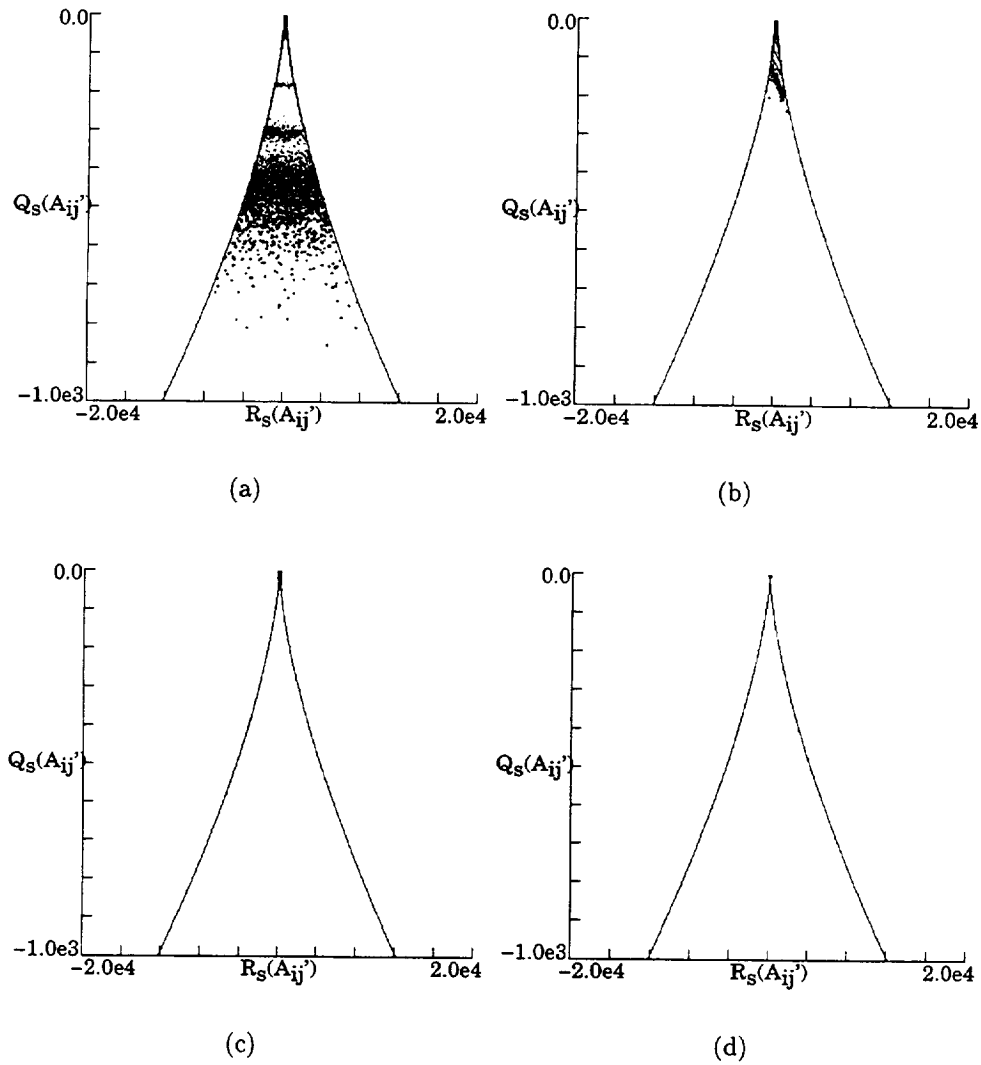


Figure 4.7: Time evolution of logarithmic contour plots of joint pdf of Q_s vs R_s for A'_{ij} at (a) $\tau = 0.0$. (b) $\tau = 1.32$. (c) $\tau = 2.65$. (d) $\tau = 5.30$.

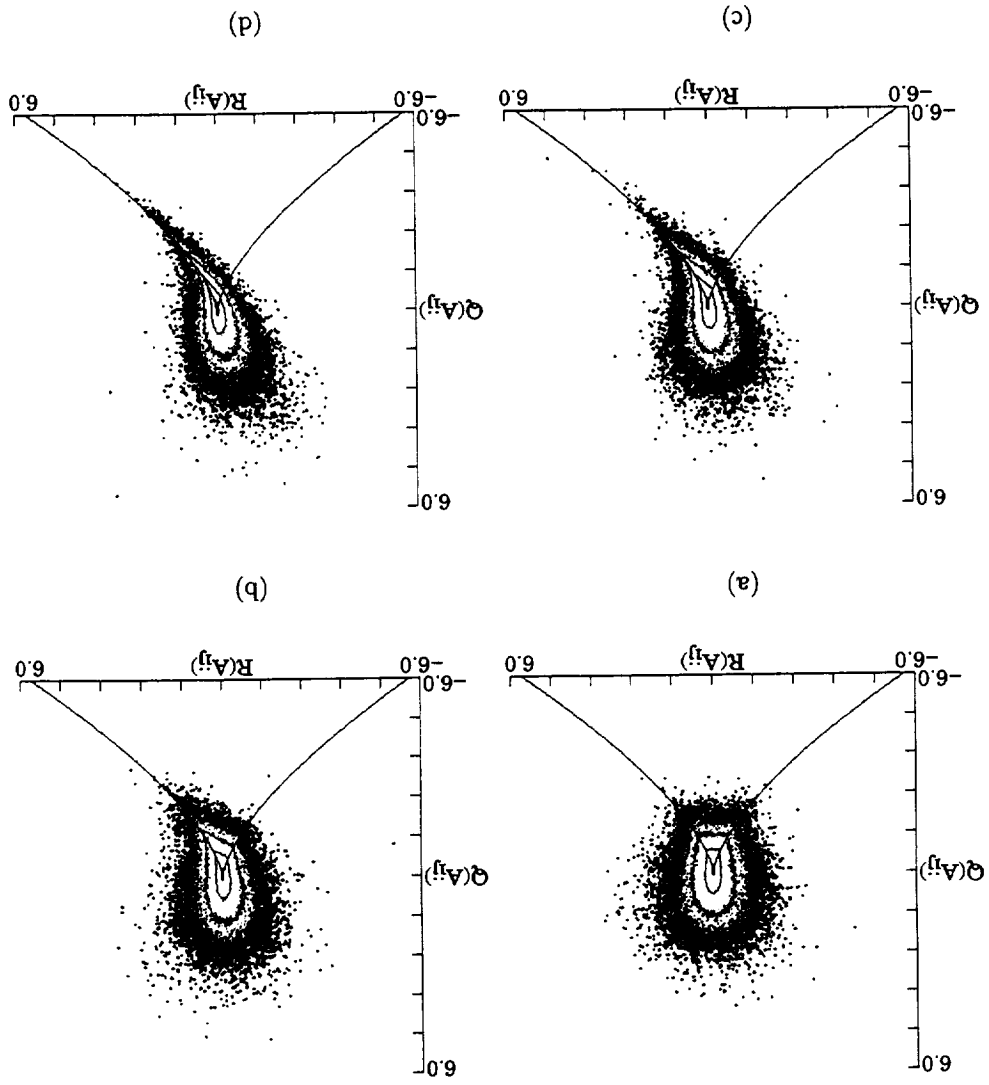


Figure 4.8: Time evolution of logarithmic contour plots of joint pdf of Q vs R for A_{ij} at (a) $\tau = 0.0$, (b) $\tau = 1.32$, (c) $\tau = 2.65$, (d) $\tau = 5.30$.

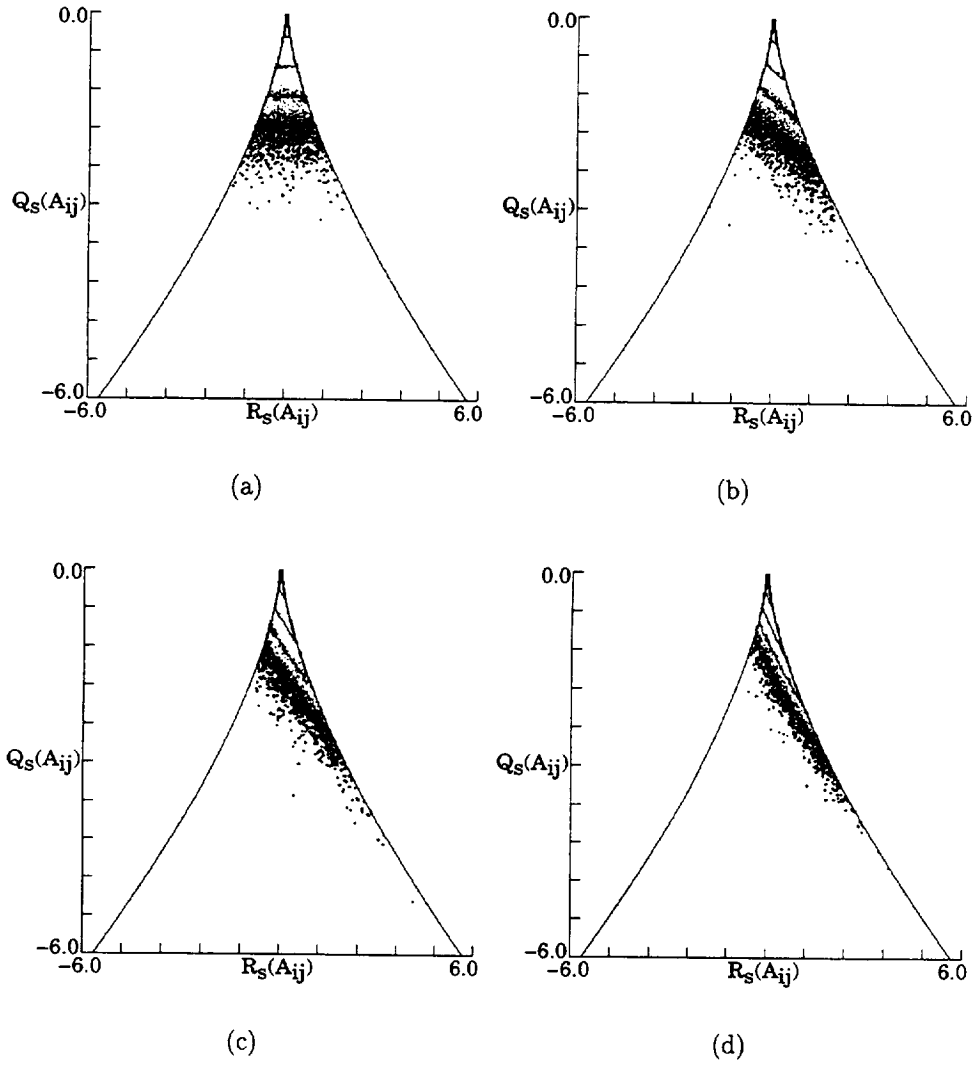


Figure 4.9: Time evolution of logarithmic contour plots of joint pdf of Q_s vs R_s for A_{ij} at (a) $\tau = 0.0$. (b) $\tau = 1.32$. (c) $\tau = 2.65$. (d) $\tau = 5.30$.

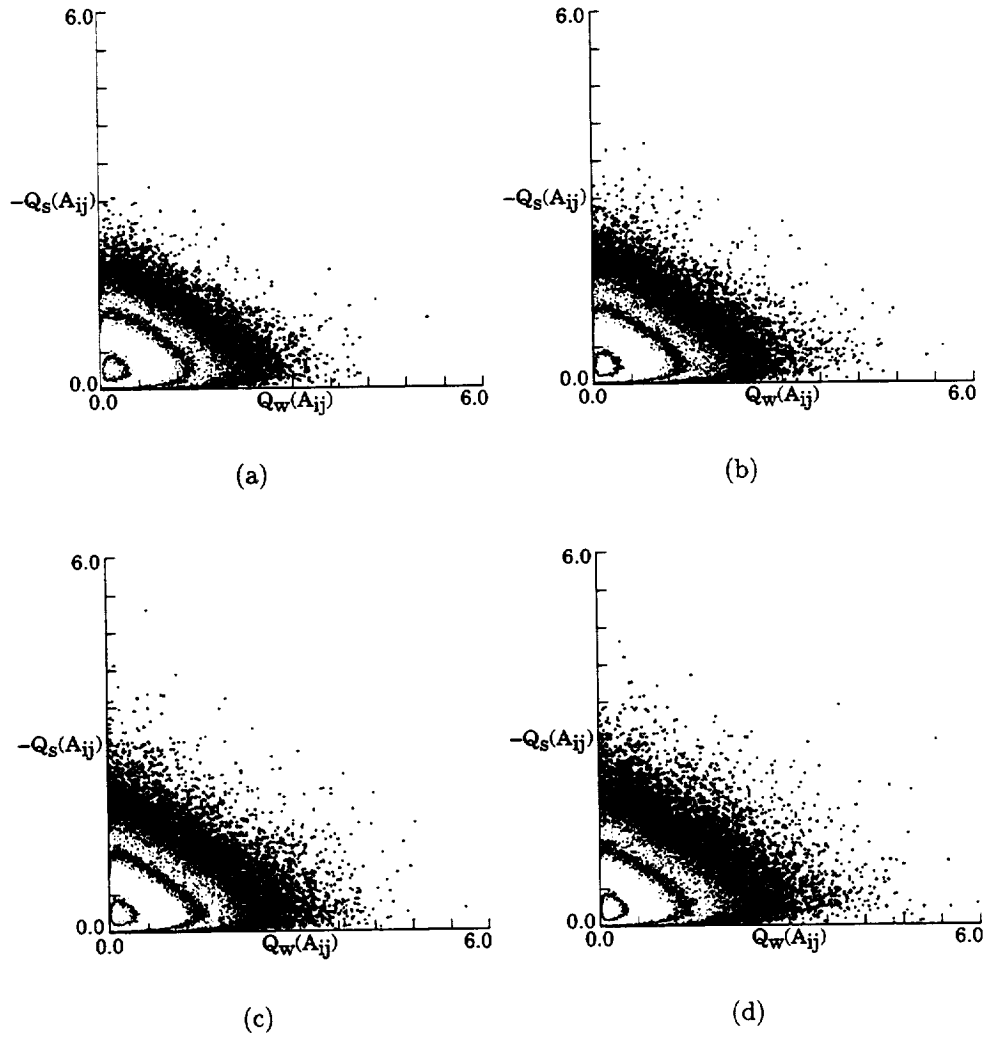


Figure 4.10: Time evolution of logarithmic contour plots of joint pdf of $-Q_s$ vs Q_w for A_{ij} at (a) $\tau = 0.0$. (b) $\tau = 1.32$. (c) $\tau = 2.65$. (d) $\tau = 5.30$.

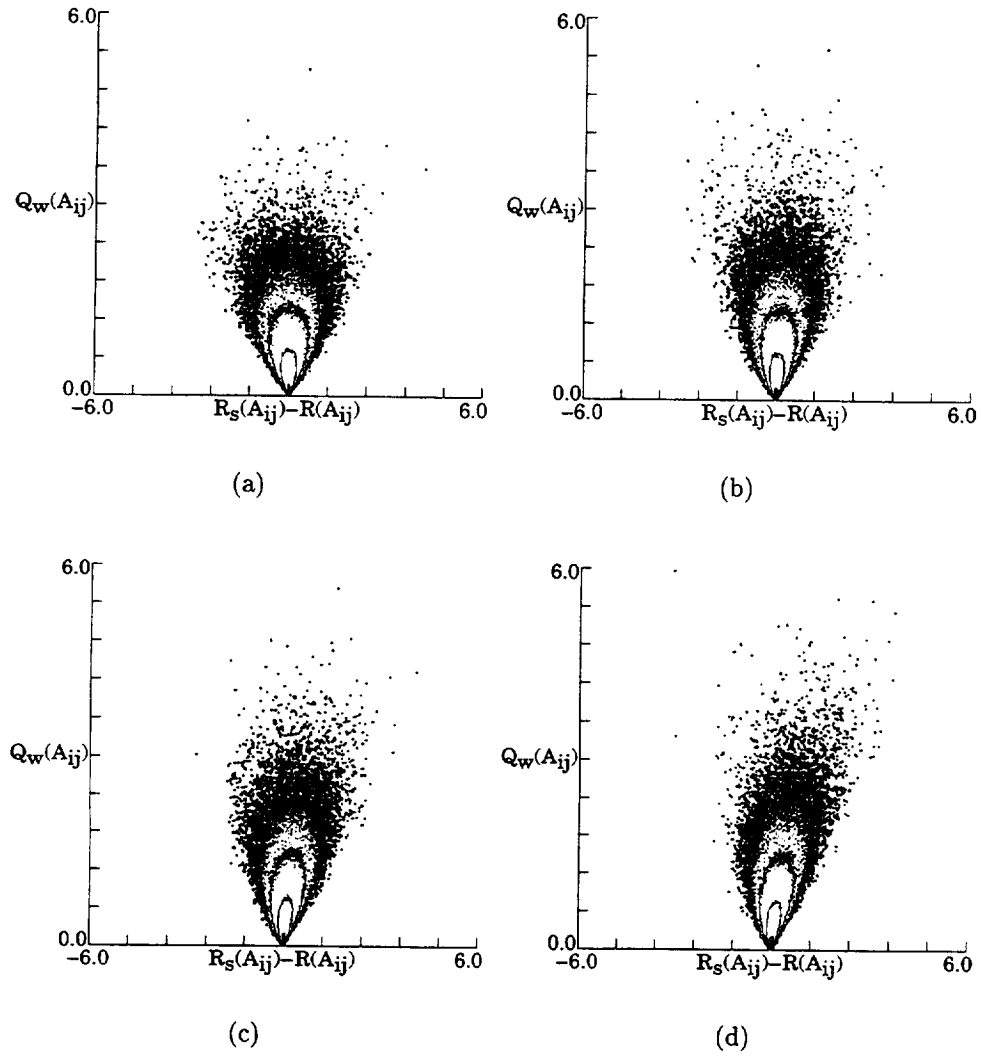


Figure 4.11: Time evolution of logarithmic contour plots of joint pdf of Q_w vs $(R_s - R)$ for A_{ij} at (a) $\tau = 0.0$. (b) $\tau = 1.32$. (c) $\tau = 2.65$. (d) $\tau = 5.30$.

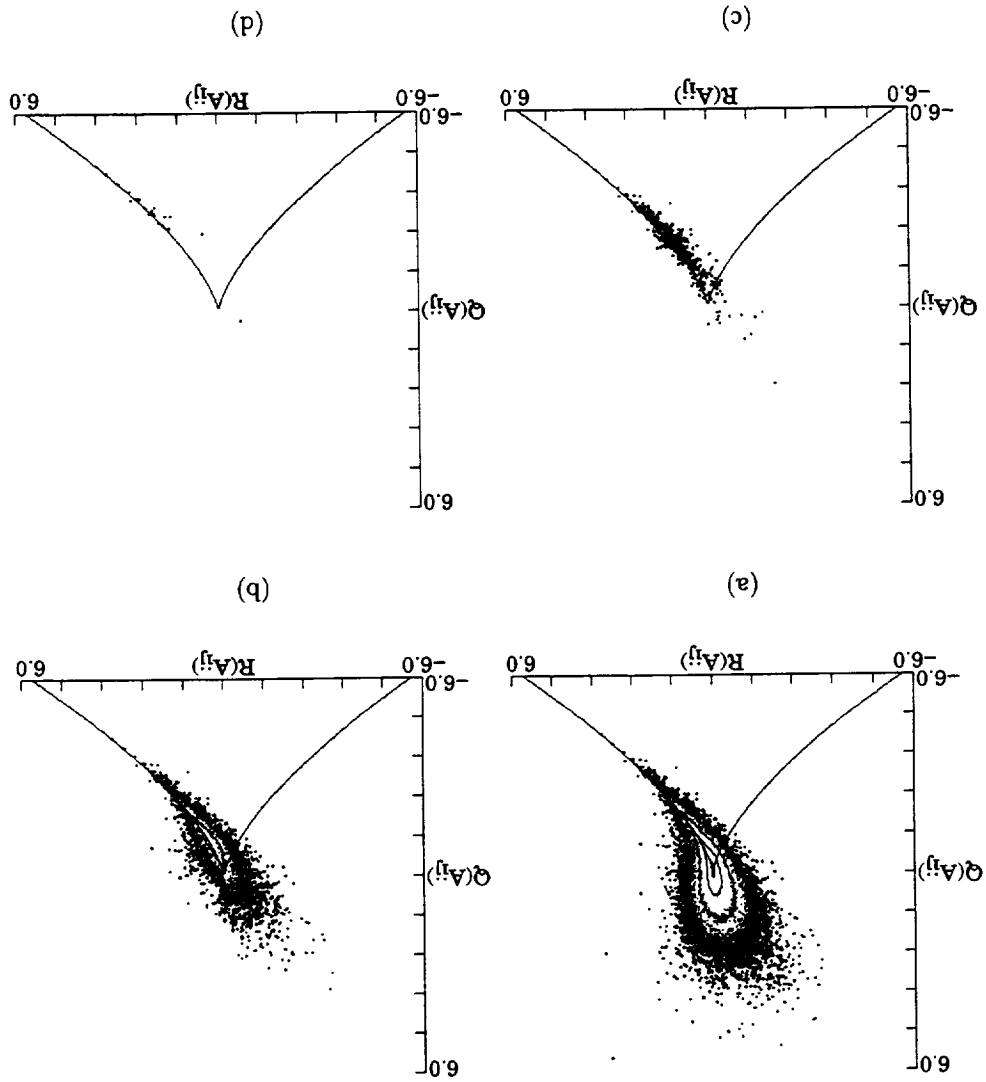


Figure 4.12: Logarithmic contour plots of joint pdf of Q vs R for A_{ij} . $\tau = 5.3$. Data conditioned at various levels of maximum local dissipation. (a) 0% (All data points). (b) 25%. (c) 50%. (d) 75%.

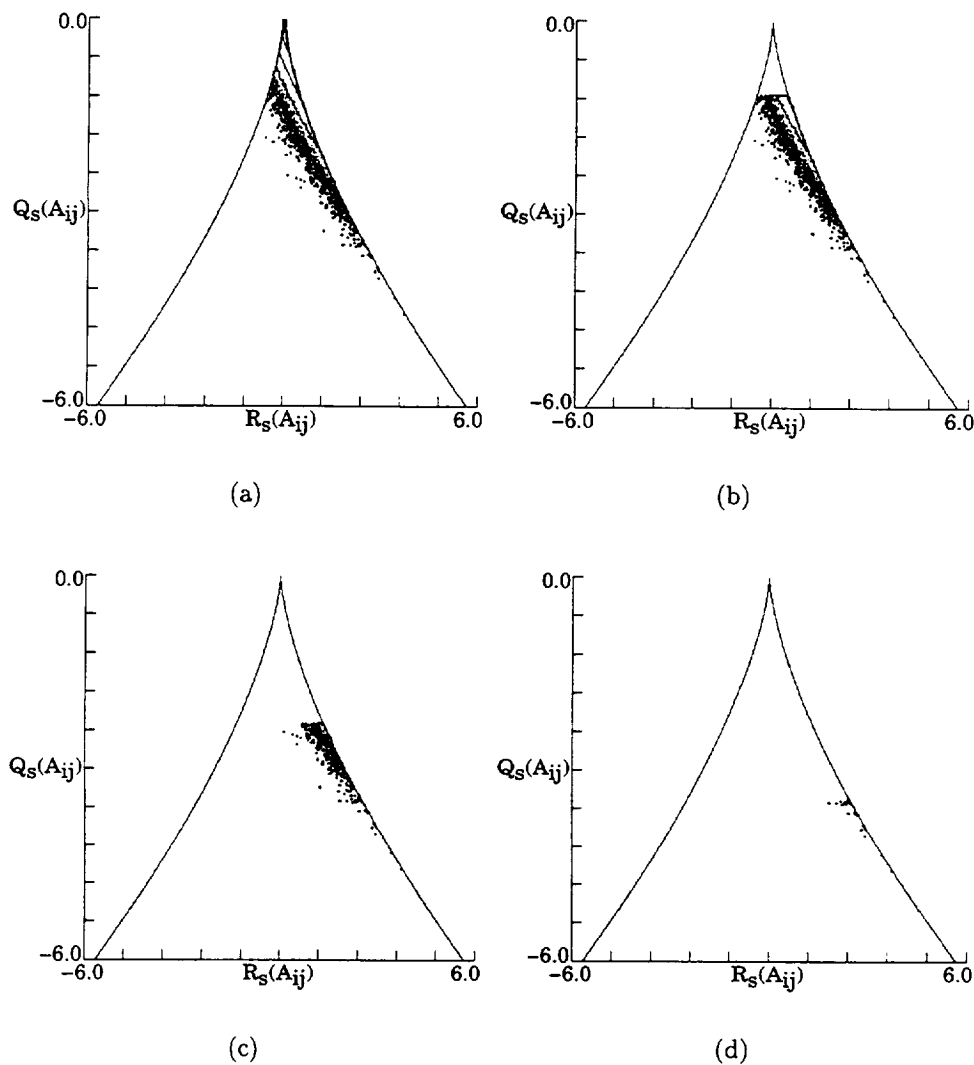


Figure 4.13: Logarithmic contour plots of joint pdf of Q_s vs R_s for A_{ij} . $\tau = 5.3$. Data conditioned at various levels of maximum local dissipation. (a) 0% (All data points). (b) 25%. (c) 50%. (d) 75%.

4.2.2 Strain-rate distribution

The three principal eigenvalues (strain-rates) of the symmetric tensor of A_{ij} were determined and sorted in descending order such that:

$$\alpha \geq \beta \geq \gamma. \quad (4.46)$$

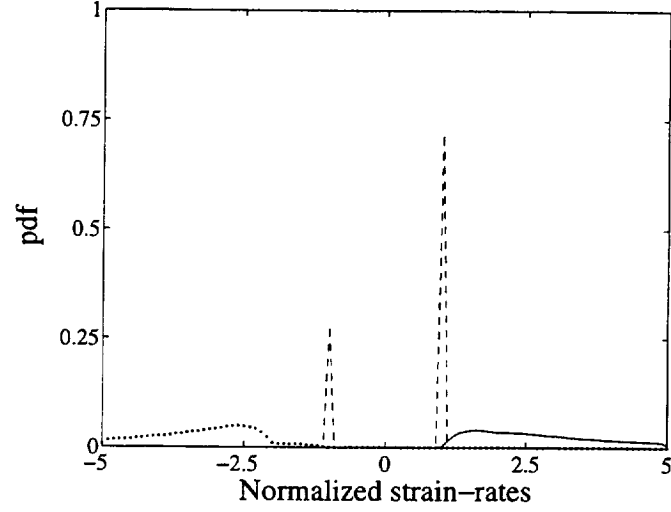
Each eigenvalue was normalized by the magnitude of the intermediate principal eigenvalue, $|\beta|$ so that the intermediate principal eigenvalue is either +1 or -1. Figure 4.14 shows the probability density functions of these normalized eigenvalues. The first plot includes all the data points while the second plot includes only data points with local dissipation higher than 25% of the maximum local dissipation in the flow. Most of the data points are observed to have positive β . This observation is more pronounced with the conditioned data. The maxima for α and γ are ≈ 1.5 and -2.5 for the conditioned data.

4.2.3 Vorticity-strain alignment

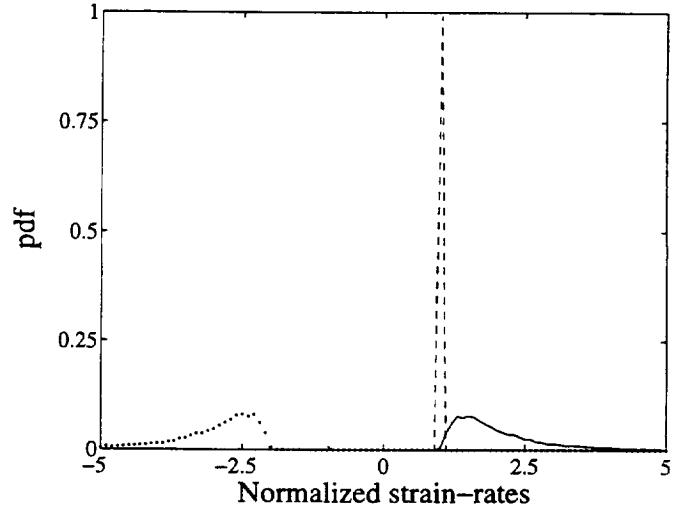
Ashurst *et al.*[1], Sondergaard[30] and Tsinober *et al.*[32] observed strong preferential alignment of the vorticity vector with the intermediate principal strain-rate direction. This alignment was stronger when data was conditioned at higher local dissipation regions. Figure 4.15 plots the probability density functions of the alignment angle between the vorticity vector and the three principal eigenvectors of the rate-of-strain tensor of this homogeneous isotropic flow. The vorticity vector ω_i is related to the A_{ij} tensor by:

$$\begin{aligned} \omega_1 &= A_{32} - A_{23}; \\ \omega_2 &= A_{13} - A_{31}; \\ \omega_3 &= A_{21} - A_{12}. \end{aligned} \quad (4.47)$$

The alignment angle, θ is obtained from the dot product between this vorticity vector and each of the three principal eigenvectors of the rate-of-strain tensor corresponding to the principal eigenvalues α , β and γ . The vorticity vector is aligned exactly with the eigenvector when $\cos \theta = 1.0 (\theta = 0)$ and non-aligned when $\cos \theta = 0 (\theta = 90)$.



(a)



(b)

Figure 4.14: Probability density function of principal strain-rates normalized by $|\beta|$. $\tau = 5.30$. —: α . ---: β . \cdots : γ . (a) All data points. (b) $|Q_s(A_{ij})| \geq 25\%|Q_s(A_{ij})|_{max}$.

Figure 4.15 shows that the vorticity vector tends to align with the principal eigenvector corresponding to eigenvalue β . This preferred alignment is more pronounced when data are conditioned with local dissipation greater than 25% of the maximum local dissipation in the flow. This same vorticity vector is observed to non-align with the principal eigenvector corresponding to γ , the most compressive strain-rate direction. This non-alignment of the vorticity vector with the most compressive strain-rate direction was also observed by Sondergaard[30] in the plane wake simulation.

4.3 Validation of the pressure Hessian tensor

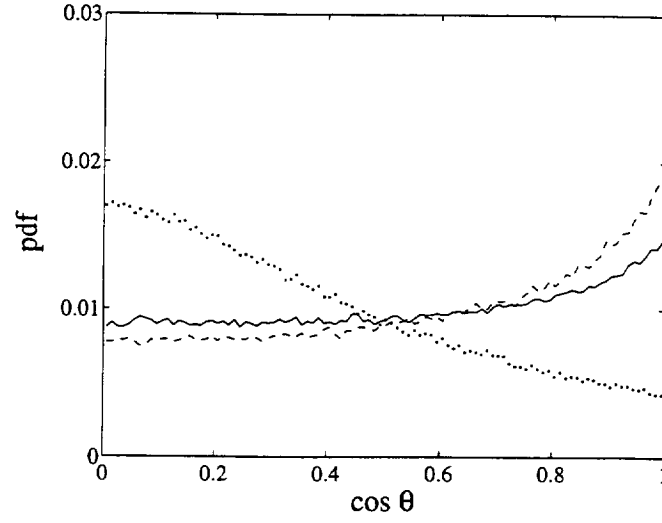
The pressure p at every grid point in the flow is determined using equation 4.10. Differentiating this pressure twice spatially gives the pressure Hessian tensor, P_{ij} :

$$P_{ij} = \frac{\partial^2 p}{\partial x_i \partial x_j}. \quad (4.48)$$

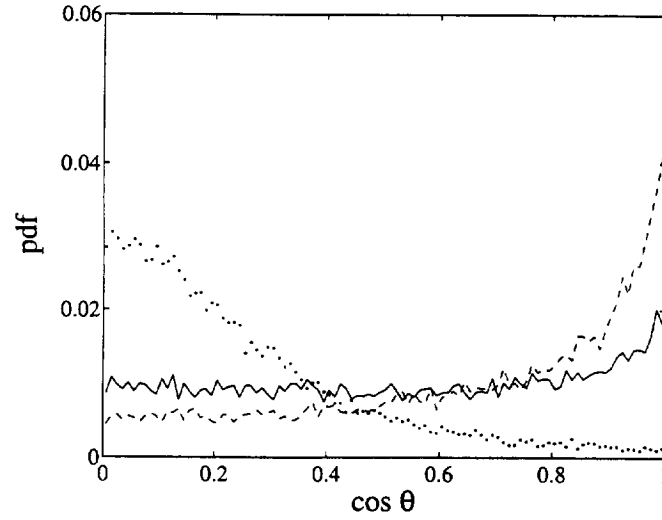
P_{ij} tensor is symmetrical by definition. Unlike the A_{ij} tensor, the trace of this P_{ij} tensor is *not* zero, as indicated by equation 2.3 which gives the relationship between A_{ij} tensor and the trace of the pressure Hessian tensor. This relationship is used to validate the numerical calculation of pressure by plotting $Q(A_{ij})$ vs $0.5P(P_{ij})$ (both equal to $-\frac{1}{2}A_{ik}A_{ki}$) at $\tau = 0$ in figure 4.16. $P(P_{ij})$ is the first invariant (trace) of P_{ij} :

$$\frac{1}{2}P(P_{ij}) = \frac{1}{2} \frac{\partial^2 P}{\partial x_i \partial x_i} = -\frac{1}{2}A_{ik}A_{ki} = Q(A_{ij}). \quad (4.49)$$

Notice that the data points do not all fall exactly on the $Q(A_{ij}) = 0.5P(P_{ij})$ straight line. This is because $Q(A_{ij})$ was obtained by multiplying the A_{ij} 's in the physical space; whereas the pressure derivatives were determined in the Fourier space before being transformed to physical space. The wavenumbers included in the discrete Fourier transforms are limited within the range of $\pm N/2$, where N is the number of grid points used in the simulation. Therefore, the calculated pressure derivatives contain only information from wavenumbers within $\pm N/2$. On the other hand, individual A_{ij} in physical space also contains wavenumbers within the range of $\pm N/2$. However, the products of $A_{ik}A_{ki}$ are performed in the physical space, which increases



(a)



(b)

Figure 4.15: Probability density function of cosine of angle θ between vorticity vector and principal strain-rate directions. $\tau = 5.30$. —: α . ---: β: γ . (a) All data points. (b) $|Q_s(A_{ij})| \geq 25\%|Q_s(A_{ij})|_{max}$.

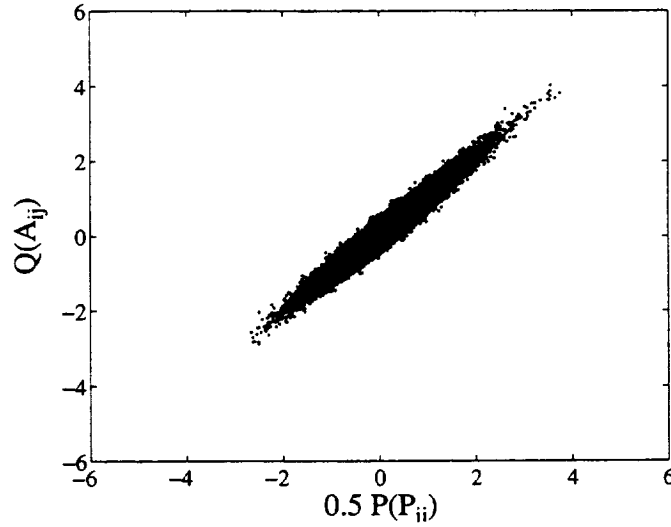


Figure 4.16: Comparison of $Q(A_{ij})$ with $0.5P(P_{ij})$.

the effective range of wavenumbers represented by the products. Therefore, $A_{ik}A_{ki}$ contains information of higher wavenumbers outside the range $\pm N/2$. Hence, there is slight difference between them. To compare $0.5P(P_{ij})$ to $Q(A_{ij})$, the correlation coefficient between them was determined. This correlation coefficient was determined to be 0.965, with correlation coefficient of 1.0 being exactly the same.

4.4 Classification of local flow topologies of H_{ij}

The characteristics of H_{ij} tensor is of the most interest in this thesis. Equation 2.4 shows that the behavior of velocity gradient tensor A_{ij} is governed by H_{ij} tensor, referred to as *acceleration* gradient tensor.

To study the behavior of the A_{ij} tensor, Cantwell [4] derived the analytical solution of A_{ij} when $H_{ij} = 0$ and proposed an intermediate asymptotic model[5] for A_{ij} when $H_{ij} \neq 0$. Ultimately, the questions that need to be answered are: What are the characteristics of H_{ij} ? How does it behave in a turbulent flow? Are there any similarities and differences between the local flow topologies of H_{ij} and A_{ij} tensors?

There are three invariants for each H_{ij} tensor:

$$\begin{aligned} P(H_{ij}) &= H_{ii} = 0; \\ Q(H_{ij}) &= -\frac{1}{2}H_{mn}H_{nm}; \\ R(H_{ij}) &= -\frac{1}{3}H_{mn}H_{nk}H_{km}. \end{aligned} \quad (4.50)$$

This H_{ij} tensor may be decomposed into a symmetric and an anti-symmetric tensor:

$$\begin{aligned} H_{ij} &= S_{ij|h} + W_{ij|h}; \\ S_{ij|h} &= \frac{1}{2}(H_{ij} + H_{ji}); \\ W_{ij|h} &= \frac{1}{2}(H_{ij} - H_{ji}). \end{aligned} \quad (4.51)$$

The second invariants of the $S_{ij|h}$ and $W_{ij|h}$ tensors are represented by $Q_s(H_{ij})$ and $Q_w(H_{ij})$ respectively. Unlike the invariants of A_{ij} tensor, the exact physical meanings of $Q_s(H_{ij})$ and $Q_w(H_{ij})$ are still unclear. The principal eigenvalues of the symmetric $S_{ij|h}$ tensor will also be determined and referred to as the *acceleration* strain-rates (as opposed to the principal eigenvalues of the A_{ij} tensor which are known as the true strain-rates). Similarly, the *equivalent* vorticity vector will also be determined from H_{ij} tensor using corresponding definition for the true vorticity vector obtained from the A_{ij} tensor:

$$\begin{aligned} \omega_{h1} &= H_{32} - H_{23}; \\ \omega_{h2} &= H_{12} - H_{21}; \\ \omega_{h3} &= H_{31} - H_{13}. \end{aligned} \quad (4.52)$$

Equation 2.5 gives the definition of H_{ij} from the pressure derivatives and the second derivative of A_{ij} . This same H_{ij} can also be obtained using equation 2.4. The results obtained from both equations were compared by plotting $Q(H_{ij})$ versus $R(H_{ij})$ in figure 4.17. The H_{ij} tensor obtained from equation 2.5 is exact within the wave frequency range of $\pm N/2$. All the calculations were performed using the Fourier coefficients before being transformed to physical space. On the other hand,

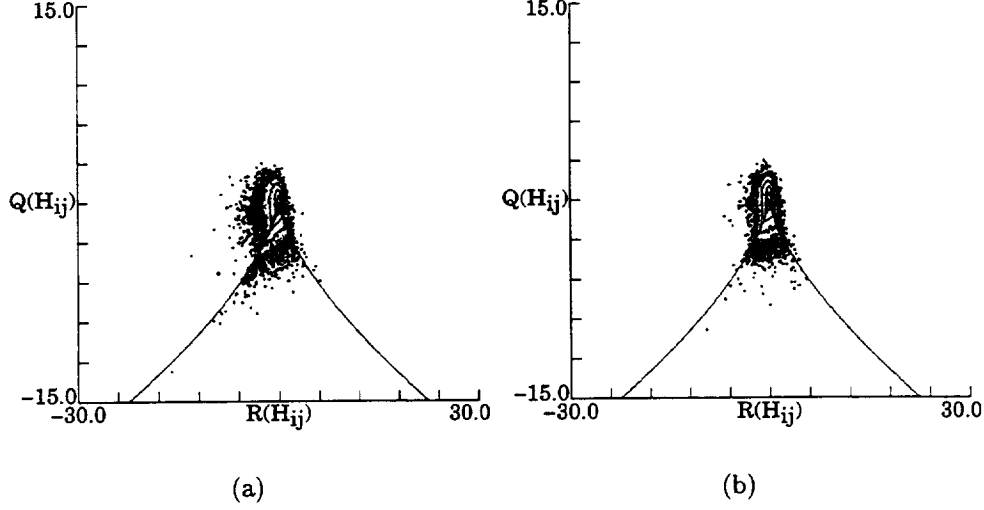


Figure 4.17: Logarithmic contour plots of joint pdf of Q vs R for H_{ij} obtained using (a) time derivatives and product of A_{ij} . (b) pressure cross-derivatives and second derivative of A_{ij} .

the H_{ij} tensor obtained from equation 2.4 contained the the products of $A_{ik}A_{kj}$ obtained from the physical space. Therefore, these products contain information of higher wave numbers outside the range of $\pm N/2$, as explained in the earlier section. However, equation 2.4 requires the information of $\partial A_{ij}/\partial t$. This time derivative of A_{ij} is determined using a second order accurate numerical method. Therefore, the accuracy of H_{ij} tensor determined from equation 2.4 is limited by the accuracy of the numerical method used in getting the time derivatives.

In the rest of this chapter, the H_{ij} tensor is determined from equation 2.5. Calculation of H_{ij} using this equation is preferred because it requires only information at a single time. The H_{ij} tensor is also normalized by the instantaneous mean strain-rate:

$$H_{ij} = \frac{H'_{ij}}{\overline{(s_{ij}s_{ij})}}. \quad (4.53)$$

H'_{ij} is the dimensional gradient obtained from the simulation.

Figure 4.18 depicts the time sequence of $Q(H_{ij})$ versus $R(H_{ij})$ from $\tau = 0.0$ to $\tau = 5.30$. Almost all the data points are below the discriminant curve initially, indicating that H_{ij} tensor is symmetric with real principal eigenvalues. This H_{ij} tensor is completely dominated by the symmetrical pressure cross-derivatives when initial Reynolds number is large. As the flow evolves, the joint pdf of the invariants slowly transforms into the skewed tear-drop structure shown in the final plot. The contour plot of joint pdf of Q versus R does not approach any self-similar structure. Instead, the invariants of this H_{ij} tensor grow relatively larger as the flow decays. Data points with high gradients are observed to move towards the lower left quadrant in the Q - R plot. These data points have equivalent local flow topologies of stable-node/saddle/saddle. These observations are opposite to the results obtained for A_{ij} tensor shown in figure 4.8. The tendency for data points to lie on the lower left quadrant of the Q - R plot is also observed in the relatively higher Reynolds number simulation of an evolving planar wake (Chapter 5) and a Burgers vortex (Appendix D).

Figure 4.19 shows the time evolution of the joint pdf of the second and third invariants of the acceleration rate-of-strain tensor. As the flow evolves, the joint pdf of the invariants skews toward the lower left quadrant. The magnitude of the gradients also grows relatively larger as the flow decays. The higher contour levels form straight lines extending towards the lower left quadrant of the Q_s - R_s plot. The equivalent local flow topologies for these data points are stable-node/saddle/saddle. The intermediate principal eigenvalues of this acceleration rate-of-strain tensor are negative for these data points.

Figure 4.20 shows that Q_s is much larger than Q_w at earlier times when the H_{ij} tensor is symmetric. These two invariants become comparable in magnitude as the flow evolves. Figure 4.21 shows the contour plot of the joint pdf of Q_w versus $(R_s - R)$. The contour plot “explodes” from the origin and forms the characteristic “tear-drop” shaped structure. This structure tilts towards the negative $(R_s - R)$ axis at later times.

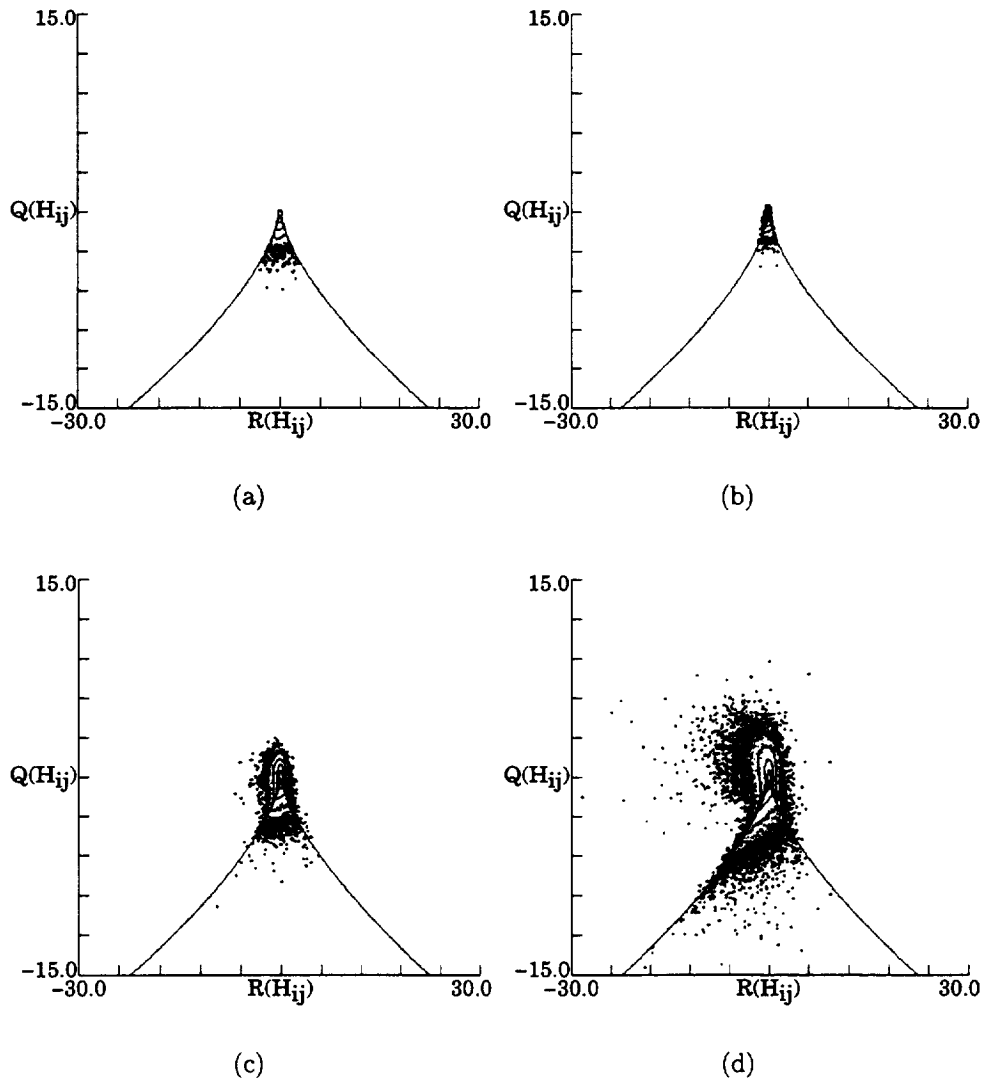


Figure 4.18: Time evolution of logarithmic contour plots of joint pdf of Q vs R for H_{ij} at (a) $\tau = 0.0$. (b) $\tau = 1.32$. (c) $\tau = 2.65$. (d) $\tau = 5.30$.

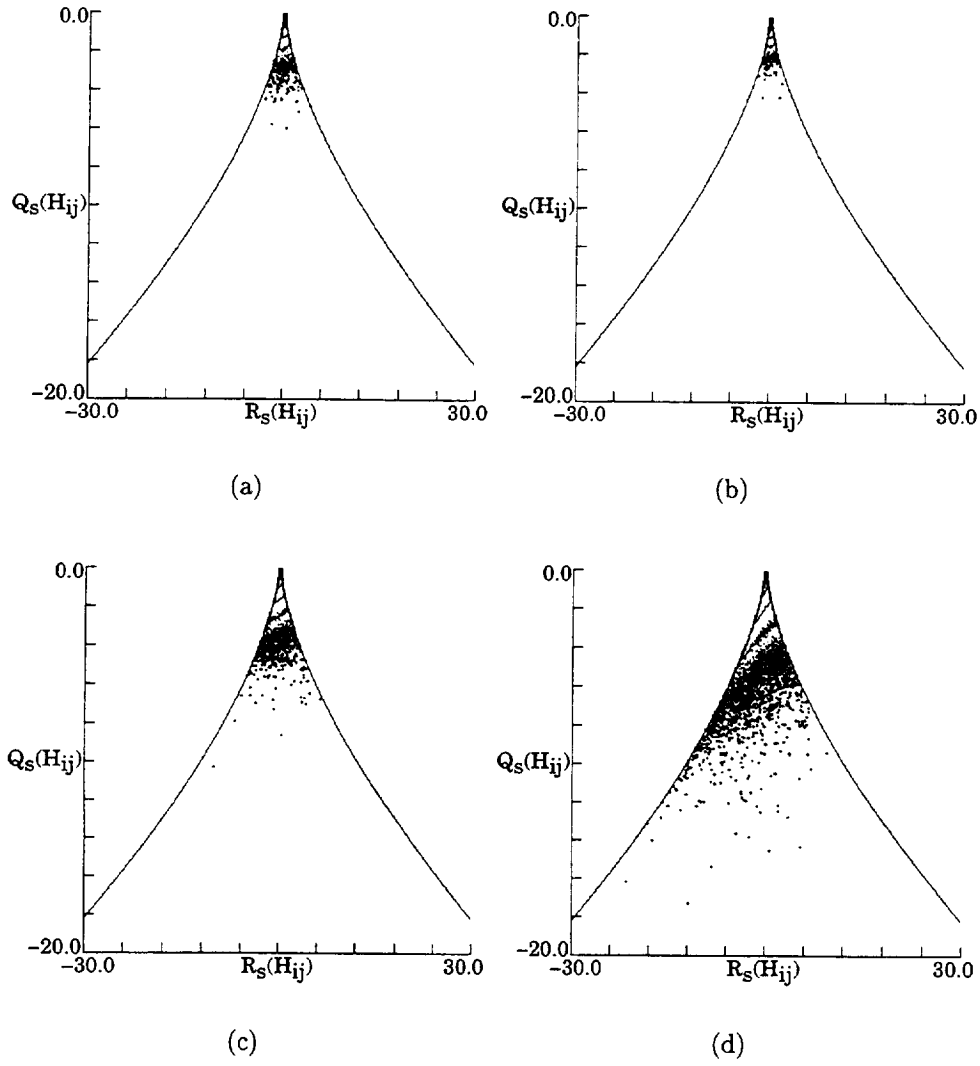


Figure 4.19: Time evolution of logarithmic contour plots of joint pdf of Q_s vs R_s for H_{ij} at (a) $\tau = 0.0$. (b) $\tau = 1.32$. (c) $\tau = 2.65$. (d) $\tau = 5.30$.

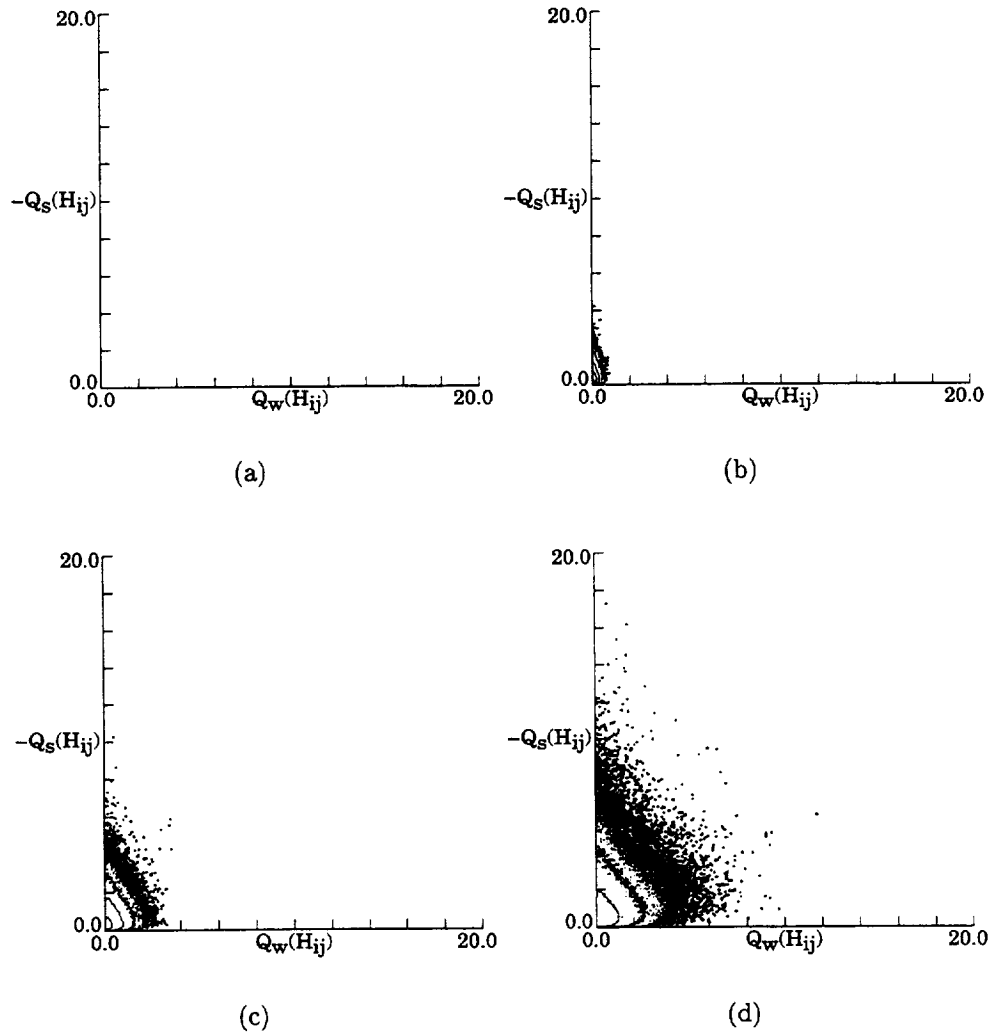


Figure 4.20: Time evolution of logarithmic contour plots of joint pdf of $-Q_s$ vs Q_w for H_{ij} at (a) $\tau = 0.0$. (b) $\tau = 1.32$. (c) $\tau = 2.65$. (d) $\tau = 5.30$.

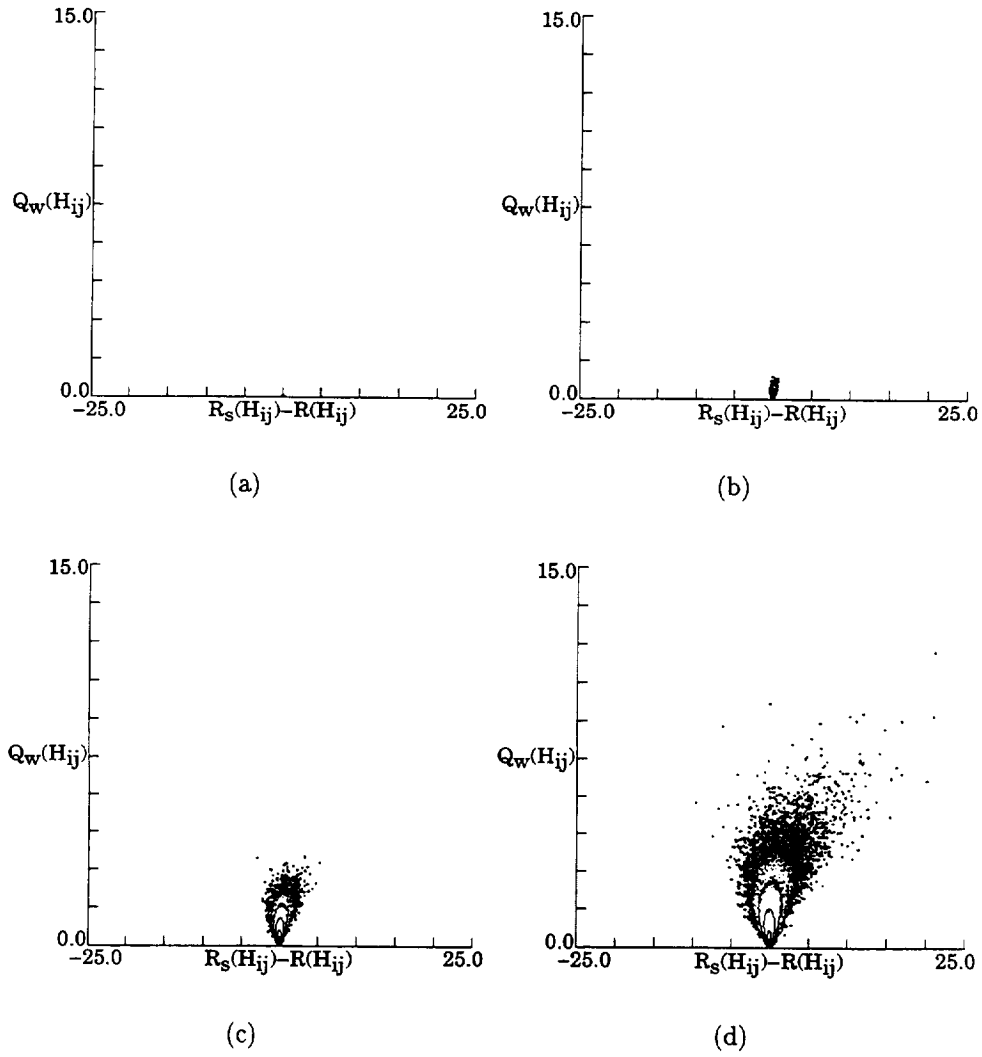


Figure 4.21: Time evolution of logarithmic contour plots of joint pdf of Q_w vs $(R_s - R)$ for H_{ij} at (a) $\tau = 0.0$ (b) $\tau = 1.32$ (c) $\tau = 2.65$ (d) $\tau = 5.30$

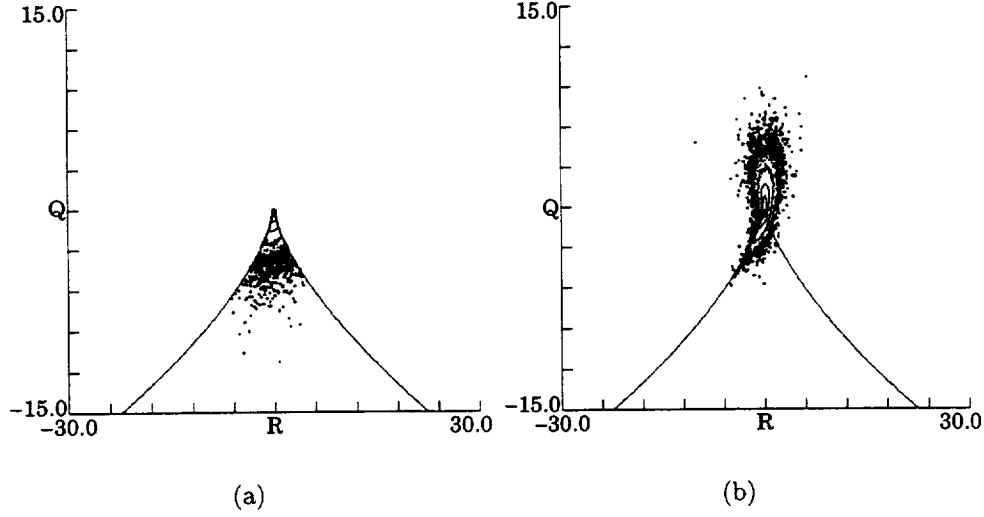


Figure 4.22: Logarithmic contour plots of joint pdf of Q vs R for (a) $-(\partial^2 p / \partial x_i \partial x_j - (\delta_{ij}/3)\partial^2 p / \partial x_k \partial x_k)$. (b) $\nu \partial^2 A_{ij} / \partial x_k \partial x_k$. $\tau = 5.30$.

4.4.1 Contribution from components of H_{ij}

In addition to studying the time evolution of the invariants of H_{ij} tensor, the relative contribution from the components of H_{ij} tensor was also analyzed. The H_{ij} tensor consists of the trace-free pressure derivatives term and the third derivative of the A_{ij} , expressed in equation 2.5. Figure 4.22 compares the Q - R invariant plots of the trace-free pressure cross-derivatives and the $\nu \partial^2 A_{ij} / \partial x_k \partial x_k$ tensors. The invariant plot for the pressure cross-derivatives indicates that this tensor is symmetric ($\partial^2 p / \partial x_i \partial x_j = \partial^2 p / \partial x_j \partial x_i$). Therefore, all data points lie below the discriminant curve. The invariant plots of Q_s versus R_s , $-Q_s$ versus Q_w , and Q_w versus $(R_s - R)$ for this pressure term are redundant since $Q = Q_s$, $R = R_s$ and $Q_w = 0$. On the other hand, the Q - R invariant plot for the $\nu \partial^2 A_{ij} / \partial x_k \partial x_k$ tensor shows that this is the term that contributes all the “rotational” part of the H_{ij} tensor.

4.4.2 Effects of conditioning with local dissipation

How does the behavior of H_{ij} tensor change when data points are conditioned with different dissipation levels ? Figures 4.23 and 4.24 show the contour plots of the joint pdf of Q versus R and Q_s versus R_s when data points are conditioned with local dissipation levels of 25%, 50% and 75% of the maximum local dissipation in the flow. Data points with higher local dissipation tend to move closer towards the left discriminant curve. These data points are observed to lie along this discriminant curve when conditioned at the highest local dissipation levels.

4.4.3 Acceleration strain-rate distribution

The three eigenvalues of the symmetric part of the H_{ij} tensor were determined and sorted in descending order such that:

$$\alpha_h \geq \beta_h \geq \gamma_h \quad (4.54)$$

These principal eigenvalues will be referred to as the acceleration strain-rates. The probability density functions for these acceleration strain-rates (each normalized by the magnitude of the intermediate acceleration strain-rate, $|\beta_h|$) were determined in the way described for the strain-rate distribution of A_{ij} . Figure 4.25 shows the probability density functions of the acceleration strain-rate distribution. When data points are conditioned with local dissipation greater than 25% of the maximum local dissipation in the flow, the intermediate acceleration principal eigenvalue is predominantly negative. These data points have preferred local acceleration strain topology of stable-node/saddle/saddle. The distributions for α_h and γ_h remain relatively broad, with small peaks at approximately 2.5 and -1.5 respectively.

4.4.4 Equivalent vorticity - acceleration strain alignment

An equivalent vorticity vector is defined from the components of the H_{ij} tensor using similar definitions for the true vorticity vector:

$$\omega_{h1} = H_{32} - H_{23};$$

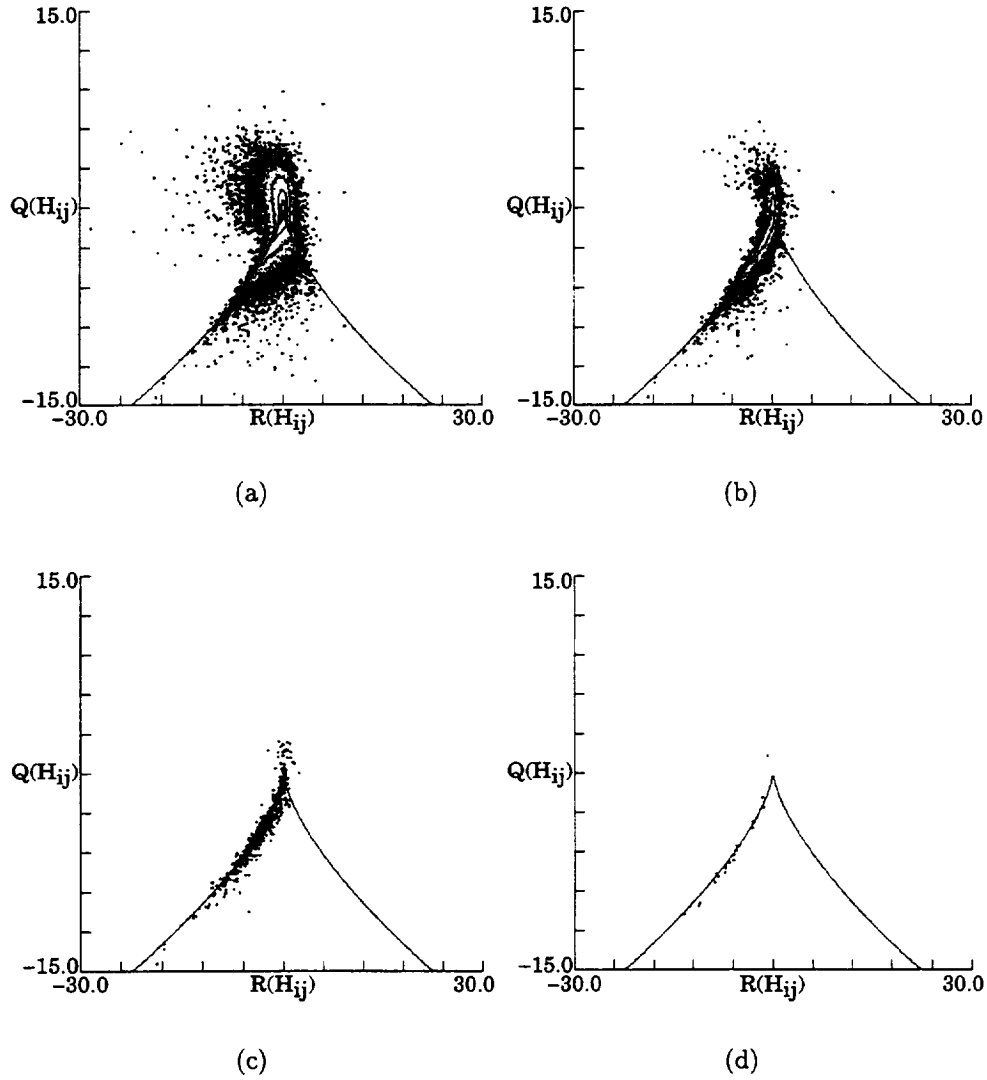


Figure 4.23: Logarithmic contour plots of joint pdf of Q vs R for H_{ij} . $\tau = 5.3$. Data conditioned at various levels of maximum local dissipation. (a) 0% (All data points). (b) 25%. (c) 50%. (d) 75%.

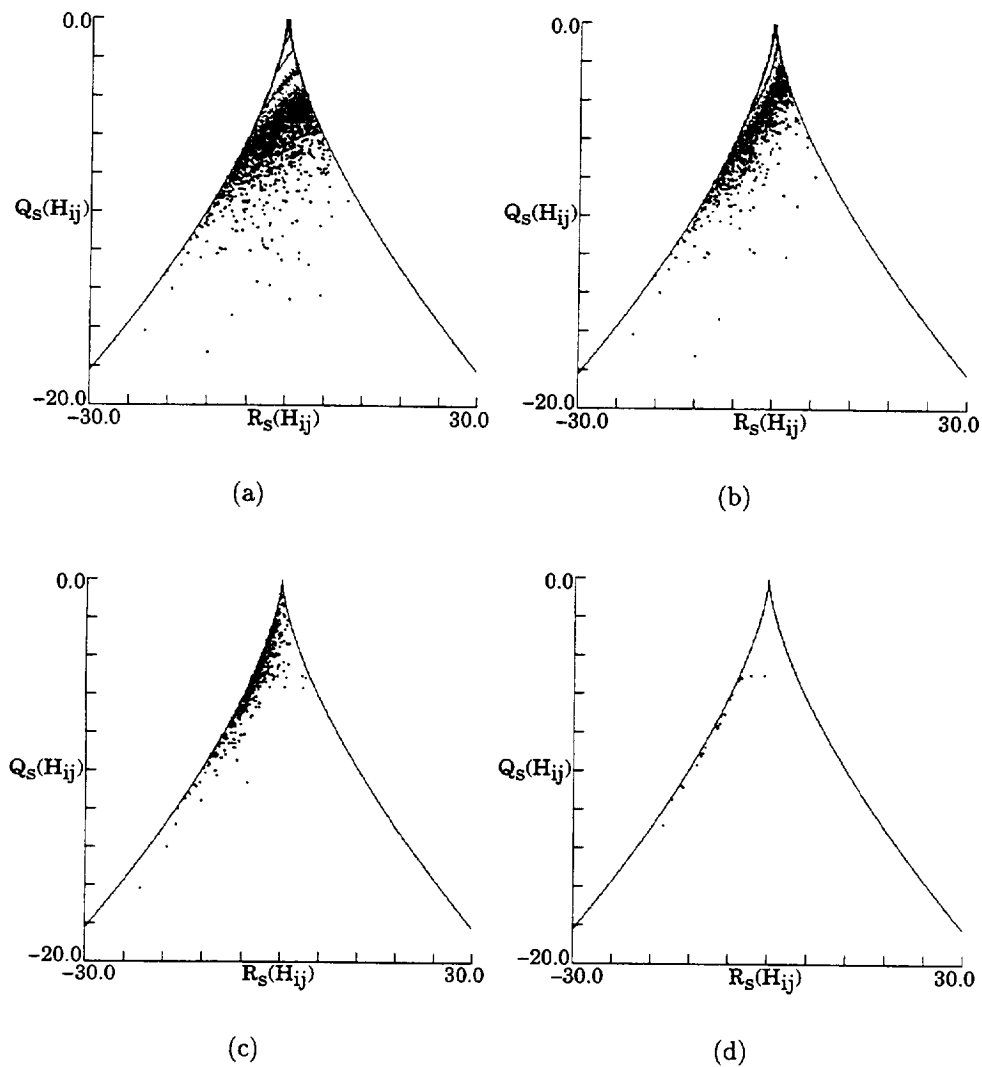
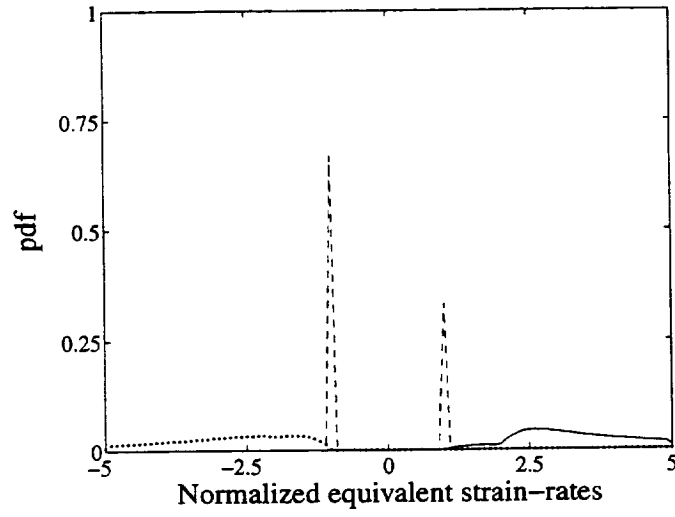
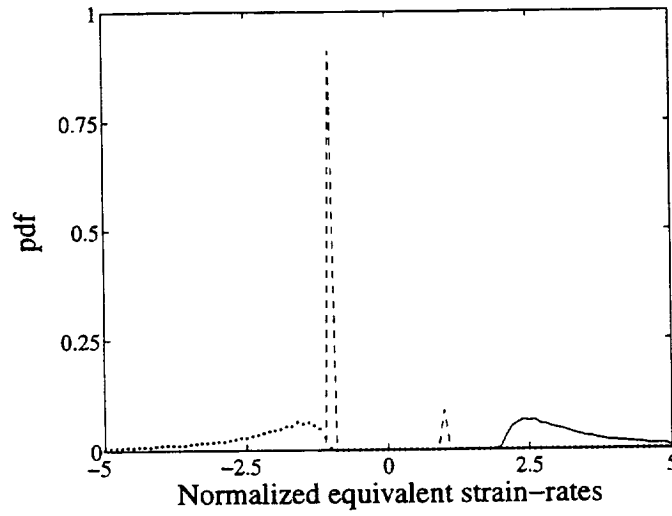


Figure 4.24: Logarithmic contour plots of joint pdf of Q_s vs R_s for H_{ij} . $\tau = 5.3$. Data conditioned at various levels of maximum local dissipation. (a) 0% (All data points). (b) 25%. (c) 50%. (d) 75%.



(a)

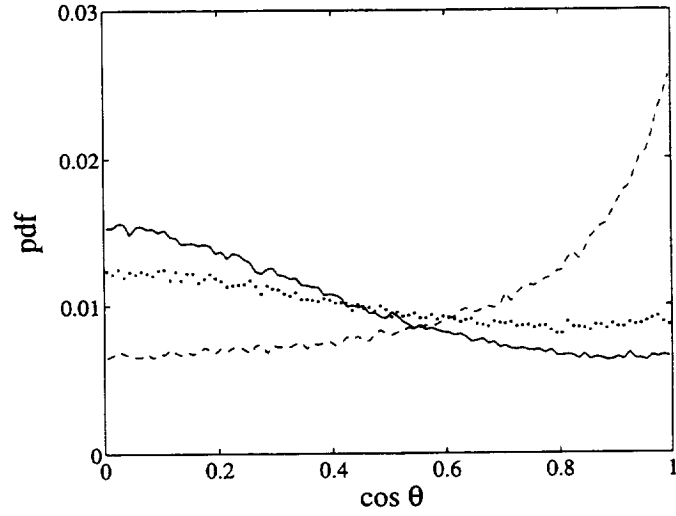


(b)

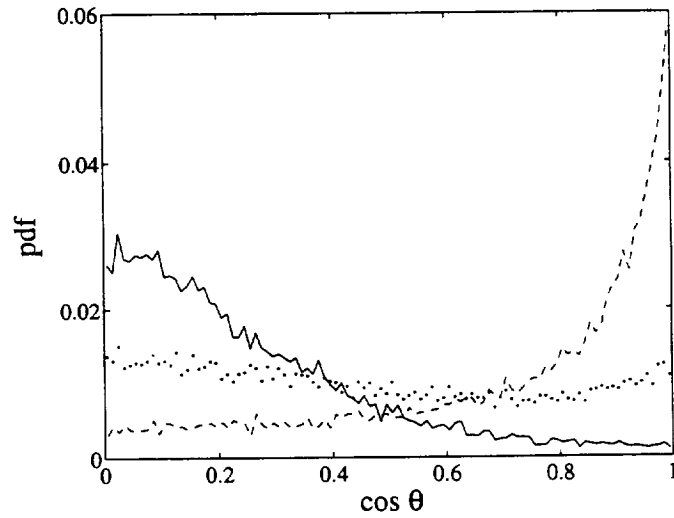
Figure 4.25: Probability density function of acceleration strain-rates normalized by $|\beta_h|$. $\tau = 5.30$. —: α_h . ---: β_h . ···: γ_h . (a) All data points. (b) $|Q_s(A_{ij})| \geq 25\%|Q_s(A_{ij})|_{max}$.

$$\begin{aligned}\omega_{h2} &= H_{13} - H_{31}; \\ \omega_{h3} &= H_{21} - H_{12}.\end{aligned}\tag{4.55}$$

Figure 4.26 shows the cosine of the angle between the equivalent vorticity vector and the three acceleration strain-rate directions. Both plots indicate that there is preferential alignment of the equivalent vorticity vector with the intermediate acceleration strain-rate. This result corresponds to the earlier observation found for the vorticity-strain alignment in the same flow. However, unlike the vorticity-strain alignment results, the equivalent vorticity tends to non-align with α_h . (Recall that the vorticity vector tends to non-align with the most compressive strain, γ).



(a)



(b)

Figure 4.26: Probability density function of cosine of angle θ between equivalent vorticity vector and the acceleration strain-rate directions. $\tau = 5.30$. —: α_h . ---: β_h: γ_h . (a) All data points. (b) $|Q_s(A_{ij})| \geq 25\%|Q_s(A_{ij})|_{max}$.

Chapter 5

Temporally evolving plane wake

5.1 Introduction

Sondergaard[30] performed a direct numerical simulation on a temporally evolving plane wake to study the effects of the initial conditions on the evolution of the plane wake; including the development of three-dimensionality, the mean flow, structure, growth rate and the mean properties of the far-wake turbulence. To overcome the limitations on the resolution due to restricted computer resources, Sondergaard employed a temporal formulation, where the spatially evolving flow is approximated by a temporally evolving flow as it convects downstream. This formulation approximates the view of an observer convecting downstream with the flow structures of interest. Therefore, “time” in the temporal formulations becomes the measure of the level of development of the flow instead of “space” in the case of spatial formulation. By using temporal formulations, Sondergaard was able to achieve better resolution of the smaller scales.

Certain assumptions are made in all temporal formulations. One of them is that the stream-wise rate of change is small compared to the scale of the structures being studied. Hence the mean flow may be approximated as being locally parallel. The other assumption made is that the computational domain can safely be limited to only a few large structures to achieve better resolution of the smaller scales. Doing

so confines the development of the large scale motions to a computational box which, at late times in the evolution, may only be a few wake widths long.

5.2 Brief description of the flow

The main intent of this work by Sondergaard was to examine the effect of the choice of the initial conditions on the development of the incompressible plane wake. All the flows were started from a laminar base flow. A small number of disturbance modes of specific wavelengths including fundamental, subharmonic and sub-subharmonic were then superimposed onto the base flow. These disturbance modes were chosen to be the most unstable eigenfunctions as predicted by linear theory.

5.2.1 Numerical method

Calculating free shear flows using spectral methods in turbulent flows which are periodic in two directions and have a non-periodic compact vorticity in the third direction posed many challenges. Different approaches have been used to approximate the infinite direction and incorporating the spectral method at the same time, all with well documented draw backs. Sondergaard avoided the draw backs encountered by these previous methods with the use of an algorithm similar to the one presented by Corral & Jiménez[9] together with an unique way of dividing the non-periodic infinite direction into three domains. One of the domains contained all the vorticity in the flow while the other domains were vorticity free and extend from infinity to meet the vorticity-containing domain at the boundaries from above and below. The vorticity magnitude and vorticity gradient at the boundaries where the domains meet were forced to be zero. In this way, the vorticity-containing domain can be treated as fully periodic and can be solved with the standard pseudo-spectral technique. All the quantities in the simulation have been normalized by the initial wake half width and the initial free-stream velocity. A growing uniform grid was also used in the non-periodic infinite direction to maximize the resolution while keeping the vorticity at

the edges of the vorticity-containing domain small to satisfy the asymptotic matching condition.

5.2.2 Initial condition

The initial condition for this time developing plane wake consists of a Gaussian mean velocity profile in the stream-wise direction while the mean velocities in the other two directions were set to zero. In this way, the only non-zero mean vorticity profile is in the non-periodic infinite direction. Small two dimensional or three dimensional disturbances which are periodic in the stream-wise and span-wise directions were then added to the mean flow. These disturbances may be along any or all of the fundamental, subharmonic or sub-subharmonic stream-wise wavelength; with disturbance phase angle ϕ if desired. The disturbance phase angle is defined with respect to the two-dimensional fundamental disturbance, with $\phi = 2\pi$ represents a physical shift of one fundamental wavelength. The amplitude of each disturbance eigenfunction was chosen such that the initial magnitude was found to be small enough for the initial wake growth to be within linear regime while at the same time large enough to allow the wake to become non-linear without excessive computational resources.

5.3 Classification of local flow topologies of A_{ij}

Flow simulations at two different Reynolds numbers were analyzed in this chapter. The first flow is a three dimensional simulation with a stream-wise disturbance added onto the subharmonic wavenumber in addition to the two dimensional disturbance along the fundamental mode. The Reynolds number for this flow based on the initial wake half width and the initial velocity defect is 346. This flow is identified as wk346 in the analysis. The other flow is another three dimensional simulation with a three dimensional disturbance along the subharmonic wavelength together with a two dimensional disturbance along the fundamental wavelength. The Reynolds number based on the same initial wake half width and initial defect velocity of this flow is 2768. This flow is identified as wk2768. Both flows have pairs of oblique waves with

equal and opposite span-wise wavenumbers oriented 60° to the span-wise direction. The choice of three-dimensional modes was motivated by the stability analysis which suggested that wave pairs at near 60° to the span-wise direction are the most unstable modes.

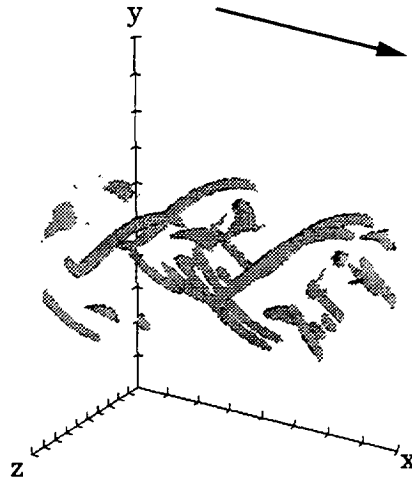
The instantaneous mean strain-rate is used to normalize the velocity and acceleration gradients in the flow such that:

$$A_{ij} = A'_{ij}/\Omega; \quad H_{ij} = H'_{ij}/\Omega^2, \\ \Omega = \left(\frac{(s_{ij}s_{ij})^2}{s_{ij}s_{ij}} \right)^{1/2} \quad (5.1)$$

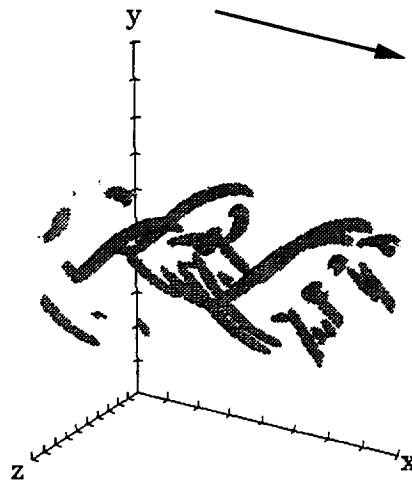
A'_{ij} and H'_{ij} are the un-normalized gradients obtained from the simulation.

Figure 5.1 shows the iso-contour surfaces for enstrophy density and discriminant $D = (27/4)R^2 + Q^3$ for wk346 at time $t = 102.7$. The free-stream is flowing along the stream-wise x direction, as indicated in both plots. The vertical y -axis extends to infinity in both directions to capture all the vorticity in the domain calculated. The well defined span-wise rollers along the z -direction were depicted very nicely in both iso-contour surfaces. Figures 5.2 to 5.5 show the time evolution contour plots of the joint pdf of various invariants for wk346 at four different times. The basic characteristics of these figures are very similar to those obtained by Sondergaard for the same flow without the normalization shown in equation 5.1. The contour plot of the joint pdf “explodes” from the origin at early time and peaks at time $t = 102.7$ before the magnitude of the gradients decreases as the flow approaches self-similar regime. The joint pdf maintains a familiar “tear-drop” structure with high gradient exhibiting a tendency towards the upper left quadrant of the Q - R plot (with local topology of stable focus-stretching) and the lower right quadrant (with local topology of unstable-node/saddle/saddle).

The initial shape of the joint pdf of the Q_s - R_s invariant plot shows a very distinct structure determined by the initial condition. However, this structure grows towards the general shape observed in the later times as the flow evolves. Most data points with high dissipation have a tendency towards the lower right quadrant of the Q_s - R_s plot, almost hugging the right discriminant curve.



(a)



(b)

Figure 5.1: Iso-contour surfaces for wk346 at $t = 102.7$. (a) local enstrophy density $|\omega| = 2.8$. (b) local discriminant $D = 5.0$.

The joint pdf of the $-Q_s-Q_w$ plot shows that data points have comparable local dissipation and local enstrophy density initially. However, the local enstrophy density began to dominate as the flow evolved and developed well defined span-wise rollers with relatively weak stream-wise stretching between the rollers. Once the rollers were established, the three dimensional disturbances grew rapidly and the stream-wise structures became more intense, under the influence of the straining field. Therefore, the magnitude of the local dissipation and the local enstrophy density becomes comparable again at the latest time shown.

The joint pdf of the Q_w-R_s-R invariant plots show that data points with the highest local enstrophy density usually occur at regions with positive vortex-stretching terms. These structures are very similar to those observed in the homogeneous isotropic simulation.

Figures 5.6 to 5.9 show the time evolution of the joint pdf of various invariants for flow wk2768 at two different times; after the flow has fully developed and is approaching the asymptotic regime. The magnitude of the highest gradients and the fraction of the flow containing the high gradient motions are larger in this higher Reynolds number flow. Otherwise, the higher Reynolds number has very little effect on the general behavior and the overall shape of the joint pdf. The development cycle of exploding from the origin at initial condition and decaying as the flow approached self-similar regime was concluded by Sondergaard to be independent of Reynolds number.

5.4 Classification of local flow topologies of H_{ij}

The H_{ij} tensor for the wake flows is determined from equation 2.4, repeated here for reference purposes:

$$\frac{\partial A_{ij}}{\partial t} + u_k \frac{\partial A_{ij}}{\partial x_k} + A_{ik} A_{kj} - A_{km} A_{mk} \frac{\delta_{ij}}{3} = H_{ij} \quad (5.2)$$

Figures 5.10 to 5.13 show the joint pdf of the invariant plots of the H_{ij} tensor for wk346 at two different times. The flow is fully developed and begins to decay. The Q - R plots show that most data points lie below the discriminant curve, indicating that

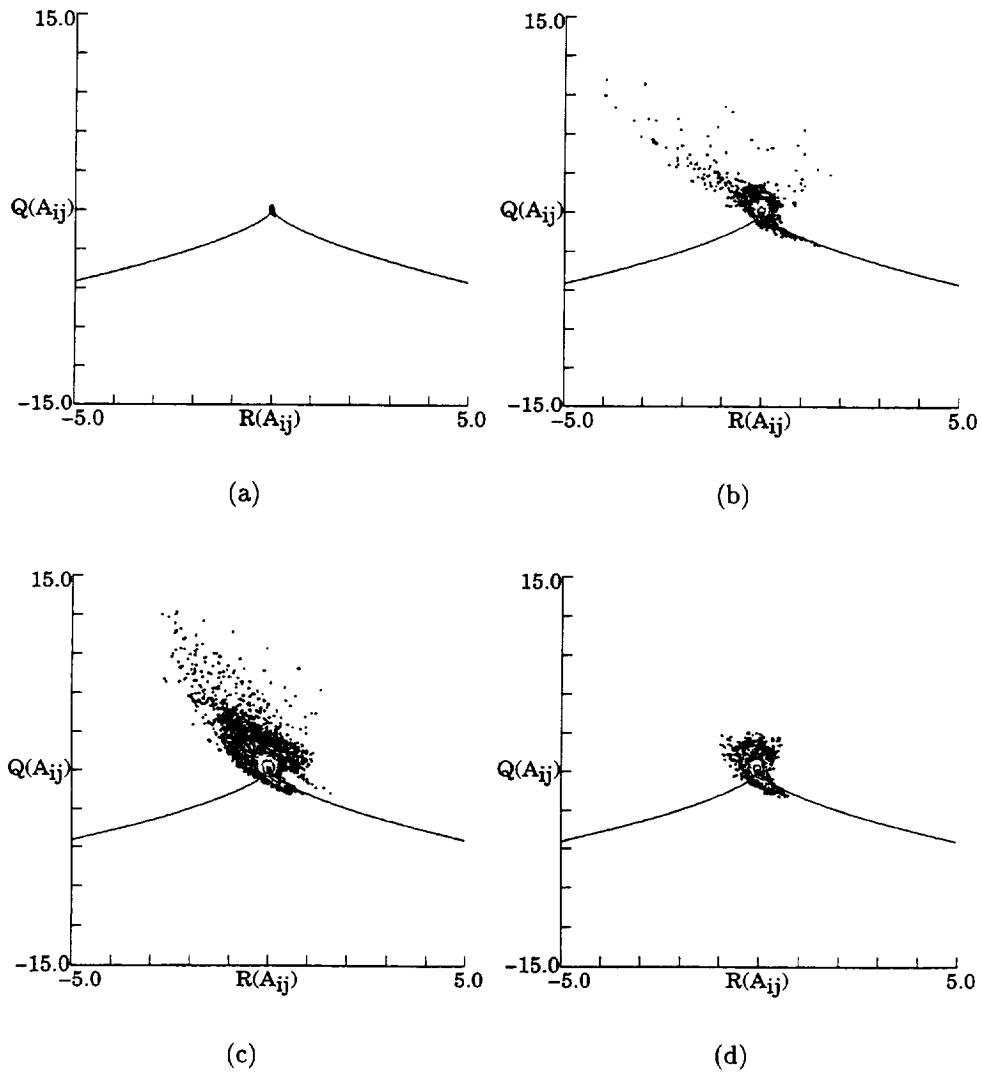


Figure 5.2: Time evolution of logarithmic contour plots of joint pdf of Q vs R for wk346, A_{ij} . (a) $t=22.8$. (b) $t=52.8$. (c) $t=102.7$. (d) $t=204.8$.

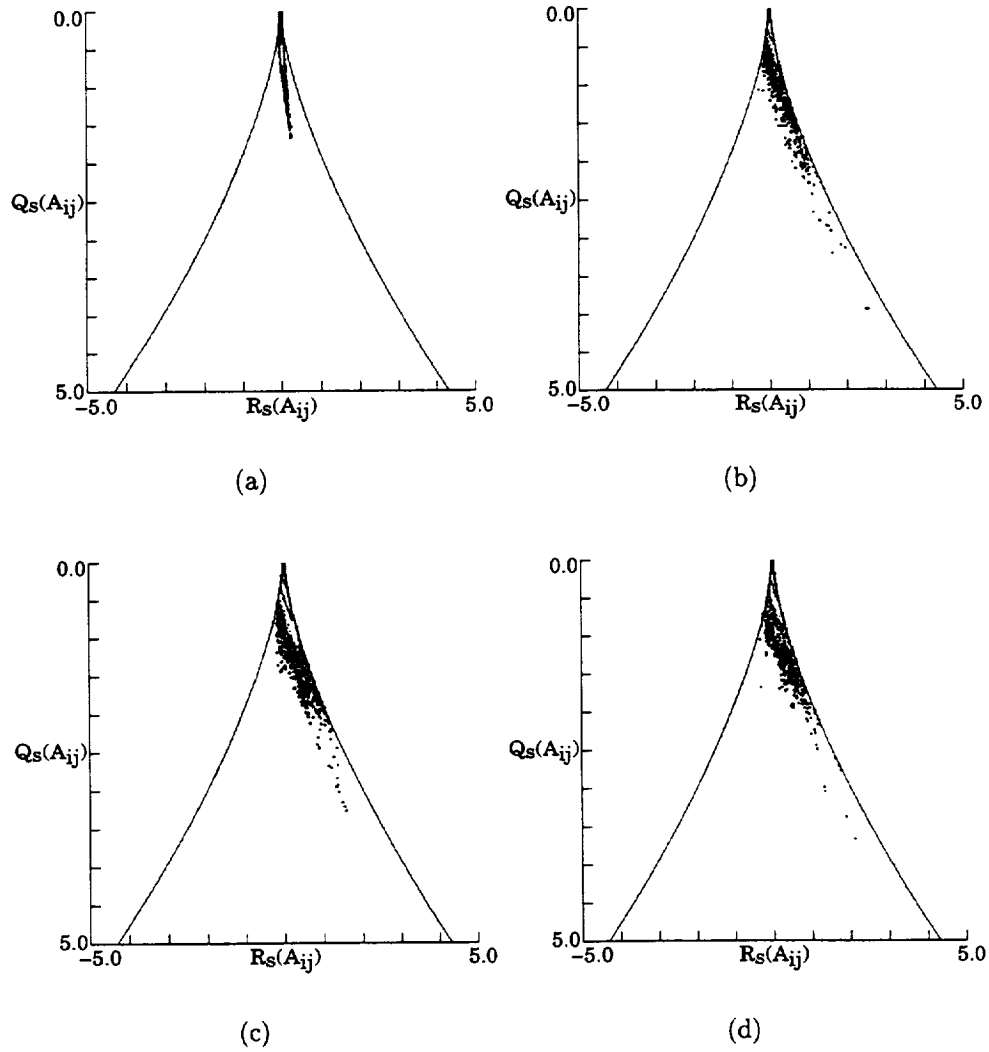


Figure 5.3: Time evolution of logarithmic contour plots of joint pdf of Q_s vs R_s for wk346, A_{ij} . (a) $t=22.8$. (b) $t=52.8$. (c) $t=102.7$. (d) $t=204.8$

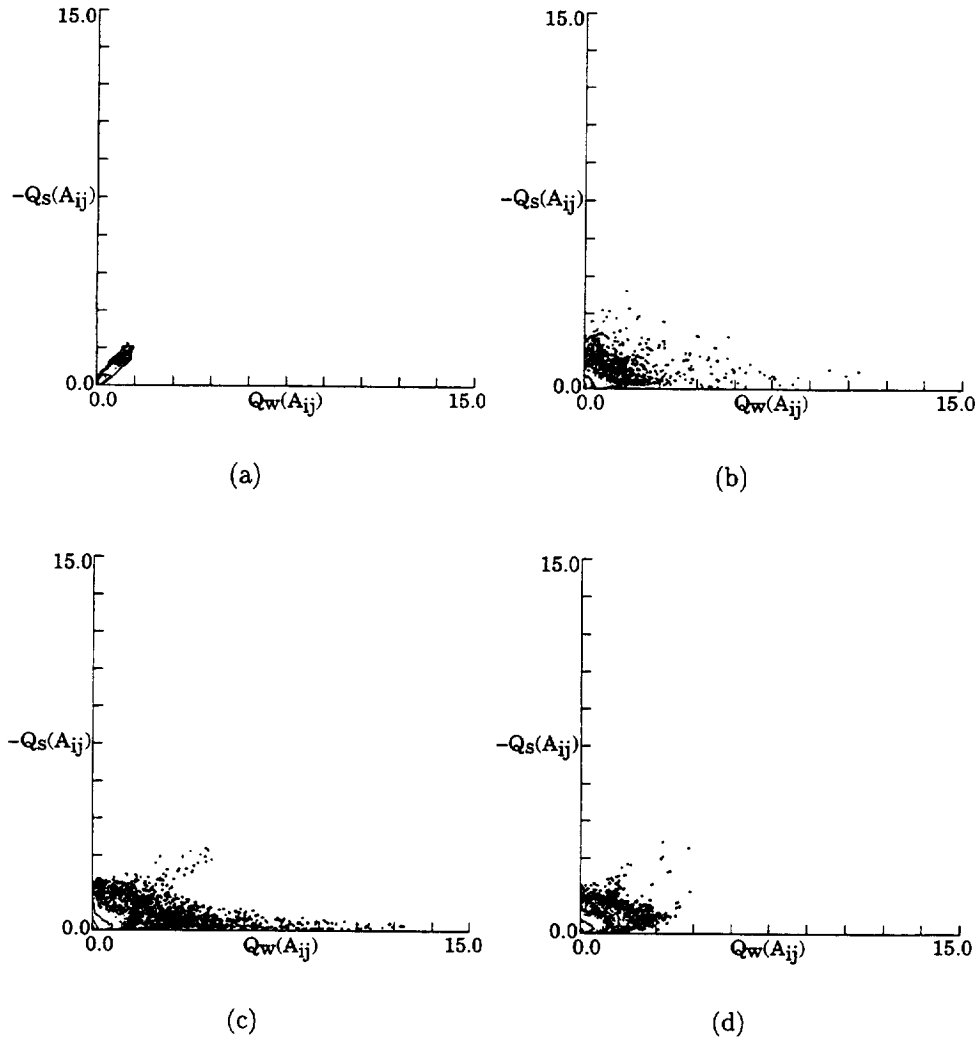


Figure 5.4: Time evolution of logarithmic contour plots of the joint pdf of $-Q_s$ vs Q_w for wk346, A_{ij} . (a) $t=22.8$. (b) $t=52.8$. (c) $t=102.7$. (d) $t=204.8$.

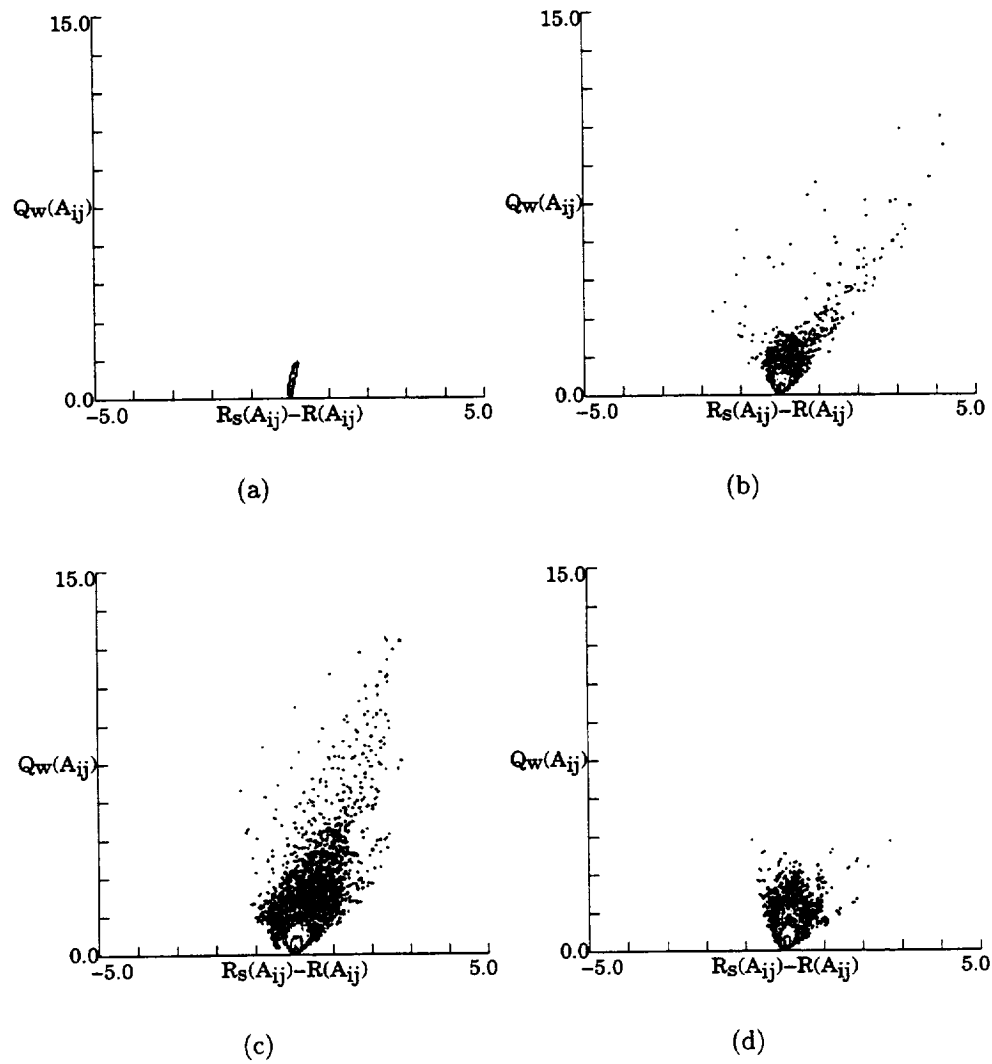
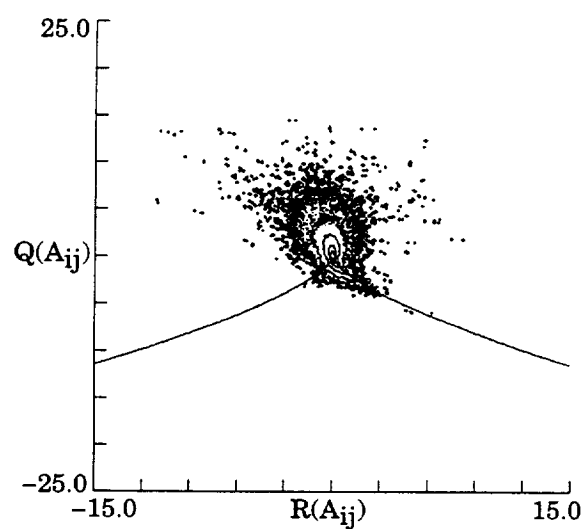
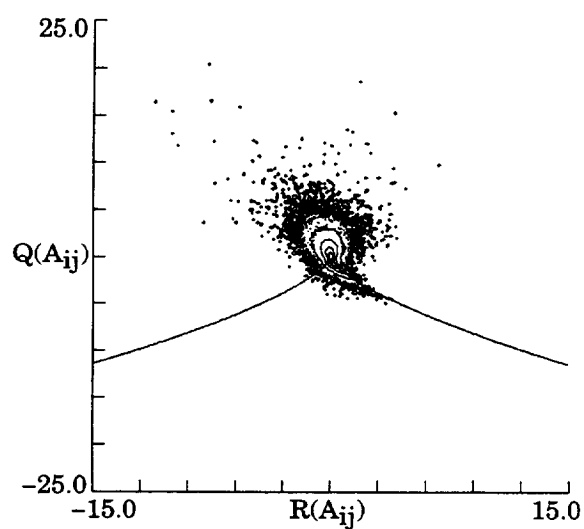


Figure 5.5: Time evolution of logarithmic contour plots of joint pdf of Q_w vs $(R_s - R)$ for wk346, A_{ij} . (a) $t=22.8$. (b) $t=52.8$. (c) $t=102.7$. (d) $t=204.8$.

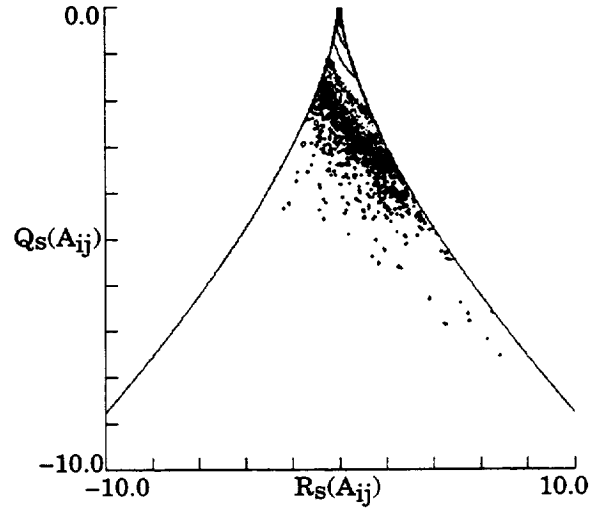


(a)

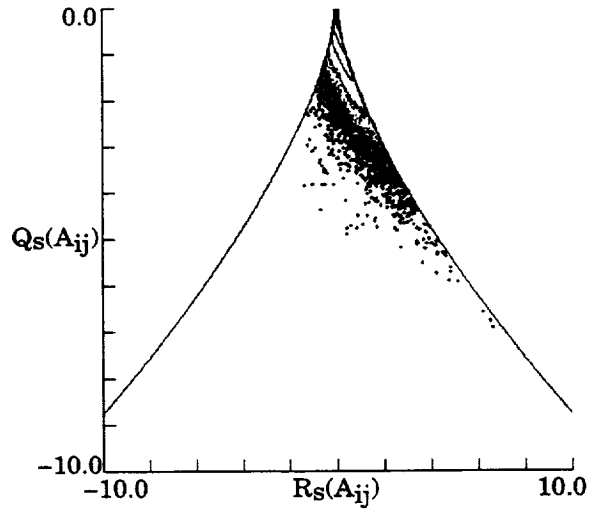


(b)

Figure 5.6: Time evolution of logarithmic contour plots of joint pdf of Q vs R for wk2768, A_{ij} . (a) $t=99.8$. (b) $t=194.6$.

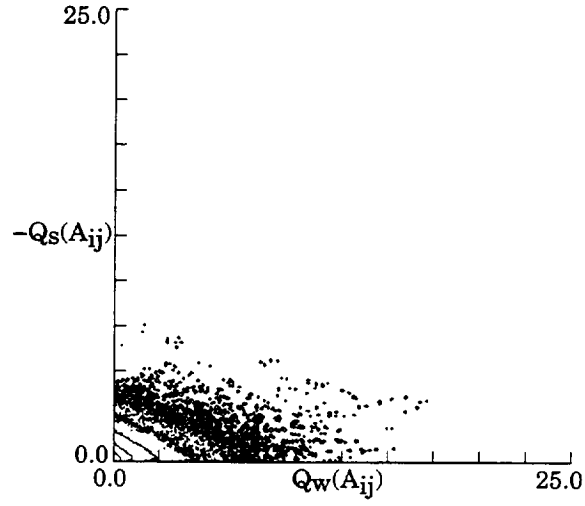


(a)

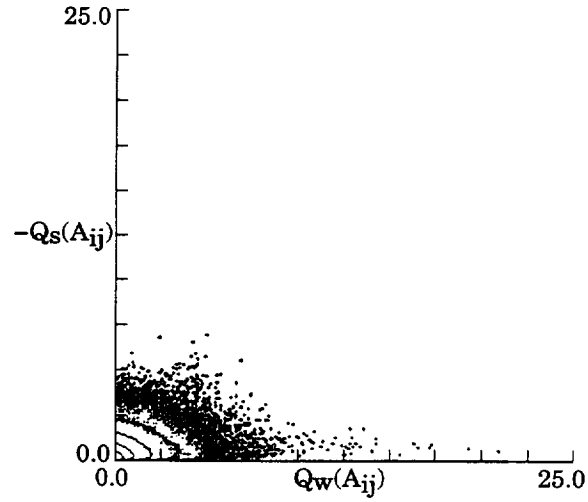


(b)

Figure 5.7: Time evolution of logarithmic contour plots of the joint pdf of Q_s vs R_s for wk2768, A_{ij} . (a) $t=99.8$. (b) $t=194.6$.

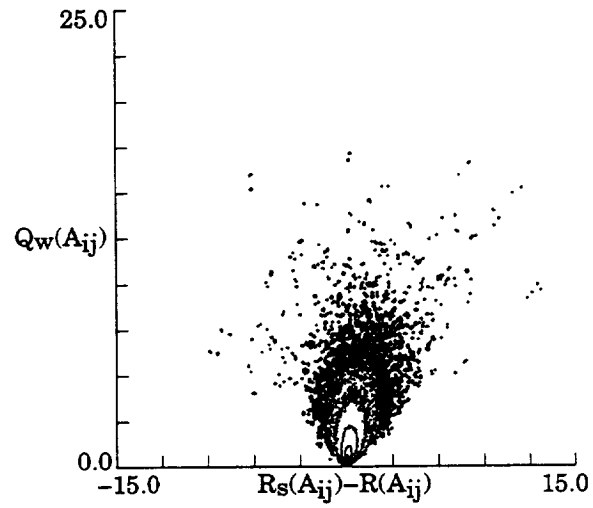


(a)

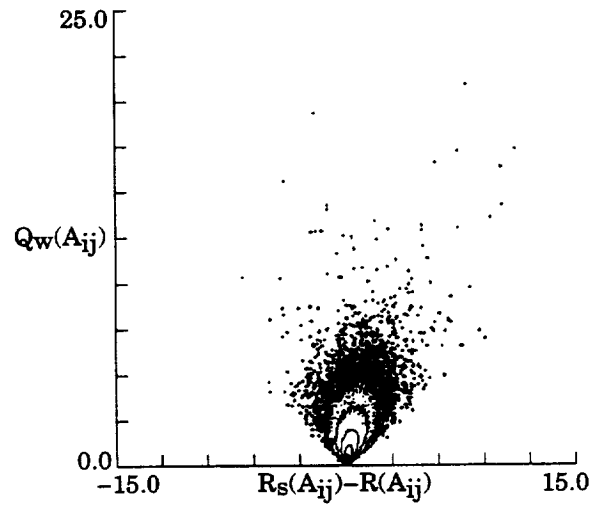


(b)

Figure 5.8: Time evolution of logarithmic contour plots of joint pdf of $-Q_s$ vs Q_w for wk2768, A_{ij} . (a) $t=99.8$. (b) $t=194.6$.



(a)



(b)

Figure 5.9: Time evolution of logarithmic contour plots of joint pdf of Q_w vs $(R_s - R)$ for wk2768, A_{ij} . (a) $t=99.8$. (b) $t=194.6$.

these data points have symmetrical H_{ij} tensors. This is because when the Reynolds number is relatively high, the viscous effect becomes relatively less significant when compared to the effects of the pressure Hessian. Since the pressure Hessian tensor is symmetric, the H_{ij} tensor tends to be symmetric as well. Therefore, most of the data points were observed to lie below the discriminant curve. At later time, the magnitude of the gradients are much smaller with most data points close to the origin. When examined closely (looking at the magnified plot), the data points in the higher contour levels are observed to move towards the lower left quadrant of the Q - R plot, exhibiting similar trend observed for the homogeneous isotropic flow.

The joint pdf of the Q_s - R_s plots also exhibit trend of moving towards the lower left quadrant. The higher contour levels are almost linear and parallel, showing strong preference for topology of stable-node/saddle/saddle. Data points with high $Q_s(H_{ij})$ are *not* necessary the same data points that are found in the high local dissipation region, indicated by high $Q_s(A_{ij})$. The effect of local dissipation on the behavior of the H_{ij} tensor will be illustrated in the later subsections. Figure 5.12 shows that data points in wake flows have significantly higher equivalent local dissipation compare to the equivalent local enstrophy density. The structure formed by the joint pdf of Q_w -($R_s - R$) is also similar to the “tear-drop” shape.

5.4.1 Effects of Reynolds number

Figures 5.14 to 5.17 show the H_{ij} invariant plots of the higher Reynolds number simulation wk2768. Data for this simulation were selected at close to the evolution times for wk346 for comparison purposes. The shapes of the joint pdf of various invariants remain very similar to those of wk346. The effect of higher Reynolds number increases the magnitude of the highest gradients, as reflected by the increase in axis scales.

5.4.2 Effects of conditioning with local dissipation

The behavior of the H_{ij} tensor for data points that reside in different local dissipation regions are shown in figures 5.18 to 5.25 for both flows. These data points are

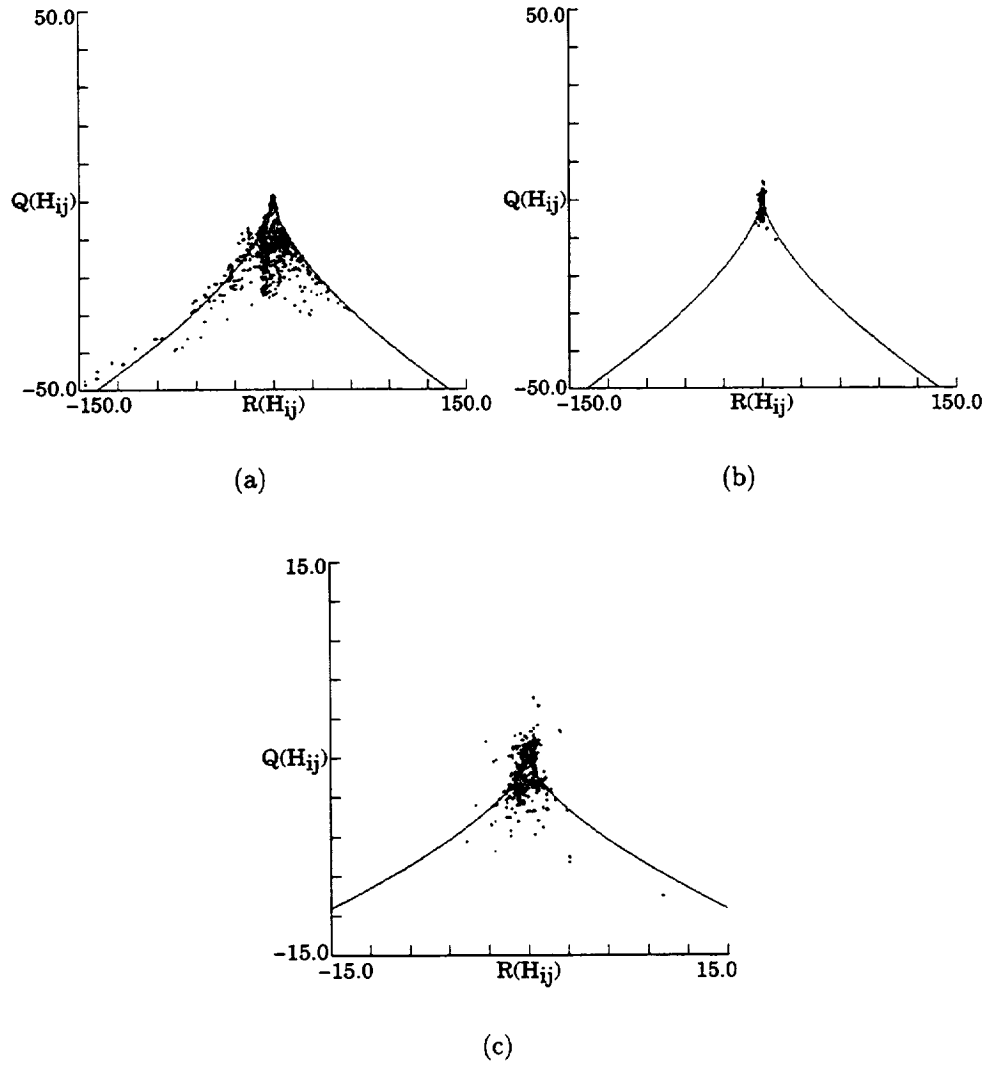


Figure 5.10: Time evolution of logarithmic contour plots of joint pdf of Q vs R for $wk346, H_{ij}$. (a) $t=102.7$. (b) $t=204.8$. (c) same as (b), with magnified axis scales.

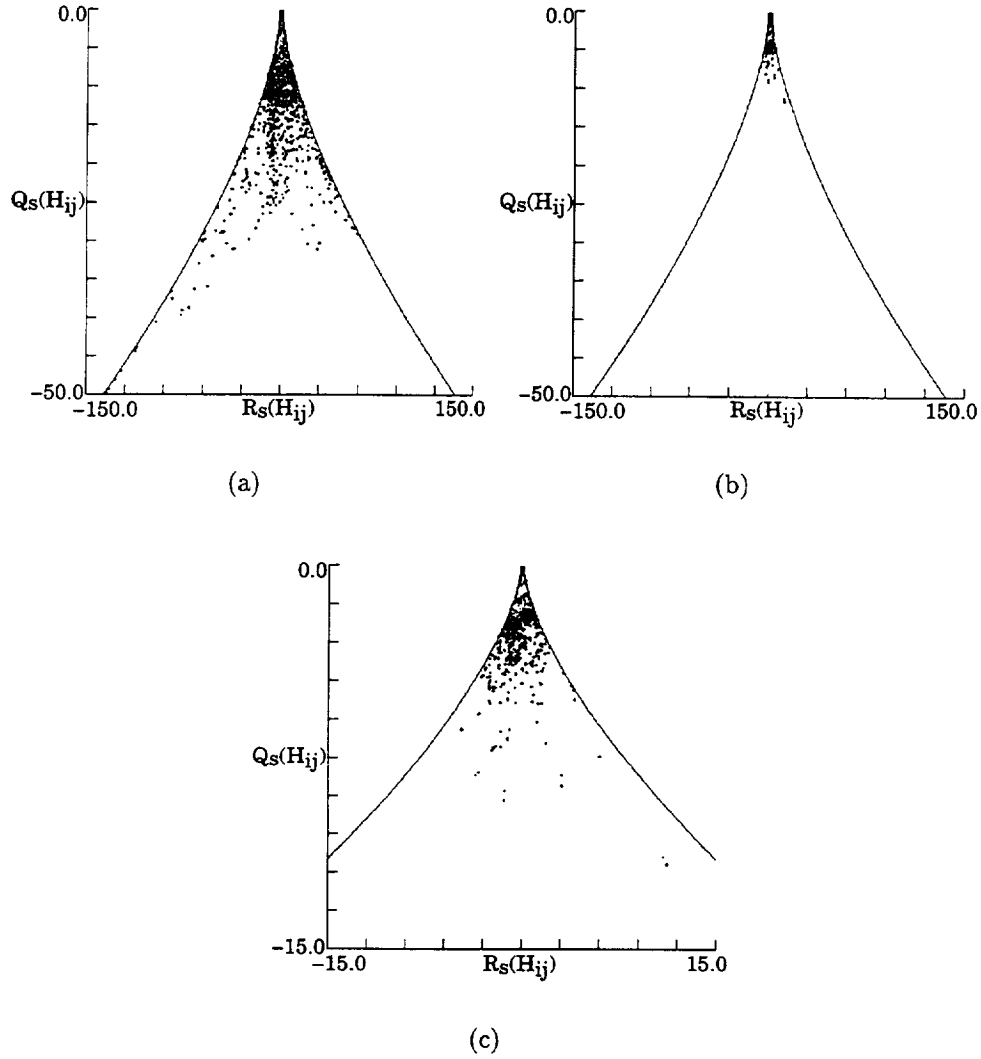
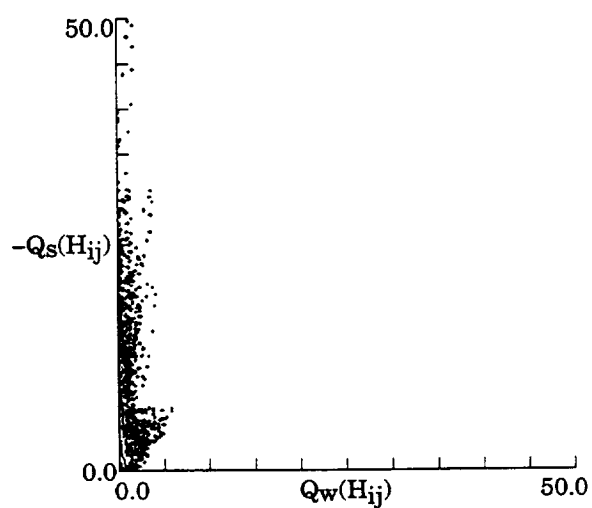
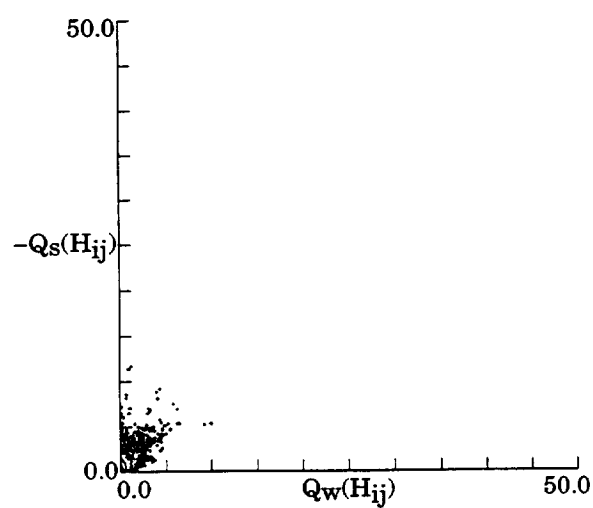


Figure 5.11: Time evolution of logarithmic contour plots of joint pdf of Q_s vs R_s wk346, H_{ij} . (a) $t=102.7$. (b) $t=204.8$. (c) same as (b), with magnified axis scales.

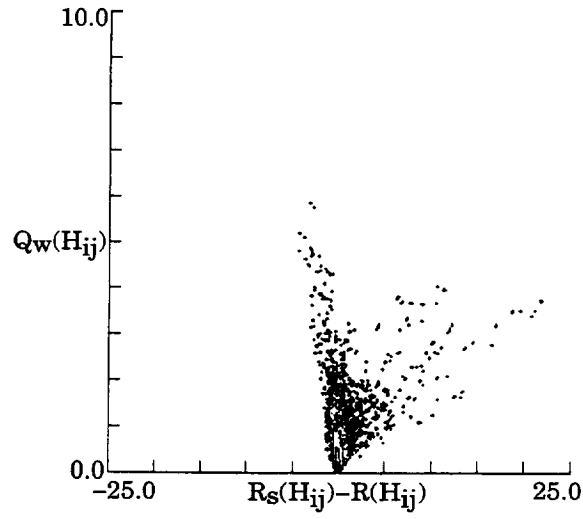


(a)

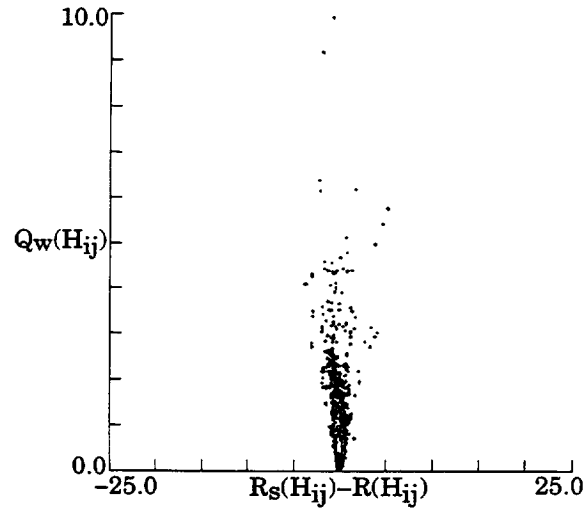


(b)

Figure 5.12: Time evolution of logarithmic contour plots of joint pdf of $-Q_s$ vs Q_w for wk346, H_{ij} . (a) $t=102.7$. (b) $t=204.8$.



(a)



(b)

Figure 5.13: Time evolution of logarithmic contour plots of joint pdf of Q_w vs $(R_s - R)$ for wk346, H_{ij} . (a) $t=102.7$. (b) $t=204.8$.

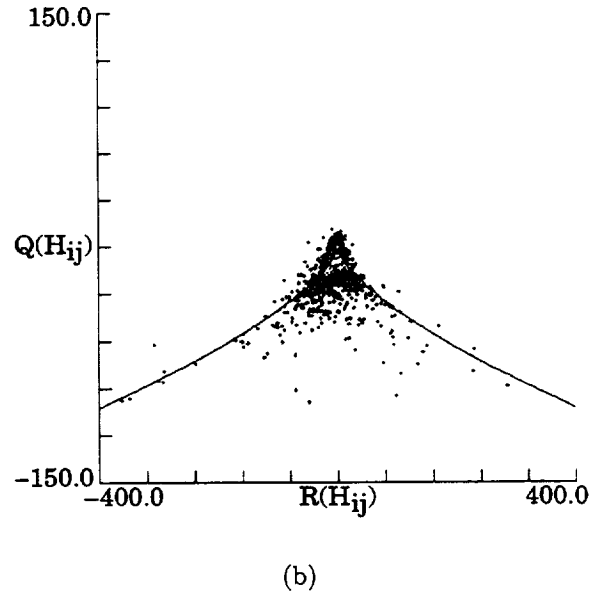
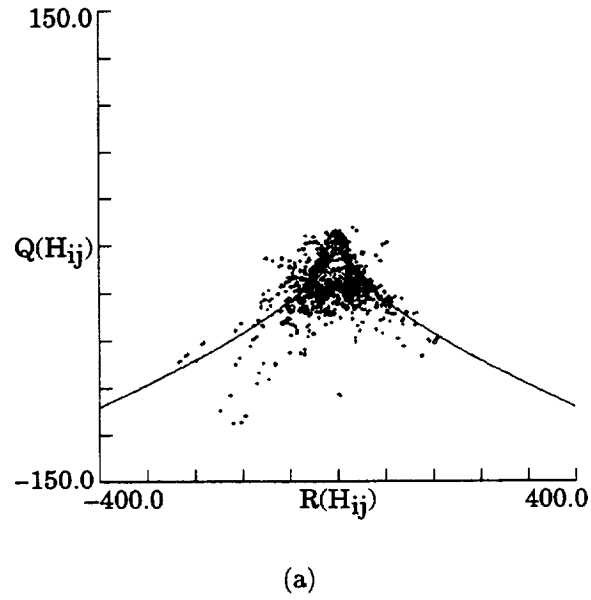
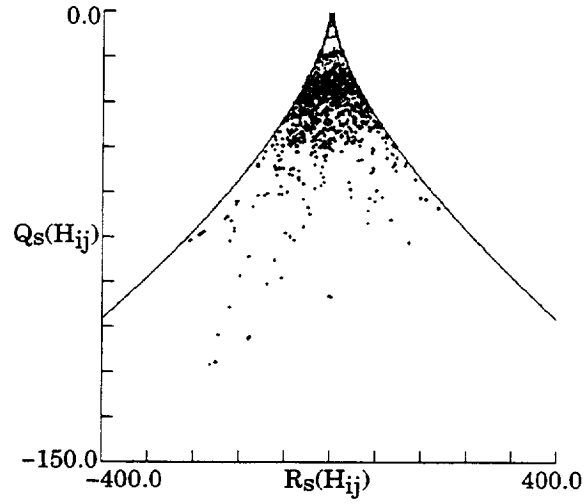
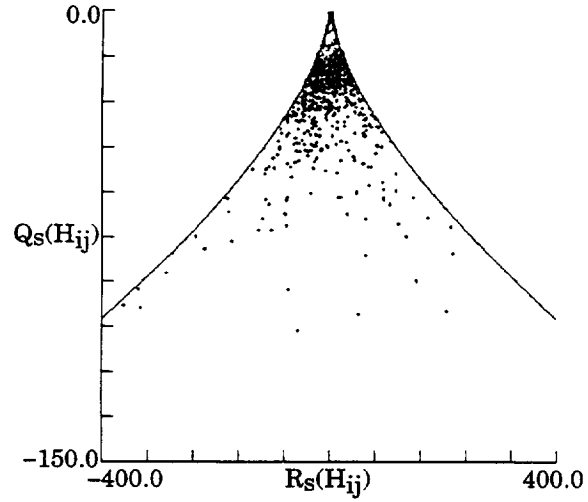


Figure 5.14: Time evolution of logarithmic contour plots of the joint pdf of Q vs R for wk2768, H_{ij} . (a) $t=99.8$. (b) $t=194.6$.

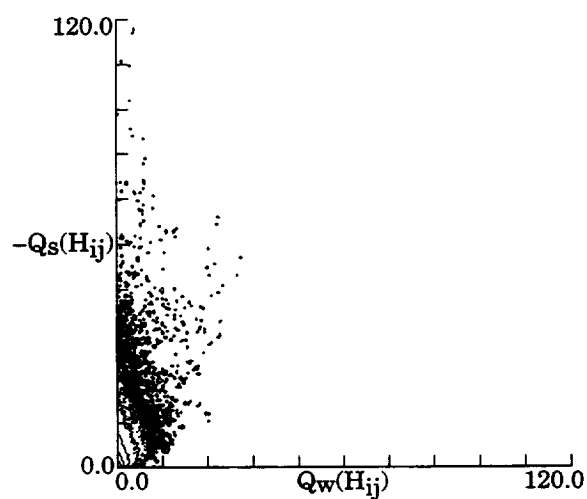


(a)

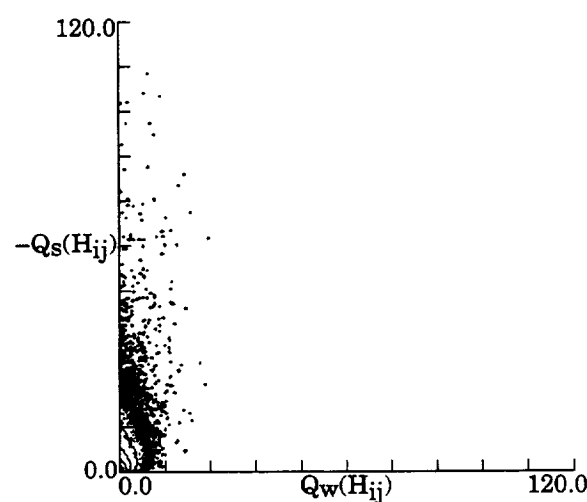


(b)

Figure 5.15: Time evolution of logarithmic contour plots of joint pdf of Q_s vs R_s for wk2768, H_{ij} . (a) $t=99.8$. (b) $t=194.6$.



(a)



(b)

Figure 5.16: Time evolution of logarithmic contour plots of joint pdf of $-Q_s$ vs Q_w for wk2768, H_{ij} . (a) $t=99.8$. (b) $t=194.6$.

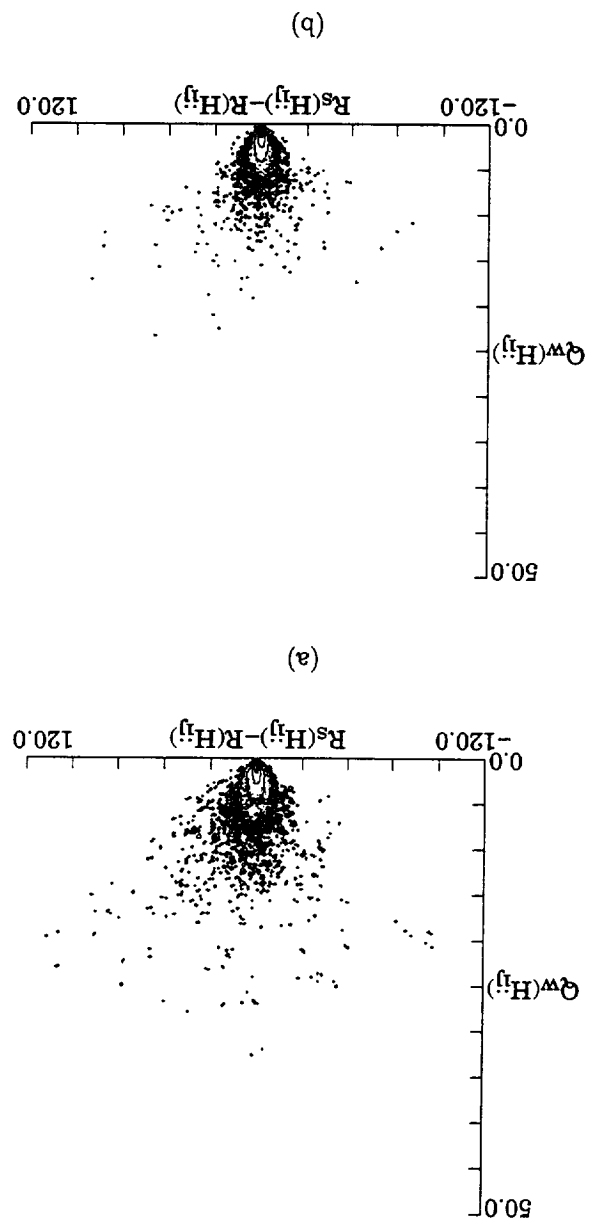


Figure 5.17: Time evolution of logarithmic contour plots of joint pdf of Q_w vs $(R_s - R)$ for wk2768, H_{IJ} . (a) $t=99.8$. (b) $t=194.6$.

conditioned at different levels of local dissipation. The levels vary from 0% of the maximum local dissipation (all data points are included) to 75% of the maximum local dissipation in the flow. As the conditioning levels increases, the magnitude of the invariants of H_{ij} are observed to decrease very rapidly. This observation indicates that the *magnitude* of the H_{ij} tensor gets smaller when the conditioning level of the local dissipation increases. This conclusion is arrived from the results in figure 5.10(a), which shown that most H_{ij} tensor is symmetric since most of the data points lie below the discriminant curve. From the definition of $Q(H_{ij})$, when H_{ij} tensor is symmetric, then

$$Q(H_{ij}) \sim H_{ik}H_{ki} \sim H_{ik}H_{ik} \sim |H_{ij}|^2. \quad (5.3)$$

When data is conditioned at higher local dissipation levels, $Q(H_{ij})$ is very small, as observed in figures 5.18 to 5.25. Hence, magnitude of H_{ij} gets smaller when data is conditioned at higher local dissipation levels.

The result that the magnitude of H_{ij} tensor is small at high local dissipation regions is very interesting. This result indicates that in regions of high local dissipation (i.e. high velocity gradients), the magnitude of H_{ij} can be small. In these regions, the analytical solution of the Restricted Euler model may be applicable.

5.4.3 Effects of conditioning with local enstrophy density

The behavior of the H_{ij} tensor for data points with different local enstrophy density are shown in figures 5.26 to 5.33. As the conditioning levels increases from 0% to 75% of the maximum local enstrophy density, the magnitudes of the invariants of H_{ij} are not observed to get smaller accordingly. Instead, data points with high local enstrophy density levels correspond to high gradients in all the plots shown. This result indicated that the magnitude of H_{ij} is small only in the high local dissipation regions, but not necessary in the high local enstrophy density regions.

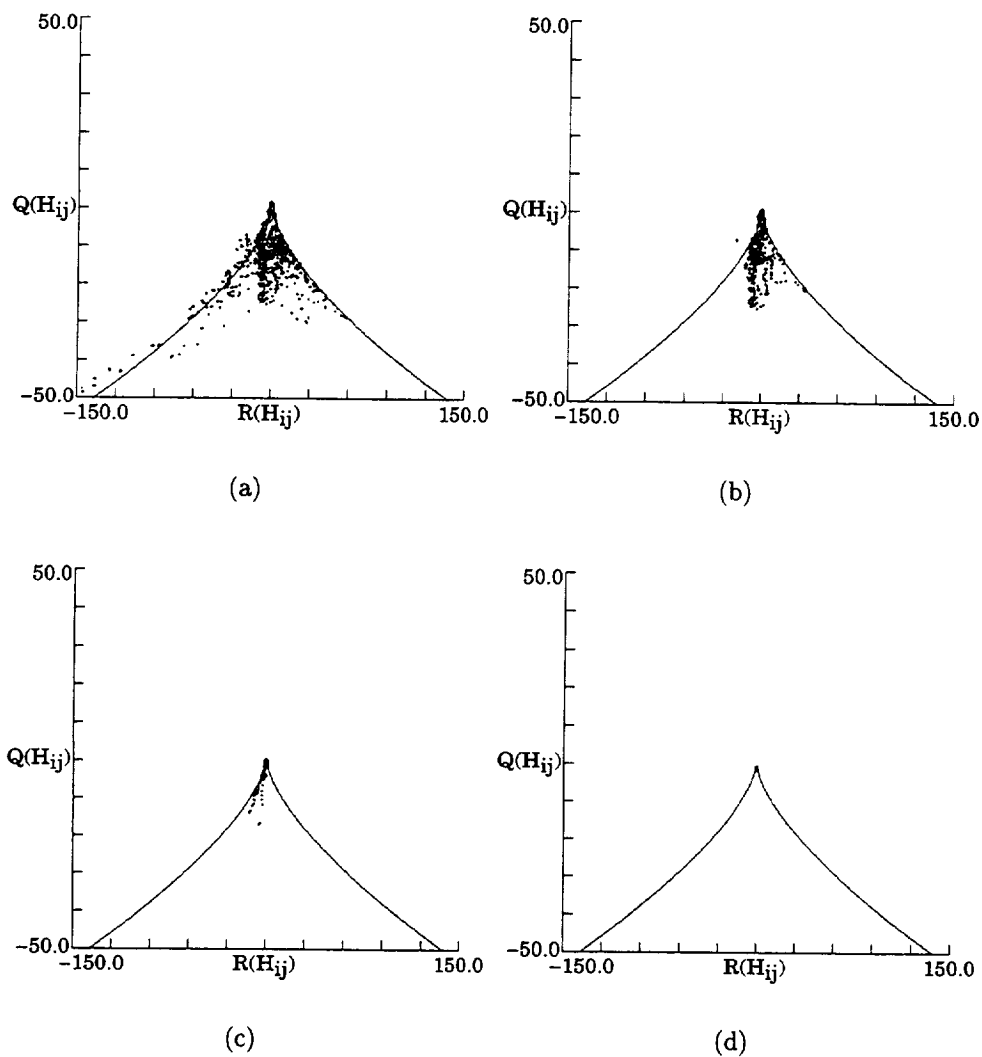


Figure 5.18: Logarithmic contour plots of joint pdf of Q vs R for $wk346$, H_{ij} . $t=102.7$. Data conditioned at various levels of maximum local dissipation. (a) 0% (All data points). (b) 25%. (c) 50%. (d) 75%.

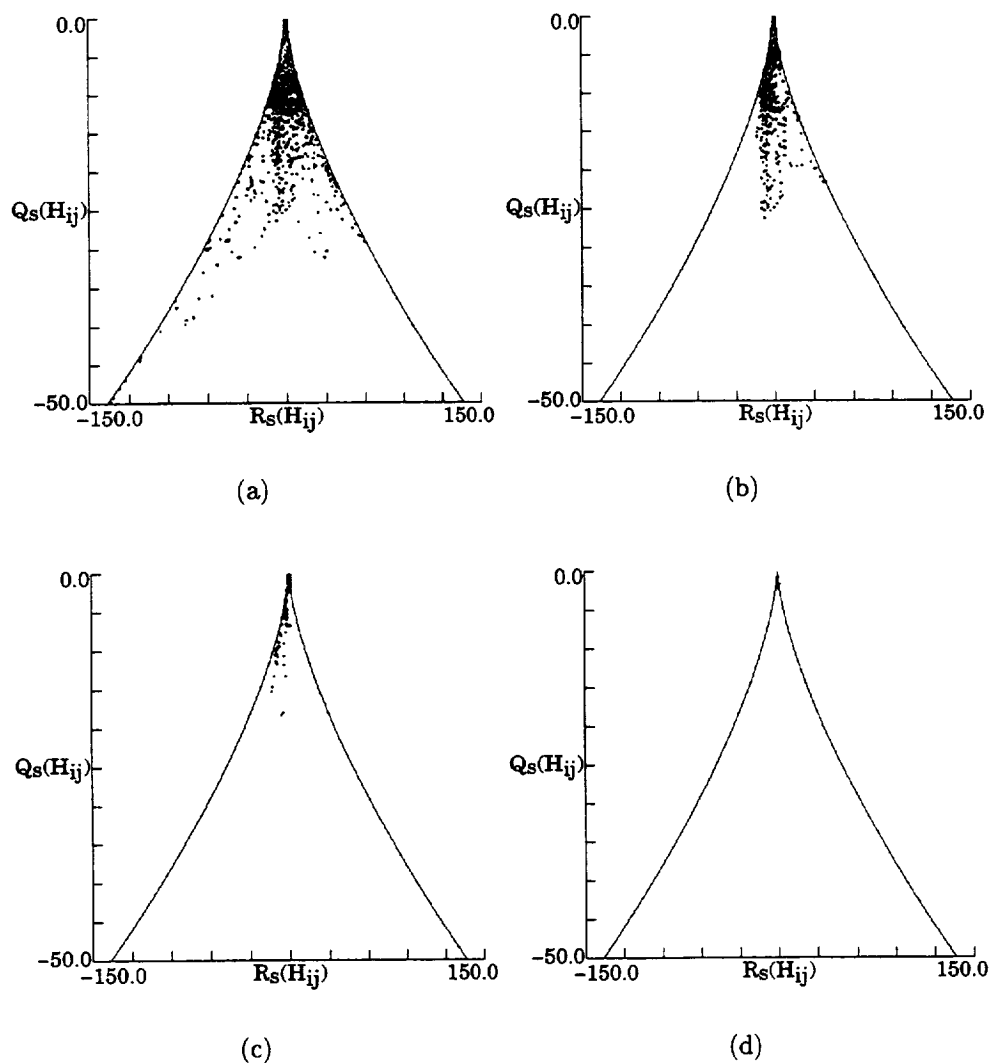


Figure 5.19: Logarithmic contour plots of joint pdf of Q_s vs R_s for wk346, H_{ij} . $t=102.7$. Data conditioned at various levels of maximum local dissipation. (a) 0% (All data points). (b) 25%. (c) 50%. (d) 75%.

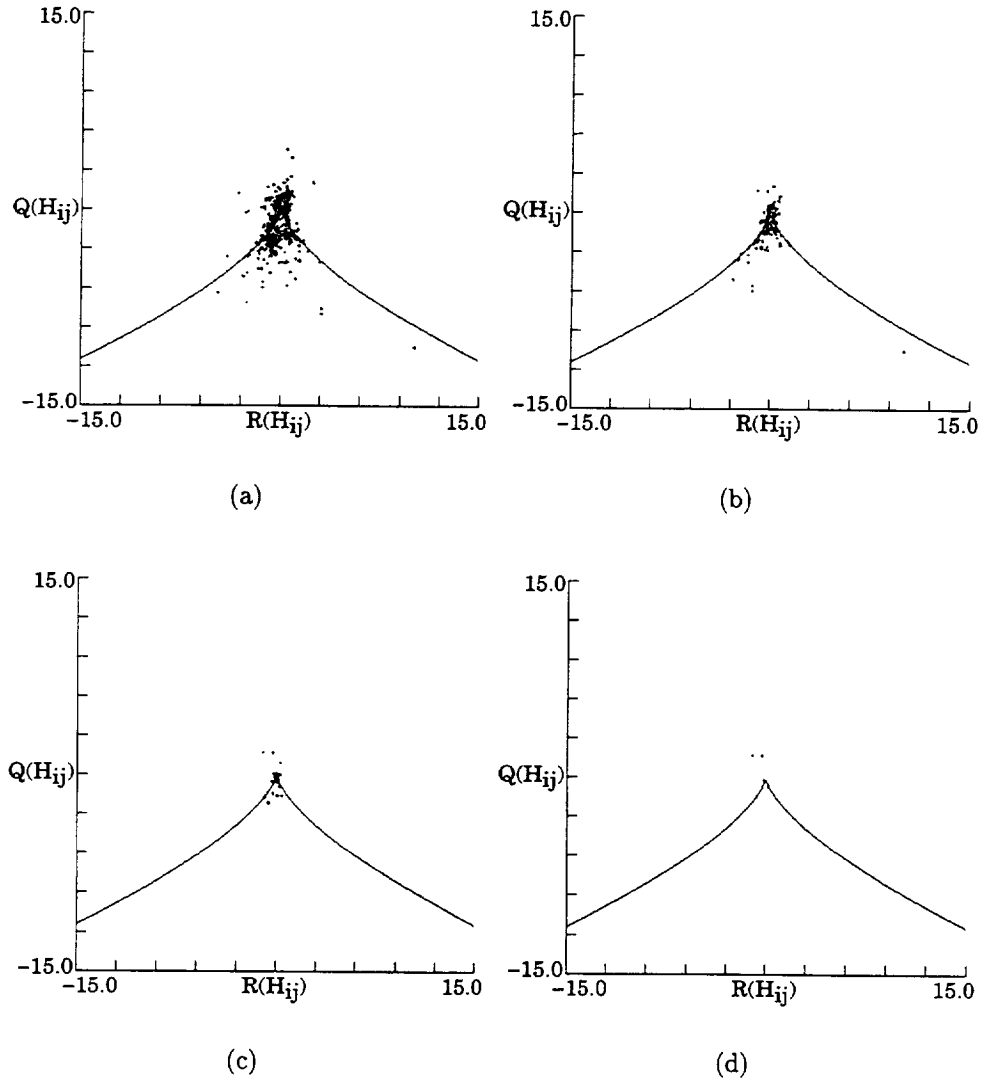


Figure 5.20: Logarithmic contour plots of joint pdf of Q vs R for $wk346$, H_{ij} . $t=204.8$. Data conditioned at various levels of maximum local dissipation. (a) 0% (All data points). (b) 25%. (c) 50%. (d) 75%.

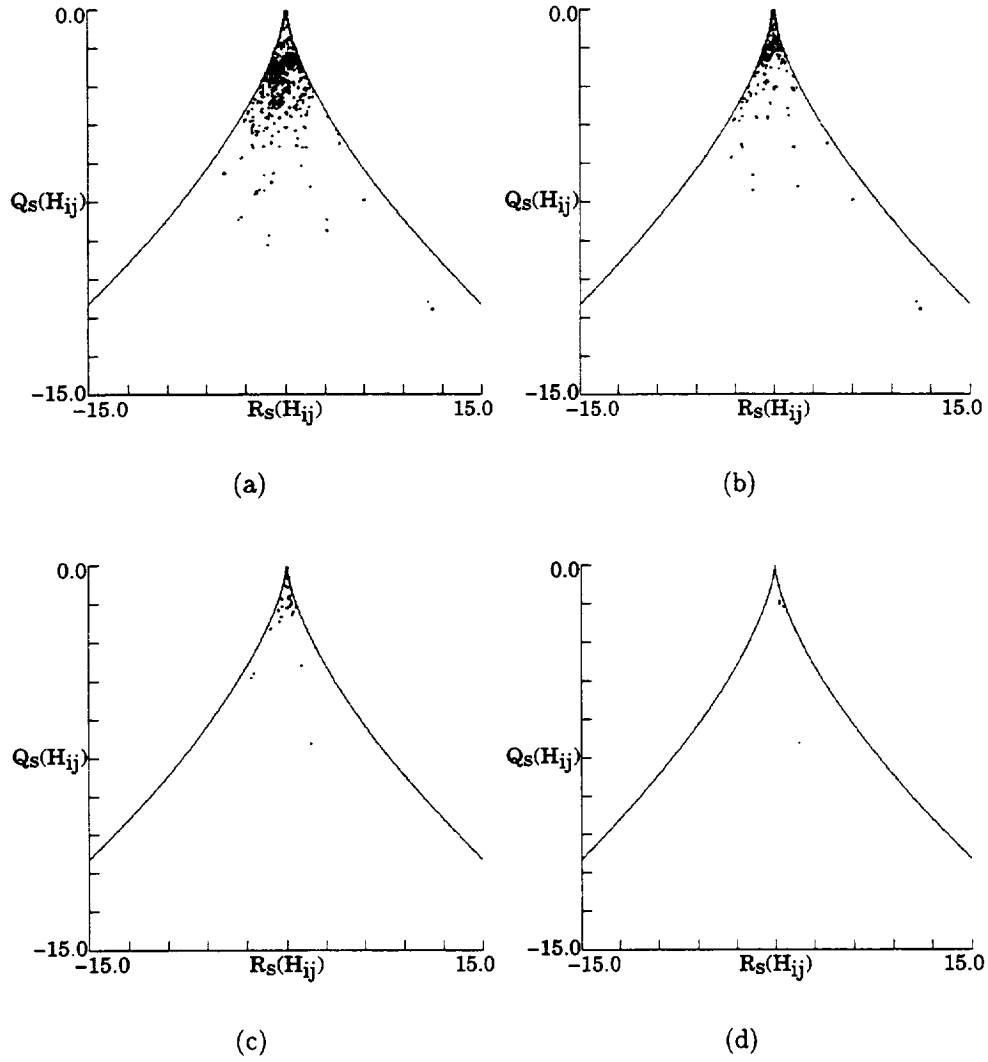


Figure 5.21: Logarithmic contour plots of joint pdf of Q_s vs R_s for wk346, H_{ij} . $t=204.8$. Data conditioned at various levels of maximum local dissipation. (a) 0% (All data points). (b) 25%. (c) 50%. (d) 75%.

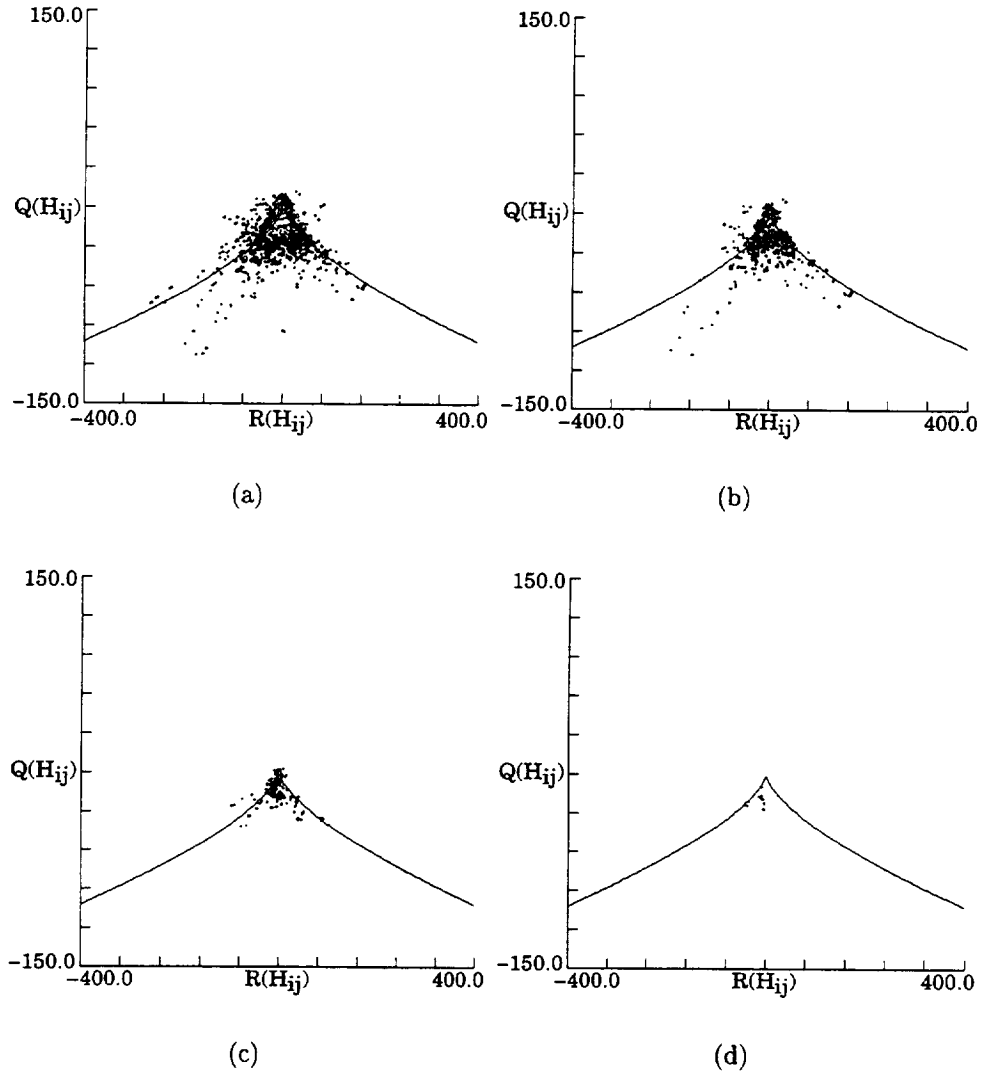


Figure 5.22: Logarithmic contour plots of joint pdf of Q vs R for $wk2768$, H_{ij} . $t=99.8$. Data conditioned at various levels of maximum local dissipation. (a) 0% (All data points). (b) 25%. (c) 50%. (d) 75%.

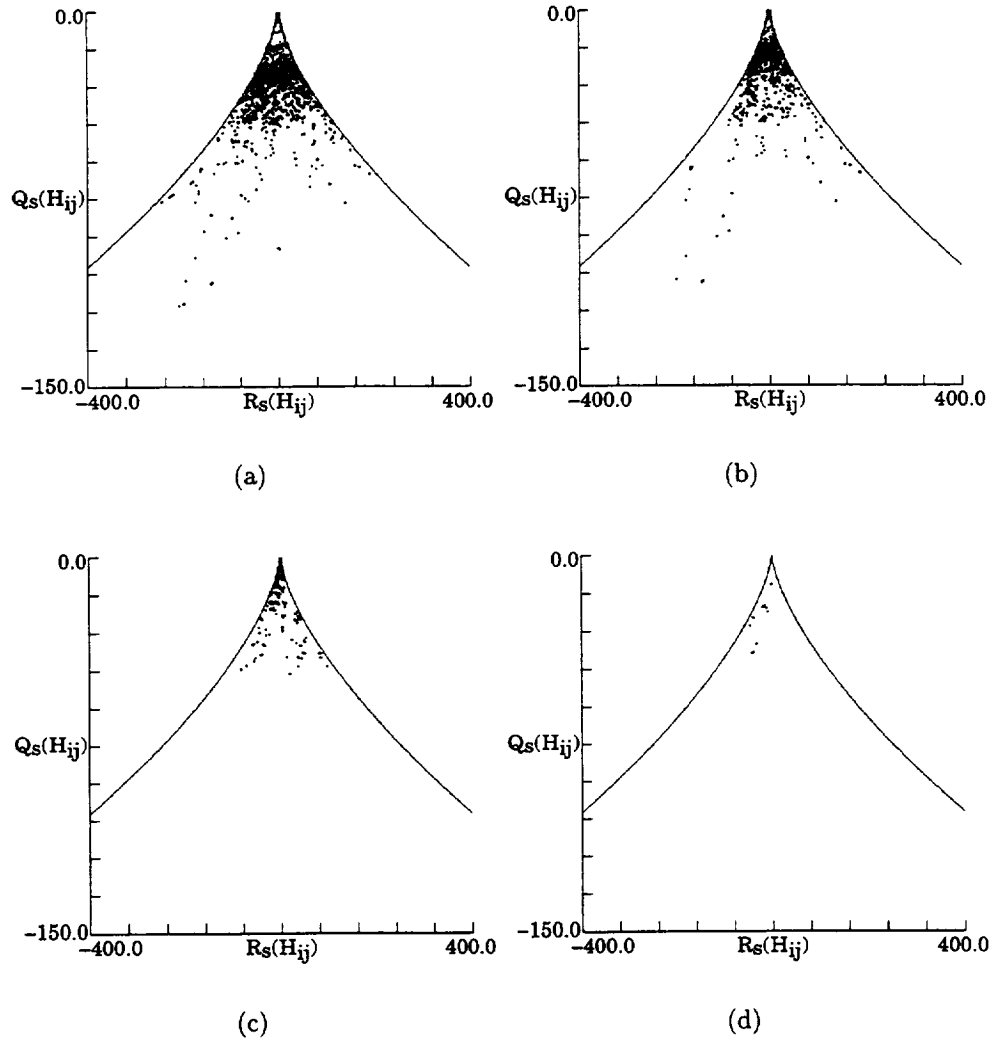


Figure 5.23: Logarithmic contour plots of joint pdf of Q_s vs R_s for wk2768, $t=99.8$. Data conditioned at various levels of maximum local dissipation. (a) 0% (All data points). (b) 25%. (c) 50%. (d) 75%.

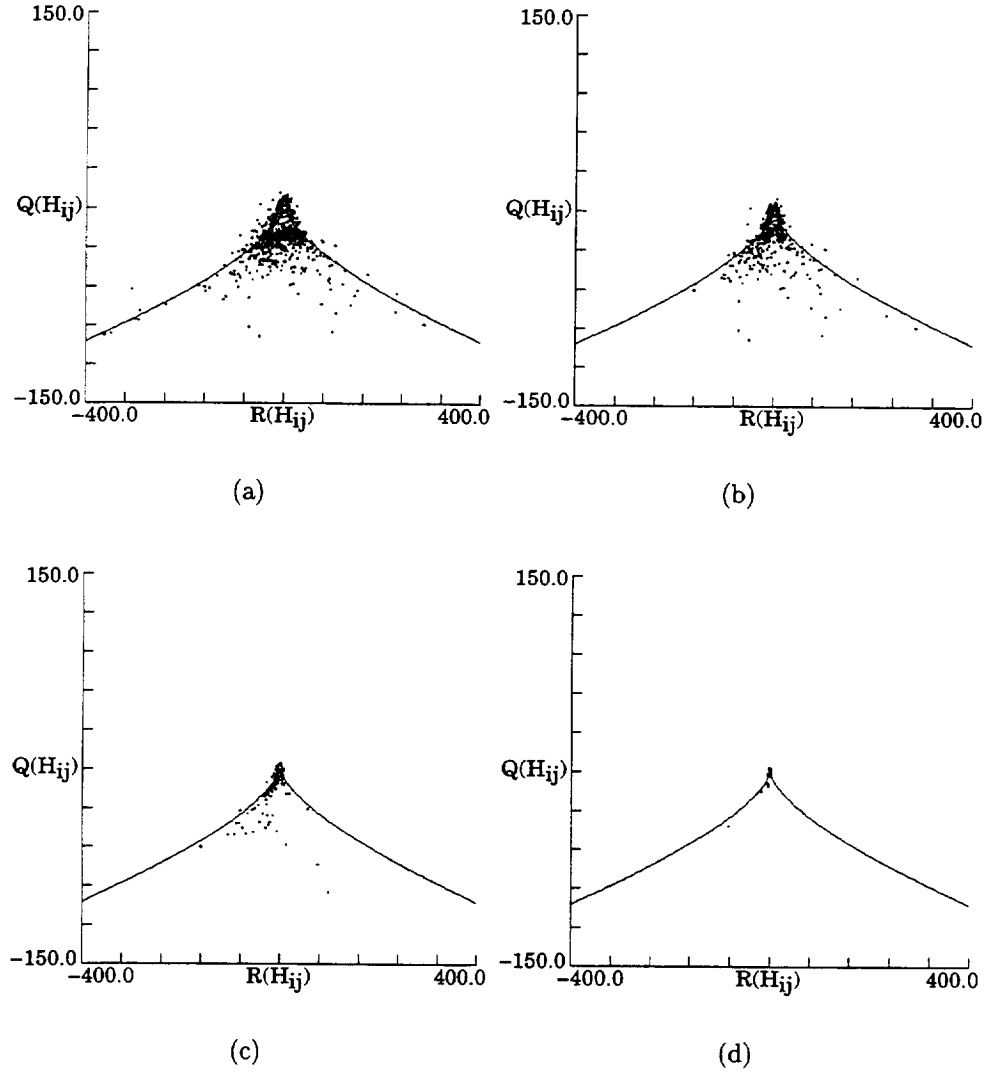


Figure 5.24: Logarithmic contour plots of joint pdf of Q vs R for $wk2768$, H_{ij} . $t=194.6$. Data conditioned at various levels of maximum local dissipation. (a) 0% (All data points). (b) 25%. (c) 50%. (d) 75%.

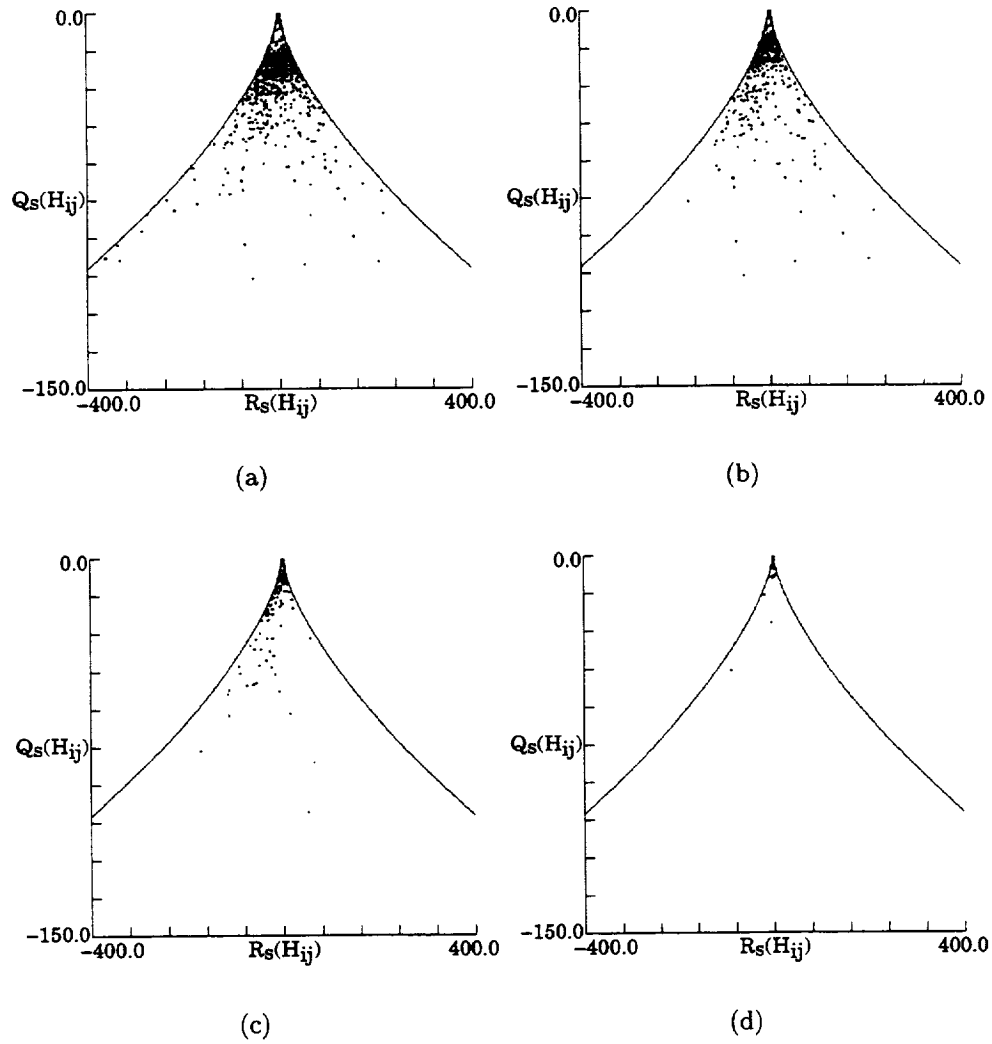


Figure 5.25: Logarithmic contour plots of joint pdf of Q_s vs R_s for wk2768, H_{ij} . $t=194.6$. Data conditioned at various levels of maximum local dissipation. (a) 0% (All data points). (b) 25%. (c) 50%. (d) 75%.

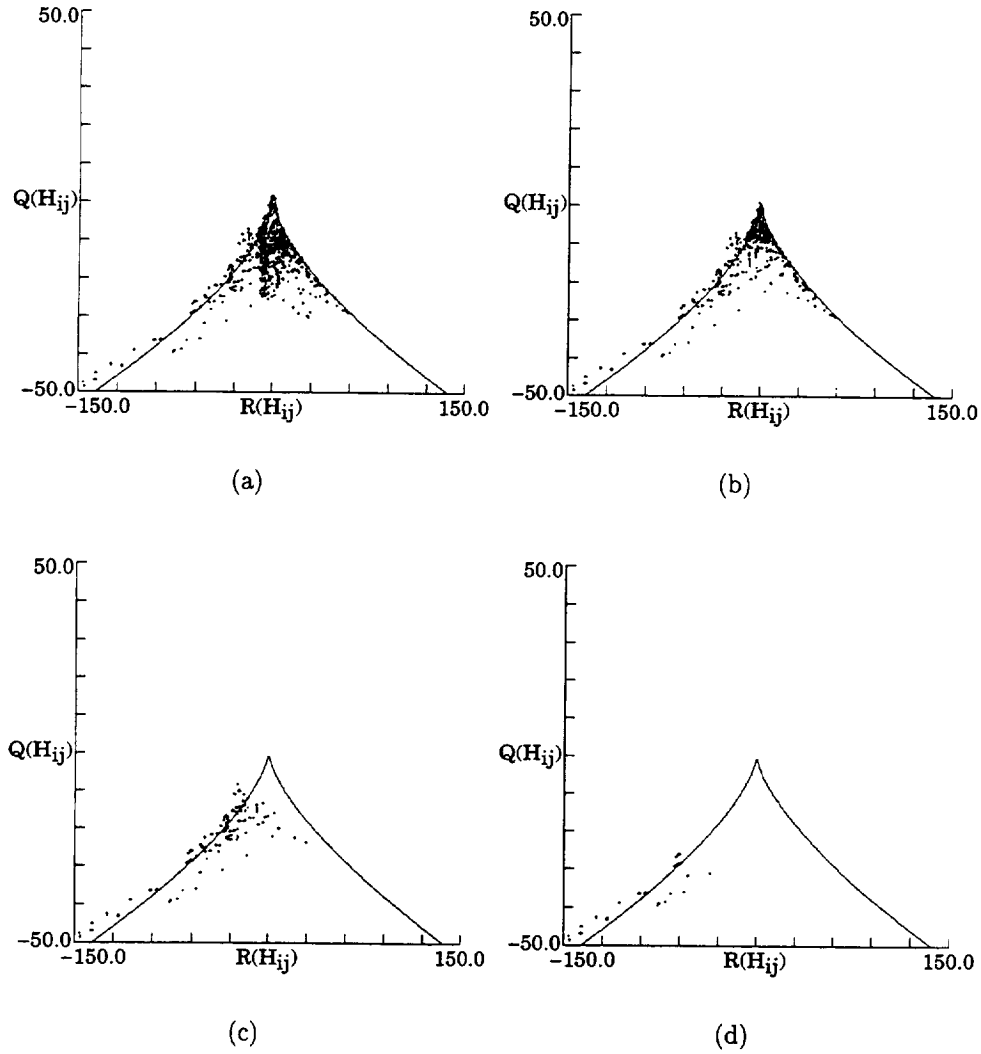


Figure 5.26: Logarithmic contour plots of joint pdf of Q vs R for $wk346$, H_{ij} . $t=102.7$. Data conditioned at various levels of maximum local enstrophy density. (a) 0% (All data points). (b) 25%. (c) 50%. (d) 75%.

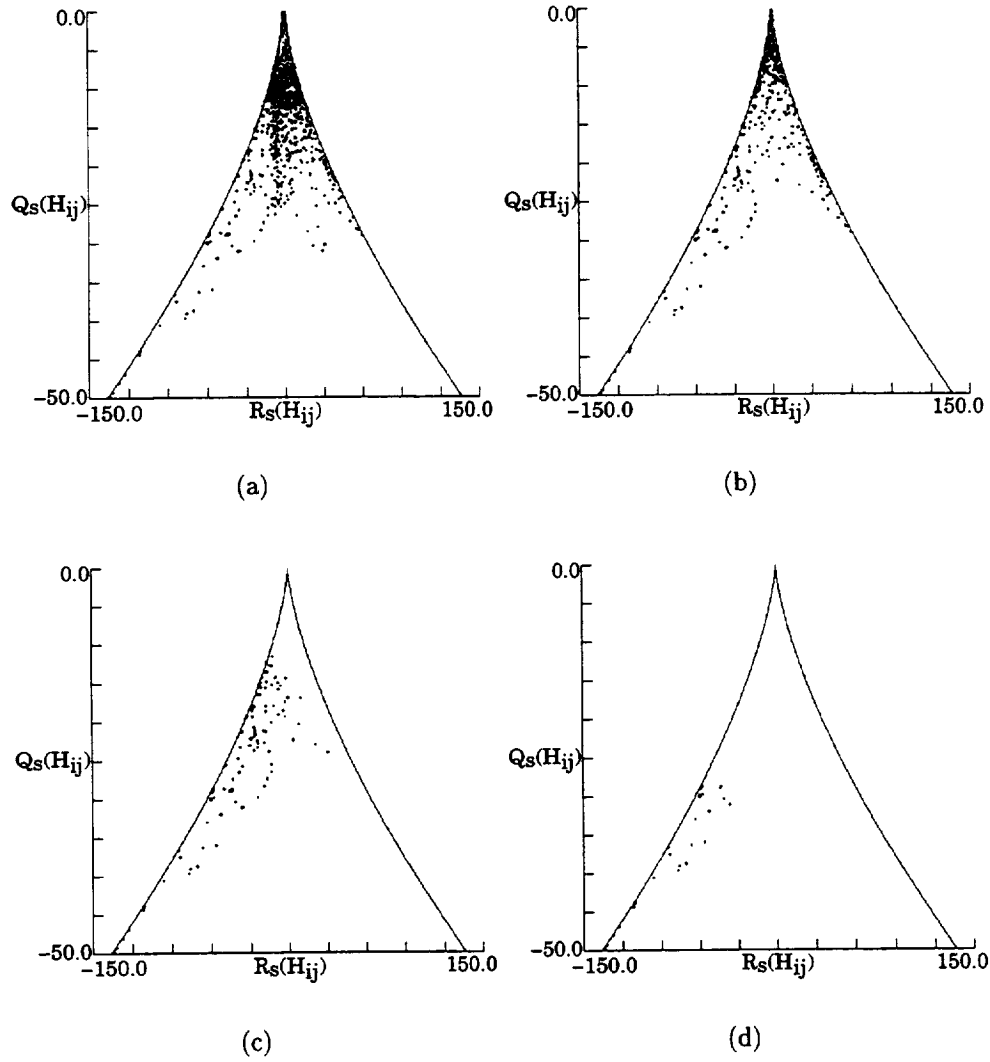


Figure 5.27: Logarithmic contour plots of joint pdf of Q_s vs R_s for wk346, H_{ij} . $t=102.7$. Data conditioned at various levels of maximum local enstrophy density. (a) 0% (All data points). (b) 25%. (c) 50%. (d) 75%.

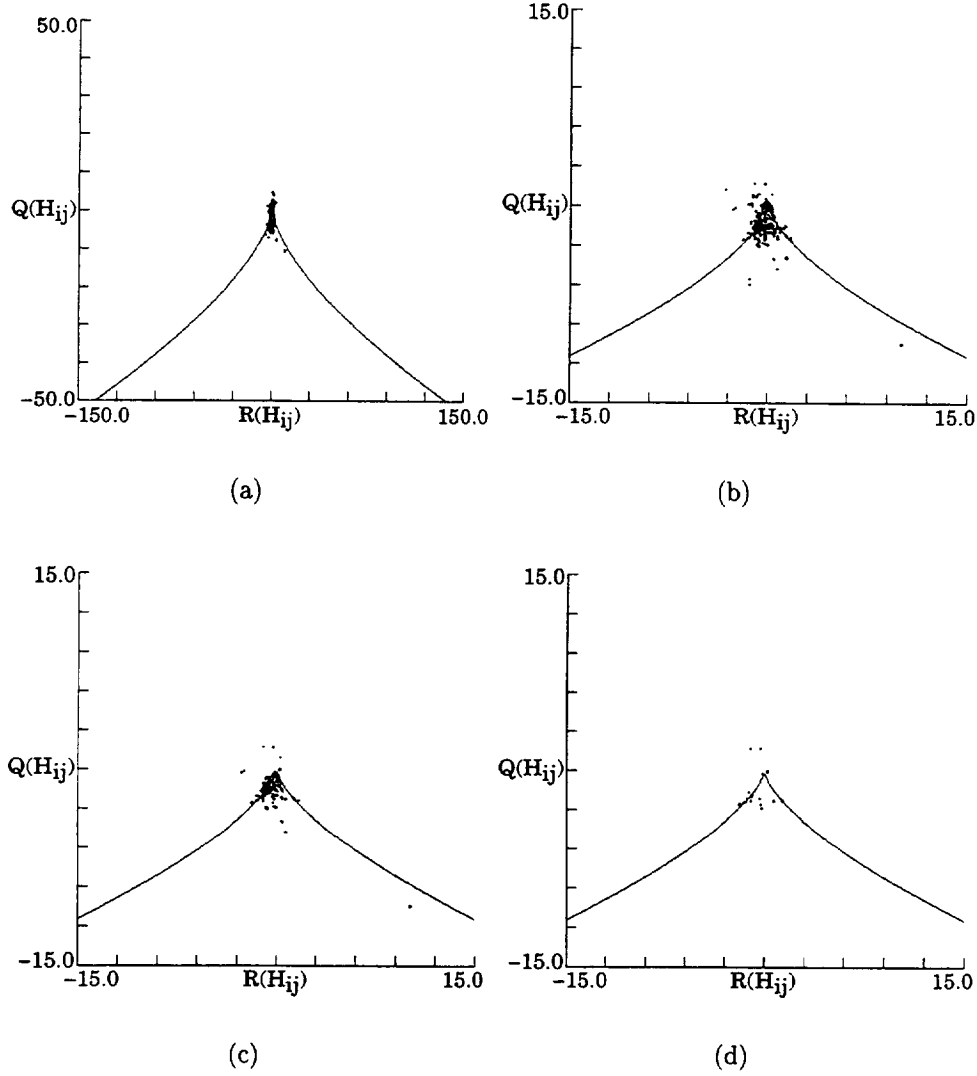


Figure 5.28: Logarithmic contour plots of joint pdf of Q vs R for $wk346$, H_{ij} . $t=204.8$. Data conditioned at various levels of maximum local enstrophy density. (a) 0% (All data points). (b) 25%. (c) 50%. (d) 75%.

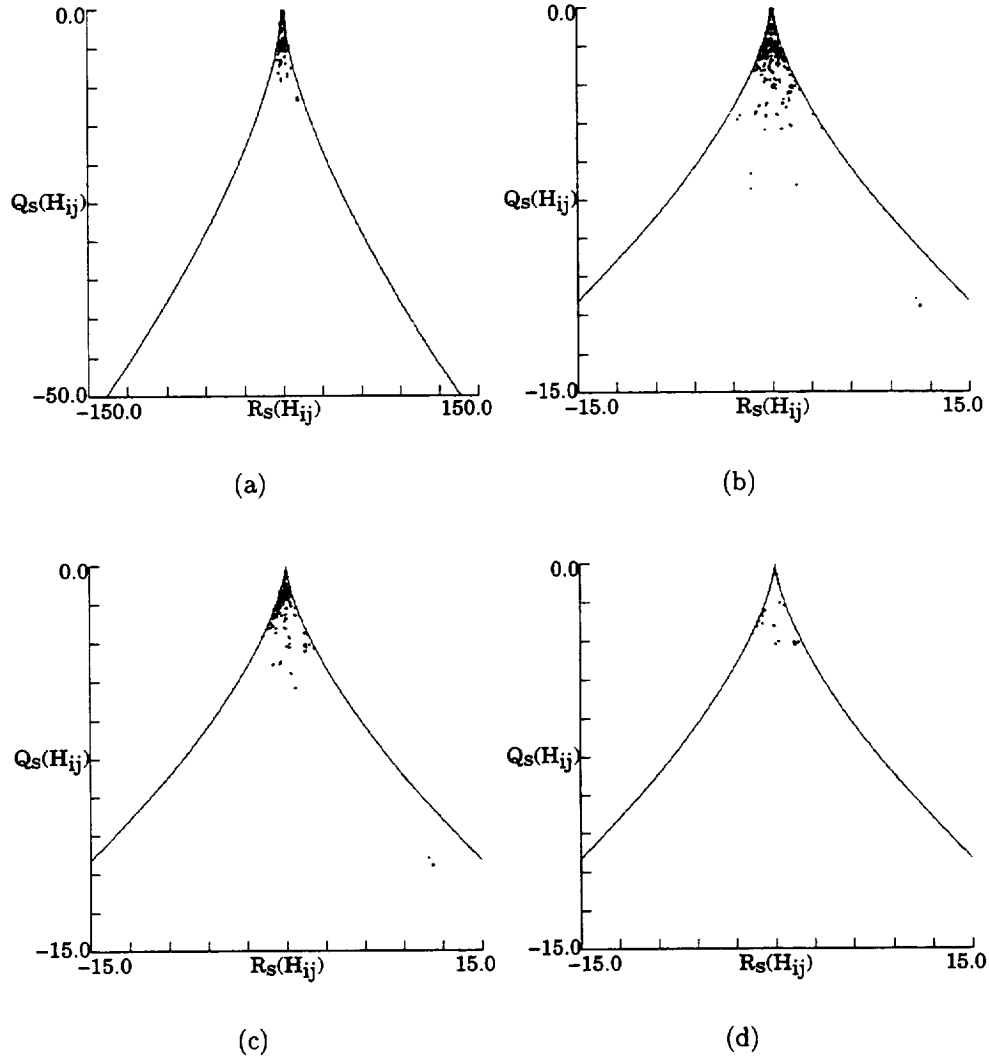


Figure 5.29: Logarithmic contour plots of joint pdf of Q_s vs R_s for wk346, H_{ij} . $t=204.8$. Data conditioned at various levels of maximum local enstrophy density. (a) 0% (All data points). (b) 25%. (c) 50%. (d) 75%.

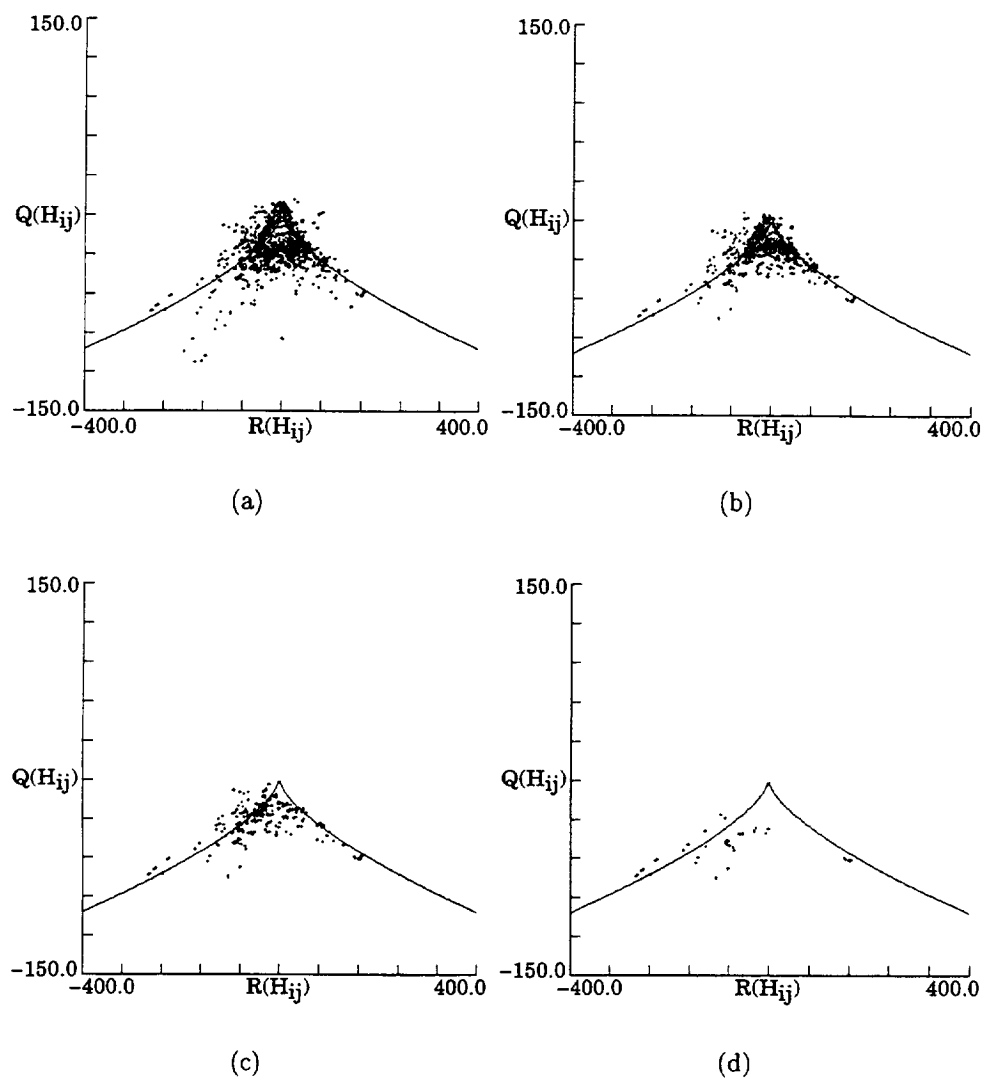


Figure 5.30: Logarithmic contour plots of joint pdf of Q vs R for $wk2768$, H_{ij} . $t=99.8$. Data conditioned at various levels of maximum local enstrophy density. (a) 0% (All data points). (b) 25%. (c) 50%. (d) 75%.

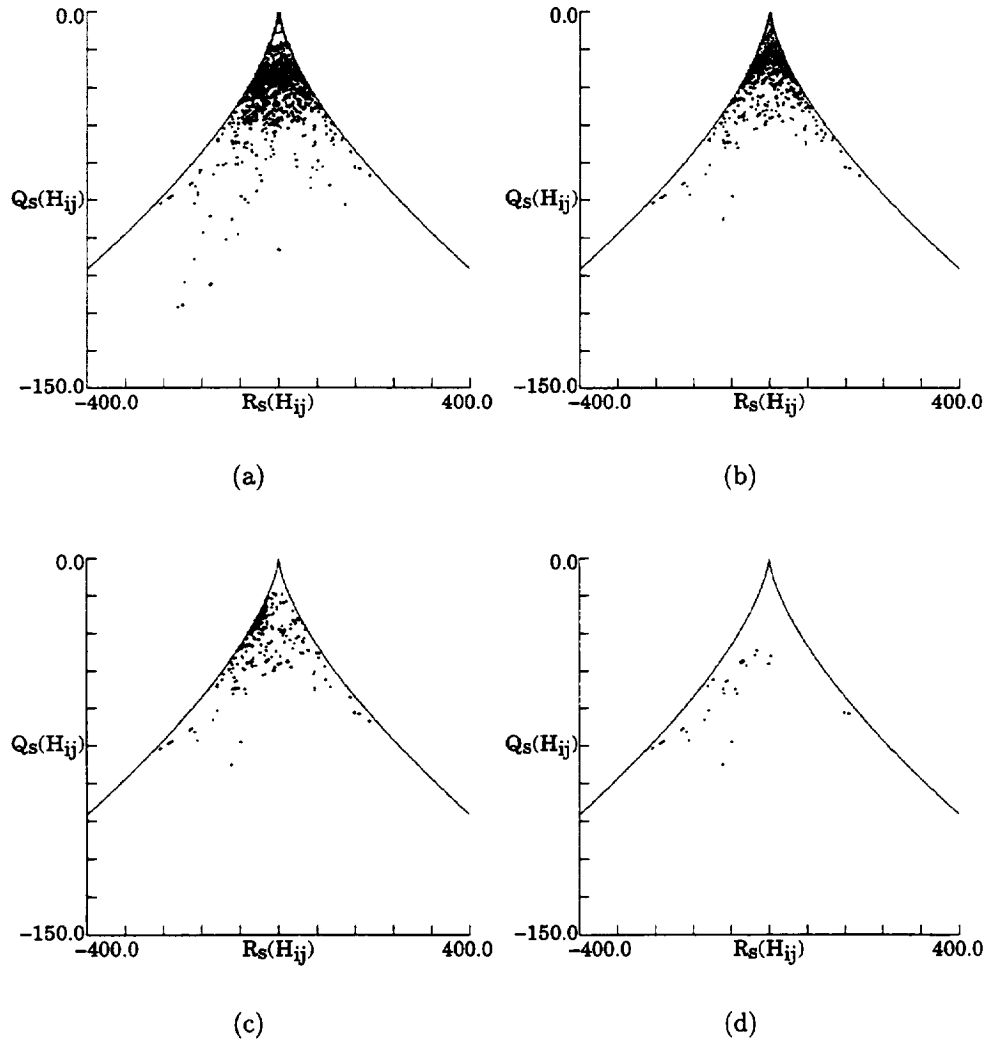


Figure 5.31: Logarithmic contour plots of joint pdf of Q_s vs R_s for wk2768, H_{ij} . $t=99.8$. Data conditioned at various levels of maximum local enstrophy density. (a) 0% (All data points). (b) 25%. (c) 50%. (d) 75%.

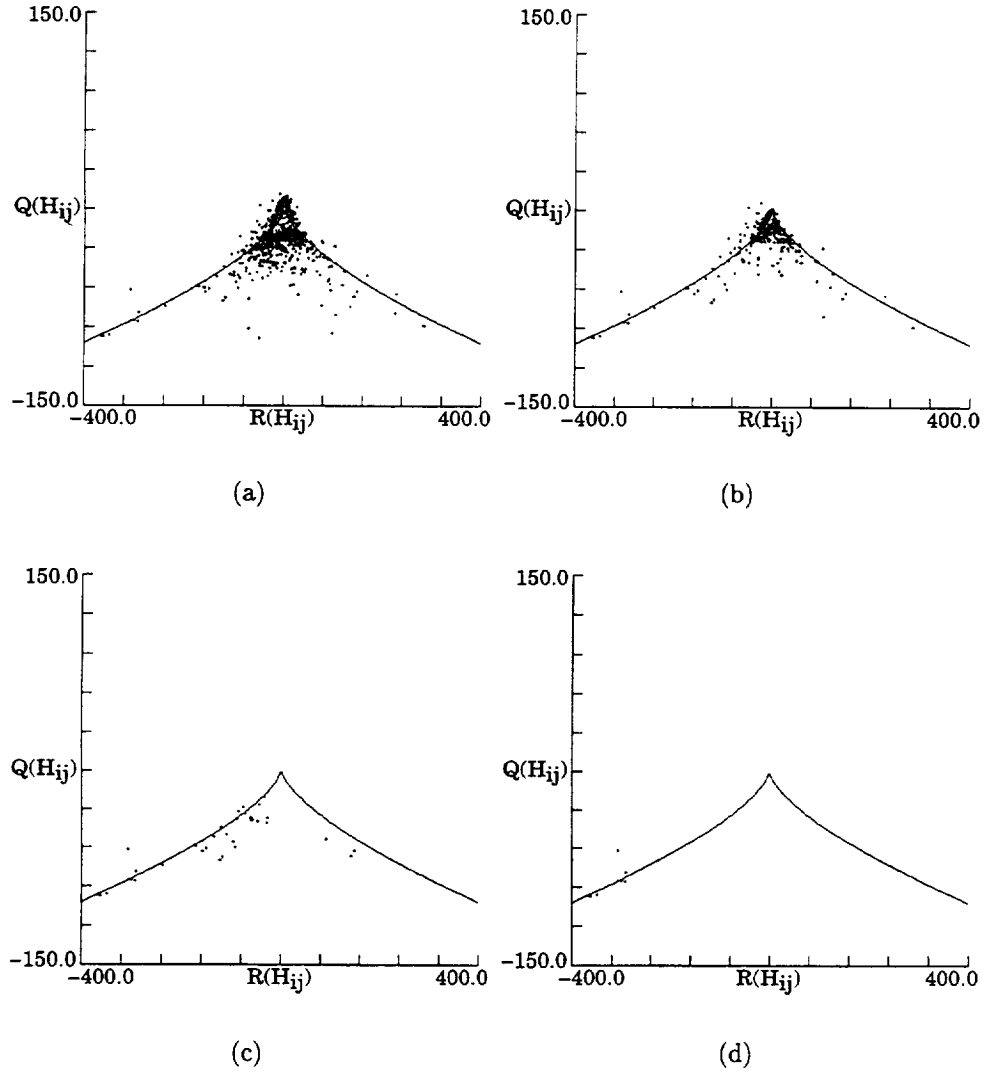


Figure 5.32: Logarithmic contour plots of joint pdf of Q vs R for wk2768, H_{ij} . $t=194.6$. Data conditioned at various levels of maximum local local enstrophy density. (a) 0% (All data points). (b) 25%. (c) 50%. (d) 75%.

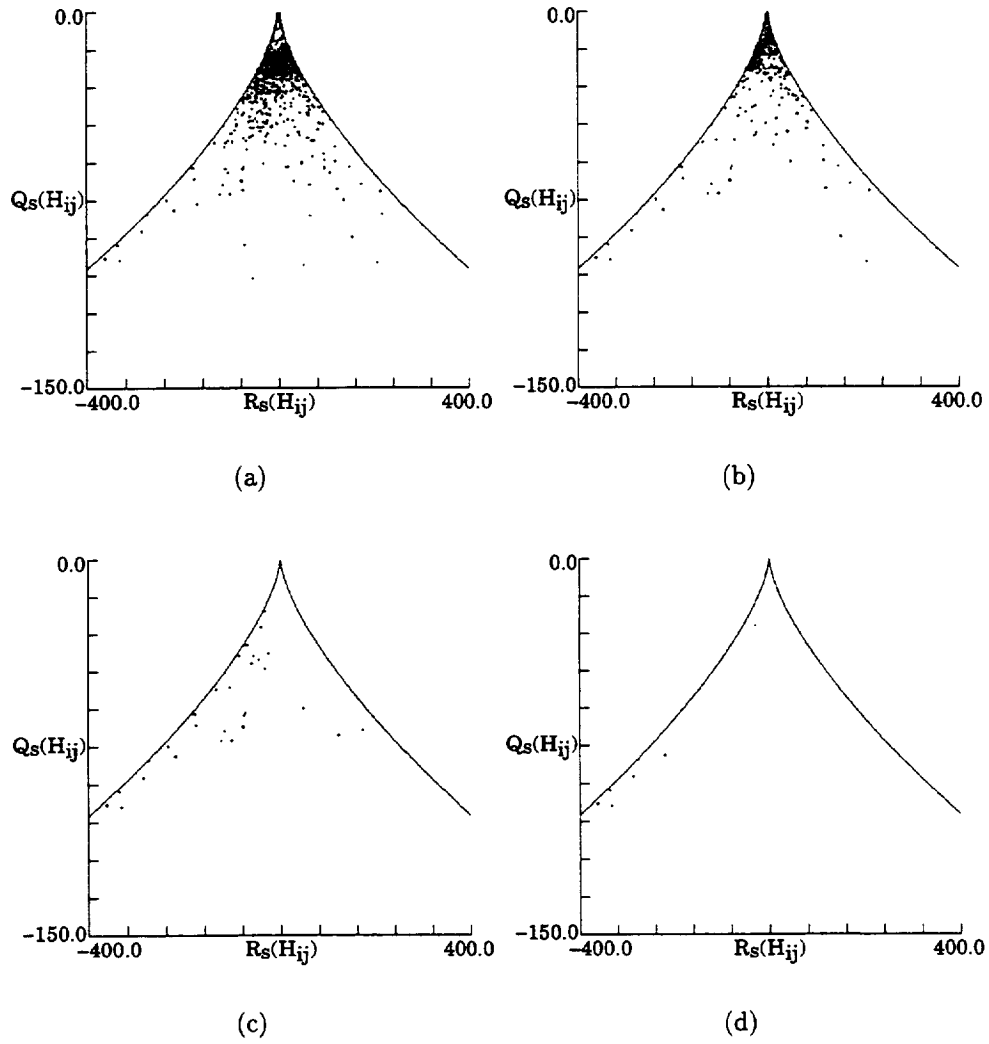


Figure 5.33: Logarithmic contour plots of joint pdf of Q_s vs R_s for $wk2768$, H_{ij} . $t=194.6$. Data conditioned at various levels of maximum local (a) 0% (All data points). (b) 25%. (c) 50%. (d) 75%.

5.4.4 Acceleration strain-rate distribution

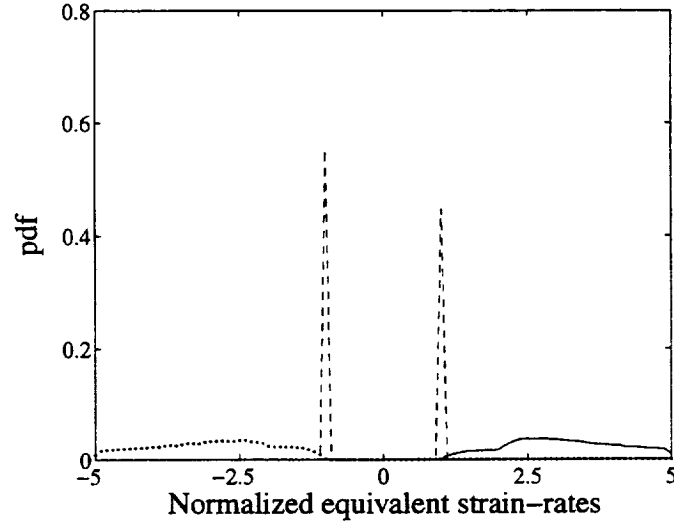
It was observed by Sondergaard that when the strain-rates of the velocity gradient tensor were sorted in descending order $\alpha \geq \beta \geq \gamma$; the ratio of these strain-rates was found to be $\alpha : \beta : \gamma \approx 1.5 : 1.0 : -2.5$ for data points conditioned in the high local dissipation regions. Positive β indicates that the local rate-of-strain topology is of the type unstable-node/saddle/saddle. This distributions is insensitive to Reynolds number and holds for all the three-dimensional wakes simulated by Sondergaard. Defining the principal eigenvalues of the symmetric part of the H_{ij} tensor as the acceleration strain-rates, and sort them in descending order such that $\alpha_h \geq \beta_h \geq \gamma_h$, the acceleration strain-rates distribution was also studied in a similar fashion.

The probability density functions of these principal eigenvalues for wk346 and wk2768 are shown in figures 5.34 to 5.37. All the eigenvalues have been normalized by the magnitude of the intermediate principal eigenvalue $|\beta_h|$ so that the normalized intermediate principal eigenvalue can only take on values of ± 1.0

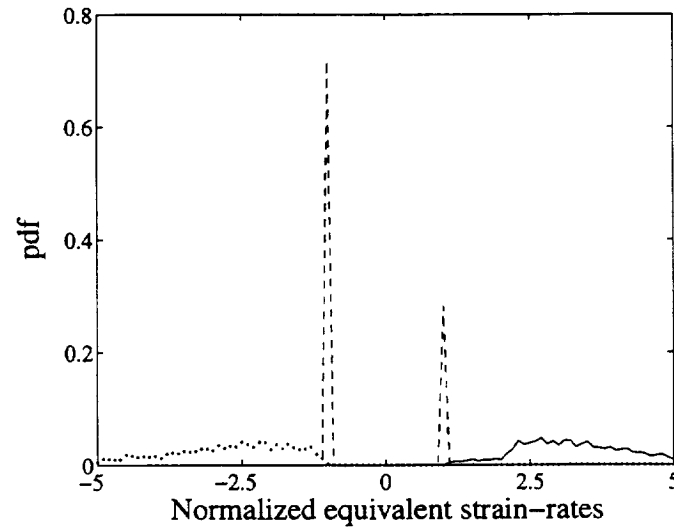
Two different plots are shown in each figure. The first plot includes all the data points in the flow while the other include points conditioned with local dissipation higher than 25% of the maximum local dissipation in the flow. More negative intermediate principal eigenvalue β_h than the positive ones are observed in the distribution functions, indicating that the local flow topology of stable-node/saddle/saddle is preferred to the unstable-node/saddle/saddle. The distribution for α_h and γ_h are almost symmetrical on both sides of the distribution functions. No significant peaks are observed for the broad α_h and γ_h distributions. Similar results are observed for flows at different times and Reynolds numbers.

5.4.5 Equivalent vorticity-acceleration strain alignment

Sondergaard reported preferential alignment of the vorticity vector with the intermediate rate-of-strain tensor direction and non-aligned with the most compressive rate-of-strain direction by studying the alignment probability density function of the alignment angle between the vorticity vector with the three principal strain-rates direction.

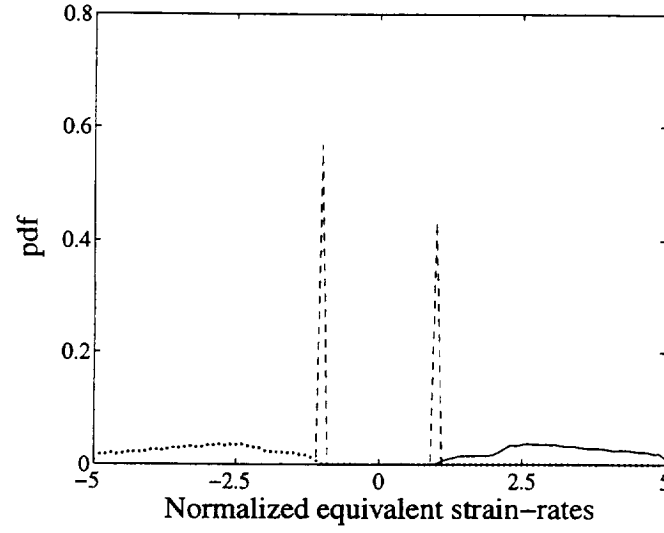


(a)

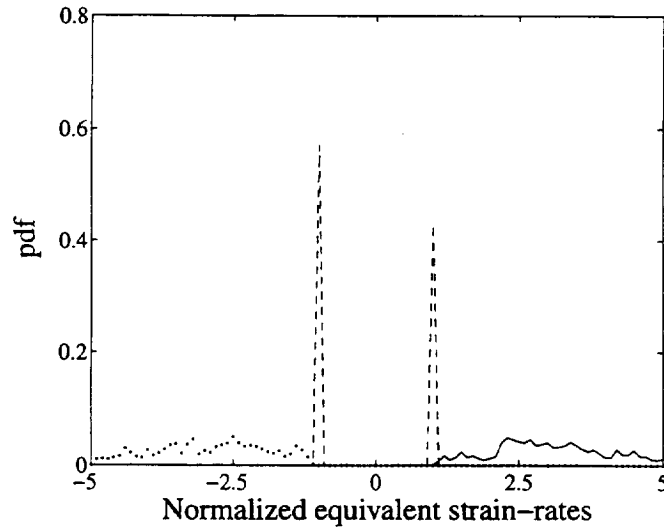


(b)

Figure 5.34: Probability density function of the principal acceleration strain-rates normalized by $|\beta_h|$ for wk346, $t=102.7$. —: α_h . ---: β_h: γ_h . (a) All data points. (b) $|Q_s(A_{ij})| \geq 25\%|Q_s(A_{ij})|_{max}$



(a)



(b)

Figure 5.35: Probability density function of the principal acceleration strain-rates normalized by $|\beta_h|$ for wk346, $t=204.8$. —: α_h . ---: β_h: γ_h . (a) All data points. (b) $|Q_s(A_{ij})| \geq 25\%|Q_s(A_{ij})|_{max}$

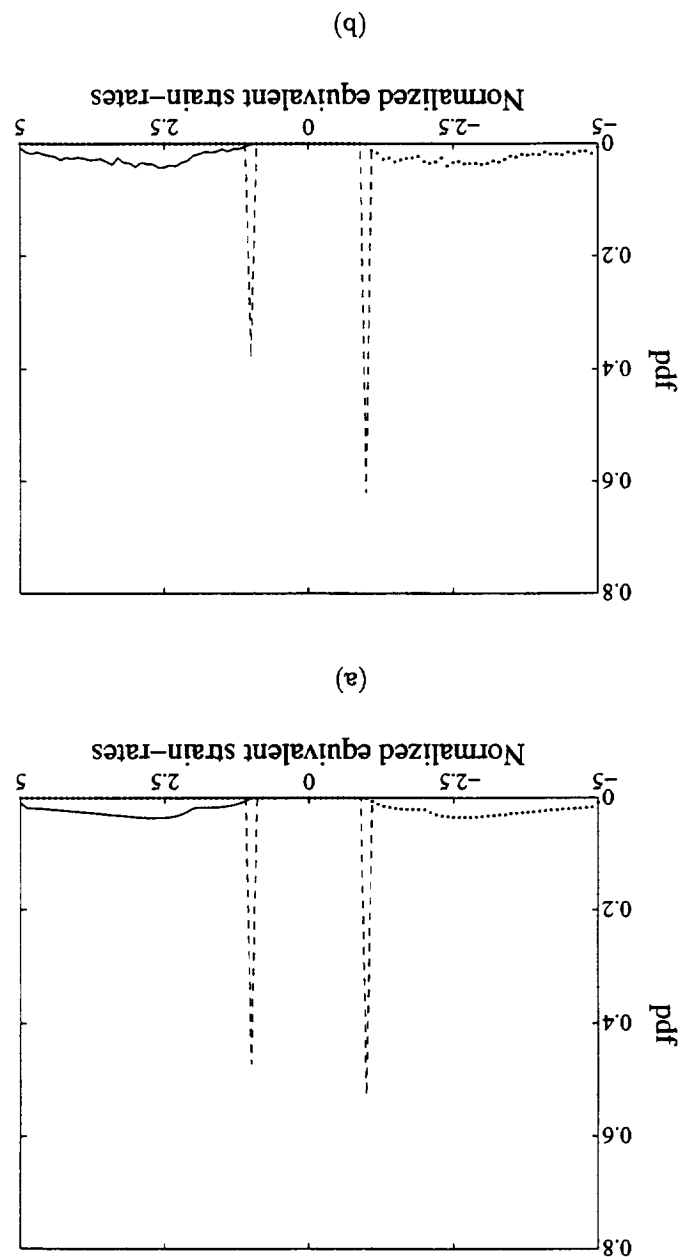
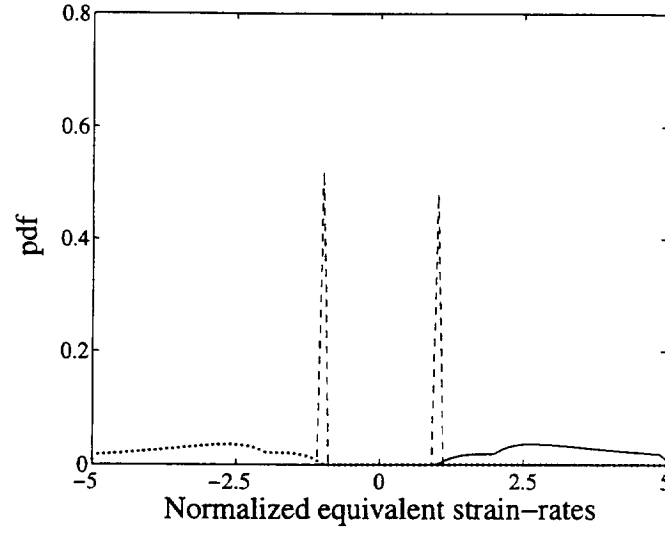
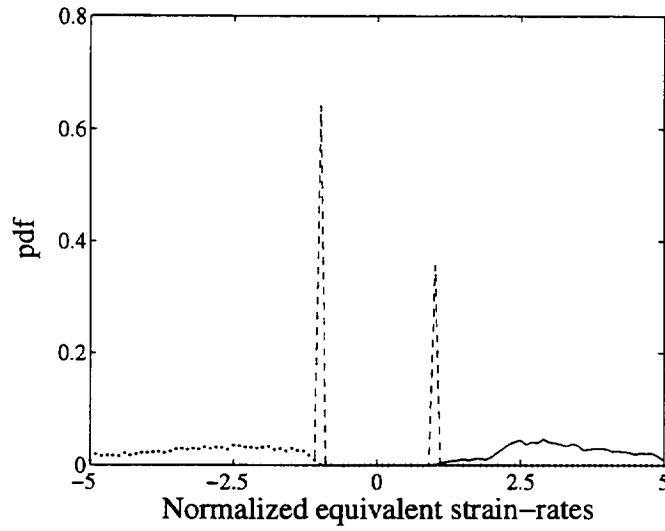


Figure 5.36: Probability density function of the principal acceleration strain-rates normalized by $|\beta_h|$ for wk2768, $t=99.8$. —: α_h . ---: β_h: γ_h . (a) All data points. (b) $|Q_s(A_{ij})| \geq 25\% |Q_s(A_{ij})|_{max}$



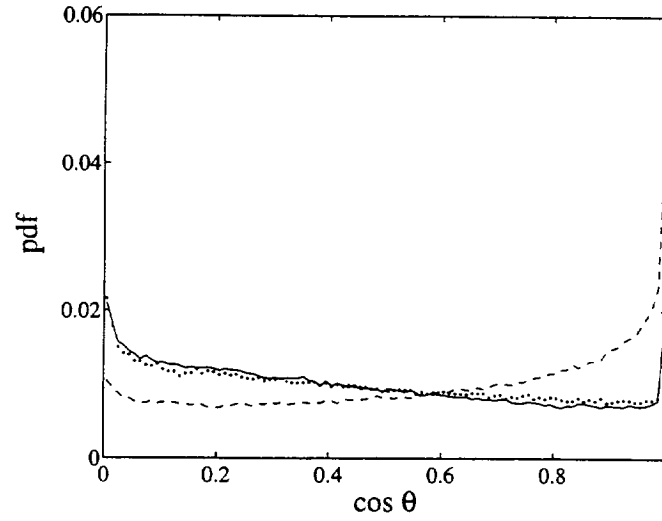
(a)



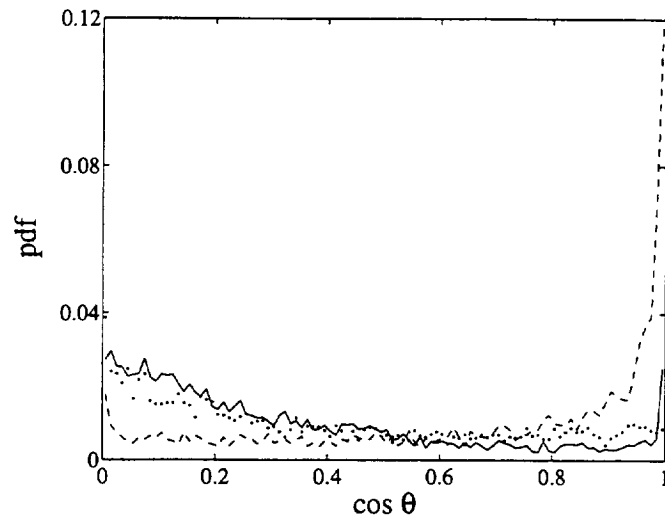
(b)

Figure 5.37: Probability density function of the principal acceleration strain-rates normalized by $|\beta_h|$ for wk2768, $t=194.6$. —: α_h . ---: β_h: γ_h . (a) All data points. (b) $|Q_s(A_{ij})| \geq 25\%|Q_s(A_{ij})|_{max}$

To compare the results between the velocity gradient tensor and the acceleration gradient tensor, similar studies were done for the H_{ij} tensor by studying the alignment angle between the equivalent vorticity vector (as defined in equation 4.55) with the acceleration strain-rates ($\alpha_h > \beta_h > \gamma_h$). Figures 5.38 to 5.41 plot the probability density functions of the cosine of the alignment angle θ between the equivalent vorticity with the three acceleration rate-of-strain directions of the H_{ij} tensor for both wk346 and wk2768. θ is any one of the three alignment angles between the equivalent vorticity and the acceleration rate-of-strain direction. The density functions do not show any significant difference between α_h and γ_h in all the plots. However, there is a strong preference for the equivalent vorticity vector to align with the intermediate rate-of-strain, β_h direction. This tendency becomes more pronounced (as indicated by the increased density functions levels) when data are conditioned with local dissipation of more than 25% of the maximum local dissipation in the flows. This observation appears to be independent of Reynolds number.

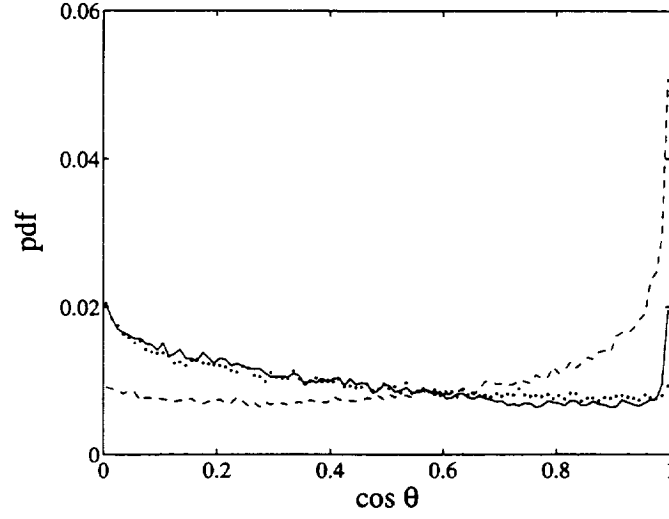


(a)

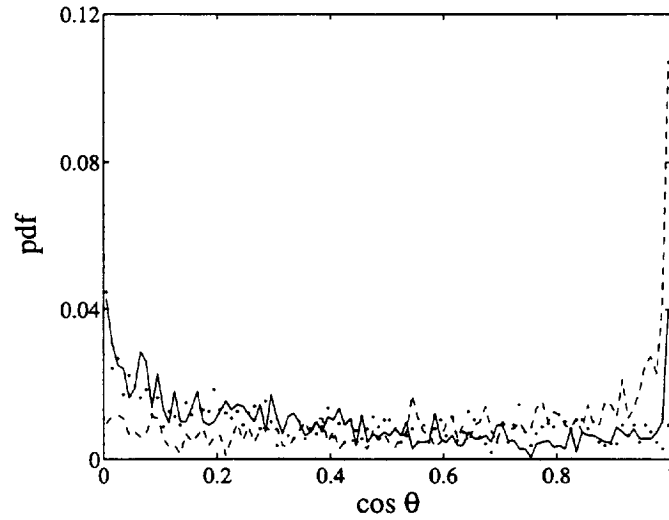


(b)

Figure 5.38: Probability density function of cosine of angle θ between the equivalent vorticity vector and the equivalent principal strain-rate directions for wk346, $t=102.7$. —: α_h . ---: β_h: γ_h . (a) All data points. (b) $|Q_s(A_{ij})| \geq 25\% |Q_s(A_{ij})|_{max}$

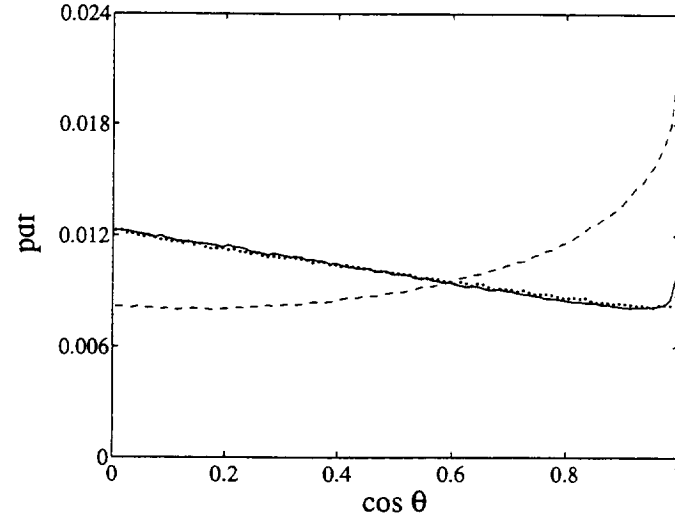


(a)

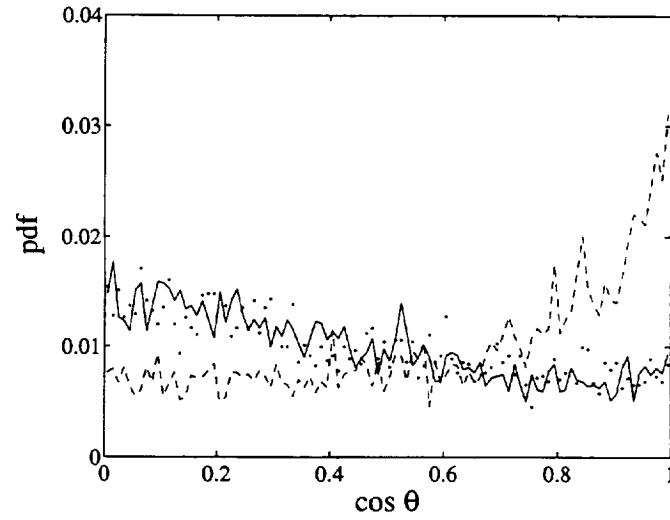


(b)

Figure 5.39: Probability density function of cosine of angle θ between the equivalent vorticity vector and the equivalent principal strain-rate directions for wk346, $t=204.8$. —: α_h . ---: β_h: γ_h . (a) All data points. (b) $|Q_s(A_{ij})| \geq 25\% |Q_s(A_{ij})|_{max}$

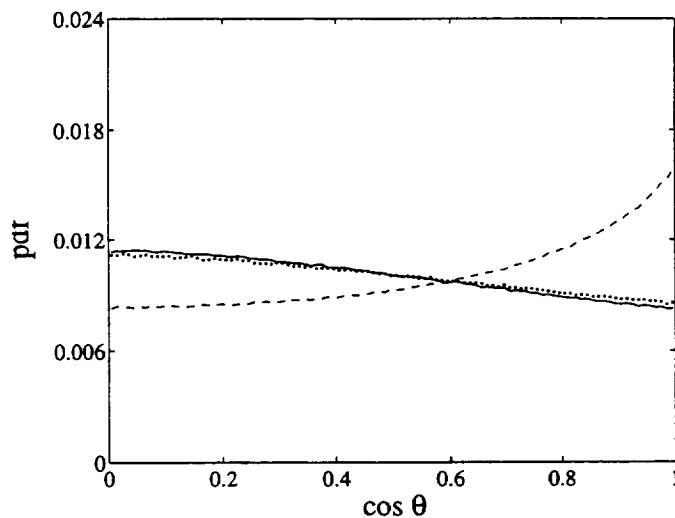


(a)

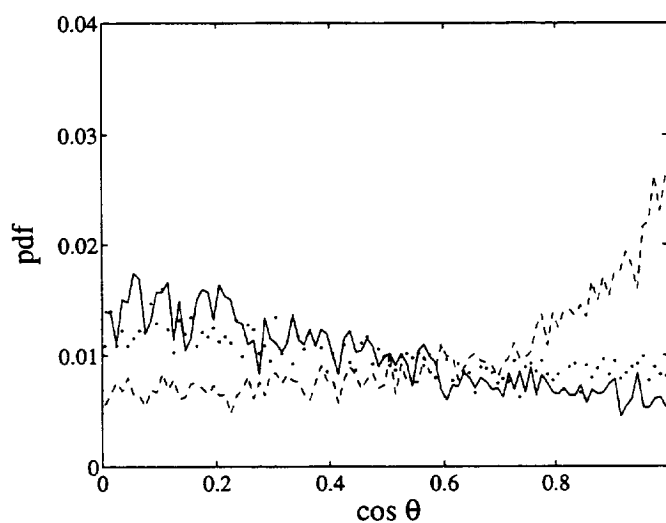


(b)

Figure 5.40: Probability density function of cosine of angle θ between the equivalent vorticity vector and the equivalent principal strain-rate directions for wk2768, $t=99.8$. —: α_h . ---: β_h . ···: γ_h . (a) All data points. (b) $|Q_s(A_{ij})| \geq 25\% |Q_s(A_{ij})|_{\max}$



(a)



(b)

Figure 5.41: Probability density function of cosine of angle θ between the equivalent vorticity vector and the equivalent principal strain-rate directions for wk2768, $t=194.6$. —: α_h . ---: β_h: γ_h . (a) All data points. (b) $|Q_s(A_{ij})| \geq 25\%|Q_s(A_{ij})|_{max}$

Chapter 6

Conclusions

The Lagrangian behavior of the velocity gradient tensor was studied using results from three direct numerical simulation of turbulent flows: an inviscid calculation of interactions between two vortex tubes, a homogeneous isotropic flow and a temporally evolving planar wake. Analysis of these flows revealed strong preference for the intermediate principal eigenvalue of the rate-of-strain tensor to be positive, with preferred local strain topology of unstable-node/saddle/saddle. There is also a preference for the vorticity vector to align with this intermediate principal eigenvector. These preferences were found to be stronger when data were conditioned at higher local dissipation regions. All these observations support earlier findings of other direct numerical simulated flows, including homogeneous isotropic flow and homogeneous shear flow[1], mixing layer[31], channel flow[2] and turbulent boundary layer[32]. These flows are very different in terms of large-scale motions and Reynolds numbers, indicating that these observations may be universal characteristics that are flow-independent.

A model of the evolution of A_{ij} based on the solution of a Restricted Euler equation contained asymptotic behavior consistent with these observations. This solution was compared with results obtained from an incompressible Euler calculation of two interacting vortex tubes. A coherent structure within this inviscid calculation was observed to exhibit characteristics predicted by the Restricted Euler model. This coherent structure evolved with the flow as the calculation approached singularity, always near the peak vorticity in the flow. Invariants of data points within this

structure have linear relationships of the form:

$$\lambda_a^3 + \lambda_a Q + R = 0, \quad (6.1)$$

$$\lambda_s^3 + \lambda_s Q_s + R_s = 0. \quad (6.2)$$

λ_a was concluded to be the most positive principal eigenvalue of the velocity gradient tensor while λ_s was the intermediate principal eigenvalue of the rate-of-strain tensor. Both λ_a and λ_s were found to be 0.40. The invariants of the velocity gradient tensor for data within this structure have relationships similar to those predicted by the Restricted Euler model.

The tensor H_{ij} , which is the anisotropic part of the acceleration gradient tensor, was studied in two different viscous flows: a relatively low Reynolds number decaying homogeneous isotropic flow in a periodic box, and a temporally evolving plane wake at two different Reynolds numbers. The magnitude of the invariants of the H_{ij} tensor of the homogeneous isotropic flow increased as the flow decayed. The intermediate acceleration strain-rate in this flow inclined to be negative, with a local strain topology of stable-node/saddle/saddle. Furthermore, the equivalent vorticity vector preferred to align with this intermediate acceleration strain-rate direction.

Behavior of acceleration gradient tensor of a temporally evolving planar wake at two different Reynolds numbers was also studied. The intensity of the highest gradients increased when the Reynolds number of this flow was higher. Otherwise, the shapes of the contour plots of the joint probability density function of the invariants of H_{ij} remained very similar. The H_{ij} tensor was found to be nearly symmetric in this moderately high Reynolds number simulation. The intermediate acceleration strain-rate also inclined to be negative, with local strain topology stable-node/saddle/saddle. A strong preferential alignment between the equivalent vorticity and the intermediate acceleration strain-rate direction was also observed. The most interesting result from the study of this flow was that the magnitude of H_{ij} was very small when data were conditioned at higher local dissipation regions. This result was not observed for the relatively low Reynolds number simulation of homogeneous isotropic flow. All the results obtained for the wake simulation were nearly the same at the two Reynolds numbers studied.

Appendix A

Velocity gradient tensor with random components

A velocity gradient tensor A_{ij} needs to be constructed such that its components are obtained from a random number generator with mean $E(x) = 0.0$ and variance $\sigma^2 = 1.0$. To make this velocity gradient tensor more “realistic”, the tensor needs to be forced to satisfy the continuity constraint for incompressible flow. Furthermore, in the case of isotropic flow, the volume integral of the second invariant Q must be zero due to the balance of the pressure gradients acting on the surface of a control volume. Therefore, the constructed A_{ij} would have to satisfy the condition that $E(Q) = 0.0$ as well.

To satisfy both conditions, the velocity gradient tensor A_{ij} is constructed from the sum of a symmetric tensor S_{ij} and an anti-symmetric tensor W_{ij} such that $A_{ij} = S_{ij} + W_{ij}$. The components of S_{ij} and W_{ij} tensors are obtained from a random number generator, which generates random numbers x with mean $E(x) = 0.0$ and variance $\sigma^2 = 1.0$. Forcing the trace of the S_{ij} tensor to zero, the components of S_{ij} are:

$$\begin{aligned} S_{11} &= x_1 - \frac{1}{3}(x_1 + x_2 + x_3), \\ S_{22} &= x_2 - \frac{1}{3}(x_1 + x_2 + x_3), \\ S_{33} &= x_3 - \frac{1}{3}(x_1 + x_2 + x_3), \end{aligned}$$

$$\begin{aligned}
S_{12} &= S_{21} = x_4, \\
S_{13} &= S_{31} = x_5, \\
S_{23} &= S_{32} = x_6.
\end{aligned} \tag{A.1}$$

Similarly, the components of the anti-symmetric tensor W_{ij} are:

$$\begin{aligned}
W_{11} &= W_{22} = W_{33} = 0.0, \\
W_{12} &= -W_{21} = x_7, \\
W_{13} &= -W_{31} = x_8, \\
W_{23} &= -W_{32} = x_9.
\end{aligned} \tag{A.2}$$

x_1, x_2, \dots, x_9 are nine different random numbers obtained from the random number generator. The A_{ij} tensor constructed this way satisfies the continuity constraint.

The second condition that the volume integral of Q must be zero can be satisfied by forcing the expected value of Q to zero, i.e. $E(Q) = 0.0$. Noting that S_{ij} tensor is symmetric and W_{ij} tensor is anti-symmetric,

$$Q = -\frac{1}{2}A_{im}A_{mi} = -\frac{1}{2}S_{im}S_{im} + \frac{1}{2}W_{im}W_{im} \tag{A.3}$$

Put

$$E(Q) = -\frac{1}{2}E(S_{im}S_{im}) + \frac{1}{2}E(W_{im}W_{im}) = 0.0. \tag{A.4}$$

Then

$$E(S_{im}S_{im}) - E(W_{im}W_{im}) = 0.0. \tag{A.5}$$

Now,

$$\begin{aligned}
E(S_{im}S_{im}) &= E(S_{11}^2 + S_{12}^2 + S_{13}^2 + S_{21}^2 + S_{22}^2 + S_{23}^2 + S_{31}^2 + S_{32}^2 + S_{33}^2) \\
&= E(S_{11}^2) + E(S_{12}^2) + E(S_{13}^2) + E(S_{21}^2) + \dots + E(S_{33}^2).
\end{aligned}$$

For the case when $E(x) = 0.0$,

$$\sigma^2 = E(x^2) - E(x)^2 = E(x^2), \tag{A.6}$$

and, for independent variables x ,

$$E(x_i x_j) = E(x_i)E(x_j) = 0.0; \quad i \neq j. \quad (\text{A.7})$$

Therefore, from $E(x_1^2) = E(x_2^2) = E(x_3^2) = \sigma^2 = 1.0$, and $E(x_1 x_2) = E(x_1 x_3) = E(x_2 x_3) = 0.0$, then

$$E(S_{im} S_{im}) = 8\sigma^2. \quad (\text{A.8})$$

To make $E(Q) = 0.0$, the variance of every component of W_{ij} tensor needs to be modified by a factor a , such that $E(Q) = E(S_{im} S_{im} - W_{im} W_{im}) = 0.0$. Therefore,

$$8\sigma^2 - 6a^2\sigma^2 = 0.0 \Rightarrow a^2 = \frac{4}{3}. \quad (\text{A.9})$$

Finally, the velocity gradient tensor A_{ij} with random number components which satisfies both the continuity and $E(Q) = 0.0$ constraints is obtained by adding S_{ij} and W_{ij} tensors together, such that:

$$\begin{aligned} S_{11} &= x_1 - \frac{1}{3}(x_1 + x_2 + x_3), \\ S_{22} &= x_2 - \frac{1}{3}(x_1 + x_2 + x_3), \\ S_{33} &= x_3 - \frac{1}{3}(x_1 + x_2 + x_3), \\ S_{12} &= S_{21} = x_4, \\ S_{13} &= S_{31} = x_5, \\ S_{23} &= S_{32} = x_6. \end{aligned} \quad (\text{A.10})$$

and,

$$\begin{aligned} W_{11} &= W_{22} = W_{33} = 0.0, \\ W_{12} &= -W_{21} = \sqrt{4/3}x_7, \\ W_{13} &= -W_{31} = \sqrt{4/3}x_8, \\ W_{23} &= -W_{32} = \sqrt{4/3}x_9. \end{aligned} \quad (\text{A.11})$$

Appendix B

De-aliasing technique

Consider a three-dimensional convolution sum:

$$\hat{w}(\mathbf{k}) = \sum_{|\mathbf{p}|, |\mathbf{q}| < k_c} \hat{u}(\mathbf{p}) \hat{v}(\mathbf{q}); \quad \mathbf{p} + \mathbf{q} = \mathbf{k}. \quad (\text{B.1})$$

k_c is the Nyquist “frequency”. This alias-free sum can be evaluated using only two sets of grids as well as truncating wave-vector modes outside a specified range, as described by Orszag[23]. Two sets of grids $\bar{\mathbf{x}}(\mathbf{j})$ and $\tilde{\mathbf{x}}(\mathbf{j})$ are selected such that:

$$\begin{aligned} \bar{\mathbf{x}}(\mathbf{j}) &= \frac{\pi}{k_c} (j_1, j_2, j_3); \quad 0 \leq j_m < 2k_c, \quad m = 1, 2, 3. \\ \tilde{\mathbf{x}}(\mathbf{j}) &= \frac{\pi}{k_c} (j_1 + \frac{1}{2}, j_2 + \frac{1}{2}, j_3 + \frac{1}{2}); \quad 0 \leq j_m < 2k_c, \quad m = 1, 2, 3. \end{aligned} \quad (\text{B.2})$$

The velocities represented on these two sets of grid points are:

$$\bar{u}(\mathbf{j}) = \sum_{|\mathbf{k}| < k_c} \hat{u}(\mathbf{k}) \exp[i\mathbf{k} \cdot \bar{\mathbf{x}}(\mathbf{j})], \quad (\text{B.3})$$

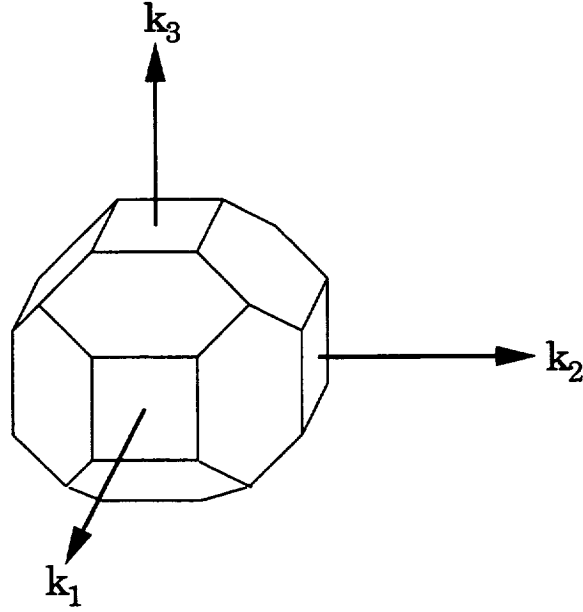
$$\tilde{u}(\mathbf{j}) = \sum_{|\mathbf{k}| < k_c} \hat{u}(\mathbf{k}) \exp[i\mathbf{k} \cdot \tilde{\mathbf{x}}(\mathbf{j})], \quad (\text{B.4})$$

$$\bar{v}(\mathbf{j}) = \sum_{|\mathbf{k}| < k_c} \hat{v}(\mathbf{k}) \exp[i\mathbf{k} \cdot \bar{\mathbf{x}}(\mathbf{j})], \quad (\text{B.5})$$

$$\tilde{v}(\mathbf{j}) = \sum_{|\mathbf{k}| < k_c} \hat{v}(\mathbf{k}) \exp[i\mathbf{k} \cdot \tilde{\mathbf{x}}(\mathbf{j})]. \quad (\text{B.6})$$

The transforms of both $\widehat{\bar{u} \cdot \bar{v}}$ and $\widehat{\tilde{u} \cdot \tilde{v}}$ are:

$$\bar{w}(\mathbf{k}) = \frac{1}{(2k_c)^3} \sum_{0 \leq j < 2k_c} \bar{u} \cdot \bar{v} \exp[-i\mathbf{k} \cdot \bar{\mathbf{x}}(\mathbf{j})]; \quad (\text{B.7})$$

Figure B.1: Region of retained Fourier modes defined by D .

$$\tilde{w}(\mathbf{k}) = \frac{1}{(2k_c)^3} \sum_{0 \leq j < 2k_c} \tilde{u} \cdot \tilde{v} \exp[-ik \cdot \tilde{x}(\mathbf{j})]. \quad (\text{B.8})$$

Therefore,

$$\frac{1}{2}[\bar{w}(\mathbf{k}) + \tilde{w}(\mathbf{k})] = \hat{w}(\mathbf{k}) + \sum_{\mathbf{n}} \hat{w}(\mathbf{k} + 2k_c \mathbf{n}); \quad (|\mathbf{k}| < k_c). \quad (\text{B.9})$$

The term involving \mathbf{n} represents the spurious aliasing errors. Patterson[24] has shown that only two of the three components are independently ± 1 while the remaining one is zero. Consequently, equation B.9 involves aliasing only to the extent of wave-vectors that are “doubly aliased”.

To remove the doubly-aliased terms, Orszag[23] considered a region D such that $\hat{u}(\mathbf{k}) = \hat{v}(\mathbf{k}) = 0$ for \mathbf{k} outside the region:

$$D = \begin{cases} |k_\alpha| < k_c & \alpha = 1, 2, 3 \\ |k_\alpha \pm k_\beta| < \frac{4k_c}{3} & \alpha, \beta = 1, 2, 3, \quad \alpha \neq \beta \end{cases} \quad (\text{B.10})$$

This inequality defines the region D bounded by an 18-sided polyhedron, as shown in the perspective sketch of figure B.1. If \mathbf{k} is outside the region D , then the doubly-aliased terms in equation B.9 must be identically zero since there are no nonzero

components of $\hat{u}(\mathbf{p})$, $\hat{v}(\mathbf{q})$ that can contribute to $\hat{w}(\mathbf{k}+2k_c\mathbf{n})$ such that $\mathbf{k}+2k_c\mathbf{n} = \mathbf{p}+\mathbf{q}$ with $\mathbf{k}, \mathbf{p}, \mathbf{q} \in D$. Therefore, if the spectral truncation is made so that the only excitable Fourier modes lie within the region D , then three-dimensional alias-free convolution sums are computable exactly on just the two sets of grids $\bar{x}(\mathbf{j})$ and $\tilde{x}(\mathbf{j})$.

Appendix C

Energy and velocity derivatives spectra

The energy spectrum for the homogeneous isotropic flow was determined and shown in figure C.1(a). This energy spectrum is plotted against the magnitude of the three dimensional wave number vector, k . Both the energy spectrum $E(k)$ and the wave number k are defined as:

$$E(k) = u_1(k)^2 + u_2(k)^2 + u_3(k)^2, \quad (\text{C.1})$$

and

$$k = \sqrt{k_1^2 + k_2^2 + k_3^2}. \quad (\text{C.2})$$

k_1 , k_2 and k_3 are the wave numbers in the three spatial directions. The Kolmogorov $k^{-5/3}$ scaling was superimposed onto the same plot, for comparison. Only a very small portion of the energy spectrum exhibits the $k^{-5/3}$ scaling, indicating that this low Reynolds number simulation is not close to the “turbulent” flow. However, the spectrum shows that the grid size used in the simulation is sufficient to resolve all the wave numbers.

In calculating the velocity gradient tensor, $A_{ij} = \partial u_i / \partial x_j$, there is a concern that the grid size used in the simulation may not be able to resolve this velocity gradient at higher wave numbers. To validate the resolutions, the spectrum of A_{ij} , denoted as $E_A(k)$, was determined in a similar way as the energy spectrum with $E_A(k)$ defined

as:

$$E_A(k) = A_{11}(k)^2 + A_{22}(k)^2 + A_{33}(k)^2. \quad (\text{C.3})$$

The $E_A(k)$ spectrum is plotted in figure C.1(b). This spectrum shows that the grid size used in the simulation is able to resolve the higher wavenumbers of the velocity derivatives.

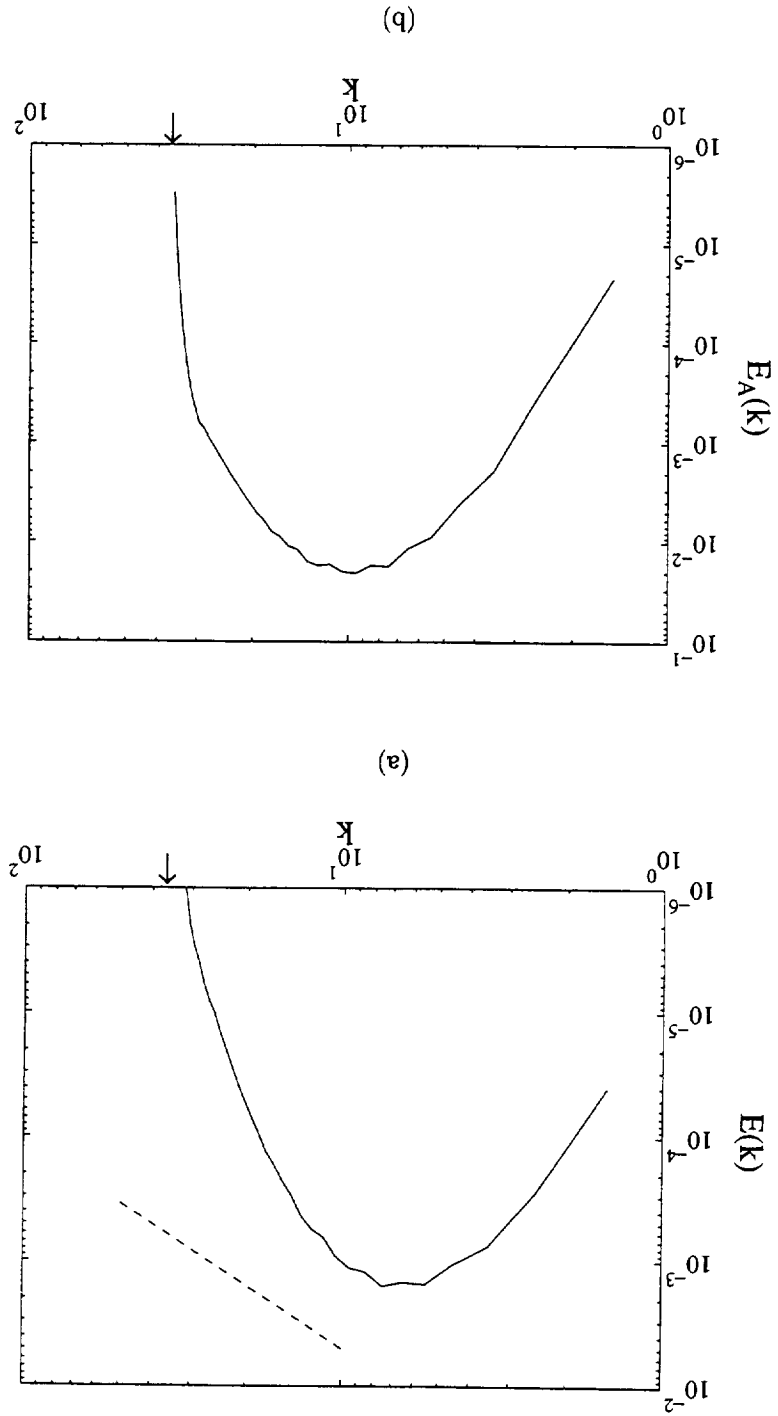
Higher derivatives of the velocity fields were required in calculating the H_{ij} tensor from either equation 2.4 or 2.5. To get a “feel” for the resolution of these higher velocity derivatives, the spectra for $\partial A_{ij}/\partial x_m$ and $\partial^2 A_{ij}/\partial x_m \partial x_m$ were determined in a similar way as the energy spectrum. These spectra are defined as:

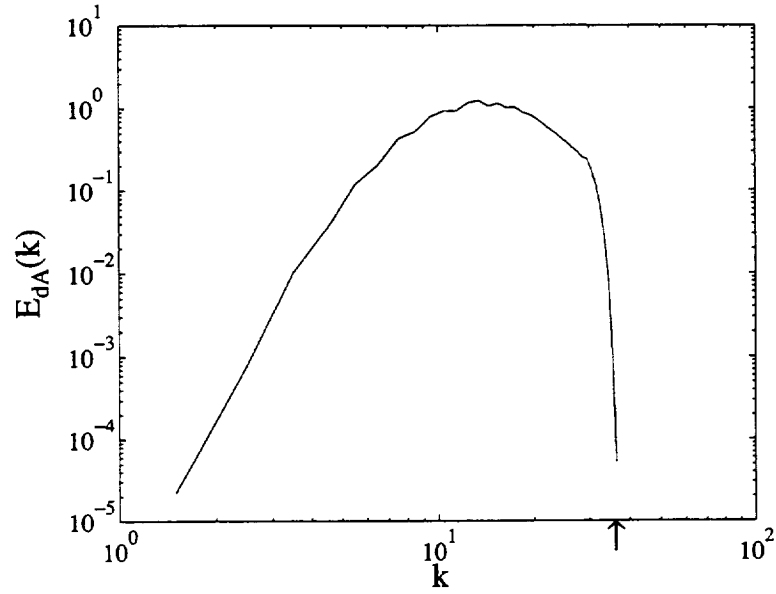
$$E_{dA}(k) = \frac{\partial A_{11}}{\partial x_1}(k)^2 + \frac{\partial A_{22}}{\partial x_2}(k)^2 + \frac{\partial A_{33}}{\partial x_3}(k)^2. \quad (\text{C.4})$$

$$E_{d2A}(k) = \frac{\partial^2 A_{11}}{\partial x_m \partial x_m}(k)^2 + \frac{\partial^2 A_{22}}{\partial x_m \partial x_m}(k)^2 + \frac{\partial^2 A_{33}}{\partial x_m \partial x_m}(k)^2; \quad m = 1, 2, 3. \quad (\text{C.5})$$

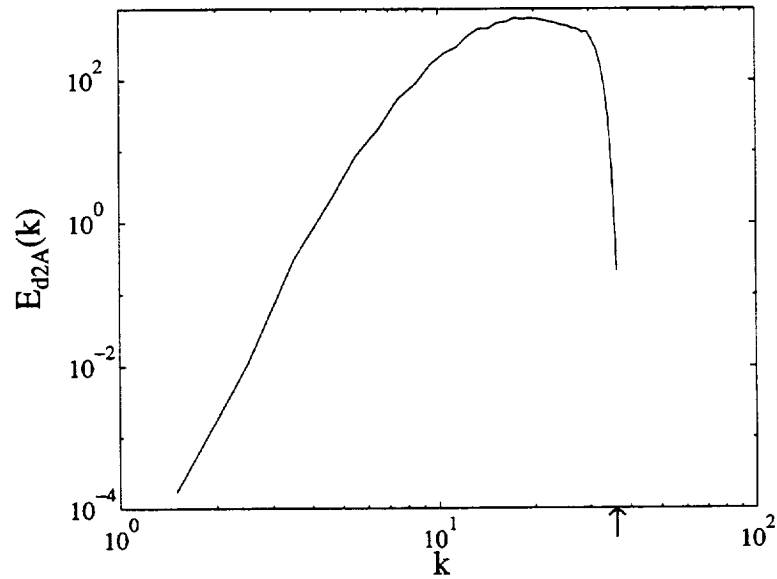
As the derivatives get higher, the higher wave numbers become more dominant since these derivative were obtained spectrally by multiplying the wave numbers to the velocity field. At higher wave numbers, the “energy” of these derivatives become much more significant compared to those obtained for the energy spectrum, as seen in the spectra shown in figure C.2. The abrupt cut-off of the spectra at the maximum k was due to the range of the wave numbers used in the simulation to remove aliasing errors, as explained in Appendix B.

Figure C.1: Energy and velocity gradient spectra for homogeneous isotropic flow at $\tau = 5.30$. \downarrow indicates the maximum wave number, k_{max} , resolved in the simulation. (a) —: energy spectrum. ---: Kolmogorov $k^{-5/3}$ scaling. (b) A_{ij} spectrum.





(a)



(b)

Figure C.2: Spectra for the higher derivatives of the velocity gradient tensor for homogeneous isotropic flow at $\tau = 5.30$. \uparrow indicates the maximum wave number, k_{max} , resolved in the simulation. (a) $\partial A_{ij}/\partial x_m$ spectrum. (b) $\partial^2 A_{ij}/\partial x_m \partial x_m$ spectrum.

Appendix D

Acceleration gradient tensor of Burgers vortex

Assuming a *steady* Burgers vortex with velocity field $u_i(x, y, z)$:

$$u_1 = -\frac{1}{2}x - Re \ y(1 - e^{-r^2})/r^2. \quad (D.1)$$

$$u_2 = -\frac{1}{2}y + Re \ x(1 - e^{-r^2})/r^2. \quad (D.2)$$

$$u_3 = z. \quad (D.3)$$

x , y and z are the three Cartesian coordinates with z being the vertical axis and $r = \sqrt{x^2 + y^2}$. $Re = \Gamma/8\pi\nu$ is the Reynolds number where Γ and ν are the circulation and the viscosity of the flow respectively.

D.1 The velocity gradient tensor A_{ij}

From the velocity field $u_i(x, y, z)$, the velocity gradient tensor $A_{ij} = \partial u_i / \partial x_j$ was obtained by taking the corresponding derivatives of u_1 , u_2 and u_3 with x , y and z :

$$A_{11} = -\frac{1}{2} + Re \left[\frac{2xy}{r^4} (1 - e^{-r^2} - r^2 e^{-r^2}) \right]. \quad (D.4)$$

$$A_{12} = -\frac{Re}{r^2} (1 - e^{-r^2}) + Re \left[\frac{2y^2}{r^4} (1 - e^{-r^2} - r^2 e^{-r^2}) \right]. \quad (D.5)$$

$$A_{21} = \frac{Re}{r^2}(1 - e^{-r^2}) - Re \left[\frac{2x^2}{r^4}(1 - e^{-r^2} - r^2 e^{-r^2}) \right]. \quad (D.6)$$

$$A_{22} = -\frac{1}{2} - Re \left[\frac{2xy}{r^4}(1 - e^{-r^2} - r^2 e^{-r^2}) \right]. \quad (D.7)$$

$$A_{33} = 1.0. \quad (D.8)$$

$$A_{13} = A_{23} = A_{31} = A_{32} = 0.0. \quad (D.9)$$

Notice that the A_{ij} tensor is not symmetrical since $A_{12} \neq A_{21}$. Equations 1.16 to 1.18 give the definitions of the various invariants of the A_{ij} tensor for incompressible flow. Since the first invariant P is zero for all incompressible flow, the second and third invariants were determined to be:

$$Q(A_{ij}) = -\frac{3}{4} - Re^2 \left[\frac{1}{r^4}(1 - e^{-r^2} - r^2 e^{-r^2})^2 - e^{-2r^2} \right]. \quad (D.10)$$

$$R(A_{ij}) = -\frac{1}{4} + Re^2 \left[\frac{1}{r^4}(1 - e^{-r^2} - r^2 e^{-r^2})^2 - e^{-2r^2} \right]. \quad (D.11)$$

D.2 The acceleration gradient tensor, H_{ij}

The definition of the acceleration gradient tensor, H_{ij} was derived in equation 2.4. In the case of a steady Burgers vortex, the expression for the H_{ij} tensor can be simplified to:

$$H_{ij} = u_k \frac{\partial A_{ij}}{\partial x_k} + A_{ik} A_{kj} - (A_{km} A_{mk}) \frac{\delta_{ij}}{3}. \quad (D.12)$$

The various components of the H_{ij} tensor were determined with the help of a symbolic mathematical software, MAPLE[6]. With the various derivatives involved, the expressions of the components of the H_{ij} tensor are very complex. However, employing the fact that the Burgers vortex is an axisymmetric flow, these expressions could be simplified by studying only the case along any radial r -axis. Assuming $x = r$ and $y = 0$, the various components of the H_{ij} tensor are:

$$H_{11} = -\frac{1}{12}(-28Re^2 + 56Re^2 e^{-r^2} + 32Re^2 r^2 e^{-r^2} - 28Re^2 e^{-2r^2} - 32Re^2 r^2 e^{-2r^2} + 3r^4)/r^4. \quad (D.13)$$

$$H_{12} = Re e^{-r^2}. \quad (D.14)$$

$$H_{21} = Re e^{-r^2}(-1 + 2r^2). \quad (D.15)$$

$$H_{22} = -\frac{1}{12}(20Re^2 - 40Re^2 e^{-r^2} - 16Re^2 r^2 e^{-r^2} + 20Re^2 e^{-2r^2} + 16Re^2 r^2 e^{-2r^2} + 3r^4)/r^4. \quad (D.16)$$

$$H_{33} = -\frac{1}{6}(4Re^2 - 8Re^2 e^{-r^2} - 8Re^2 r^2 e^{-r^2} + 4Re^2 e^{-2r^2} + 8Re^2 r^2 e^{-2r^2} - 3r^4)/r^4. \quad (D.17)$$

$$H_{13} = H_{23} = H_{31} = H_{32} = 0.0. \quad (D.18)$$

Notice that the H_{ij} tensor is again not symmetrical since $H_{12} \neq H_{21}$. The invariants of H_{ij} have also been calculated using MAPLE. The first invariant $P(H_{ij})$ is again zero. The expressions for the second and third invariants are:

$$\begin{aligned} Q(H_{ij}) = & -2Re^2 e^{-2r^2} r^2 - \frac{3}{16} + Re^2 e^{-2r^2} - \frac{Re^2(1 - e^{-r^2})e^{-r^2}}{r^2} + \\ & \frac{1/2C_2 - 16/3Re^4(1 - e^{-r^2})^2 e^{-2r^2}}{r^4} + \\ & \frac{28}{3} \frac{Re^4(1 - e^{-r^2})^3 e^{-r^2}}{r^6} - \frac{13}{3} \frac{Re^4(1 - e^{-r^2})^4}{r^8}. \end{aligned} \quad (D.19)$$

$$\begin{aligned} R(H_{ij}) = & Re^2 e^{-2r^2} r^2 - \frac{1}{32} - \frac{1}{2}Re^2 e^{-2r^2} + \frac{8}{3}Re^4 e^{-3r^2}(1 - e^{-r^2}) + \\ & \frac{(-\frac{1}{4}Re^2(1 - e^{-r^2})e^{-r^2} - \frac{4}{3}Re^4 e^{-3r^2}(1 - e^{-r^2}) - \frac{4}{3}C_1)}{r^2} + \frac{\frac{1}{8}C_2 + 2C_1}{r^4} + \\ & [-\frac{20}{9}Re^4(1 - e^{-r^2})^3 e^{-r^2} - \frac{4}{9}Re^2(1 - e^{-r^2})e^{-r^2}(-\frac{2}{3}C_2 + \frac{16}{9}C_1) - \\ & \frac{4}{9}Re^2(1 - e^{-r^2})e^{-r^2}(\frac{5}{6}C_2 + \frac{16}{9}C_1) + \frac{8}{9}Re^2(1 - e^{-r^2})e^{-r^2}(-\frac{7}{6}C_2 + \frac{64}{9}C_1)]/r^6 + \\ & [\frac{5}{9}C_2(\frac{5}{6}C_2 + \frac{16}{9}C_1) - \frac{224}{27}Re^6(1 - e^{-r^2})^4 e^{-2r^2} + \frac{11}{18}Re^4(1 - e^{-r^2})^4 + \\ & \frac{2}{9}C_2(-\frac{2}{3}C_2 + \frac{16}{9}C_1) - \frac{7}{9}C_2(-\frac{7}{6}C_2 + \frac{64}{9}C_1)]/r^8 + \\ & \frac{92}{9} \frac{Re^6(1 - e^{-r^2})^5 e^{-r^2}}{r^{10}} - \frac{70}{27} \frac{Re^6(1 - e^{-r^2})^6}{r^{12}}. \end{aligned} \quad (D.20)$$

where :

$$C_1 = Re^4(1 - e^{-r^2})^2 e^{-2r^2}, \quad (D.21)$$

$$C_2 = Re^2(1 - e^{-r^2})^2. \quad (D.22)$$

There is an apparent singularity at $r = 0$ since both invariants Q and R involve terms with denominator containing r raised to various powers. This apparent singularity was removed using L'Hospital's rule, giving:

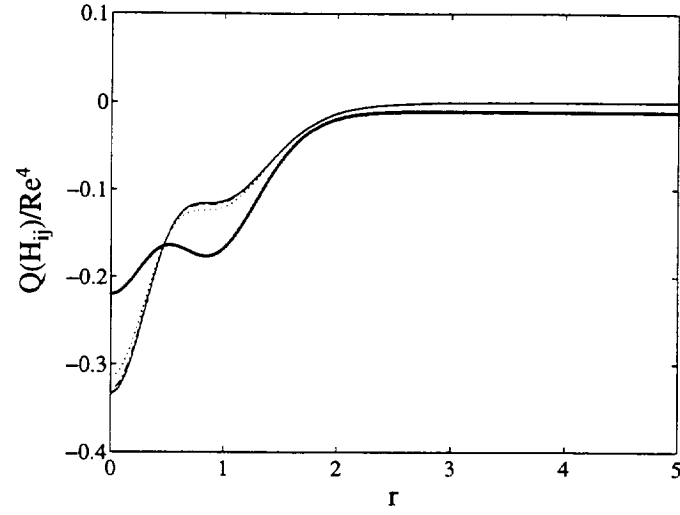
$$Q(H_{ij})|_{r=0} = -\frac{3}{16} + \frac{1}{2}Re^2 - \frac{1}{3}Re^4. \quad (D.23)$$

$$R(H_{ij})|_{r=0} = -\frac{1}{32} - \frac{5}{8}Re^2 - \frac{5}{6}Re^4 - \frac{2}{27}Re^6. \quad (D.24)$$

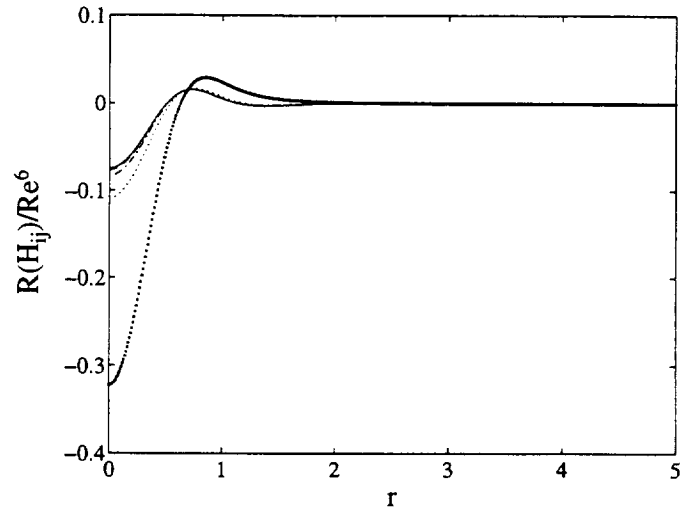
D.3 Behavior of $Q(H_{ij})$ and $R(H_{ij})$ with r

Figure D.1(a) shows the variations of $Q(H_{ij})/Re^4$ with r for Reynolds numbers of 2, 5, 10, 20 and 50. $Q(H_{ij})$ is normalized by Re^4 so that a self-similar solution for $Q(H_{ij})/Re^4$ is obtained for large Reynolds numbers ($Re \geq 50$). A self-similar solution is also obtained for $R(H_{ij})/Re^6$ when the Reynolds number is large, as shown in figure D.1(b).

Figure D.2 plots $Q(H_{ij})/Re^4$ against $R(H_{ij})/Re^6$, with the discriminant curve $D = (27/4)R^2 + Q^3 = 0.0$ superimposed onto the plot. The self-similar solution for large Reynolds number begins on a point that lies exactly on the discriminant curve with $Q(H_{ij})/Re^4 = -0.333$ and $R(H_{ij})/Re^6 = -0.074$ at $r = 0.0$. As r increases, this solution osculates the other discriminant curve at $Q(H_{ij})/Re^4 = -0.117$ and $R(H_{ij})/Re^6 = 0.015$ before approaching the origin.



(a)



(b)

Figure D.1: Normalized $Q(H_{ij})$ and $R(H_{ij})$ versus r . $\bullet\bullet\bullet: Re = 2$. $\cdot\cdot\cdot: Re = 5$. $\cdot\cdot\cdot\cdot: Re = 10$. $---: Re = 20$. $—: Re = 50$. (a) $Q(H_{ij})/Re^4$ vs r . (b) $R(H_{ij})/Re^6$ vs r .

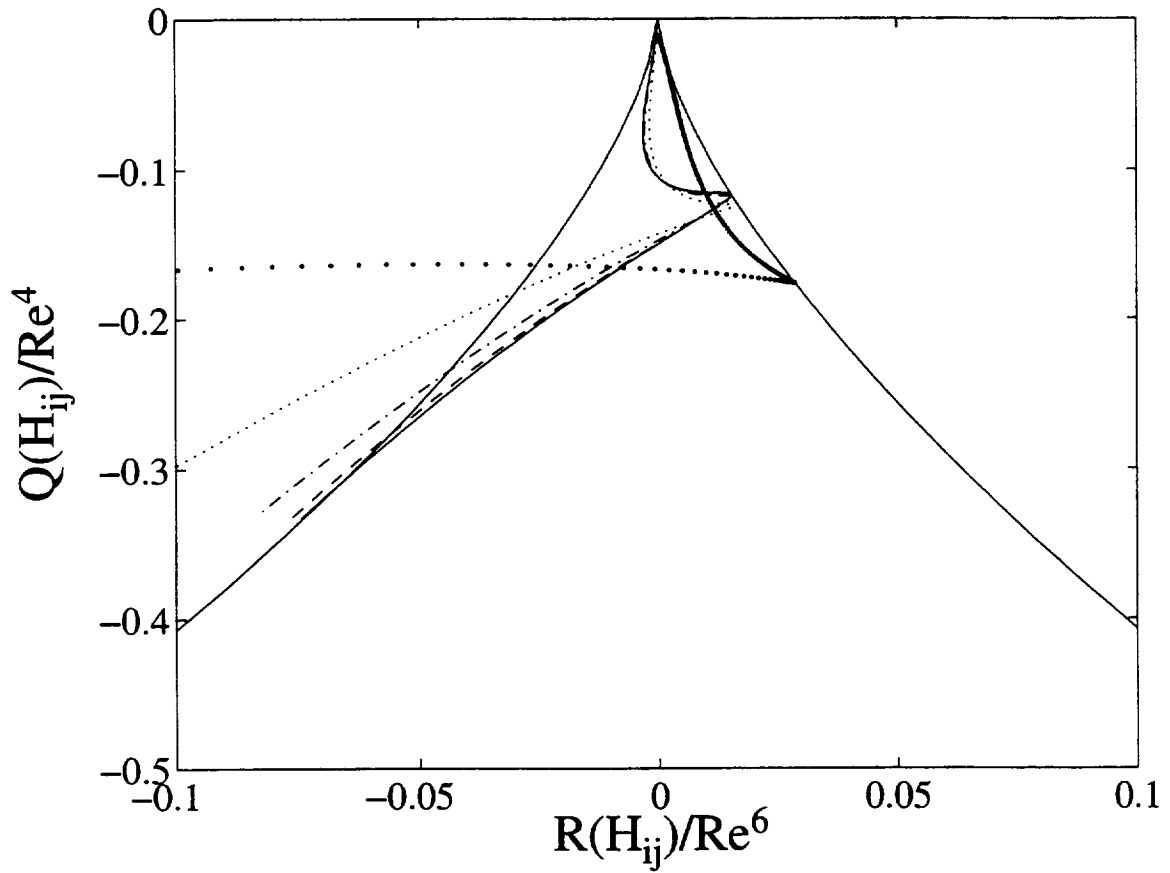


Figure D.2: $Q(H_{ij})/Re^4$ versus $R(H_{ij})/Re^6$. $\bullet\bullet\bullet$: $Re = 2$, \cdots : $Re = 5$, $-\cdot-\cdot-$: $Re = 10$, $----$: $Re = 20$, $—$: $Re = 50$.

Bibliography

- [1] W. T. Ashurst, A. R. Kerstein, R. M. Kerr, and C. H. Gibson. Alignment of vorticity and scalar gradient with strain rate in simulated Navier-Stokes turbulence. *Phys. Fluids*, 30 (8):2343–2353, 1987.
- [2] H. M. Blackburn, N. N. Mansour, and B. J. Cantwell. Topology of fine-scale motions in turbulent channel flow. *To appear in J. Fluid Mech.*, 1996.
- [3] G. W. Bluman and S. Kumei. *Symmetries and Differential Equations*. Springer-Verlag, 1989.
- [4] B. J. Cantwell. Exact solution of a Restricted Euler equation for the velocity gradient tensor. *Phys. Fluids A*, 4 (4):782–793, 1992.
- [5] B. J. Cantwell. On the behavior of velocity gradient tensor invariants in direct numerical simulations of turbulence. *Phys. Fluids A*, 5 (8):2008–2013, 1993.
- [6] D. Chen and C. Moler. *Symbolic Math toolbox, for use with MATLAB*. The Math Works Inc., first edition, 1993.
- [7] J. H. Chen, M. S. Chong, J. Soria, R. Sondergaard, A. E. Perry, M. Rogers, R. Moser, and B. J. Cantwell. A study of the topology of dissipating motions in direct numerical simulations of time-developing compressible and incompressible mixing layers. *Proceedings of the Center for Turbulence Research Summer Program, CTR-S90*, 1990.
- [8] M. S. Chong, A. E. Perry, and B. J. Cantwell. A general classification of three-dimensional flow fields. *Phys. Fluids A*, 2 (5):765–777, 1990.

- [9] R. Corral and J. Jiménez. Fourier/chebyshev methods for the incompressible Navier-Stokes equations in infinite domains. *Comp. Fluid Dyn.*, 1:361–368, 1992.
- [10] J. H. Ferziger, J. H. Kline, R. K. Avva, S. N. Bordalo, and K. L. Tzuoo. Zonal modelling of turbulent flows — philosophy and accomplishments, near-wall turbulence. *Zaric Memorial Conference*, page 800, 1990.
- [11] S. S. Girimaji and S. B. Pope. A diffusion model for velocity gradients in turbulence. *Phys. Fluids A*, 2 (2):242–256, 1990.
- [12] S. S. Girimaji and C. G. Speziale. A modified restricted Euler equation for turbulent flows with mean velocity gradients. *Phys. Fluids*, 7 (6):1438–1446, 1995.
- [13] J. R. Herring and R. M. Kerr. Development of enstrophy and spectra in numerical turbulence. *Phys. Fluids*, 5 (11):2792–2798, 1993.
- [14] J. O. Hinze. *Turbulence*. McGraw-Hill Book Company, second edition, 1975.
- [15] J. Jiménez. Kinematic alignment effects in turbulent flows. *Phys. Fluids A*, 4 (4):652–656, 1992.
- [16] Von Kármán. *J. Roy Aeronaut. Soc.*, 41:1109, 1937.
- [17] R. M. Kerr. Evidence for a singularity of the three-dimensional, incompressible Euler equations. *Phys. Fluids A*, 5 (7):1725–1746, 1993.
- [18] R. M. Kerr and F. Hussain. Simulation of vortex reconnection. *Physica D*, 37:474, 1989.
- [19] S. J. Kline, B. J. Cantwell, and G. M. Lilley. Comparison of computation and experiment. *Proceedings, 1980-1981 AFOSR-HTTM-Stanford Conference on Complex Turbulent Flows, Stanford University*, 1–3, 1982.
- [20] D. L. Marcus and J. B. Bell. Vorticity intensification and transition to turbulence in the three-dimensional Euler equations. *Commun. Math. Phys.*, 147:371, 1992.

- [21] M. V. Melander and F. Hussain. Cross-linking of two antiparallel vortex tubes. *Phys. Fluids A*, 1:633, 1989.
- [22] R. B. Pelz O. N. Boratav and N. J. Zabusky. Reconnection in orthogonally interacting vortex tubes: Direct numerical simulations and quantifications. *Phys. Fluids A*, 4 (3):581–605, 1992.
- [23] S. A. Orszag. Numerical simulation of incompressible flows within simple boundaries: I. Galerkin (spectral) representations. *Stud. Appl. Math*, 50:293–327, 1971.
- [24] G. S. Patterson and S. A. Orszag. Spectral calculations of isotropic turbulence: efficient removal of aliasing interactions. *Phys. Fluids*, 14:2538–2541, 1971.
- [25] A. Pumir and E. D. Siggia. Collapsing solutions to the 3-D Euler equations. *Phys. Fluids A*, 2 (2):220–241, 1990.
- [26] W. Rodi. A new algebraic relation for calculating the Reynolds stress. *Z. Angew. Math.*, 56:219, 1976.
- [27] W. Rodi. Recent developments in turbulence modelling. *Presented at 3rd International Symposium on Refined Flow Modelling and Turbulence Measurement*, 1988.
- [28] R. S. Rogallo. Numerical experiments in homogeneous turbulence. *NASA Technical Memorandum 81315*, 1981.
- [29] G. R. Ruetsch and M. R. Maxey. Small-scale features of vorticity and passive scalar fields in homogeneous isotropic turbulence. *Phys. Fluids A*, 3 (6):1587–1597, 1991.
- [30] R. Sondergaard. *Direct numerical simulation of a temporally evolving incompressible plane wake: Effect of initial conditions on evolution and topology*. PhD thesis, Stanford University, 1995.
- [31] J. Soria, R. Sondergaard, B. J. Cantwell, M. S. Chong, and A. E. Perry. A study of the fine-scale motions of incompressible time-developing mixing layers. *Phys. Fluids*, 6 (2):871–884, 1994.

- [32] A. Tsinober, E. Kitt, and T. Dracos. Experimental investigation of the field of velocity gradients in turbulent flows. *J. Fluid Mech.*, 242:169–192, 1992.
- [33] P. Vieillefosse. Local interaction between vorticity and shear in a perfect incompressible fluid. *J. Physique*, 43:837–842, 1982.
- [34] P. Vieillefosse. Internal motion of a small element of fluid in an inviscid flow. *Physica A*, 125:150–162, 1984.
- [35] A. Vincent and M. Meneguzzi. The spatial structure and statistical properties of homogeneous turbulence. *J. Fluid Mech.*, 225:1–20, 1991.

